ATOMISTIC INSIGHTS INTO PHOTOCATALYTIC MECHANISMS: MODELING SELECTED PROCESSES WITH DENSITY FUNCTIONAL THEORY

Pavle Nikačević

UNIVERSITAT
ROVIRA i VIRGILI

Atomistic Insights into Photocatalytic Mechanisms: Modeling Selected Processes with Density Functional Theory

PAVLE NIKAČEVIĆ

DOCTORAL THESIS
2023

UNIVERSITAT ROVIRA I VIRGILI
ATOMISTIC INSIGHTS INTO PHOTOCATALYTIC MECHANISMS: MODELING SELECTED PROCESSES WITH DENSITY
FUNCTIONAL THEORY
Pavle Nikačević

UNIVERSITAT ROVIRA I VIRGILI
ATOMISTIC INSIGHTS INTO PHOTOCATALYTIC MECHANISMS: MODELING SELECTED PROCESSES WITH DENSITY
FUNCTIONAL THEORY
Pavle Nikačević

Pavle Nikačević

Atomistic Insights into Photocatalytic Mechanisms: Modeling Selected Processes with Density Functional Theory

DOCTORAL THESIS

Supervised by
Prof. Núria López Alonso

Institute of Chemical Research of Catalonia
(ICIQ)
and Rovira i Virgili University (URV)

Tarragona
2023

Institut Català d'Investigació Química
Av. Països Catalans, 16
43007 Tarragona. Spain

Prof. Núria López Alonso, group leader in the Institute of Chemical Research of Catalonia,

I STATE that the present study, entitled "**Atomistic Insights into Photocatalytic Mechanisms: Modeling Selected Processes with Density Functional Theory**", presented by Pavle N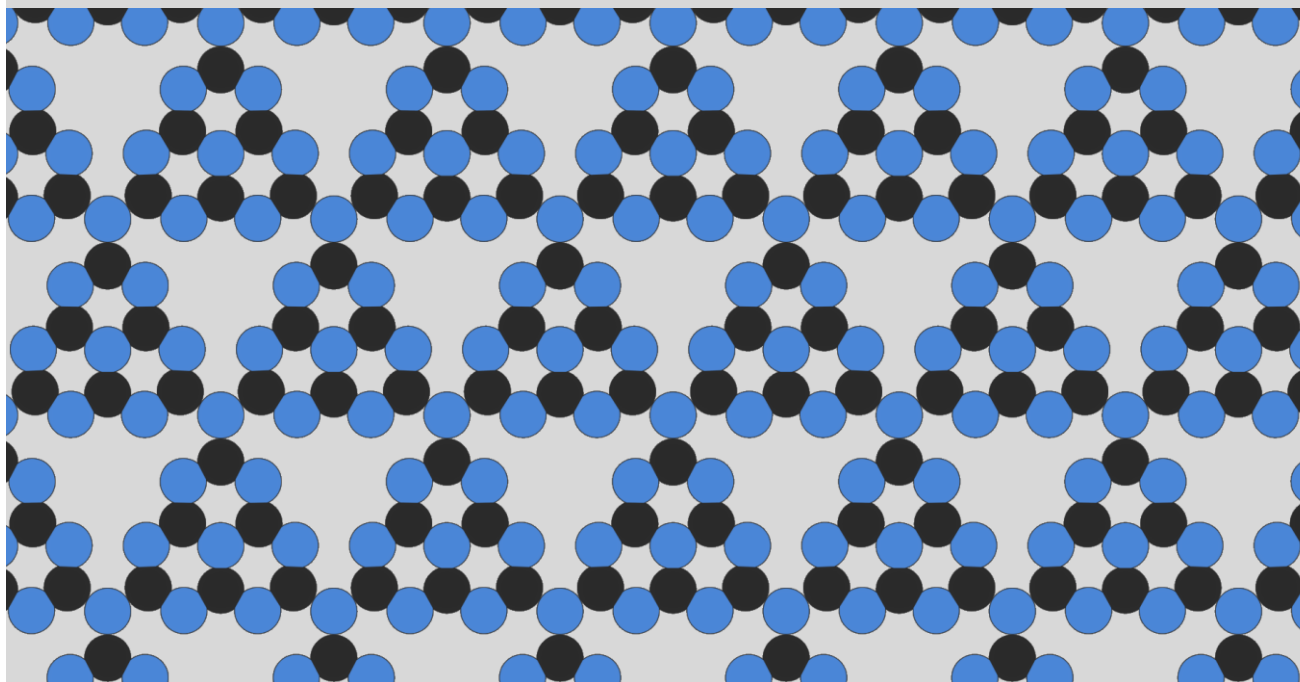ikačević for the award of the degree of Doctor of Chemical Science and Technology, has been carried out under my supervision at the Institut Català d'Investigació Química, ICIQ.

Tarragona, June 27th, 2023

Prof. Núria López Alonso

Sponsors

Acknowledgments

Here I will thank people that I consider to be direct positive influences that have led me to where I am today. There will be important people that I have not included, either for the sake of brevity or because I forgot, and I apologize to them.

To start, I would like to thank the people with whom I spent most of my childhood: my parents Čedo and Dragica, my grandparents Mićko, Andrijana, Mikoš and Slobodanka, my cousins Boća, Ljubiša and Darko, my best childhood friends Joca and Coka, and my neighbors Mira and Lulana.

Throughout the years until the end of high school, I made many great friendships that have lasted until today. In order not to forget anyone, I would like to thank all of them without mentioning anyone by name. You know who you are anyway. During this time, I also met some amazing teachers who had patience with me even though I was a menace as a student, and I thank them for that.

I would like to thank the people I met at the Petnica Science Center seminars when I was a high school student. The seminars were the crucial point that made me decide to pursue a B. Sc. in Chemistry. They also gave me the knowledge and confidence that enabled me to sail through my undergraduate studies at the University of Belgrade with ease. This was also made possible by the motivation of my classmate Aleksa, who to this day remains the person with the most brilliant scientific mind I have ever met.

I would like to thank ICIQ for accepting me as a summer fellow in 2018. In particular, I thank Prof. J. R. Galán-Mascarós and the members of his group, whose pleasant personalities made me return to the same institution for my Master's degree. I thank Prof. Tamara Todorović for supervising my B. Sc. thesis, together with the members of her group. I also thank Dr. Vladimir Blagojević, who co-supervised my work and introduced me to solid state DFT.

I thank Franziska for teaching me everything I needed to write my first paper. I thank Prof. Núria López for having me in her group and teaching me how to be a scientist, both from a technical and personal perspective. I also thank everyone in the computational office (and the ICIQ staff in general) for generously helping me solve technical, administrative, and personal problems. At ICIQ I have met some wonderful people under whose influence I have matured into an adult and who will be my lifelong friends. I thank them as well, with a special mention to Kosta, Franziska, Scott, and Julian. I thank the people in the Solar2Chem project for making the workshops very enjoyable. I thank the people who organized and supervised my stays at the DTU and EPFL and the friends I made there. I thank Beethoven for giving me hope in moments of sorrow. I thank again Prof. J. R. for

Contents

Abbreviations

AGI	Artificial General Intelligence
AI	Artificial Intelligence
AIMD	Ab Initio Molecular Dynamics
CBM	Conduction Band Minimum
COF	Covalent Organic Framework
CHE	Computational Hydrogen Electrode
DFA	Density Functional Approximation
DFT	Density Functional Theory
EnT	Energy Transfer
GC-DFT	Grand-Canonical Density Functional Theory
GGA	Generalized Gradient Approximation
g-CN	Graphitic Carbon Nitride
HAP	Hydroxyapatite
HER	Hydrogen Evolution Reaction
HF	Hartree–Fock
HPER	Hydrogen Peroxide Evolution Reaction
LHO	Linear Harmonic Oscillator
LSPR	Localized Surface Plasmon Resonance
MD	Molecular Dynamics
MEP	Minimum Energy Path
ML	Machine Learning
MOF	Metal-Organic Framework
mpg-CN	Mesoporous Graphitic Carbon Nitride
NEB	Nudged Elastic Band
OER	Oxygen Evolution Reaction
PAW	Projector-Augmented Wave
PCET	Proton-Coupled Electron Transfer
PCN	Polymeric Carbon Nitride
PDE	Partial Differential Equation
PDS	Potential-Determining Step
PES	Potential Energy Surface

PET	Photoinduced Electron Transfer
SHE	Standard Hydrogen Electrode
QD	Quantum Dot
QP	Quasiparticle
VBM	Valence Band Maximum
XPS	X-ray Photoelectron Spectroscopy
XRD	X-Ray Diffraction

List of publications

1. Influence of Oxygen Vacancies and Surface Facets on Water Oxidation Selectivity toward Oxygen or Hydrogen Peroxide with $BiVO_4$. P. Nikačević, F. Hegner, J. R. Galán-Mascarós, and N. López. *ACS Catal.* **2021**, *11* (21), 13416—13422.

2. Mixed Excitonic Nature in Water-Oxidized $BiVO_4$ Surfaces with Defects. R. Steinitz-Eliyahu, D. Hernangómez-Pérez, F. Hegner, P. Nikačević, N. López, and S. Refaely-Abramson. *Phys. Rev. Mater.* **2022**, *6*, 065402.

3. Insights into the Role of Graphitic Carbon Nitride as a Photobase in Proton-Coupled Electron Transfer in (sp^3)C–H Oxygenation of Oxazolidinones. A. Galushchinskiy, Y. Zou, J. Odutola, P. Nikačević, J. Shi, N. Tkatchenko, N. López, P. Farràs, and O. Savateev. *Angew. Chem. Int. Ed.* **2023**, *135*, e202301815.

4. Co-Doped Hydroxyapatite as Photothermal Catalyst for Selective CO_2 Hydrogenation. P. Yong, H. Szalad, P. Nikačević, G. Gorni, S. Goberna, L. Simonelli, J. Albero, N. López, H. García. *Appl. Catal. B* **2023**, *333*, 122790.

Pavle Nikačević has done the complete computational part for publications No. 1, 3, and 4. He participated in the writing process of all four publications and was the main writer of publication No. 1.

Abstract

Rising global energy demand and the environmental impact of fossil fuels have increased the need for sustainable energy solutions. Photocatalysis offers a way to harness solar energy to produce renewable fuels and industrially viable chemicals, and to degrade organic pollutants. This thesis explores the use of atomistic modeling based on Density Functional Theory to systematically model, understand, and optimize various photocatalytic processes. The research is focused on three studies: The influence of oxygen vacancies on the water oxidation mechanism on bismuth vanadate, showing that the removal of vacancies shifts the selectivity from oxygen to hydrogen peroxide; the mechanism of photocatalytic oxazolidinone oxidation to oxazolidinedione on carbon nitride, demonstrating the necessity of proton-coupled electron transfer from the substrate to the catalyst, enabled by light absorption; and photothermal carbon dioxide hydrogenation to carbon monoxide on cobalt-doped hydroxyapatite, showing that increasing the doping level changes the mechanism and nature of photoabsorption from intragap-state-induced to localized-surface-plasmon-resonance-induced. These results reveal a complex interplay between catalyst structure, nature of light absorption, and reaction mechanism, and provide valuable insights for the design of more efficient photocatalysts.

Chapter 1

Introduction

1.1 Mitigating the Global Energy Crisis: A Multi-Angle Approach

Since the Industrial Revolution, the use of fossil fuels has become essential to the functioning of society.[1] The unprecedented pace of technological progress brought about by the revolution, coupled with a rapidly growing world population and the nature of the capitalist mode of production,[2] has led to an exponential increase in energy demand (**Figure 1.1**). The massive emission of CO_2 produced by the burning of fossil fuels has contributed to an increase in the average global temperature (**Figure 1.2**), which is expected to exceed the targeted 2 °C increase over pre-industrial levels.[3] Global warming is responsible for a wide range of environmental effects that are progressively harming life on Earth.[4, 5] In addition, it is estimated that airborne particulate matter ($PM_{2.5}$) produced by the combustion of fossil fuels leads to more than 10 million premature human deaths each year.[6] These factors constitute a global energy crisis, which is considered one of the most important problems for mankind to solve.[7] Such a complex problem can only be addressed by approaching it from multiple angles,[8] such as:

- The **scientific** angle, concerned with providing an understanding of natural principles that can lead to new technologies for more sustainable energy production;

- The **technological** angle, concerned with the optimization of energy production processes to make them practical on an industrial scale;

- The **political** angle, which aims to optimize sustainable energy production by changing legal policies;[9]

- The **socioeconomic** angle, which deals with the high economic impact that would occur in society if the fossil fuel industry, one of the largest industries in the world,[10] were to be replaced by an alternative;

- The **educational** angle, which is concerned with raising awareness among the general population about the severity of the crisis and the impact of individual as well as collective actions.

In this thesis, I focus on the scientific angle*.
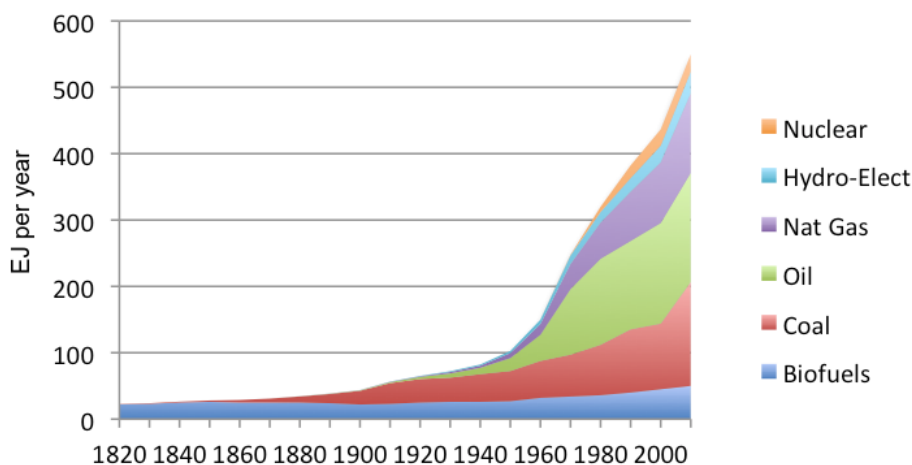
Figure 1.1: The global energy consumption in the last 200 years (EJ: Exajoule). The figure is taken from ref. [11].
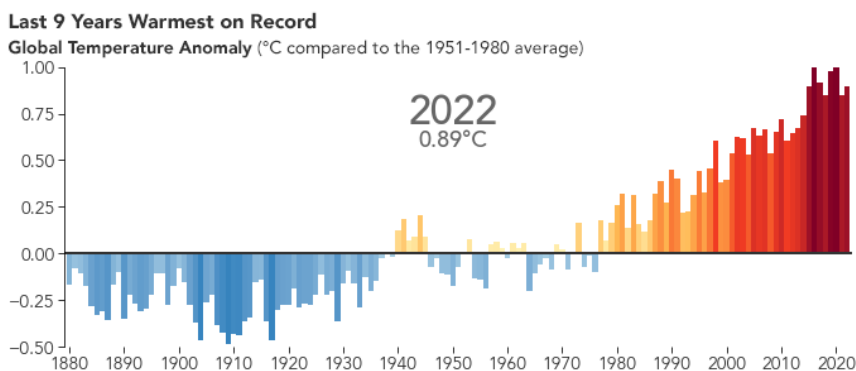
Figure 1.2: The global yearly average temperature in the last 150 years. The figure is taken from ref. [12].

---

*It is, however, not possible to draw strict boundaries between the angles.

1.2 A Sustainable Alternative to Fossil Fuels: Solar Energy

The Sun is a major source of energy on Earth—it is estimated that the Sun provides the Earth with as much energy in one hour as is used worldwide in a year.[13] Although fossil fuels represent indirect solar energy accumulated by living organisms over hundreds of millions of years, the direct use of solar energy is a more sustainable approach that avoids the problems associated with fossil fuel combustion. In fact, technologies that use direct solar energy (or simply "solar energy") have been known since the 19th century,[14] but their more serious development began only after the oil crises of the 1970s.[15] Today, solar energy is widely used for various purposes, such as generating electricity or heat, where it is converted into electrical or thermal energy, respectively. In addition, solar energy can be converted into chemical energy through photocatalysis. The products obtained are known as "solar chemicals", which can be used either as a sustainable alternative to their conventionally produced counterparts, or to store and subsequently generate energy themselves (solar fuels). Alternatively, instead of producing a desired solar chemical, photocatalysis can be used as a means of degrading harmful substances.[16]

1.3 Heterogeneous Photocatalysis

Photocatalysis can be traced back to the early 20th century, when it was discovered that substances could be degraded by light in the presence of certain compounds, such as ZnO and uranium salts.[17] A major breakthrough came in 1972,[18] when a TiO_2 electrode was shown to split water when irradiated, producing H_2 and O_2. Today, numerous photocatalytic processes are known, and I explore some of them in the following paragraphs. I only discuss heterogeneous photocatalytic processes where the reactant and the catalyst are in different phases (solid, liquid, or gas),[19] as these are the subject of my research.[†]

1.3.1 What Makes a Good Catalyst: The Scope of Heterogeneous Photocatalysts

Since every electrically charged particle interacts with photons, all matter composed of atoms can absorb light to some extent. Chemical systems

---

[†]Homogeneous photocatalysis, on the other hand, deals with processes where the reactant and the catalyst are in the same phase.[20] Homogeneous photocatalysts are considerably more difficult to separate from the reaction mixture and reuse, making them less sustainable.

absorb light through various mechanisms, such as rotational and vibrational transitions.[21] The mechanism primarily responsible for catalytic activity is absorption by the electrons, which excites an electron and leaves a positively charged "hole" in the electronic structure. The high-energy electron and the hole (photogenerated carriers) interact electrostatically (exciton binding). After the carriers are separated from the exciton, they can interact with the reactant, changing its electronic structure, resulting in its reduction (in the case of electrons) or oxidation (in the case of holes). For the photocatalytic process to be effective, the photogenerated carriers must be separated from the exciton long enough for them to interact with the reactant rather than recombine with each other. One way to achieve this separation is to ensure that there is an energy gap between the highest-energy electrons in the ground state and the lowest-energy electrons in the excited state. This is the case in semiconductors and insulators, where there is a band gap between the energy of the occupied electronic states (valence band) and the vacant electronic states (conduction band). However, because the catalyst does not absorb photons with energy lower than that required to excite the electrons, insulators could only function as photocatalysts with light of a sufficiently low wavelength, such as ultraviolet (UV) light. This leaves semiconductors as the most suitable photocatalysts for solar light. Furthermore, if a system catalyzes one process efficiently, it will not necessarily be efficient for another process due to specific interactions between the catalyst and the reactant. I will now review several classes of widely used photocatalysts, some of which I have studied in my own work, and discuss what makes them efficient for the processes they catalyze.

Bulk semiconductors: Although the materials in this class are often nanostructured or made into thin films, they also exist in a bulk, 3D form. Some of the subclasses belonging to this class are metal oxide catalysts such as ZnO, lead halite perovskites such as $CsPbBr_3$,[22] and traditional III-V[‡] semiconductors such as GaAs. The catalysts belonging to this class are often stable, have a large specific surface area and good adsorption properties, but are often difficult to modify and exhibit poor exciton dynamics as well as fast recombination of photogenerated carriers.[23]

Out of these, I have worked with the subclass of metal oxide catalysts. The subclass contains binary oxides such as ZnO and TiO_2 which are some of the oldest known photocatalysts, as well as the mixed metal oxides such as $SrTiO_3$. Since these photocatalysts suffer from fast recombination, they are often modified by doping or metal deposition, both of which can facilitate

---

[‡]The Roman numerals correspond to the old names of the periodic table groups 13 and 15 and indicate the number of valence electrons of the atoms in the group.

charge separation and increase the lifetime of photogenerated carriers.[24]

One of the catalysts used in my work, $BiVO_4$, is also a notable member of this subclass. It has a relatively narrow band gap of 2.4 eV and is inexpensive, stable in aqueous solution, and non-toxic.[25] To improve its photocatalytic performance, $BiVO_4$ can be modified in several ways.[26] When the catalyst surface is modified with graphene, an improved degradation of dyes is observed due to the improved charge separation and increased specific surface area.[27–31] An improved dye degradation was also observed with $BiVO_4$ doped with non-metals such as S,[32] B,[33] and F,[34] as well as with wide range of metals.[26] Another strategy to slow down recombination in $BiVO_4$ is combining it with another semiconductor to make a composite catalyst.[26] This can be done with TiO_2,[35] Cu_2O,[36] polymeric carbon nitride,[37] Bi_2WO_6,[38] as well as BiOCl.[39]

As stated above, the performance of bulk semiconductor photocatalysts can be improved by depositing metals on them. The electron cloud in the deposited metallic nanoparticle can interact with light in a process called localized surface plasmon resonance (LSPR),[40] leading to an improved light absorption and charge transfer to the semiconductor.[41] An example of such a catalyst is Co-doped hydroxyapatite where metallic Co nanoparticles deposit onto the Co-hydroxyapatite semiconductor surface,[42] also used in my work.

Organic polymers: Photocatalysts in this group include carbon nitrides, π-conjugated polymers, and covalent organic frameworks (COFs).[43–45] Also called "soft photocatalysts",[43] they are composed of earth-abundant light elements and are often cheaper and less toxic than inorganic semiconductors while retaining their stability and versatility.[45] They exhibit high exciton binding energies, which allows for the absorption of a wider spectrum of light,[46] but hinders charge separation.[47]

The class that I have used in my work are carbon nitrides, consisting of polymeric carbon nitride (PCN), poly(heptazine imide) (PHI), and poly(triazine imide) (PTI). They have high oxidative and reductive power and are easily synthesized from inexpensive precursors.[43, 48, 49] Unlike bulk semiconductors, they are often micro- and nanostructured, as porosity and surface area can strongly influence their photocatalytic performance.[45]

In my work I have used PCN, also called "melon". It has a complex structure consisting of heptazine units linked into chains by imide bridges, but also highly condensed in certain domains.[50] PCN has the most negative conduction band among carbon nitrides and the widest band gap.[45] When exfoliated into nanosheets, PCN has a large surface area and its active sites are better exposed.[51] In addition, exfoliation leads to improved charge

transfer and increased photocatalytic activity.[52, 53] Another way to modify PCN is to increase its porosity;[54] mesoporous PCN has a large surface area (> 400 m^{2}g^{-1}),[55] which leads to improved charge separation and better light harvesting ability.[53]

It has also been shown that amorphization of PCN leads to enhanced photocatalytic activity by breaking the intralayer hydrogen bonds, which improves light absorption and slows down recombination by introducing shallow intragap states.[56] On the other hand, defect sites can inhibit photocatalytic performance by introducing deep intragap states that can trap photogenerated carriers in the material.[45] However, defects in PCN have also been shown to improve performance by accelerating interfacial charge transfer.[57] One particular type of defect, nitrogen vacancy, has shown the ability to separate charges and increase catalytic efficiency by acting as a trap for photogenerated carriers.[58, 59] The defects in PCN can be introduced by doping with metals or non-metals, which also allows tuning of the band gap.[49, 60] However, since defects are not always beneficial, the influence of defects needs to be studied for each particular case.[45]

Metal–organic frameworks (MOFs): MOFs consist of metal clusters (nodes) coordinated by organic ligands (links) that form a periodic network in one, two, or three spatial dimensions. They are a broad group of compounds with different possible metal nodes, organic links, pore sizes and topologies. Their tunability and a band gap range between 1.0 and 5.5 eV make some of them suitable photocatalysts.[61, 62] However, they are often expensive, unstable,[63] and have poor conductivity and selectivity.[23] To optimize their performance, several strategies for their modification have been proposed, including metal and ligand functionalization, photosensitization, doping with metallic nanoparticles, and encapsulation.[61]

Quantum dots (QDs): QDs are small clusters of atoms (2–8 nm in size) at which scale quantum effects become relevant.[23] Specifically, the continuous energy levels in materials become discrete, as in atoms, which changes the way they interact with light. Because of this, the band gap of QDs can be tuned by changing their size, and their unique properties make them among the most attractive materials for future photocatalysis.[23] However, their instability and surface trapping of photogenerated carriers require them to be incorporated into composite materials for practical use, such as encapsulation in MOFs and combination with PCN.[64] QD materials can be broadly divided into the following subclasses:[23] elemental metal QDs, II-VI group QDs, III-V group QDs, I-III-IV group QDs, and perovskite QDs.

1.3.2 Useful Processes: The Scope of Heterogeneous Photo-catalytic Reactions

Having introduced the main classes of photocatalysts, I will now review the most important processes in science and industry in which photocatalysts are used.

Water splitting: As the most abundant molecule on the Earth's surface, not only non-toxic, but also making up the majority of the mass of living organisms, water is an ideal resource for sustainable energy. Using photons with an energy higher than 1.23 eV (wavelength below 1000 nm) and a suitable catalyst, water can be split into hydrogen and oxygen gases:

$$2H_2O \rightarrow 2H_2 + O_2 \tag{1.1}$$

Hydrogen produced in this way is referred to as "green hydrogen". When used as a fuel, the only combustion product is water, making it a completely sustainable fuel.

In photocatalytic water splitting, photogenerated holes in the valence band (VB) oxidize water in the oxygen evolution reaction (OER):

$$2H_2O + 4h^+ \rightarrow O_2 + 4H^+ \tag{1.2}$$
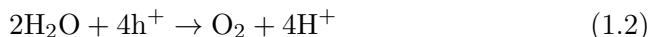
while electrons in the conduction band (CB) reduce water (or protons, as shown) in the hydrogen evolution reaction (HER):

$$2H^+ + 2e^- \rightarrow H_2 \tag{1.3}$$

giving the overall reaction as shown in the equation (1.1).

For the process to be feasible, the photocatalyst must have a band gap greater than 1.23 eV, or more specifically:

- a conduction band maximum (CBM) potential higher than the potential for HER

- a valence band maximum (VBM) potential lower than the potential for OER

Since water splitting was first discovered with TiO_2, Ti-based catalysts were the first to be investigated. Further investigation revealed that the oxides active for water splitting are those of metal cations with either d^0 or d^{10} electronic configurations, since their CBM is often close to or more negative than the HER potential.[65] However, these oxides often have a band gap of more than 3 eV due to the VBM located on the O_{2p} electrons of about 3 V at pH $= 0$. Further investigations have focused on increasing the

VBM to narrow the band gap and keep the overpotential as low as possible. This can be achieved by using oxynitrides due to the more negative potential of the N_{2p} electrons;[66] by doping the oxides with metals with partially filled d orbitals to introduce higher occupied electronic states;[67] by adding metals with filled s orbitals such as Bi.[68] In fact, Bi in $BiVO_4$ makes the VBM higher but still suitable for OER. However, its CBM is not high enough for HER and needs to be tuned by doping.[69] Other promising catalysts for water splitting have been investigated, including CoO,[70] d^0 or d^{10} metal chalcogenides,[71] carbon nitrides,[49] as well as MOFs.[72]

Band-edge energetics are not the only parameter affecting water splitting efficiency. Since water oxidation is a complex process involving the transfer of four electrons, kinetic factors further increase the overpotential. These factors can vary widely from catalyst to catalyst, and to gain further insight, the specific multi-step mechanism of water oxidation for a given catalyst must be considered. Some typical methods to reduce the overpotential include co-catalyst deposition[73] and surface nanolayer coating.[74]

In the water splitting described above, both HER and OER occur on a single semiconductor. Alternatively, water splitting can be performed using a semiconductor with a suitable CBM for HER and coupling it to another with a suitable VBM for OER,[75] along with an aqueous redox mediator (or solid electron mediator) to recombine the photogenerated carriers from the separate catalysts.[65] Such a setup allows the use of semiconductors with narrower band gaps and light with an energy lower than 1.23 eV, but requires twice as many photons and is even more kinetically demanding.

Organic synthesis: Photocatalysis can be used in the synthesis of industrially useful organic compounds such as agrochemicals and pharmaceuticals.[76] Photogenerated carriers from the catalyst are transferred to the organic molecule (substrate), converting the substrate into a reactive intermediate that then undergoes a series of transformations to the desired product. I will now review some of the classes of photocatalysts introduced above and discuss their applications in organic synthesis.

Among bulk semiconductors, metal oxides are the most widely used, especially TiO_2.[76] They can be used for oxidation as well as various C–C and C–X bond formation reactions, including cross-coupling and cyclization.[77] In addition to TiO_2, notable metal oxide catalysts include Bi(III)-based compounds,[78] ZnO,[79] Nb_2O_5,[80] and WO_3.[81] These compounds are stable, inexpensive, and nontoxic, but they have a wide band gap, a CBM potential too high for reduction reactions, and often exhibit poor selectivity and fast carrier recombination.[77] To mitigate some of these problems, cadmium chalcogenides such as CdS and CdSe can be used,[82, 83] since they

have a narrower band gap and can be easily made into QDs, allowing tuning of the band edges.[84] It is also possible to use lead halide perovskites such as $CsPbBr_3$, which has been shown to catalyze disulfide formation.[85]

Another widely used class in organic synthesis are organic polymers. In particular, carbon nitrides are among the most studied materials for heterogeneous photocatalysis.[49, 76, 86] They can be used for selective oxidation of alcohols to aldehydes and ketones,[87] secondary amines to imines,[88] sulfides to sulfoxides,[89] alkylarenes to carbonyl compounds,[90] and benzene to phenol.[91] Furthermore, they can be used to catalyze a wide range of cross-coupling,[86, 88, 92–97] as well as oxidative coupling reactions.[98–100] They have also been shown to catalyze heterocyclizations,[88, 94, 101–103] which are particularly important in the production of pharmaceuticals and agrochemicals.[86, 104] Other subclasses of organic polymers, i.e., π-conjugated polymers (in particular, conjugated microporous polymers) and COFs, can also be used for a variety of oxidation, cyclization, and coupling reactions.[76]

From the previous paragraphs, it can be concluded that the bulk semiconductors and organic polymers are the classes of photocatalysts used in the vast majority of organic transformations. However, MOFs have emerged as a promising class for reactions involving the generation of reactive oxygen species. Therefore, MOFs are particularly well suited for oxidation of amines and oxidative coupling.[76]

CO_2 reduction: Converting CO_2 into fuels such as methanol is another sustainable means of energy storage. Combustion of these fuels would produce CO_2, but the net amount of CO_2 in the atmosphere would ideally remain constant. To reduce CO_2, another molecule needs to be oxidized, and a sustainable way to do this is through photocatalytic water oxidation, as introduced above (equation (1.2)). The process can be done indirectly by splitting water and producing H_2, which then photocatalytically reduces CO_2.[105] However, since it is difficult to reduce CO_2 and oxidize water CO_2 simultaneously, CO_2 is often reduced directly with the electrons coming from a sacrificial electron donor.[106] Alternatively, as with water splitting, the semiconductor used for water oxidation can be coupled to another used for CO_2 reduction.[107]

Reduction begins with electron transfer to the CO_2 molecule. This is an energetically demanding process that can be facilitated by the simultaneous transfer of a proton or by the adsorption of CO_2 on the catalyst surface, which bends the molecule and increases its electron affinity, thereby activating it.[108] From here, reduction can proceed along several pathways:[106]

$$CO_2 + 2H^+ + 2e^- \rightarrow HCOOH \qquad (1.4)$$
$$CO_2 + 2H^+ + 2e^- \rightarrow CO + H_2O \qquad (1.5)$$
$$CO_2 + 4H^+ + 4e^- \rightarrow HCHO + H_2O \qquad (1.6)$$
$$CO_2 + 6H^+ + 6e^- \rightarrow CH_3OH + H_2O \qquad (1.7)$$
$$CO_2 + 8H^+ + 8e^- \rightarrow CH_4 + 2H_2O \qquad (1.8)$$
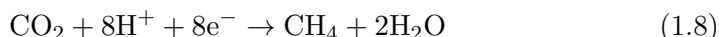
These pathways, along with the HER (equation (1.3)), make selectivity a key consideration in catalyst design. The reactions that produce the listed products involve 2 to 8 electron transfers, making kinetic considerations important. The reactions are pH dependent, as is the solubility of CO_2 (due to its hydrolysis to HCO_3^- and CO_3^{2-}), further complicating selectivity.

The nature of the binding of CO_2 to the surface is the first parameter influencing the further mechanism and selectivity. Monodentate binding through O to a surface metal atom and binding through C to a surface oxygen atom lead to the formation of the $^\bullet$COOH intermediate, while bidentate binding through O's to the metal leads to the formate intermediate.[106] Both can lead to the formation of different products.

TiO_2 is the most commonly used photocatalyst for CO_2 reduction. However, its CBM is not negative enough to efficiently reduce CO_2, and its VBM is at a potential high enough to oxidize most organic compounds (including the obtained products of CO_2 reduction) to CO_2.[106] The catalyst efficiency can be improved by doping or depositing metal nanoparticles exhibiting LSPR.[109, 110] Nevertheless, even bare TiO_2 has been shown to photocatalytically reduce CO_2 to hydrocarbons in the simplest reaction setups.[111]

Improvements over TiO_2 can be achieved using strategies analogous to water splitting: Increasing VBM to less oxidative potentials to reduce the band gap, increasing CBM to ensure that CO_2 can be efficiently reduced, mitigating recombination, and increasing surface area through nanofabrication.[112] This led to the use of d^{10} metal oxides,[113] d^0 metal (oxy)nitrides,[114] sulfides,[107] phosphides,[115] as well as carbon nitrides[114] and MOFs.[116]

Other applications: Other notable applications of photocatalysis include environmental remediation, where it is expected to become the dominant method in the future,[19] and includes the degradation of organic pollutants such as dyes, disinfection, as well as the reduction of heavy metals,[117]. Photocatalysis is also used in materials such as self-cleaning glass,[118] where the photocatalytic nature of the material surface leads to the degradation of dirt and prevents staining.

1.4 Understanding Photocatalytic Processes with Computational Chemistry

The progressive development of computers since the early 20th century has led to the emergence of computational chemistry as an indispensable aid to experimental data in the elucidation of photocatalytic processes. Today, computational models are widely used to explain the underlying mechanisms of chemical processes and to identify promising catalysts before they are tested in the laboratory. I will now explore several aspects of modeling photocatalysis.[119]

1.4.1 Atomistic Modeling

This approach explicitly considers the quantization of matter into atoms and is concerned with how the interaction of atoms and molecules leads to the phenomena observed on a larger scale. At the atomistic scale, quantum mechanical effects become significant, and any attempt to model a system with as few non-theoretical empirical parameters as possible must employ a quantum mechanical description of the electrons. This is often done using Density Functional Theory (DFT), which relies on approximations that make it less accurate than some other quantum mechanical methods, but its relatively low computational cost allows simulations of photocatalytic processes in systems up to a few hundred atoms in size.[119] DFT is also the main method that I have used in the work covered in this thesis. I will now describe several different applications of DFT-based atomistic modeling. The methods mentioned here are described in detail in the following chapter.

Geometric structure of the catalyst: Computational simulations are routinely used to obtain specific information about the geometric structure of the catalyst. This includes defect formation energies which shed light on the nature of defects such as dopants and vacancies in the material structure.

Electronic structure of the catalyst: Atomistic simulations are used to obtain the energies of the band edges, the Fermi level, and the intragap states, as well as the work functions. These can elucidate the suitability of the photocatalyst for a given reaction, the nature of the light absorption, and the electrical conductivity.

Gibbs energies of adsorption: The calculation of Gibbs energies of adsorption is perhaps the most common type of computation that is performed

in the study of photocatalytic processes. After constructing a suitable model of the photocatalyst, the study usually proceeds with the adsorption of the reactants on the catalyst surface. The adsorption energies obtained are used as an important descriptor that can reveal information such as the active sites of the catalyst and the most suitable surface facet for the reaction, as well as the mode of adsorption of the reactants. The study often proceeds by modeling the adsorption of the reaction intermediates. Obtaining these parameters is a key step in elucidating the reaction mechanism and determining catalytic activity and selectivity.

Energy barriers: To obtain the reaction kinetics, it is not enough to calculate the adsorption energies. Energy barriers for the transition between different intermediates are also required, and these can be calculated using a method such as Nudged Elastic Band (NEB).

Excited states: Modeling of the excited states is important for photocatalysis, but usually requires more suitable (and computationally expensive) methods than regular DFT, such as Time-Dependent DFT.[120]

Molecular dynamics: While quantum mechanics must be taken into account when simulating electronic motion, the movement of nuclei can be simulated with reasonable accuracy using Newton's second law of motion. This is emphasized in Ab Initio Molecular Dynamics (AIMD), which models the evolution of a system over time:

1. At any given moment, the energy of the system and the forces acting on its atoms are calculated using a quantum chemical method;

2. The atoms are moved for an arbitrarily short time by the forces acting on them according to classical mechanics;

3. Steps 1. and 2. are repeated as many times as needed.

The simplest molecular dynamics (MD) approach deals with molecules in their electronic ground state (also called Born–Oppenheimer MD). On the other hand, non-adiabatic MD, which takes into account electronic transitions, is particularly suitable for photocatalysis,[119] but is computationally expensive and limited to a few applications.[121]

1.4.2 Continuum Modeling

Another common approach is continuum modeling. It treats matter as continuous and smooth rather than as a set of discrete particles, making the approach less accurate but also less computationally expensive than atomistic

modeling. It is based on solving sets of differential equations and provides a bridge between atomistic modeling and experiments.[119] In the following paragraphs I describe some of its applications.

Implicit solvent models: These are coupled with the atomistic models to include the effect of solvents on the Gibbs energies obtained. In such a model, the solvent molecules are not explicitly included, but are represented by a continuum dielectric, which is included by modifying the equations of the DFT formalism.

Microkinetic models: By entering kinetic constants for the reactions occurring at the catalyst surface and adsorption energies into the model based on a set of material balance equations, one obtains the reaction rates and surface coverage by different species.[122] The input parameters can be obtained from the atomistic modeling described above.

Multiphysics models: These models are based on solving partial differential equations (PDEs) that correspond to various physical laws governing macroscale processes (such as Fick's laws for diffusion, Poisson's equation for electric potential, and the Butler–Volmer equation relating potential to current density). By inputting the initial concentrations of species, reactor geometry, sets of desired PDEs, and appropriate boundary conditions, these models predict the movement and distribution of species throughout the photocatalytic reactor.[119] Just as the input parameters for a microkinetic model can be obtained from the atomistic models, the input parameters for a multiphysics model can be obtained from the microkinetic model in a so-called "multiscale" approach.[119]

1.4.3   A Note on Machine Learning and the Future Prospects

Machine learning (ML) methods have enabled scientists to extract information and find intricate correlations in a system of interest by using large data sets to "train" an algorithm that predicts parameters of the system without having to perform new direct simulations as described above.[123] In the context of atomistic simulations relevant to photocatalysis, ML methods can be used to explore the space of atomic configurations to find materials with desired properties,[124] create models of atomic structure suitable for fast computation,[125] calculate the potential energy of complex systems,[126] as well as obtain accurate excited state properties.[127]

Beyond research in photocatalysis, ML has broader societal implications,[128, 129] particularly through the development of Artificial General Intelligence (AGI). AGI systems would have the potential to perform any

cognitive task beyond human capabilities.[130] Their emergence could lead to severe socioeconomic disruption[131] and existential risks if not properly aligned with human values.[132–134] In a 2013 survey of AI experts,[135] the median estimate for the development of AGI was between 2040 and 2075, with 18% predicting existentially catastrophic consequences; however, recent advances suggest that AGI may emerge sooner.[136] This has led numerous figures in AI and related fields to advocate for prioritizing the mitigation of risk of extinction from AI alongside other global risks such as pandemics and nuclear war.[137] However, if AGI safety issues are resolved in time, its assistance could prove to be the key factor in overcoming problems such as the global energy crisis.

1.5 Objectives

The goal of this thesis is to develop a systematic atomistic modeling approach and use it to rationalize different photocatalytic processes. When modeling each individual process, the aim is to break it down into aspects of interest and construct an appropriate computational model for each of these aspects, making sure that the model is consistent with the available experimental data. After obtaining simulation results with these models, the aim is to systematize the results into a feasible reaction mechanism. This systematic approach is presented for three different processes with varying degrees of complexity and availability of experimental data. To ensure that the results are reproducible by other researchers, the data for all relevant simulations are uploaded to the ioChem-BD repository, where they are openly accessible.[138].

1.5.1 Summary of Objectives by Chapter

Chapter 3: Activity, Selectivity, and Stability: Water Oxidation on Bismuth Vanadate

The goal is to understand the influence of oxygen vacancies and exposed surface facets on water oxidation on the $BiVO_4$ catalyst. To achieve this, I investigate the nature of the vacancies on the $BiVO_4$ surface using DFT and construct a corresponding model of the catalyst. I then study the oxygen evolution reaction and the hydrogen peroxide evolution reaction on the catalyst model to elucidate the activity and selectivity. Finally, I study the stability of the vacancies on the catalyst surface.

Chapter 4: The Influence of Electronic Structure: Oxazolidinone Oxidation on Carbon Nitride

The aim of this work is to rationalize the experimentally observed photocatalytic oxidation of oxazolidinones to oxazolidinediones on a carbon nitride catalyst. I build the catalyst model based on the experimental observations, rationalize the necessity of light for the reaction using DFT, and model the intermediates of two possible reaction pathways to elucidate the mechanism.

Chapter 5: Mixed Catalytic Systems: CO_2 Reduction on Co-Doped Hydroxyapatite

The goal is to rationalize the experimentally observed photothermal hydrogenation of CO_2 to CO on a Co-doped hydroxyapatite catalyst. I construct several models of the catalyst to represent systems with different doping levels and make sure that the model agrees with the experimental data. I rationalize the light absorption by the modeled systems using the GW method and model the reactant adsorption on the catalyst using DFT to elucidate the reaction mechanism on the systems with different doping levels.

Chapter 2

Theoretical Background

2.1 Quantum Mechanical Modeling of the Electronic Structure

In this chapter, I introduce the quantum chemical methods used in my work. I present the methods without rigorous derivations and proofs of their validity, which can be found in the respective references. I begin with the formalism of the quantum mechanics, which is the mathematical foundation of these methods, but is often neglected by those who merely apply quantum chemistry. The reader who is unfamiliar with some of the concepts in the following paragraphs should consult the refs. [139],[140], or [141].

2.1.1 Motivation for the Development of Quantum Mechanics

In the early 20th century, experiments by physicists (such as Davisson and Germer's electron diffraction) showed something unprecedented—phenomena at the smallest scales were found to be fundamentally probabilistic, which a deterministic theory of classical mechanics could not explain. A new theory of mechanics was needed—it was called "quantum mechanics". Classical mechanics views the measurement uncertainty as an external factor arising from the imperfection of our instruments, which can be reduced by using more precise ones. The theory of classical mechanics itself is free of uncertainty and produces exact results. The instruments used to measure quantum mechanical phenomena cannot be perfect either, but the crucial difference is that, unlike in classical mechanics, measurement is integral to quantum mechanical theory and is associated with an inherent, theoretical uncertainty. Whereas classical mechanics gives a yes-or-no answer to the question of whether a particle will be found in a volume of a

given size at a given time (i.e., the probability is either 1 or 0), quantum mechanics gives a finite probability (i.e., the probability is between 0 and 1). While classical mechanics describes a state of the system as a set of precise coordinates, quantum mechanics describes it as a set of probability densities in the whole space, namely the wave function $\psi(\mathbf{r}, t)$. The wave function of a particle is defined in such a way that the probability of finding the particle in a volume $d^3r = \mathrm{d}x\mathrm{d}y\mathrm{d}z$ at time t is equal to $|\psi(\mathbf{r}, t)|^2 d^3r$. Since the probability of finding the particle in the whole space must be equal to 1, integrating the probability over the whole space must also equal 1. Therefore, the wave function must be square-integrable. The space of wave functions $\mathcal{F}$ is actually smaller than the whole space of square-integrable functions (the wave function must also be sufficiently continuous and infinitely differentiable).[139]

It is easy to show that the space of wave functions $\mathcal{F}$ defined above has the structure of a vector space. This makes linear algebra particularly suitable for the treatment of wave functions, which is why the formalism of quantum mechanical theory is often developed in the language of linear algebra. This also allows us to talk about a general system state (without a representation within a particular basis set) $|\psi\rangle$ in a Hilbert space $\mathcal{E}$ instead of wave functions in the particular (Cartesian coordinate) representation $\psi(\mathbf{r}) = \langle\mathbf{r}|\psi\rangle$. Now we can develop the formalism.

2.1.2 Postulates of Quantum Mechanics: Formalizing Physics into a Mathematical Theory

A mathematical theory is a set of propositions (called theorems) expressed within an underlying logical system. An example of such a theory is Zermelo–Fraenkel set theory with the Axiom of Choice included (ZFC),[142] which is the most commonly used foundation of modern mathematics. It contains an infinite number of theorems expressed in the language of first-order logic. In order to define the theory, we need to find a way to implicitly and finitely list all of the infinite theorems contained within it. This is done by choosing a subset of the theorems (called axioms) from which every theorem of the theory can be logically derived. In the case of ZFC, there are infinitely many such sets of axioms to choose from. The conventionally chosen sets of axioms are those that provide the most practical value, and one such example for ZFC is the following: Axiom of Extensionality, Sum Axiom, Power Set Axiom, Axiom of Regularity, Axiom of Infinity, Axiom Schema of Replacement, Axiom of Choice.[143] If it turns out that some axioms lead to a logical contradiction within the theory, they are replaced or fixed in a way that mitigates the contradiction but still allows for the properties and theorems that we want our theory to have.

In an analogous way, we develop a physical theory of quantum mechanics by selecting a set of appropriate axioms (also called postulates) from which desirable properties and theorems emerge (in the case of a physical theory, the properties and theorems must be consistent with the experiments). Here I present such a set of postulates:[139]

1. **The state of a system at time t_0 is defined by $|\psi(t_0)\rangle \in \mathcal{E}$.** Any set of collinear vectors in $\mathcal{E}$ corresponds to the same physical state, and therefore the (pure) states are usually represented as unit vectors (normalized).

2. **Every measurable physical quantity $\mathcal{A}$ is bijectively mapped to $\hat{A}$ acting on $\mathcal{E}$.** The operator $\hat{A}$ is Hermitian and its eigenvectors span the state space $\mathcal{E}$, i.e., it is an *observable*.

3. **The only possible result of measuring $\mathcal{A}$ is an eigenvalue of $\hat{A}$.** The measurement results are discrete if the physical quantity in question is quantized (hence the "quantum" in quantum mechanics). In this case, the eigenvalue spectrum of the corresponding operator is also quantized.

4. **When the quantity $\mathcal{A}$ corresponding to the observable with a discrete (or a continuous and non-degenerate) spectrum is measured on a system in the normalized state $|\psi\rangle$, the probability $\mathcal{P}(a_n)$ (or $\mathrm{d}\mathcal{P}(\alpha)$) of obtaining the eigenvalue a_n (or a result between α and $\alpha + \mathrm{d}\alpha$) is equal to:**

$$\mathcal{P}(a_n) = \sum_{i=1}^{g_n} |\langle u_i^n | \psi \rangle|^2$$

   or:

$$\mathrm{d}\mathcal{P}(\alpha) = |\langle v_\alpha | \psi \rangle|^2$$

   Here, g_n is the degree of degeneracy of a_n and $\{\, |\, u_i^n\rangle \,\}$ is an arbitrary orthonormal set of vectors spanning the subspace $\mathcal{E}_n$ associated with a_n (and conversely, $|v_\alpha\rangle$ is the eigenvector corresponding to α).

5. **If the measurement of the quantity $\mathcal{A}$ on the system $|\psi\rangle$ yields the value a_n, the state of the system after the measurement is the normalized projection of $|\psi\rangle$ onto the eigensubspace of $\mathcal{A}$ for the eigenvalue a_n:**

$$|\psi\rangle \xrightarrow{a_n} \frac{P_n}{\sqrt{\langle \psi | P_n | \psi \rangle}} |\psi\rangle$$

The measurement is said to "collapse" the wave packet. This provides a way to prepare a system in a perfectly known state: If the observable has no degenerate eigenvalues (or if a complete set of commuting observables (CSCO) is used in a series of measurements), the system after the measurement will necessarily be in the eigenstate associated with the obtained eigenvalue(s) of the observable(s). On the other hand, if the observables do not share a common eigenbasis (e.g., momentum and position), the measurement of one will affect the other (the uncertainty principle). The fact that the measurement fundamentally affects the system has an important implication: The observer is integral in quantum mechanical theory.*

6. **Evolution of the state $|\psi(t)\rangle$ is determined by the following equation:**

$$i\hbar\frac{\mathrm{d}}{\mathrm{d}t}|\psi(t)\rangle = \hat{H}(t)|\psi(t)\rangle \tag{2.1}$$

This is the quantum mechanical analog of the Newton's second law: The Schrödinger equation.[145] As in classical mechanics, the Hamiltonian operator, $\hat{H}$, is correlated with the total energy of the system. In quantum chemistry, however, the Schrödinger equation usually refers only to a special case where the state $|\psi\rangle$ is time-independent:

$$\hat{H}|\psi\rangle = E|\psi\rangle \tag{2.2}$$

The time-independent state is an eigenstate of the Hamiltonian and the corresponding eigenvalue, E, is its energy. We have effectively reduced the Schrödinger equation to the eigenequation of the Hamiltonian, which is what I will call it instead of "Schrödinger equation" because what it describes is conceptually different. The exact solution of the Hamiltonian eigenequation only exists for certain simple systems, the most notable of which are the particle in a box, the linear harmonic oscillator (LHO), and the hydrogen atom. Fortunately, there are often ways to reduce a more complex problem to one of these, which is the basis of quantum chemistry.

There are alternative sets of postulates to these, as well as different but equivalent mathematical formulations of the quantum mechanical theory. By stating the postulate of the evolution of a quantum state differently, one can obtain the Feynman's path integral formulation.[146] The resulting formulation of quantum mechanics is intuitive and shows a clear correlation between classical and quantum mechanics, and allows for an easy incorporation of special relativity. This approach is also useful in many-body

---

*Note the similarity to the central role of observer in Kantian epistemology.[144]

perturbation theory, which is further discussed below as one of the methods used in my work. If $K(2,1)$ is defined as the probability amplitude that a particle arrives at the point in space-time $(\mathbf{r}_2, t_2)$ starting from $(\mathbf{r}_1, t_1)$:[139]

1. **$K(2,1)$ is a sum of infinite partial amplitudes, each corresponding to a single space-time path connecting the two points.**

2. **The partial amplitude $K_\Gamma(2,1)$ corresponding to the path Γ is determined by:**

$$K_\Gamma(2,1) = Ne^{\frac{i}{\hbar}S_\Gamma} \tag{2.3}$$

where N is a normalization constant and S_Γ is the *action* calculated along Γ:

$$S_\Gamma = \int_\Gamma \mathcal{L}(\mathbf{r}, \mathbf{p}, t)\mathrm{d}t$$

The Schrödinger equation can be shown to follow as a consequence of these postulates. The amplitude $K(2,1)$ is called the *propagator*, and in the case of a Hamiltonian that does not explicitly depend on time, it can be expressed as:

$$K(2,1) = \theta(t_2 - t_1) \sum_n \phi_n^*(\mathbf{r}_1)\phi_n(\mathbf{r}_2)e^{-\frac{i}{\hbar}E_n(t_2-t_1)}$$

where ϕ_n and E_n are an eigenvalue of the Hamiltonian and its corresponding eigenstate, and $\theta(t_2 - t_1)$ is the step function equal to 1 when $t_2 > t_1$ and equal to 0 otherwise. Such a propagator satisfies the following equation:

$$\left(i\hbar\frac{\partial}{\partial t_2} - H\left(\mathbf{r}_2, \frac{\hbar}{i}\nabla_2\right)\right)K(2,1) = i\hbar\delta(t_2 - t_1)\delta(\mathbf{r}_2 - \mathbf{r}_1) \tag{2.4}$$

where ∇_2 is a condensed notation for the set of operators $\{\frac{\partial}{\partial x_2}, \frac{\partial}{\partial y_2}, \frac{\partial}{\partial z_2}\}$. In mathematics, the solutions of a partial differential equation of the form such as (2.4) are called *Green's functions*. Such a form is valid only in the case of a non-interacting system, but in physics, the term *Green's function* is also used for analogous solutions in the interacting case, as in many-body perturbation theory.

2.1.3 Born–Oppenheimer Approximation: Describing Chemical Systems

To describe a chemical system, we need to consider both the electrons and the nuclei. We can write the Hilbert space to which the state of our system belongs as the tensor product of the subspaces of nuclei and electrons: $\mathcal{E} = \mathcal{E}_n \otimes \mathcal{E}_e$. The state of the whole system, $|\Psi_{\text{tot}}\rangle$, can then be expressed in the

basis of tensor products of a nuclear state, $|\psi_{n,i}\rangle$, and an electronic state, $|\psi_{e,j}\rangle$:

$$|\Psi_{tot}\rangle = \sum_{i,j} c_{ij} |\psi_{n,i}\rangle \otimes |\psi_{e,j}\rangle$$

However, since the nuclei move much slower than the electrons, we can assume that the nuclei are fixed point charges at any given moment. This allows us to consider the motions of the nuclei and electrons separately, and to ignore any coupling terms in the state of the whole system, which becomes:

$$|\Psi_{tot}\rangle = |\psi_n\rangle \otimes |\psi_e\rangle$$

For such a system, the Born–Oppenheimer approximation[147] assumes that the state of the electrons can be treated as quasi-static, which is a consequence of the more general adiabatic theorem.[148] This also allows us to reduce the electronic Schrödinger equation to the eigenequation of the Hamiltonian. Quantum chemistry is mainly concerned with solving the eigenequation of the electronic Hamiltonian; the motion of the nuclei is usually treated within the framework of classical mechanics.

2.1.4 Hohenberg–Kohn Theorems: From Abstract Wave Functions to Physical Electron Density

In the previous section, we have effectively reduced the quantum mechanical model of the chemical system to the quantum mechanical model of its electronic structure. The most robust way to model the electronic structure using quantum mechanics is to consider each electron as an individual particle in the multi-electron system. However, when the system is in its ground state, Hohenberg and Kohn's first theorem allows a further simplification of this problem:[149, 150]

Theorem 1 *In the ground state, the external potential, $v(\mathbf{r})$, is (within a trivial additive constant) a unique functional of the electron density, $\rho(\mathbf{r})$.*

Since the "external" potential (i.e., the potential due to the nuclei), $v(\mathbf{r})$, uniquely determines the positions of the nuclei, which in turn together with the number of electrons determine the electronic properties of the system, **Theorem 1** implies that in the ground state there is a bijection between $\rho(\mathbf{r})$ and all the electronic properties of the system, such as the total energy, $E(\rho)$. The electron density is a function of only three variables (the spatial dimensions), making it in principle easier to handle than the wave function (the state vector as defined above) which explicitly takes into account each individual electron. However, the theorem holds only for the ground

state; any particular excited state may have multiple electronic densities corresponding to the single external potential.[151]

Hohenberg and Kohn's second theorem provides a general approach to calculating the total energy as a function of electron density:[149]

Theorem 2 *For a system within the external potential $v(\mathbf{r})$, any trial density $\tilde{\rho}(\mathbf{r})$ corresponding to the same total number of electrons maps to a total energy $E(\tilde{\rho})$ that is not lower than the energy of the ground state, E_0.*

Given the functional relation $E(\rho)$, **Theorem 2** guarantees the possibility to find the electron density of the system by the variational method.[†] The total energy functional can be decomposed into the kinetic, the electron-electron potential, and the nucleus-electron potential energy functionals ($T(\rho)$, $V_{ee}(\rho)$, $V_{ne}(\rho)$, respectively), of which only $V_{ne}(\rho)$ depends on the external potential:[150]

$$E(\rho) \;=\; \underbrace{T(\rho) + V_{ee}(\rho)}_{F(\rho)} \;+\; \underbrace{V_{ne}(\rho)}_{\int_{\mathbb{R}^3} \rho(\mathbf{r})v(\mathbf{r})\mathrm{d}\mathbf{r}} \tag{2.5}$$

Using the method of Lagrange multipliers, $E(\rho)$ can be minimized under the constraint that the number of electrons in the system is equal to N:

$$\delta\left(E(\rho) - \mu\left(\int_{\mathbb{R}^3} \rho(\mathbf{r})\mathrm{d}\mathbf{r} - N\right)\right) = 0 \tag{2.6}$$

Rewriting (2.6) as an Euler–Lagrange equation gives the basic working equation of the Density Functional Theory (DFT):[150]

$$\mu = \frac{\delta E(\rho)}{\delta \rho(\mathbf{r})} = v(\mathbf{r}) + \frac{\delta F(\rho)}{\delta \rho(\mathbf{r})} \tag{2.7}$$

The Lagrange multiplier μ is the *chemical potential*. The functional $F(\rho)$ is independent of $v(\mathbf{r})$ and is therefore a *universal functional*. Knowing its explicit form, either exact or approximate, allows the DFT to be applied to any system, as long as it is in the ground state. However, efficient computation of the exact form of this functional belongs to the class of Quantum Merlin Arthur (QMA)-hard problems,[153] of which NP problems are a subset. An algorithm that efficiently computes the universal functional would therefore prove a claim even stronger than P versus NP equality, meaning

---

[†]The formulation of Hohenberg and Kohn's DFT is valid only for the v-representable electron densities, i.e., those densities that can be mapped to the antisymmetric ground-state wave functions of a Hamiltonian dependent on $v(\mathbf{r})$. This is often not the case in practice.[150] However, modern formulations of the DFT bypass these limitations by not requiring the density to be v-representable.[152]

that such computation is probably theoretically impossible. In the following sections, I present ways to compute approximate forms of the universal functional.

2.1.5 Kohn–Sham Equations: Making DFT Usable in Practice

Before writing down an approximate form of the universal functional, we can try to break it down into parts that can be expressed exactly, and keep the approximate part as small as possible. Kohn and Sham did this by reintroducing one-electron wave functions (orbitals) into the theory through a system of hypothetical N orthonormal orbitals with a kinetic energy $T_s(\rho)$ that do not interact but still give rise to the same electron density as the real system of N electrons with a kinetic energy $T(\rho)$.[154] The universal functional $F(\rho)$ from (2.5) can be written as:

$$F(\rho) = T_s(\rho) + J(\rho) + E_{\text{xc}}(\rho) \tag{2.8}$$

where $J(\rho)$ is the Coulomb integral representing the electrostatic interaction between electrons and the functional $E_{\text{xc}}(\rho)$:

$$E_{\text{xc}}(\rho) = T(\rho) - T_s(\rho) + V_{\text{ee}}(\rho) - J(\rho) \tag{2.9}$$

is called the *exchange-correlation functional* because it includes the exchange and the correlation interactions between electrons, both of which are quantum mechanical effects. We can now rewrite (2.7):

$$\mu = v_{\text{eff}}(\mathbf{r}) + \frac{\delta T_s(\rho)}{\delta \rho(\mathbf{r})} \tag{2.10}$$

with the effective potential, $v_{\text{eff}}(\mathbf{r})$, being equal to:

$$v_{\text{eff}}(\mathbf{r}) \;=\; v(\mathbf{r}) \;\;+\;\; \underbrace{\frac{\delta J(\rho)}{\delta \rho(\mathbf{r})}}_{\int_{\mathbb{R}^3} \frac{\rho(\mathbf{r}')}{|\mathbf{r}-\mathbf{r}'|}\text{d}\mathbf{r}'} + \underbrace{\frac{\delta E_{\text{xc}}(\rho)}{\delta \rho(\mathbf{r})}}_{v_{\text{xc}}(\mathbf{r})} \tag{2.11}$$

In the case of non-interacting orbitals, $v_{\text{eff}}(\mathbf{r})$ reduces to $v(\mathbf{r})$. Since the orbitals do not interact, the total Hamiltonian can be decomposed into N one-electron Hamiltonians $\hat{h}_s$ with their eigenequations:

$$\left(\underbrace{-\frac{1}{2}\nabla^2}_{\hat{T} operator} + v_{\text{eff}}(\mathbf{r}) \right) |\psi_i\rangle = \varepsilon_i |\psi_i\rangle \tag{2.12}$$

After obtaining the eigenstates $|\psi_i(\mathbf{r}, s)\rangle$,[‡] the electronic density is calculated as:

$$\rho(\mathbf{r}) = \sum_{i,s}^{N} \langle \psi_i(\mathbf{r}, s)|\psi_i(\mathbf{r}, s)\rangle \qquad (2.13)$$

The equations (2.11), (2.12), and (2.13) are collectively called the Kohn–Sham equations. One can solve them iteratively by plugging a trial density $\rho(\mathbf{r})$ into (2.11), then the obtained potential $v_{\text{eff}}(\mathbf{r})$ into (2.12), and the obtained eigenstates $|\psi_i\rangle$ into (2.13) to obtain a new trial density.[§] When the Kohn–Sham equations are solved self-consistently and the ground-state density is obtained, the total energy of the system can easily be obtained from (2.5) and (2.8). However, before we can calculate any of these parameters, we first need to approximate the exchange-correlation potential, $v_{xc}(\mathbf{r})$. In the following section, I discuss how to do this.

2.1.6 Exchange–Correlation Functionals: DFT's Biggest Obstacle

Finally, we are left with the exchange–correlation functional; a part of the universal functional $F_{(\rho)}$ that we cannot compute exactly and need to approximate. A method that is obtained by such an approximation is called a density functional approximation (DFA).[¶] The simplest such approximation is the *Local-Density Approximation* (LDA):

$$E_{\text{xc}}^{\text{LDA}}(\rho) = \int_{\mathbb{R}^3} \rho(\mathbf{r})\varepsilon_{\text{xc}}(\mathbf{r})\mathrm{d}\mathbf{r}$$

where $\varepsilon_{\text{xc}}(\mathbf{r})$ is equal to the exchange–correlation functional for the uniform electron gas of density $\rho(\mathbf{r})$, which can be accurately calculated.[155–158]

The assumption that the exchange–correlation functional is locally the same as in the electron gas can only be justified in the systems where the electron density does not change abruptly. This is not true for atoms and molecules, so a more appropriate approximation has been developed, the *Generalized Gradient Approximation* (GGA). A GGA-type functional,

---

[‡]The eigenstate technically belongs to the tensor product of the state space and the spin space. This is implicitly taken into account when talking about spin-orbitals—one-electron wave functions that also include the electronic spin. Spin is a purely quantum observable (i.e., it has no classical mechanical analog) that describes an intrinsic angular momentum of the electron and has two eigenvalues $+\frac{1}{2}\hbar$ and $-\frac{1}{2}\hbar$.

[§]An actual computation would use more optimal algorithms than the trivial iteration which I used as a proof of concept.

[¶]In the literature, the methods that use these approximations are often referred to as DFT rather than DFA, since every practical DFT method uses an approximation to the density functional.

$E_{\text{xc}}^{\text{GGA}}(\rho, \nabla\rho)$, is a functional of both the density and its first derivative. Several such functionals have been developed, such as PBE,[159] which I used extensively in the work described in some of the following chapters.

The E_{xc} functional is sometimes modified by using the Hartree–Fock (HF) method[160] to partially calculate its exchange part, E_{x}, in what is called a *hybrid functional*. The correlation part of the functional, E_{c}, is calculated completely by DFT since it is ignored by HF. PBE0[161, 162] is an example of such a functional that contains 25% of the HF-calculated exchange and 75% of the PBE-calculated exchange. However, the inclusion of the HF-calculated exchange significantly increases the computational demand. Since PBE has been shown to produce relatively small errors in the calculation of the long-range exchange interactions, the PBE0 calculation demand can be reduced somewhat by the means of calculating the HF exchange contribution only in the short-range exchange interactions. This leads to the HSE06 functional,[163] which I have used in my work to compute the energies of unoccupied electronic states in the materials, since the "pure" GGA functionals tend to underestimate their energies.[164]

2.1.7 Motion of Nuclei: Classical and Quantum Mechanics Combined

It was noted above that the motion of nuclei is treated using classical mechanics. More precisely, if the forces acting on each atom are known, their motion is determined by Newton's second law of motion. However, the forces themselves are calculated using quantum mechanics, through the Hellmann–Feynman theorem:[165]

$$\frac{\partial E}{\partial \lambda} = \left\langle \psi \left| \frac{\partial \hat{H}}{\partial \lambda} \right| \psi \right\rangle \tag{2.14}$$

where λ is a parameter specifying nuclear positions.$^{\|}$

The forces obtained in this way can be used to calculate the time evolution of the system of interest in AIMD, but they can also be used for geometry optimization, i.e., finding a local minimum of the function of energy with respect to atomic coordinates—the Potential Energy Surface (PES). There are several computational algorithms that can be used for this purpose; the ones I used are RMM-DIIS[166] and the conjugate gradient algorhitm.[167] The RMM-DIIS algorithm is faster than the conjugate gradient when the system is close to its optimal geometry, but less stable otherwise.[168]

$^{\|}$The equation (2.14) is presented in the general form and can be easily adapted to Kohn–Sham DFT.

2.1.8   Electronic Structure Calculations in the Solid State

Solid-state materials, such as those studied in this work, are locally periodic (i.e., they have a structural pattern called a *supercell* that repeats many times through space). To model these systems, it is convenient to consider an infinitely repeating potential through a supercell equipped with the periodic boundary conditions.[169] According to the Bloch's theorem,[170] the Hamiltonian of such a system will have plane waves as eigenstates, which can be represented in the form of a wave function:[171]

$$\langle \mathbf{r} | \psi \rangle = \psi(\mathbf{r}) = e^{i\mathbf{k}\cdot\mathbf{r}} u_{\mathbf{k}}(\mathbf{r}) \tag{2.15}$$

where $\mathbf{k}$ is the wave vector associated with the crystal momentum and $u_{\mathbf{k}}(\mathbf{r})$ is a periodic function with the same periodicity as the external potential. In practice, for periodic systems, it is often easier to solve the Kohn–Sham equations in the $\mathbf{k}$-basis than in the $\mathbf{r}$-basis.[172]. Since the $\mathbf{r}$-vector space (real space) is periodic in these systems, the $\mathbf{k}$-vector space (also called *reciprocal space*) is also periodic, and its Voronoi decomposition gives unit cells called *Brillouin zones*. The periodicity of the reciprocal space allows the system to be completely described by a single Brillouin zone, conventionally the first Brillouin zone, which contains the origin of the $\mathbf{k}$-space (also called the Γ-point). One of the practically important consequences of describing a system in the $\mathbf{k}$-space is that the longer an axis of the real-space unit cell of the system is, the shorter the corresponding axis of the Brillouin zone will be. This means that for a large system, the $\mathbf{k}$-space can be sampled with fewer points ($\mathbf{k}$-points) to accurately describe the system, and *vice versa*. Similarly, if the system is non-periodic in the x-direction in real-space, the wave function component in the x-direction will be completely described by a single $\mathbf{k}$-point. For any other (periodic) direction with finite unit cell length, it is often necessary to choose various $\mathbf{k}$-points. Monkhorst and Pack have developed a method[173] that generates an optimal set of $\mathbf{k}$-points based on the input number of $\mathbf{k}$-points in each spatial direction, which is the method of choice for the work I present in this thesis.

The periodic function $u_{\mathbf{k}}(\mathbf{r})$ can be written in the exponential form:

$$u_{\mathbf{k}}(\mathbf{r}) = \sum_{\mathbf{G}} c_{\mathbf{G}} e^{i\mathbf{G}\cdot\mathbf{r}}$$

This allows us to write the wave function for a single $\mathbf{k}$-point, $\phi_{\mathbf{k}}(\mathbf{r})$, as:

$$\phi_{\mathbf{k}}(\mathbf{r}) = \sum_{\mathbf{G}} c_{\mathbf{k}+\mathbf{G}} e^{i(\mathbf{k}+\mathbf{G})\cdot\mathbf{r}} \tag{2.16}$$

For each $\mathbf{k}$-point, the summation is performed over values of $\mathbf{G}$. The square norm $|\mathbf{k}+\mathbf{G}|^2$ is proportional to the kinetic energy of the state. In a practical

calculation, only the plane waves with a kinetic energy below a certain energy cutoff are included in the basis set, neglecting the states with sufficiently high kinetic energies.

In practical DFT simulations, there are additional approximations and methods that I have used extensively in my work, but will not discuss in detail. One example is the Projector-Augmented Wave (PAW) method,[174] which "smooths out" the rapidly-oscillating wave functions near the ion cores, thereby greatly speeding up the calculation of the Kohn–Sham equations. Another such approximation is a smearing function, which describes the occupation of the Kohn–Sham states with a smooth function, as is necessary for the convergence of the self-consistent calculation.

Since the total energy is not necessarily a functional of the electron density for the system in an excited state, DFT methods can only be accurate for periodic systems in the electronic ground state. Furthermore, as mentioned above, DFT often underestimates the energies of the unoccupied electronic states. Both of these problems can be avoided in simulations of periodic systems by using a computationally expensive but practically feasible GW method.[175] The many-body interacting system of interest can be represented by a set of self-consistent equations, called Hedin's equations, which are developed from the many-body perturbation theory through the path integral formulation of quantum mechanics, as introduced in 2.1.2. Hedin's equations are formally exact, but to be computationally feasible, they are approximated by the following set of equations:[175, 176]

$$G(1,2) = G_0(1,2) + \int G_0(1,3)\Sigma(3,4)G(4,2)\mathrm{d}(3,4) \qquad (2.17)$$

$$\chi_0(1,2) = -iG(1,2)G(2,1) \qquad (2.18)$$

$$W(1,2) = v(1,2) + \int v(1,3)\chi_0(3,4)W(4,2)\mathrm{d}(3,4) \qquad (2.19)$$

$$\Sigma(1,2) = iG(1,2)W(1^+,2) \qquad (2.20)$$

The propagators in these equations describe quasiparticles (QPs) that are created when an external perturbation is applied to the system. G is the Green's function of a fully interacting QP expanded in a Dyson series into G_0 (the Green's function of a non-interacting QP) and Σ (the energy resulting from the interaction of the QP with its environment, i.e., the self-energy). χ_0 is the irreducible polarizability, which, together with the bare Coulomb interaction v, is a term in the Dyson series expansion of the full (reducible) polarizability in the exact Hedin's equations. W is the effective (screened) Coulomb interaction, also expanded in a Dyson series in (2.19). The space-time point 1^+ represents an infinitesimal increment to 1. In (2.20), the self-energy is calculated using only the propagators G and W, which give the

GW approximation its name. In practice, the initial guess for Σ is obtained from the energies of the Kohn–Sham orbitals and the self-consistent cycle is performed until the Hedin's equations are satisfied. Further simplifications are often made by requiring self-consistency only in certain quantities, such as QP energies or G. The reader interested in the derivation of the formalism is advised to consult the ref. [176], which also covers various practical aspects of using the GW method.

2.2 Modeling Photocatalytic Processes

In the following paragraphs, I introduce some key theoretical concepts used in photocatalysis. Together with the methods introduced above, they allow us to describe most chemical systems. A black box method would, in principle, allow one to represent a chemical structure of interest as a set of atomic coordinates, write down its Hamiltonian, and proceed to obtain the values of any observable, as well as its evolution over time. As the equations for a large system get complicated, the aid of a computer is required. However, due to practical limitations, it would still not be feasible to perform such a computation for all but the simplest of systems. In a more realistic example, instead of obtaining *all* the properties of the system from a single complete model, one constructs a model with respect to a subset of the aspects of the system, making necessary approximations along the way. Constructing such a model is the key task of the computational chemist, while the key skill is recognizing which approximations are appropriate in that model. This section contains some of the methods that have been particularly useful in constructing appropriate models for the photocatalytic systems that I have studied in my work.

2.2.1 Reaction Thermodynamics and Kinetics

Reaction thermodynamics and kinetics are the defining features of any catalytic process. They determine the most important properties of a catalyst: Activity, selectivity, and stability. Depending on the context, thermodynamics and kinetics can be considered for the individual reaction steps or for the net reaction. The properties of the net reaction result from the properties of the individual steps, so in this section, I consider thermodynamics and kinetics in the context of the individual steps.

Reaction thermodynamics is concerned with the equilibrium between the reactants and products. The equilibrium position is determined by the Boltzmann distribution of the reactant and product states with respect to the Gibbs energy difference, ΔG, between them. If ΔG of a reaction is negative, the reaction is exergonic and spontaneous, and if it is positive, the

reaction is endergonic and not spontaneous. At constant temperature T and pressure p, the Gibbs energy change can be expressed as:

$$\Delta G = \Delta E + \Delta E_{\text{ZPV}} + p\Delta V - T\Delta S \tag{2.21}$$

where E is the electronic energy, E_{ZPV} is the zero-point vibrational energy, V is the volume of the gas phase, and S is the entropy. The calculation of the electronic energy has been thoroughly described in the previous sections. Now I will describe the calculation process for the other terms.

E_{ZPV} represents the eigenstate of the quantum LHO Hamiltonian at 0 K. It can be expressed as:

$$E_{\text{ZPV}} = \frac{h}{2} \sum_i \nu_i$$

where ν_i are the vibrational frequencies of the system. These can be calculated by treating each chemical bond as a linear harmonic oscillator and modifying the bond lengths, calculating the energies of the resulting systems, and obtaining the frequencies from the energy vs. bond length dependence.

The term $p\Delta V$ is relevant for gases and can be calculated from the ideal gas approximation:

$$p\Delta V = k_{\text{B}}T\Delta N$$

where N is the number of gas particles. However, this term is usually neglected due to its small relative contribution.

The total entropy can be decomposed into translational, rotational, and vibrational components. The calculation of these components is system-specific and is described in the statistical thermodynamics literature.[21] When there are multiple possible microstates to consider, the configuration entropy should be taken into account and can be calculated using the Gibbs entropy formula:

$$S = -k_{\text{B}} \sum_i p_i \ln(p_i)$$

where p_i is the probability that the system is in the i-th microstate.

While the reaction thermodynamics is concerned with the Gibbs energy change between the reactants and the products, the reaction kinetics is concerned with the energy of the transition state between the reactants and the products (i.e., the energy barrier). The geometry (and therefore the energy) of this state can be calculated using the Nudged Elastic Band (NEB) method.[177, 178] In this method, a set of multiple system geometries (images) between the initial (reactant) and the final (product) states is hypothesized. This set forms a path (band) along the PES. If the band follows the minimum energy path (MEP) along the PES, the perpendicular

forces acting on the band at any point equal zero. The set of images is iteratively optimized to minimize the perpendicular (real) force acting at each image, as well as the additional (fictitious) force acting parallel to the band between any two adjacent images. The parallel force is added so that the images remain separated along the band. The image with the highest energy is often made to "climb" along the band (Climbing Image NEB)[179] by making it unaffected by the parallel force and maximizing its energy along the band. After the iterations converge, the highest-energy image is the transition state. This can be further confirmed by calculating its vibrational frequencies and making sure that exactly one frequency is an imaginary number (this is the consequence of the corresponding vibration decreasing the energy of the system). This vibration moves the image along the MEP. Any other frequency is a real, positive number, because the transition state is a saddle point on a PES.

2.2.2 Computational Hydrogen Electrode: Elucidating the Energy of Charge Carriers

Photocatalytic processes involve the transfer of charged species. To obtain the thermodynamic and kinetic parameters of such a process, we need to model the charged species. The simplest charged chemical species are the proton (H^+) and the electron (e^-), and their mutual transfer, the proton-coupled electron transfer (PCET), is the fundamental electrochemical step in any protic solvent (such as water). To obtain the ΔG of a PCET, we need the chemical potential, μ, of the proton and the electron.[180] The chemical potential of a particle i is the quantity from the equation (2.7) and can also be correlated with the Gibbs energy:[21]

$$\mu_i = \left(\frac{\partial G}{\partial N_i} \right)_{T,p,N_{j\neq i}} \tag{2.22}$$

where N_i is the number of particles i. The chemical potential of a proton can be expressed as:

$$\mu_{H+} = \mu_{H+}^{\circ} + k_B T \ln a_{H+} \tag{2.23}$$

where a_{H+} is the activity of protons in the aqueous solution and μ_{H+}° is μ_{H+} at the standard conditions ($T = 273.15$ K; $p = 1$ bar; $a_{H+} = 1$). Similarly, the chemical potential of an electron can be expressed as:

$$\mu_{e-} = \mu_{e-}^{\circ} + eU_{SHE} = \mu_{e-}^{\circ} + eU_{RHE} - k_B T \ln a_{H+} \tag{2.24}$$

where e is the elementary charge and U is the electrode potential against the standard hydrogen electrode (SHE) or the reversible hydrogen electrode (RHE).

However, it is not practically easy to obtain $\mu_{\mathrm{H^+}}^{\circ}$ and $\mu_{\mathrm{e^-}}^{\circ}$ using a periodic DFT method, since the Gibbs energies of charged systems depend linearly on the size of the supercell.[181] To overcome the problem, we need to approach the models indirectly. In the case of PCET, we can do this through the computational hydrogen electrode (CHE) approach.[182] Let us consider the hydrogen evolution reaction (HER):

$$2\mathrm{H^+} + 2\mathrm{e^-} \rightleftarrows \mathrm{H_2}(g) \tag{2.25}$$

Since the standard electrode potential, E°, for any half-reaction is defined as its electrostatic potential with respect to molecular hydrogen oxidation at standard conditions,[183] the E° for (2.25) is equal to 0. E° is related to its standard Gibbs energy of the reaction, ΔG°:

$$\Delta G^{\circ} = -zFE^{\circ} \tag{2.26}$$

where z is the number of electrons transferred in the reaction and F is the Faraday constant. By definition, ΔG° of the reaction 2.25 is equal to 0, which allows us to correlate the standard chemical potentials of the proton and electron with the standard chemical potential of molecular hydrogen, which we can calculate with DFT:

$$\mu_{\mathrm{H^+}}^{\circ} + \mu_{\mathrm{e^-}}^{\circ} = \frac{1}{2}\mu_{\mathrm{H_2}}^{\circ} \tag{2.27}$$

Combining the equations (2.23), (2.24), and (2.27), we get the way to calculate the sum of the chemical potentials of the proton and the electron:

$$\mu_{\mathrm{H^+}} + \mu_{\mathrm{e^-}} = \frac{1}{2}\mu_{\mathrm{H_2}}^{\circ} + eU_{\mathrm{RHE}} \tag{2.28}$$

Note that this approach allows us to model only the reactions where the proton and electron transfers are coupled (PCET), but not the individual proton or electron transfers. If the proton and electron transfers are not coupled, a different approximation method should be used.

2.2.3 Grand-Canonical Density Functional Theory: Obtaining Energies at an Applied Potential

The CHE method described above allows us to include the effects of applied potential and pH through the eU_{RHE} term. The Gibbs energies of reactants and products are still obtained by the DFT models, which assume electrically neutral supercells. However, at certain potentials and pH values, the real systems are not neutral, and the Gibbs energies obtained by DFT are not accurate. To obtain accurate energies at a given electrode potential,

Grand-Canonical Density Functional Theory (GC-DFT) is used.[184] In the grand canonical ensemble, the number of particles in the system is not held constant. In GC-DFT, the system is modeled in multiple states, each with a different total number of electrons resulting from different applied potentials U. The G of the system can be approximately expanded to a second order in terms of the capacitance C:[185]

$$G(U) \approx G(U_0) - \frac{1}{2}C(U - U_0)^2 \qquad (2.29)$$

where U_0 is the work function of the surface (i.e., the work required to remove an electron from the surface).

The influence of a polar solvent (such as water) on the Gibbs energies of these electrically charged systems can be significant, so the implicit solvent model is often employed used in conjunction with GC-DFT. Since the periodic DFT models require the supercell to be uncharged, the countercharges are also introduced into the solvent model in various ways. One of these is the linearized Poisson–Boltzmann equation, which allows the GC-DFT method to be applied to systems with an electronic band gap.[185]

2.2.4 General Computational Details

Here I describe the general methodology that I used in my work. Any modifications and additional methods used in the specific projects are discussed in the corresponding chapters.

For the DFT simulations, I used the Vienna Ab initio Simulation Package (VASP).[186, 187] The density functional explicitly included spin wave functions (i.e., spin polarization), and the exchange–correlation functional used was PBE.[159] Inner electrons were represented by the PAW method.[174] The Brillouin zone was sampled sampled using the Monkhorst–Pack method.[173] The electronic energy was considered converged if the energy difference between the two subsequent steps was less than 10^{-6} eV. The geometry relaxation was considered converged when the forces acting on each atom allowed to relax were less than 0.01 eV/Å.

Chapter 3

Activity, Selectivity, and Stability: Water Oxidation on Bismuth Vanadate

In this chapter, I show how computational chemistry can be used to explore the catalytic activity, selectivity, and stability in a given system, using bismuth vanadate (BiVO$_4$) as an example. The results presented in this chapter have been published in ref. [188]. All figures are adapted from the publication unless otherwise noted.

3.1 BiVO$_4$: Photocatalytic Application and Structure

3.1.1 Overview of BiVO$_4$ as a Water Splitting Catalyst

In recent years, bismuth vanadate (BiVO$_4$) has emerged as one of the most promising catalysts for photocatalytic water splitting[26, 189, 190] due to its properties as a ternary oxide and n-type semiconductor, which make it well suited for use as a photoanode material for the oxygen evolution reaction (OER). In its monoclinic scheelite form, BiVO$_4$ has demonstrated an impressive half-cell solar-to-hydrogen theoretical efficiency of 8.1%.[191] Despite these advantages, the electron conductivity and water oxidation kinetics of unmodified BiVO$_4$ remain suboptimal, limiting its practical application as an OER catalyst.[189] As a result, various strategies have been proposed to modify BiVO$_4$ photoanodes to overcome these challenges.[192–194]

In addition to its application as a photoanode material for the OER, BiVO$_4$ has been shown to catalyze the hydrogen peroxide evolution reaction (HPER),[195, 196] consuming water to produce H$_2$O$_2$ in the presence

of bicarbonate electrolyte or when modified with various materials.[197–199] HPER has a standard electrode potential of 1.78 V vs. Standard Hydrogen Electrode (SHE),[200] and $BiVO_4$ has been proposed as a potential photocatalyst for HPER production as a sustainable alternative to the conventional anthraquinone oxidation process using toxic precursors and organic solvents.[201, 202] H_2O_2 has numerous applications in the chemical industry, water treatment, metal processing, and as a bleach or oxidant,[201, 203] highlighting the need to better understand the selectivity of photocatalytic HPER with respect to the competing OER if it is to be industrially viable.

3.1.2   The $BiVO_4$ Structure

To study water oxidation on $BiVO_4$ using computational chemistry methods, we first need to describe its structure. In its monoclinic scheelite polymorph, a nanocrystal of $BiVO_4$ contains different surface facets (**Figure 3.1**), with the (001) and (011) facets accounting for 99.3% of its total surface area. The (101) facet is considered identical to the (011) facet due to their similar morphologies and surface energies (in this work, the surface facets are labeled in the body-centered, $I2/b$ setting, which is convenient for simulations).[204, 205] The facets (001) and (011) exhibit significantly different properties,[206–208] and both must be considered when studying the overall water oxidation reaction on $BiVO_4$.
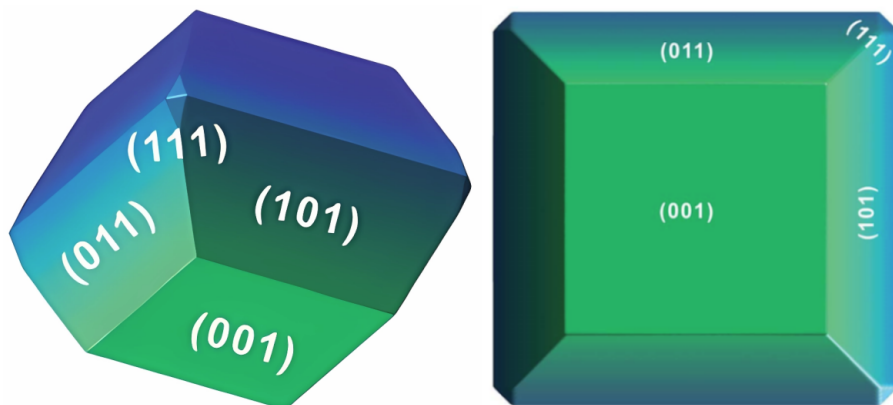
Figure 3.1: The equilibrium morphology of monoclinic scheelite $BiVO_4$ as predicted from the calculated surface energies. The figure is adapted from ref. [204].

The surfaces of $BiVO_4$ often contain structural defects,[209] the most common of which are oxygen vacancies ($\mathcal{V}_O$s).[210] The $\mathcal{V}_O$s in semiconductors can improve the conductivity and charge separation efficiency as

shallow n-type donors.[211, 212] They can also enhance visible light absorption by narrowing the band gap and improve charge transfer with the electrolyte.[213] However, $\mathcal{V}_O$s can negatively affect OER efficiency by acting as electron–hole recombination centers[214, 215] or by trapping photogenerated species and inhibiting charge transfer.[216, 217] Research suggests that while the detrimental effects originate from the bulk vacancies, the beneficial effects may originate from the surface vacancies of a semiconductor.[218–220] In BiVO$_4$, the $\mathcal{V}_O$ significantly alter its geometric[221] and electronic structure,[222–224] thereby affecting the water oxidation mechanism.

The (001) surface facet of BiVO$_4$ has been extensively studied and it has been shown that vacancies on this facet can significantly enhance photocatalytic water oxidation.[225] The most commonly studied vacancies arise from the removal of an oxygen atom from a VO$_4^{3-}$ unit, leaving a cavity containing two excess electrons without significant change in the local structure. This type of defect is localized on a single vanadium atom and is therefore called a localized vacancy ($\mathcal{V}_O^{loc}$; **Figure 3.2a**). The two electrons left by the removal of a neutral oxygen atom also remain localized at the vacancy site. Another type of oxygen vacancy, known as a split vacancy ($\mathcal{V}_O^{split}$), has been found in the bulk and on the (001) facet of BiVO$_4$.[223, 224] In this type of defect, the local structure is altered when the oxygen atom is removed; the atoms move from the $\mathcal{V}_O^{loc}$ state so that an oxygen atom from a neighboring VO$_4^{3-}$ unit forms an oxo bridge with the vanadium on which the vacancy was created (**Figure 3.2b**). The vacancy is thus shared between two neighboring vanadium atoms, unlike in $\mathcal{V}_O^{loc}$. While both $\mathcal{V}_O^{loc}$ and $\mathcal{V}_O^{split}$ have similar formation energies in the bulk, the $\mathcal{V}_O^{split}$ in the (001) subsurface layer is about 1 eV more stable than $\mathcal{V}_O^{loc}$, which undergoes an almost barrierless transition to $\mathcal{V}_O^{split}$.[223] The different electronic structures of the two vacancy types may also have a significant impact on the catalytic mechanisms and selectivity of BiVO$_4$ by affecting the conductivity of the material and its ability to separate charges efficiently.
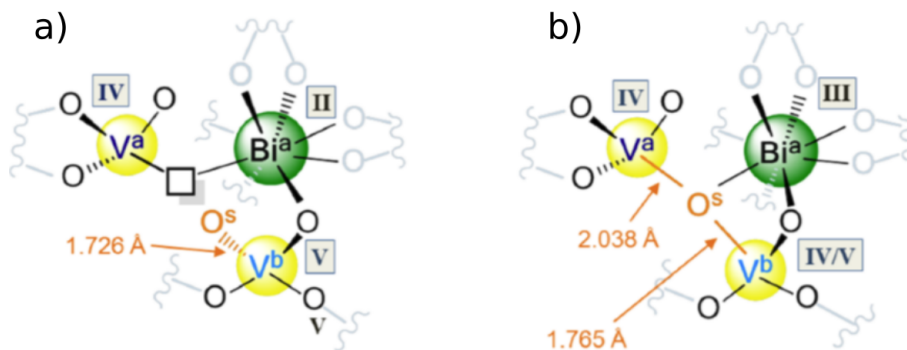
Figure 3.2: $\mathcal{V}_O^{loc}$(a) and $\mathcal{V}_O^{split}$ (b) in bulk BiVO$_4$. The figure is adapted from ref. [223].

3.1.3 Vacancies on the (011) Surface Facet

Before modeling water oxidation on BiVO$_4$, I investigated the nature of $\mathcal{V}_O$s on the (011) facet. This was done in the same way as for the (001) facet in the ref. [223]. First, I modeled the $\mathcal{V}_O^{loc}$s at 12 different positions in the (011) surface slab, as shown in **Figure 3.3a**.
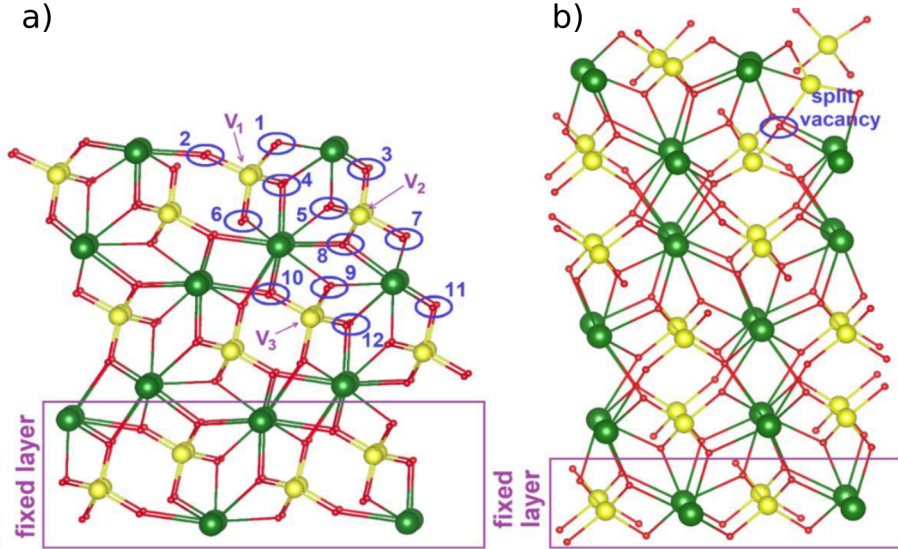
Figure 3.3: Surface slabs of the (011) (a) and (001) (b) surface facets, as modeled in this work, with different localized vacancy positions investigated for the (011) facet. "Fixed layer" represents atoms that were kept frozen during geometry optimization. Color code: Bi, V, and O are shown in green, yellow, and red, respectively (visualized with VESTA).[226]

The vacancy formation energy, ΔE_{f}, was calculated for each system according to:

$$\Delta E_{\mathrm{f}} = \frac{1}{2} E_{\mathrm{O}_2} + E_{\mathrm{vac}}^{\mathrm{slab}} - E_{\mathrm{prist}}^{\mathrm{slab}} \tag{3.1}$$

where E_{O_2}, $E_{\mathrm{vac}}^{\mathrm{slab}}$, and $E_{\mathrm{prist}}^{\mathrm{slab}}$ are the DFT electronic energies of O_2, the surface slab with vacancy, and the pristine surface slab, respectively. Of the 12 positions investigated, a $\mathcal{V}_{\mathrm{O}}^{\mathrm{loc}}$ was successfully obtained in 7, while 6 did not converge to the desired state. The formation energies are shown in **Figure 3.4**. In the remaining systems, the structure converged to a different geometry during optimization. The results show that the vacancies are more stable near the surface.

The most stable $\mathcal{V}_{\mathrm{O}}^{\mathrm{split}}$ was obtained between the V atoms in the atomic layer close to the surface (V_1 and V_2 in **Figure 3.3a**). The ΔE_{f} for this system was 3.61 eV, implying that the split vacancy is ~ 0.6 eV more stable than the most stable $\mathcal{V}_{\mathrm{O}}^{\mathrm{loc}}$. In the water oxidation modeling, such a system was used as the model of the vacancy-containing (011) surface facet, along with the (001) facet (**Figure 3.3b**).
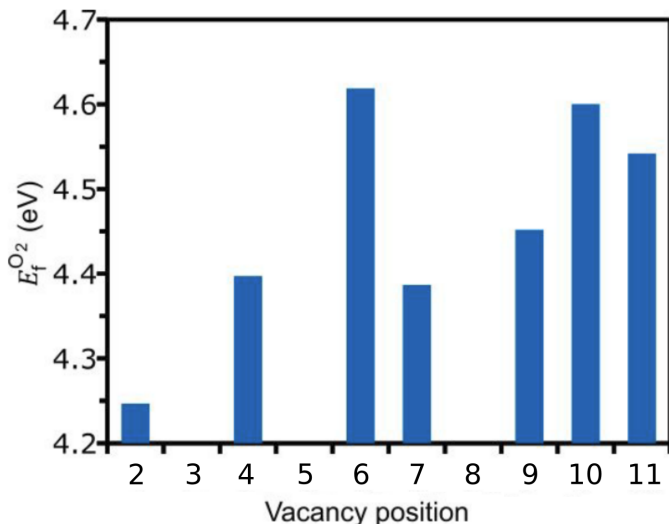
Figure 3.4: The ΔE_f of $\mathcal{V}_\mathrm{O}^\mathrm{loc}$s at different positions in the (011) facet, calculated with respect to the energy of O_2 in the gas phase.

3.2   Activity: Oxygen Evolution Reaction

Having built the model of $BiVO_4$, we can now proceed to study its water oxidation performance, starting with the catalytic activity. For this, I have chosen the electrocatalytic OER as the model reaction, which is the main process that takes place at the anode at the applied potentials up to 1.8 V vs. RHE:

$$2H_2O \rightarrow O_2 + 4H^+ + 4e^- \tag{3.2}$$

We can assess the activity of the catalyst through the applied potential required to achieve the OER. In the ideal system, the applied potential will be 1.229 V vs. SHE under standard conditions.[21] Since the OER involves a transfer of four protons and four electrons, we can divide the whole mechanism into four single-PCET-containing steps (PCET steps), each containing one PCET, and calculate the energies of the steps using the DFT-calculated energies of the involved systems within the CHE formalism (at pH = 0).[182, 208] The PCET step with the highest Gibbs energy increase determines the required potential, and is called the potential-determining step (PDS). The accuracy of this approach was confirmed by benchmarking using a modified PBE0 functional with 10% HF-calculated exchange[223] as well as with GC-DFT at an applied potential of 1.6 V vs. RHE.[188]

In $BiVO_4$, there are two possible OER mechanisms described in the literature,[227] shown in **Figure 3.5** as pathway A (expected for the pristine

(001) facet) and B (expected for the pristine (011) facet). I have modeled both of these mechanisms on the (001) and (011) surface facets, both pristine and with vacancy. The primary difference between these pathways is the presence of a peroxo bridge between Bi and V atoms (intermediates **2a**–**4a**) in pathway A, whereas pathway B involves a surface-adsorbed OOH group (intermediates **3b** and **4b**). The HPER pathway shares a common starting point with the OER pathway B—intermediate **3b** is present in both mechanisms and contains an OOH group in close proximity to a hydrogen atom. Instead of continuing the oxidation to the intermediate **4b**, hydrogen peroxide evolves directly from **3b**. An alternative HPER mechanism (not shown) involves the oxidation of another water molecule in the intermediate **1**, resulting in the formation of an OH group on a neighboring Bi atom instead of the oxo group in the intermediate **2b**. The two OH groups then combine indirectly through another water molecule between them to form hydrogen peroxide (they are too far apart to combine directly). The barrier for this process is 1.0 eV, as calculated by NEB. In the publication [188], I showed that this mechanism is less efficient than the main pathway, and I do not consider it in this thesis.
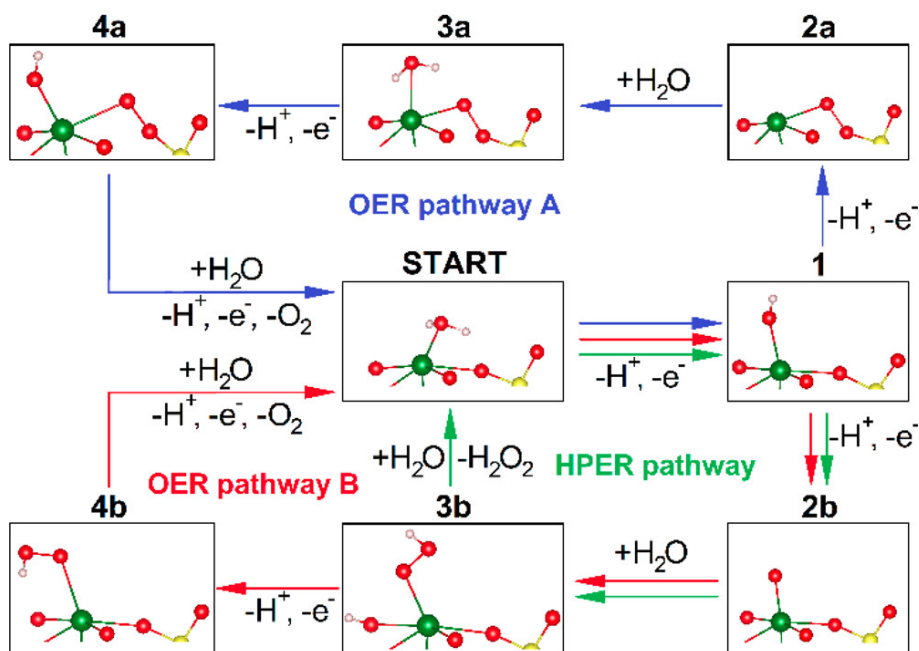
Figure 3.5: The different mechanistic pathways of water oxidation on $BiVO_4$.

From the data obtained, the reaction profiles are constructed and shown in **Figure 3.6**. The proposed mechanism for the pristine (001) facet for

OER pathway A,[227] shown in blue, is much less efficient ($\Delta G_{\text{PDS}} = 2.4$ eV) compared with the mechanism that occurs on the (001) facet with a $\mathcal{V}_{\text{O}}^{\text{split}}$, following OER pathway B, shown in red ($\Delta G_{\text{PDS}} = 1.6$ eV). The presence of the oxygen vacancy particularly affects the first PCET step, which is the PDS for the pristine system, reducing its energy by almost 2 eV. This step involves the removal of hydrogen, which is more efficient in all reaction steps that take place on a surface with a vacancy. The additional electrons introduced by the vacancy occupy high energy states within the band gap[223] and are easily removed, facilitating the PCET. Therefore, the subsurface split vacancies, similar to $\mathcal{V}_{\text{O}}^{\text{loc}}$s localized in the surface layer,[213] enhance the OER efficiency on the (001) facet, as observed in recent experimental data showing that the vacancy-rich (001) surface facet significantly improves the OER efficiency[225] and oxygen evolution kinetics.[228]
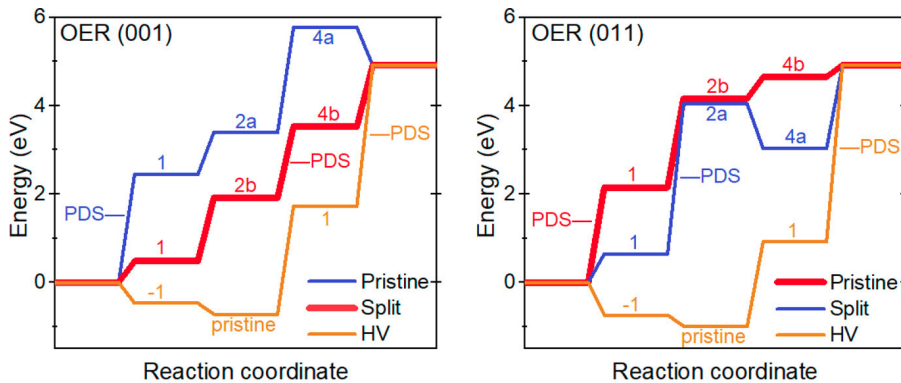
Figure 3.6: Gibbs energy profile of the OER on BiVO$_4$. Blue, OER pathway A; red, OER pathway B; brown, OER pathway HV. The optimal mechanisms (the lowest PDS) are represented by a thicker line. The pathway HV is discussed in Section 3.4.

The analogous simulations were performed for the OER on the (011) facet (**Figure 3.6**). For the pristine (011) facet, the most efficient OER pathway (pathway B, in red) was obtained as in ref. [227] with the second step being the PDS ($\Delta G_{\text{PDS}} = 2.1$ eV). However, when a vacancy was introduced, the OER efficiency was reduced compared with the pristine surface (shown in blue, $\Delta G_{\text{PDS}} = 3.4$ eV), in contrast to the results for the (001) facet. Comparing the OER between the (001) and (011) facets, we see that the OER is easier on the (001) facet because the PDS is lower in energy (1.6 eV, with vacancy) than on the (011) facet (2.1 eV, pristine). Both reactions follow pathway B, implying that the OER pathway A does not occur on either facet of BiVO$_4$.

3.3 Selectivity: Hydrogen Peroxide Evolution Reaction

In the context of my work, the selectivity is studied by comparing the catalytic activities with respect to different products. At the potentials higher than 1.8 V vs. RHE, alongside the OER, the HPER can occur:

$$2H_2O \rightarrow H_2O_2 + 2H^+ + 2e^- \tag{3.3}$$
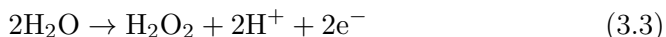
When studying HPER on $BiVO_4$, I considered a total of four systems, namely the (001) and (011) surface facets, both with and without vacancies (**Figure 3.7**). Among them, the preferred mechanism occurs on the pristine (011) facet, where the first step is the most favorable (PDS of 2.1 eV).*
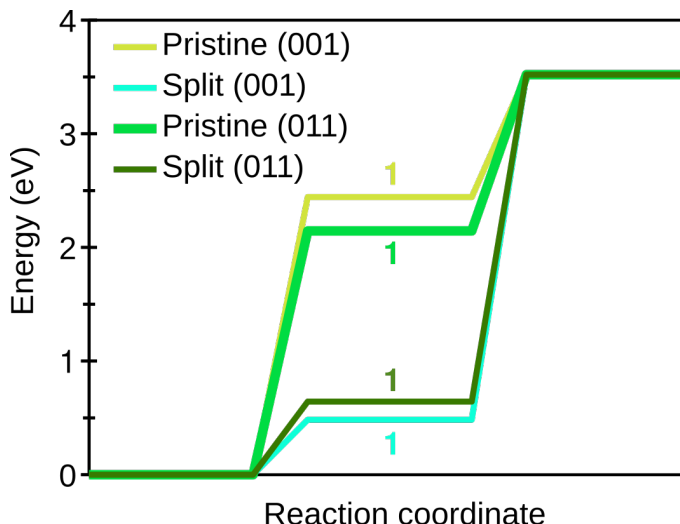
Figure 3.7: Gibbs energy profile of the HPER on $BiVO_4$. The optimal mechanism is represented by a thicker line.

The HPER on the pristine (011) facet is the second most energetically favorable water oxidation reaction on $BiVO_4$ (the most favorable overall is the OER on the (001) facet with $\mathcal{V}_O^{split}$ with the PDS of 1.6 eV). This reaction has an equivalent PDS to OER on the same surface facet (**Figure 3.6**). However, the second PCET step of the HPER, which ultimately produces hydrogen peroxide ($\Delta G = 1.4$ eV), is less energetically demanding than the second PCET step of the OER, which stops at the intermediate **2b** formation

---

*It has been shown that the PDS for HPER on the (111) surface facet is slightly lower (2.0 eV).[229] As explained above, I did not include this facet in my analysis due to its small relative surface area.

($\Delta G = 2.0$ eV). This suggests that the (011) facet is more favorable for HPER than for OER.

The results further indicate that oxygen vacancies in the subsurface enhance the oxygen evolution efficiency, while HPER is more favorable on the pristine material. These theoretical predictions are in agreement with recent experiments,[230] which have shown that V_2O_5-treated $BiVO_4$, with a lower amount of oxygen vacancies than the untreated material, favors HPER over OER. The water oxidation activity and selectivity on the four considered systems are summarized in **Figure 3.8**.
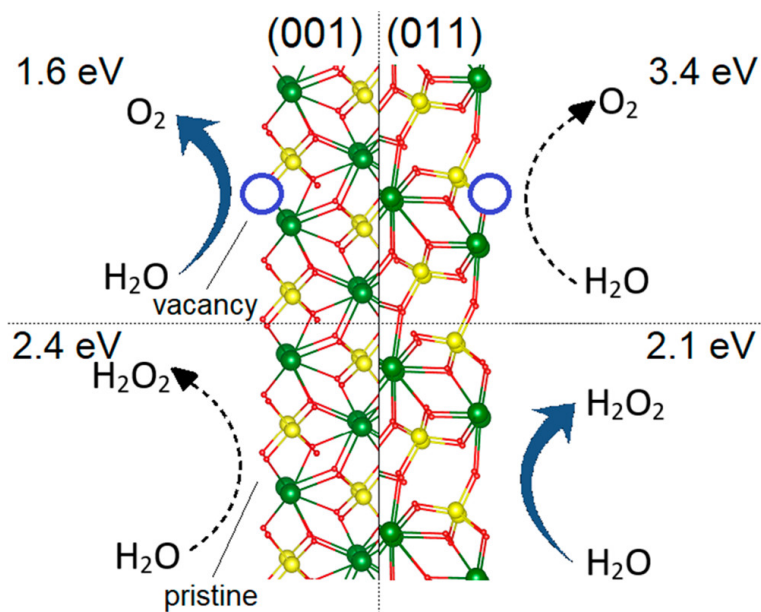
Figure 3.8: The energies of the potential-determining steps for the water oxidation reaction on $BiVO_4$, with the most favorable reactions indicated by thick arrows.

3.4   Stability: Vacancy Hydration

Like any other catalyst, $BiVO_4$ is subject to irreversible chemical changes, especially under harsh conditions. In particular, the high potentials required for water oxidation can oxidize the surface vacancies, which are critical for reaction activity and selectivity, as discussed above. The Pourbaix diagram of vacancy stability with respect to water oxidation (**Figure 3.9**) shows that vacancies are thermodynamically unstable at potentials much lower than those required for water oxidation. However, during synthesis at ele-

vated temperatures, defects such as $\mathcal{V}_O^{\text{split}}$ form in the material and become kinetically trapped after cooling, demonstrating the metastable nature of oxygen vacancies derived from the synthesis protocol.[231] In $BiVO_4$, the $\mathcal{V}_O s$ were found at 1.23 V vs. RHE at pH 9.5,[232] as well as 1.8 V vs. RHE at pH 8.3.[230] Under these conditions, the formation energies of $\mathcal{V}_O^{\text{split}}$ with respect to water can reach up to 4.4 eV on the (001) facet and 4.2 eV on the (011) facet. It is worth noting that the applied potentials required for HPER and OER are typically lower during photocatalysis, where light contributes most of the voltage. For example, anodic HPER was found to initiate at potentials lower than 1 V vs. RHE,[195] which is lower than the theoretical potential needed for this reaction to occur.
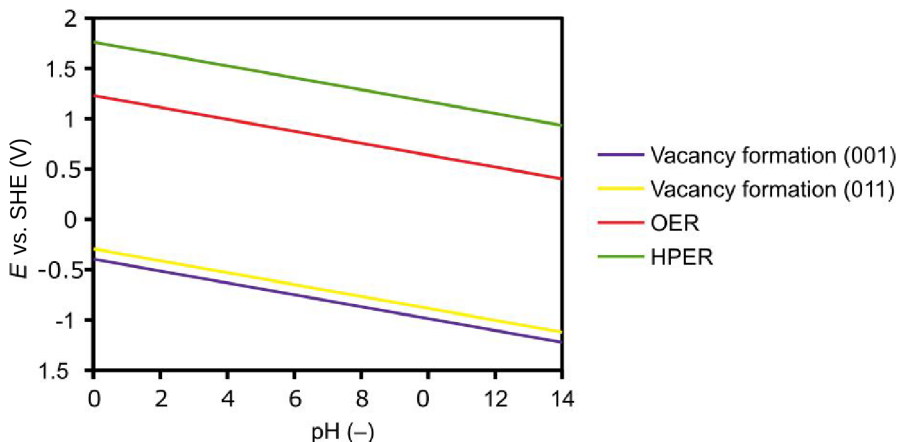
Figure 3.9: The Pourbaix diagram comparing the equilibrium potentials for $\mathcal{V}_O^{\text{split}}$ formation and water oxidation. The $\mathcal{V}_O^{\text{split}}$ on the (001)/(011) facet is stable in water in the region below the purple/yellow line. On the other hand, OER/HPER occurs in the region above the red/green line.

However, since the selectivity might be tuned towards HPER by oxidation of the vacancy, it is worth investigating how the vacancy could be oxidized in principle. Vacancy oxidation by water could start by refilling the vacancy with a water molecule, i.e., the vacancy hydration (**Figure 3.10a**). The resulting structure (hydrated vacancy) resembles a pristine surface, but the additional hydrogen atoms adsorbed on the surface oxygens provide the two extra electrons characteristic of the systems with a vacancy. The hydrated vacancy is similar in stability as $\mathcal{V}_O^{\text{split}}$, but kinetically, it should be much easier to oxidize because the surface hydrogen atoms can be readily removed. Since bicarbonate ions are required for efficient H_2O_2 evolution on $BiVO_4$,[195, 197, 198] it is possible that they play a role in restoring the pristine surface by lowering the energy barrier for vacancy hydration,

which in turn shifts the selectivity toward H_2O_2. This hypothesis could be tested experimentally by checking whether a small amount of H_2 evolves when the catalyst is immersed in the bicarbonate solution, but not when it is immersed in water. With a bicarbonate solution, one H_2 molecule should evolve for each hydrated vacancy without an applied bias (this process is exergonic according to **Figure 3.6**).

The presence of hydrated vacancies allows for a different OER mechanism to occur on $BiVO_4$ (**Figure 3.10b**), where the hydrated vacancy is oxidized to a pristine surface and the reaction continues along the OER pathway A or B until the intermediate **2a** or **2b** is reached. From here, O_2 evolves directly and the system with the vacancy is restored. **Figure 3.6** shows that this HV pathway is suboptimal on both surface facets due to the large energy needed to reintroduce the vacancy. However, the favorability of the first two PCET steps in these pathways illustrates the thermodynamic feasibility of vacancy oxidation.
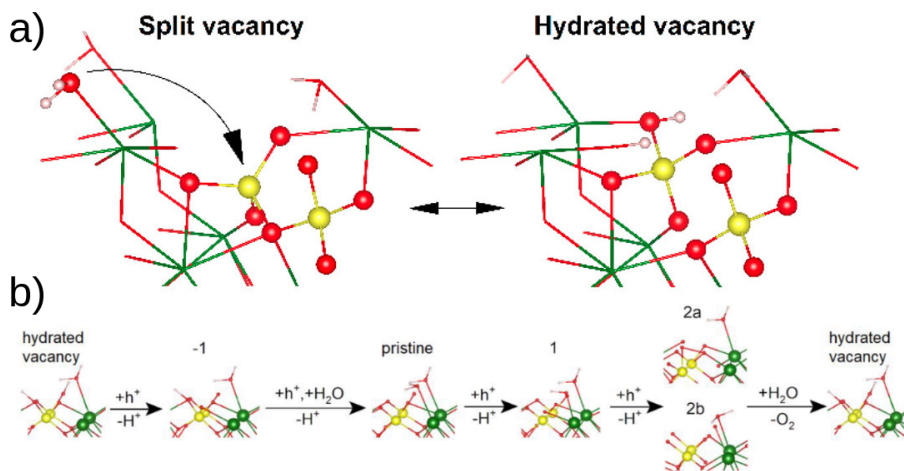
Figure 3.10: Vacancy hydration (a) and the HV OER pathway (b).

3.5 Conclusions

In this chapter, I have explored the activity, selectivity, and stability of the $BiVO_4$ catalyst in the water oxidation reaction with a computational chemistry framework using DFT. I have discussed the nature of the oxygen vacancies on the (011) surface facet. As in the (001) facet, the split vacancies were found to be more stable than their localized counterparts. After constructing the appropriate models for the systems with and without vacancies, I have simulated the water oxidation on $BiVO_4$. The results show that the material with vacancies favors OER, while the pristine material is more favorable towards HPER. The OER on the (001) facet with a vacancy was shown to be the most favorable reaction on $BiVO_4$ starting at a potential of 1.6 V vs. RHE. The second most favorable reaction is HPER on the (011) facet with an onset potential of 2.1 V vs. RHE. The accuracy of the energies from which these data were obtained was confirmed by PBE0 and GC-DFT approaches.

In addition, a new vacancy type (hydrated vacancy) is proposed in which the vacancy is filled by a water molecule but the electronic structure of the system with a vacancy is retained. Such a system is easily oxidized and the selectivity of water oxidation towards HPER can be tuned by controlling the barrier to vacancy hydration, providing a useful strategy for the design of novel photoelectrodes.

3.6 Specific Computational Details

Here I provide the additional computational details used in the work, apart from the general computational details described in Chapter 2. The exchange–correlation functional used was PBEsol.[233] The implicit solvent model and the surface-charging method based on the linearized Poisson–Boltzmann equation required for the GC-DFT framework were implemented through VASPsol.[234–236] Kinetic energy cutoff for the plane-wave basis set was set to 520 eV. The dipole corrections were employed in the direction perpendicular to the surface slab.

The Gibbs energies of the systems were calculated from the DFT electronic energies together with the zero-point energy and entropy corrections obtained from the vibrational frequency calculations as implemented in VASP. In the water oxidation reaction, the Gibbs energy of O_2 was derived from the energies of other reaction species and the standard reduction potential of oxygen (1.229 V vs. SHE) rather than from DFT. This was done to minimize the uncertainties introduced by the approximate nature of the exchange–correlation functional.

Chapter 4

The Influence of Electronic Structure: Oxazolidinone Oxidation on Carbon Nitride

It is often not sufficient to consider light irradiation only as a means of generating a photocurrent. Instead, it may be necessary to study the changes in the electronic structure of the catalyst upon irradiation (see the publication in ref. [237], which I co-authored, for an example of a study of light-induced electronic transitions in $BiVO_4$). In the current chapter, I go through a mechanistic study where the electronic structure of the catalyst plays a key role in the reaction mechanism; the oxidation of oxazolidinones to oxazolidinediones (**Figure 4.1**) using mesoporous polymeric carbon nitride (PCN; also called mesoporous graphitic carbon nitride: mpg-CN) as a photocatalyst. The results presented in this chapter have been published in ref. [238]. All figures are adapted from the publication unless otherwise noted.
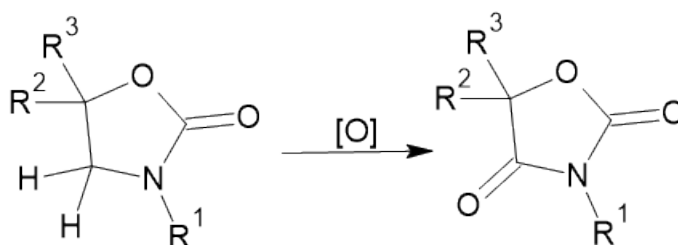
Figure 4.1: Oxidation of a 1,3-oxazolidine-2-one to the corresponding 1,3-oxazolidine-2,4-dione. The figure was prepared for this thesis (not published elswhere).

4.1 Oxazolidinedione Production

4.1.1 The Needed Compound: Oxazolidinediones and the Difficulty of their Synthesis

1,3-Oxazolidine-2,4-diones (oxazolidinediones) are a class of valuable medicinal chemistry molecules with a broad spectrum of biological activity. They have the ability to replace 1,3-thiazolidine-2,4-diones,[239] which are considered an important class of compounds in medicinal chemistry but are notorious for their problematic metabolism and binding issues. Oxazolidinediones can act as zinc-binding chemotypes in metalloproteins instead of sulfonamides and other acidic moieties due to their imidic NH behavior.[240] The hydrogen-bonding properties of oxazolidinediones have also been exploited in research on the treatment of type II diabetes, as they allow efficient binding to peroxisome proliferator-activated receptors.[241] In addition, oxazolidinediones have shown good performance as mineralocorticoid receptor antagonists.[242] Trimethadione and paramethadione are notable examples of oxazolidinediones that have been used as anticonvulsants in the treatment of epilepsy.[243] In addition, there are two commercial agrochemicals that contain the oxazolidinedione heterocyclic motif—famoxadone (a quinone outer inhibitor used as a fungicide)[244] and pentoxazone (a protoporphyrinogen oxidase inhibitor herbicide used to control weed populations in rice fields).[245]

Despite their high demand, the synthesis of oxazolidinediones remains cumbersome and challenging. In the case of 5-ylidene substituted oxazolidinediones, the ring can be formed from propargylic amides and CO_2 under basic conditions.[246] Analogous preparation of other oxazolidinediones requires cyclization of a carbonate synthon such as iso(thio)cyanate and α-hydroxycarboxylate,[242, 247] which are not readily available. A simpler approach would be the oxidation of 1,3-oxazolidine-2-ones (oxazolidinones), which are commercially available or easily prepared by reaction between isocyanates and oxiranes or from the corresponding vicinal aminoalcohols.[248] Such oxidation is not easy to achieve due to the stability of oxazolidinones against oxidation with a peak potential above 2 V vs. SHE.[249] Only a few publications have reported the successful oxidation of oxazolidinones. Namely, in 1982, Gramain et al.[250] published a study on the photocatalytic reaction of an oxazolidinone with oxygen under irradiation using a high-pressure mercury lamp and benzophenone as catalyst. The reaction was carried out at room temperature over a period of 68 hours. In 2005, Cao et al.[249] also investigated the electrolytic partial fluorination of N-substituted oxazolidinones (without acyl substituents) to give 4-fluoro derivatives, which were subsequently hydrolyzed and oxidized to diones. These works were per-

formed under rather harsh conditions, such as the presence of corrosive acidic fluoride solutions or strong UV irradiation, highlighting the need for a more sustainable approach.

4.1.2 The Reaction: Photocatalytic C–H Oxidation with Carbon Nitride

Over the past decade, there has been growing interest in the use of photoredox catalysis-driven PCET for the facile and selective modification of X–H sites in organic molecules.[251, 252] By using a molecular sensitizer with a sufficiently oxidative excited state, such as an Ir-polypyridine complex, together with a Brønsted base, the strong O–H and N–H bonds in phenols and amides can be cleaved via oxidative PCET to generate alkoxy and amidyl radicals, respectively.[253, 254] In water, a base/oxidant couple can provide the energy required for homolytic X–H bond cleavage in a substrate. The Gibbs energy required for bond cleavage in a substrate depends on the reduction potential of the excited state of the sensitizer and the pK_b of the Brønsted base.[255] In such a multisite PCET, the proton and the electron end up at different sites (i.e., the base and sensitizer, respectively).

Alternatively, photocatalysts with basic functional groups such as Eosin Y or inorganic semiconductors and oxoclusters can abstract hydrogen atoms from a substrate without the need for an auxiliary base.[256–258] In the case of PCN, its pyridinic-like nitrogen centers allow PCET from proton donors.[259–262] Studies have demonstrated its ability to mediate various organic transformations, alone or in combination with organic bases.[90, 263–266] The valence band potential of +1.45 V vs. SHE and its nitrogen-rich structure allow PCN to cleave C–H bonds with relatively high dissociation energies, such as in N-alkylamides, where C–H bond dissociations are ~ 4 eV.[266]

In the work described in this chapter, my co-authors from Max Planck Institute of Colloids and Interfaces (Alexey Galushchinskiy, Dr. Yajun Zou, and Dr. Oleksandr Savateev) have developed a method for the production of oxazolidinediones by the photocatalytic oxidation of oxazolidinone by O_2 using mesoporous PCN as a catalyst (the reaction scope is shown in **Figure 4.2**). I have contributed by rationalizing the mechanism behind this transformation using 2-(2-oxooxazolidin-3-yl)ethyl acetate (oxazolidinone **1b**) as a model substrate, which I describe in the following sections.
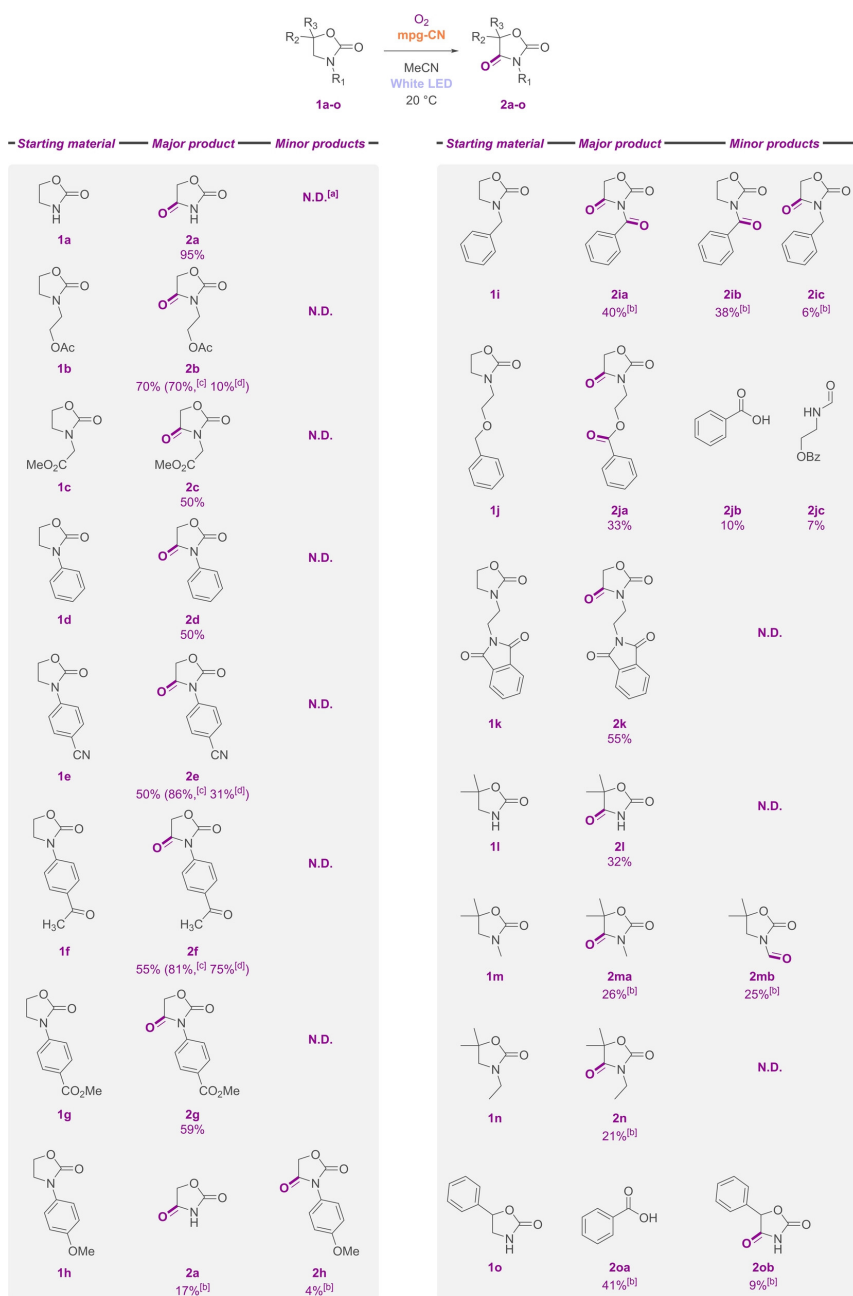
Figure 4.2: Scope of the oxazolidinone Oxidation Reaction. Reaction conditions: 1.25 mmol of oxazolidinone; 1 bar of O_2; 50 mL of acetonitrile; four 50 W white LED modules; 24–72 h (monitored by ^{1}H NMR). [a] not detected. [b] obtained by ^{1}H NMR using 1,3,5-trimethoxybenzene as internal standard. [c] and [d] 0.05 mmol of oxazolidinone and UV LED with and without PCN, respectively.

4.2 The Catalyst: Polymeric Carbon Nitride

Before modeling the reaction, an appropriate model of the catalyst (PCN) needs to be constructed. The structure of polymeric carbon nitride is complex and several model structures have been proposed.[267] A widely used model structure is graphitic carbon nitride (g-CN, **Figure 4.3a**), which gives a simulated band gap in agreement with experimental data.[50] However, g-CN contains highly condensed heptazine units, which is inconsistent with elemental analyses of real samples, which show a higher hydrogen content. Another type of structure, melon (**Figure 4.3b** and **c**), is in better agreement with elemental analysis, but has a significantly higher band gap than that measured experimentally for PCN.[50, 267] Given the importance of the photocatalytic properties of this material for the current study, the highly condensed g-CN structure was selected as the main model catalyst for the oxazolidinone oxidation reaction, and the results were compared with those obtained with the melon-type structures (details below).
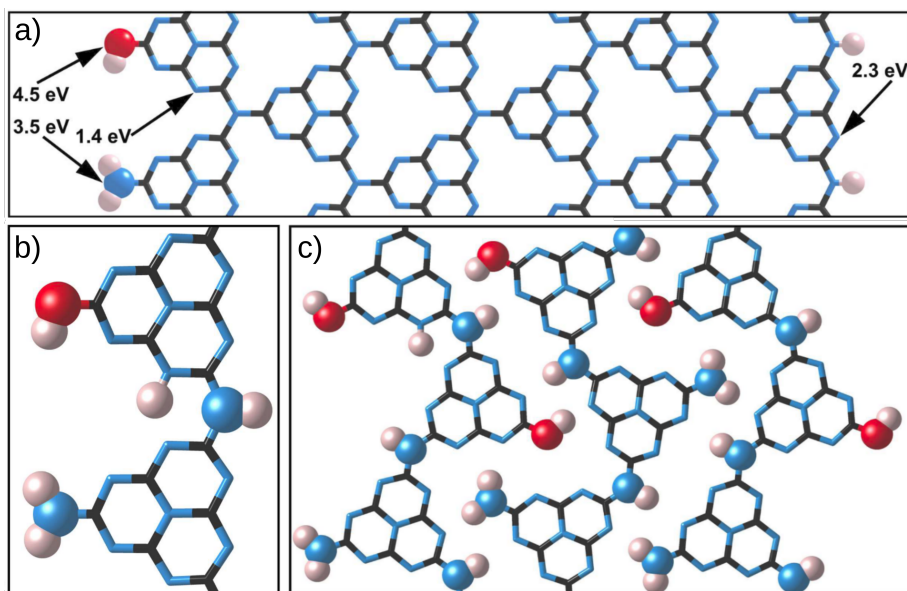
Figure 4.3: (a) The g-CN model (terminated surface g-CN) showing the energies of H adsorption at different sites. (b) The melon model with a single strand (s-melon-2D). (c) The melon model with three strands (melon-2D). The melon-2D models are shown after accepting the H atom.

The initial model of g-CN was created as an infinite two-dimensional surface (referred to as pristine g-CN). To improve the accuracy of the model, a terminated surface g-CN was developed by splitting the 2D surface and

attaching H atoms to the nitrogen atoms that were left with an incomplete octet due to the surface termination. In addition, NH_2 and OH groups were attached to carbon atoms left with an incomplete octet (as shown in **Figure 4.3**), which is consistent with the experimental finding that both groups are equally present in mesoporous PCN.[266] Of the six rows of condensed heptazine strands seen in **Figure 4.3a**, the middle two were kept fixed during geometry optimizations.

4.3 Breaking the C–H bond: Proton-Coupled Electron Transfer to Carbon Nitride

I have considered three pathways to cleave the oxazolidinone C–H bond (**Figure 4.4**). In the energy transfer (EnT), the O_2 molecule is activated by excitation to its singlet state ($^1O_2$) which subsequently oxidizes the substrate. Photoexcitation of O_2 was indeed observed in the presence of PCN.[268] However, performing the reaction with other $^1O_2$-generating photocatalysts yielded minute amounts of the desired reaction product, allowing to exclude the EnT pathway as the actual mechanism. Another possible pathway, photoinduced electron transfer (PET), involves electron transfer from the substrate to the catalyst. Cyclic voltammetry measurements showed that the oxidation potential of four investigated oxazolidinones (> 1.5 V vs. SHE) is higher than the potential of the photogenerated hole in PCN (1.4 V vs. SHE).[269] DFT simulations also revealed that the highest-energy electrons in g-CN are almost 2 eV higher in energy than the highest-energy occupied molecular orbital (HOMO) of oxazolidinone **1b**. These factors indicate that the electron transfer from the substrate to the catalyst is thermodynamically unfavorable, ruling out the PET pathway, and leaving PCET as the most likely pathway.

The PCET from the substrate to the catalyst is the first step in the oxazolidinone oxidation reaction. In g-CN, there are numerous sites where the H atom can bind and form [g-CN+H]$^\bullet$. The investigation of different binding sites (**Figure 4.3a**) of the hydrogen atom showed that the lowest energy position ($\Delta E = +1.4$ eV) corresponds to the structure in which hydrogen atom is located inside a triangular pocket formed by condensed heptazine units and attached to a nitrogen atom. A more accurate Gibbs energy change for the transfer of the H-atom to g-CN ($\Delta G = +1.5$ eV) was obtained using the electronic energy calculated with the HSE06 hybrid functional as well as the zero-point vibrational energy and entropy corrections. The obtained value is significantly lower compared with the energy of the C–H bond in oxazolidinone **1b** in vacuum (4.03 eV). This means that the highly endergonic homolytic C-H bond cleavage is facilitated in the presence

of an H-atom acceptor such as g-CN. The enhancement of C–H cleavage with g-CN is due to a remarkable stability of the [g-CN+H]$^\bullet$ system, which can be rationalized by the delocalization of the extra electron in g-CN (**Figure 4.5**).
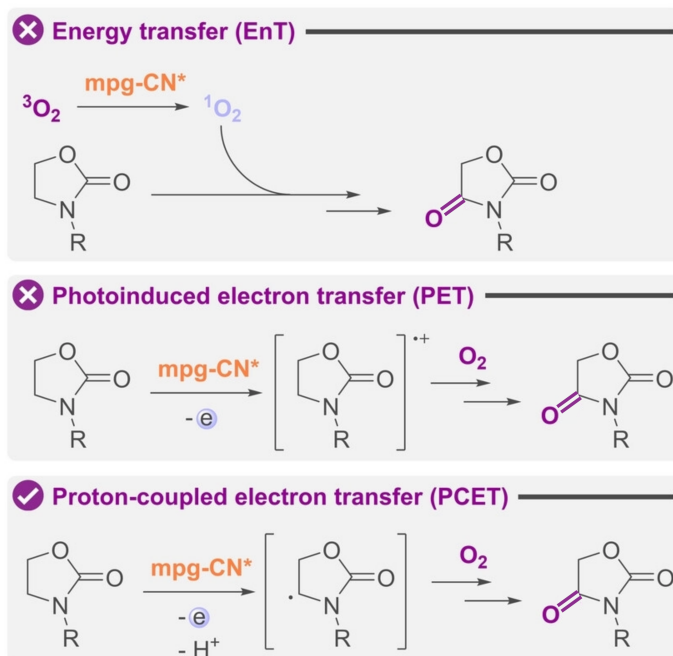
Figure 4.4: Three possible pathways (simplified) of oxazolidinone oxidation.
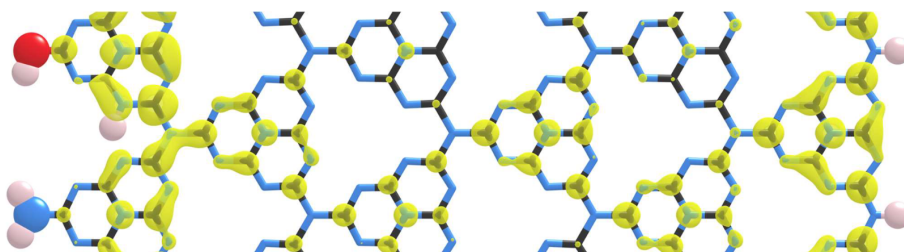
Figure 4.5: Real-space projection of the extra electron in the [g-CN+H]$^\bullet$ system, showing significant delocalization. The isosurface level was set to $5.2 \cdot 10^{-4} a_0^{-3}$ (a_0 is the Bohr radius).

The energies of H atom transfer to various systems (including the melon model of PCN) have also been calculated and are shown in **Table 4.1**. The data show that the use of the melon model or the inclusion of an implicit solvent model and multiple g-CN 2D layers do not result in significantly

different energies of H atom transfer.

Table 4.1: Electronic energy differences for H-atom transfer from oxazolidi-none **1b** to different H-atom acceptors. The main model used in the work is shown in bold.

H atom acceptor	implicit solvent[270]	ΔE (eV)
no acceptor	no	4.03
MeCN	no	2.76
MeCN	yes	2.90
g-CN pristine, one 2D layer	no	1.23
g-CN pristine, one 2D layer	yes	1.46
g-CN pristine, four 2D layers	no	1.33
g-CN terminated, one 2D layer	**no**	**1.36**
s-melon-2D (one strand)	no	1.42
melon-2D (three strands)	no	1.67

4.4 The Mechanism of Oxazolidinone Oxidation

After the endothermic first step—the PCET from oxazolidinone to the catalyst—all subsequent steps in the proposed mechanism are exothermic (**Figure 4.6**). In order for the first step to be favorable, external energy must be introduced into the system, which is done by photoexcitation of the catalyst. The electronic band gap of 2.6 eV in g-CN ensures that the catalyst in the excited state has more than enough energy to overcome the 1.5 eV required for the PCET.* The formation of $[g\text{-}CN+H]^\bullet$ can occur directly in the ground state, or in an excited state followed by relaxation to the ground state; however, this does not affect the reaction energetics because the Fermi level of the system is close to the conduction band due to the additional electron, and the excited state is energetically close to the ground state. **Int1** formed by PCET then traps an oxygen molecule, resulting in the formation of a peroxo radical **Int2** ($\Delta E = -1.3$ eV). Another possible mechanistic pathway involves the capture of the hydrogen atom from $[g\text{-}CN+H]^\bullet$ by the O_2 molecule to form $HO_2^\bullet$. However, this step

---

*In this case, the optical band gap (the energy required for photoexcitation) should be considered rather than the electronic band gap (the difference between the valence band and the conduction band). The optical band gap is often narrower than the electronic band gap because it includes the stabilizing interaction between the electron and the hole (exciton binding). Exciton binding energies can be calculated with the GW approximation and are given in ref. [271] for g-CN (0.3 eV) and melon-2D (0.8 eV). This results in optical band gaps that are still well above the energy required for PCET, even in the case of melon-2D (due to its large electronic band gap of 3.4 eV).

is +0.4 eV uphill (**Figure 4.7**) and therefore thermodynamically less favor-able and can be ruled out. In the main pathway, **Int2** recovers the H atom from [g-CN+H]$^{\bullet}$, forming a hydroperoxide intermediate **Int3** ($\Delta E = -1.1$ eV), which eliminates a water molecule, leading to the formation of **2b** ($\Delta E = -3.0$ eV).
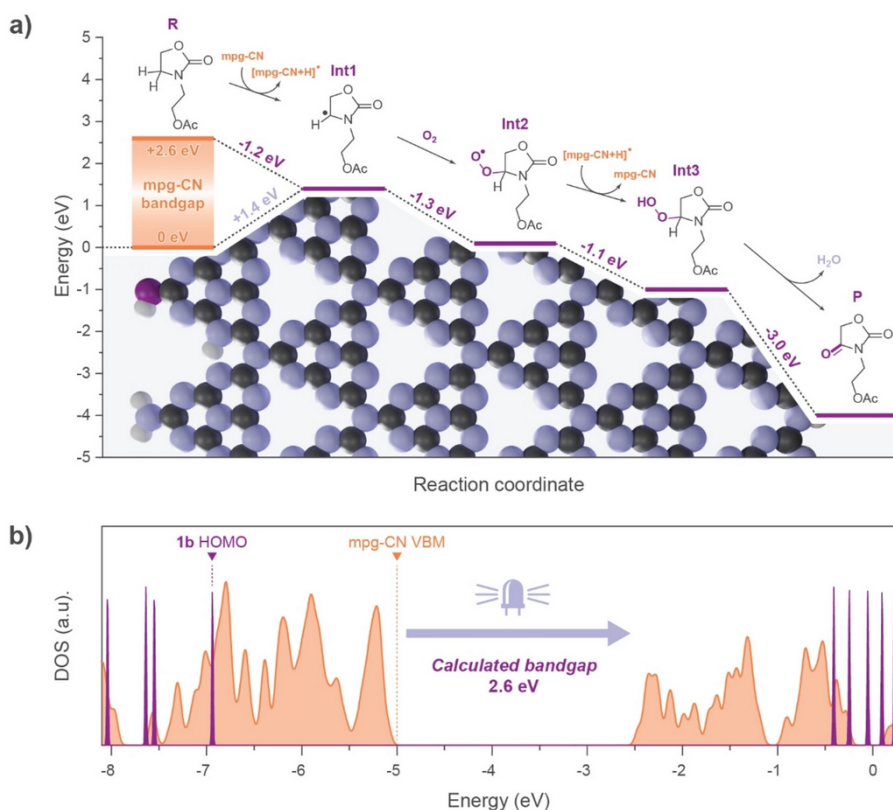
Figure 4.6: a) Proposed mechanism for the oxidation of oxazolidinone **1b** on PCN (mpg-CN) with electronic energy differences for each step. b) The electronic density of states plot for oxazolidinone **1b** (purple) and g-CN (orange). The energy scale corresponds to the energies obtained directly from the VASP output files using the PBE functional. The correspondence between the two systems was confirmed by matching the energies of the O 2s electrons between these systems (not shown).
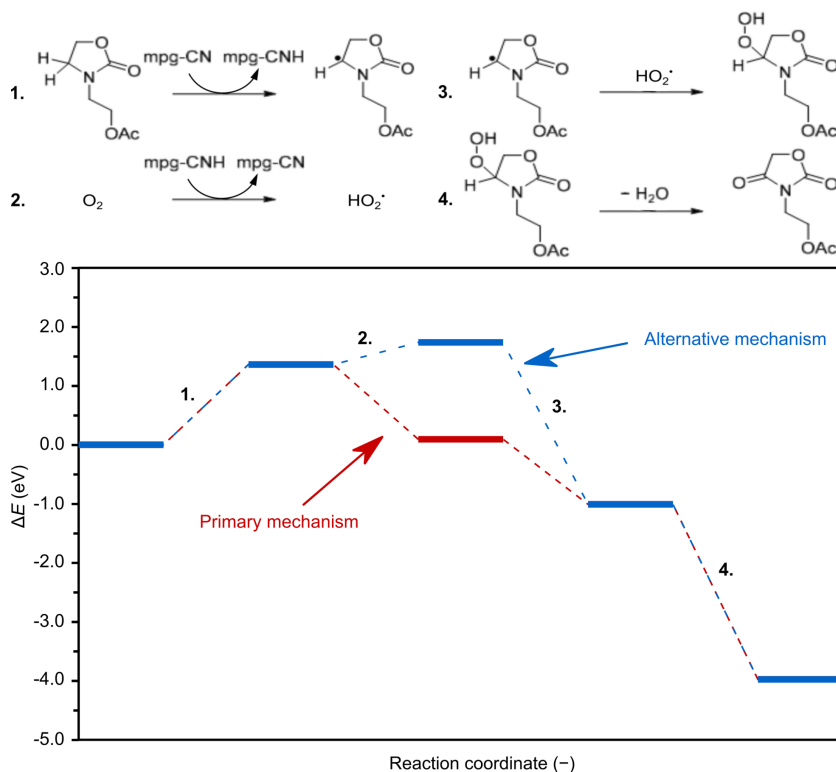
Figure 4.7: Top: Secondary mechanism for the oxidation of oxazolidinone. Bottom: Comparison of the energy profiles of the secondary and the primary mechanisms. The first and fourth steps are the same for both pathways.

4.5 Conclusions

In this chapter, I have investigated the photocatalytic oxidation mechanism of oxazolidinone to oxazolidinedione on polymeric carbon nitride. I discussed how the catalyst model used in the simulations (g-CN) was constructed. I then showed that the electronic structures of the catalyst and the substrate do not allow direct photogenerated electron transfer. This leaves proton-coupled electron transfer as the main pathway for C–H bond cleavage, followed by the spontaneous steps leading to oxazolidinedione formation. Using DFT simulations with the PBE and HSE06 functionals, I show that a $\Delta G = +1.5$ eV was found for the PCET step that cleaves the C–H bond, which is compensated by photoexcitation of the catalyst. The relatively low energy of the C–H bond dissociation is explained by the fact that g-CN is a good H-atom acceptor due to its ability to delocalize the added electron.

4.6 Specific Computational Details

Kinetic energy cutoff for the plane-wave basis set was set to 450 eV. Grimme's DFT-D3 method was used to calculate the energies in the melon-2D model due to its considerable intramolecular interactions.[272]

Chapter 5

Mixed Catalytic Systems: CO_2 Reduction on Co-Doped Hydroxyapatite

When studying a photocatalytic system that is novel or complex, the catalyst may be difficult to characterize. In this case, the catalyst model needs to be constructed from limited experimental data and special care must be taken to ensure that the predicted properties of the model are consistent with the experiments. In this chapter, I describe the work that was published in ref. [42] and concerns photothermal CO_2 reduction on hydroxyapatite (HAP) doped with Co—a novel catalyst with a complex structure. All figures are adapted from the publication unless otherwise noted.

5.1 Photothermal CO_2 Reduction on Co-Doped Hydroxyapatite

5.1.1 Transcending the Limitations of Semiconductor Photocatalysts: Localized Surface Plasmon Resonance

The production of photochemical solar fuels is limited by the suboptimal conversion of light to chemical energy and harvesting in semiconductor-based photocatalysts,[273] which primarily capture UV and visible blue light.[274] In a semiconductor photocatalyst, photons with energy equal to or greater than the semiconductor band gap generate electron–hole pairs. The main challenges in the catalyst design are to increase the efficiency of charge separation and to reduce the recombination kinetics to allow time for electron transfer with substrate molecules adsorbed on the particle surface.

In contrast to conventional semiconductors,[275, 276] metal nanoparticles supported on thermally insulating materials interact with visible and near-infrared photons via localized metal surface plasmon resonance (LSPR).[40] This process leads to enhanced catalytic conversion rates at the metal nanoparticle due to localized heating and generation of "hot carriers" that affect the electronic structure of the species involved in the reaction.[277–279] Feng et al.[280] described a plasmonic structure consisting of porous silica needles embedded with Co nanoparticles. This photocatalyst absorbs light over the entire solar spectrum, enabling efficient photothermal conversion of CO_2 to CO and CH_4 without external heating under 20 suns of illumination. In addition, Guo et al.[281] prepared a Cu-doped HAP catalyst that exhibited exceptional activity in the reverse water gas shift reaction, under 40 suns of light irradiation and without the need for external heating. In the catalyst, the formation of Cu nanoparticles responsible for LSPR on the HAP structure was observed. As is discussed in later sections, the Co-doped HAP studied in this work also supports the formation of LSPR-enabling metallic Co nanoparticles that enhance the CO_2 reduction performance.

5.1.2 Co-Doped Hydroxyapatite as a CO_2 Reduction Catalyst

HAP ($Ca_{10}(PO_4)_6(OH)_2$) is a well-known structure found in minerals, bones and teeth. It can be easily synthesized on a large scale using abundant raw materials, and offers significant stability and structural adaptability, allowing for numerous partial cation substitutions.[282] For example, Ca ions can be partially replaced by various divalent cations, including Sr^{2+}, Ba^{2+}, Zn^{2+}, Cu^{2+}, or Co^{2+}. In addition, the thermal insulating properties of HAP-based materials make them highly suitable as photothermal catalysts by locally trapping heat and maintaining a high temperature at the reaction site. In the work described in this chapter, my colleagues at the Polytechnic University of Valencia (Dr. Peng Yong, Horațiu Szalad, and Dr. Josep Albero Sancho) developed a series of Co-doped HAP photocatalysts with increasing Co content for selective gas-phase CO_2 hydrogenation. Co-doped HAP was shown to be a highly active and CO-selective photothermal CO_2 hydrogenation catalyst (**Figure 5.1**) under 1-sun illumination and controlled external heating. The maximum CO rate achieved was 62 mmol·g^{-1}·h^{-1} at 15 mol% Co (relative to total metal content) and 400 °C, with the material demonstrating stability for 90 hours of operation under continuous gas flow. My role was to elucidate the catalyst structure and model the mechanism of CO_2 reduction as a function of Co content based on the experimental data obtained.
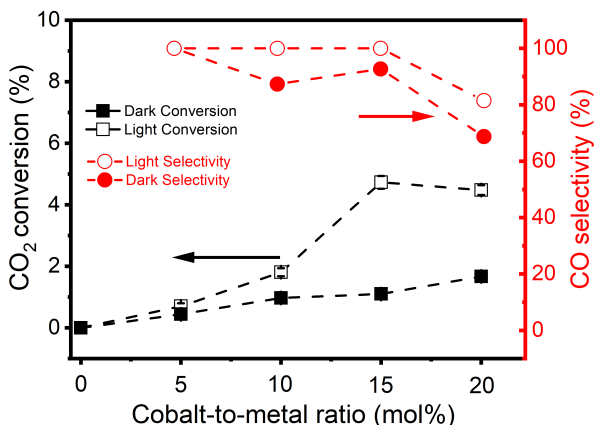
Figure 5.1: HAP activity of CO_2 hydrogenation and selectivity towards CO as a function of Co content.

5.2 A Complex Catalyst: The Structure of Co-Doped Hydroxyapatite

Hydroxyapatite (HAP) in its bulk form was represented by a hexagonal unit cell (**Figure 5.2**) containing 10 Ca atoms at two different positions, M1 and M2.[282] Simulations show that cobalt preferentially substitutes calcium at the M2 position by 0.29 eV. The substitution of a Co atom with Ca in the unit cell (Co-HAP) gives a theoretical Co loading of 5.8 wt%, which is consistent with the inductively coupled plasma optical emission spectroscopy (ICP-OES) measurement of the $Co_{10}HAP^*$ sample (5.88 wt%). This indicates that Co indeed substitutes Ca in the structure. The X-ray absorption near edge structure (XANES) measurements showed a common rising edge for Co-doped HAP samples as well as CoO and $Co(OH)_2$ references at about 7716 eV, indicating that Co is in the +2 oxidation state.[280] The Co atoms in the computational model were obtained in the correct oxidation state, since the magnetic moments of the Co atoms are either 3 μ_B or 1 μ_B, corresponding to the high-spin and low-spin d^7 configurations, respectively.

Both experimental and simulated (**Figure 5.3**) X-ray diffraction (XRD) patterns of Co-doped HAP show a strong similarity to pristine HAP patterns, although the diffraction peaks become broader, indicating reduced crystallinity. Higher Co loadings in $Co_{15}HAP$ and $Co_{20}HAP$ samples resulted in the disappearance of the HAP diffraction peaks. These results suggest that at low Co/Ca ratios, Co can be incorporated into the HAP

---

*In the notation Co_xHAP, x refers to the initial molar ratio of Co with respect to Co + Ca.
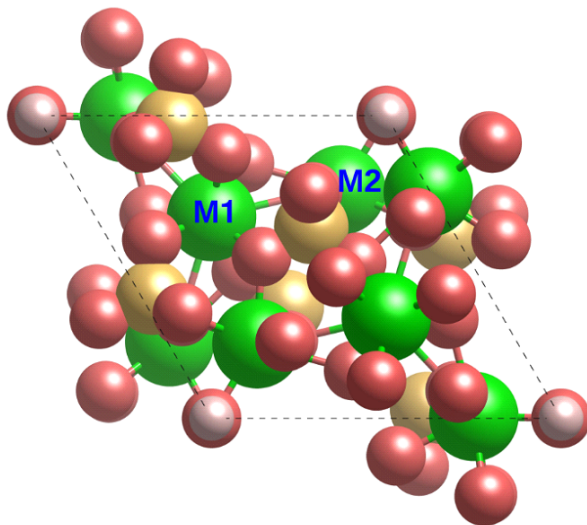
Figure 5.2: M1 and M2 positions in HAP. Color code—O: Red, Ca: Green, P: Yellow, H: White.

structure, causing a slight distortion of the crystal lattice due to the ionic radius difference between Ca^{2+} and Co^{2+}.[282] However, further Co incorporation leads to phase segregation and loss of crystallinity. In fact, high resolution transmission electron microscopy (HR-TEM) showed the presence of a separate phase in the form of 1–2 nm large nanoparticles when the Co loading is high enough (from $Co_{10}HAP$ onward). The nanoparticles were identified as Co_3O_4 by my co-authors based on the results of optical, Raman, and X-ray photoelectron spectroscopy (XPS).

After the sample was activated for 2 h in H_2 flow at 400 °C, the Raman and XPS measurements indicated a reduction of Co_3O_4 nanoparticles to Co^{2+} and metallic Co^0. On the other hand, the reduction of Co^{2+} starts only at about 650 °C according to the temperature programmed reduction (TPR) data, which is significantly higher than what was used for the CO_2 reduction reaction. No changes were observed in the XPS spectra for Ca $2p$ and P $2p$, indicating that the HAP structure is unaffected by activation.

The surface of Co-HAP was modeled as the (0001) surface slab of HAP[283, 284] with one calcium atom replaced by cobalt. Atoms in the bottom half of the structure were held fixed during geometry optimization. Comparison of the relative energies associated with the substitution of calcium ions by cobalt at different positions (**Figure 5.4**) revealed the tendency of Co to segregate toward the surface where the metallic Co nanoparticles eventually form. The nanoparticles were modeled as the
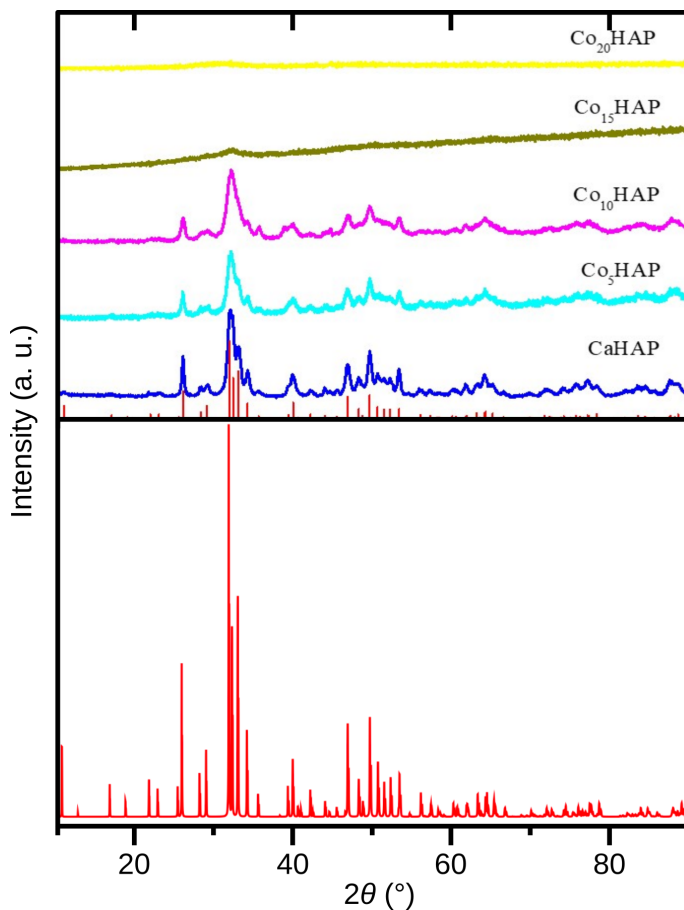
Figure 5.3: Top: Measured XRD patterns of the pristine (Ca)HAP and Co-doped HAP samples. The standard pattern of HAP from the International Centre for Diffraction Data (file no. 09-0432) is shown in red. Bottom: Simulated XRD pattern of Co-HAP using VESTA.

(0001) surface slab of hcp–Co. Oxygen vacancy formation was also studied on the (0001) surface facet of HAP. For the pristine HAP (0001) facet, the calculated Gibbs energy change to form a vacancy (and produce H_2O) is 2.1 eV. In the presence of Co, the Gibbs energy of vacancy formation decreases to 1.1 eV.
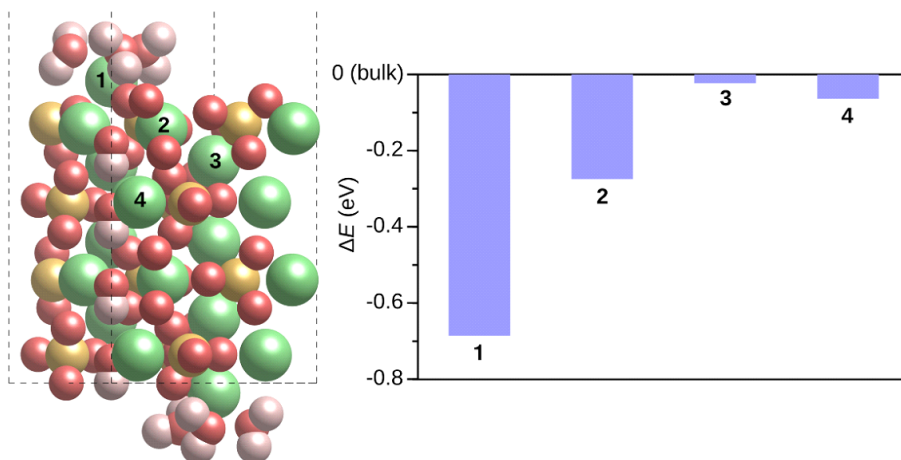
Figure 5.4: The studied positions of Co doping and the change in electronic energy when Ca is substituted by Co. The substitution in bulk HAP is set to 0 as a reference. More negative values indicate a thermodynamically easier substitution. In these simulations, the metal atoms at the surface were capped with three H_2O molecules to maintain a similar coordination as in the bulk and to emphasize the fact that the material is synthesized in water.

5.3 Co-Doped HAP as a Photocatalyst

5.3.1 The Origin of Light Absorption in Co-doped HAP: Intragap States and LSPR

The CO_2 reduction performance of HAP is significantly enhanced by light, as shown in **Figure 5.1**. Optical spectra have revealed the catalyst's ability to absorb visible and near-infrared light, which is not exhibited by the pristine HAP due to its large band gap (**Figure 5.5a**). The Co-doped HAP model introduced above allows for two ways for HAP to absorb light. The first occurs in the Co-HAP phase, where the intragap states introduced by cobalt (**Figure 5.5b**) allow for various electronic transitions not possible in the pristine HAP. In particular, there are five new intragap states (some occupied and some empty) within about 2 eV of the valence band maximum (VBM). The absorbed light excites the catalyst, affecting the adsorption of reactants (see Section 5.4.1).

The second way to absorb light is by LSPR, which is enabled by the Co nanoparticles. Such a phenomenon can enhance the reaction via two mechanisms: (1) increase of the local temperature and (2) the generation of "hot" carriers (photogenerated electrons and holes with high energies), which
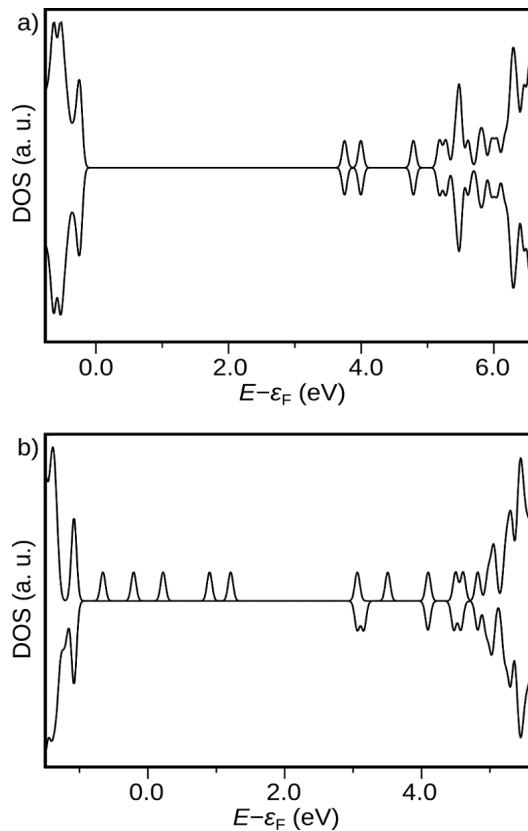
Figure 5.5: The Density of States for the (0001) surface facet of (a) pristine HAP and (b) Co-HAP. The results were obtained using the GW method, which gives more accurate energies of the unoccupied states compared to DFT.

further improve the reaction kinetics.[285] The local temperature increase, ΔT_{NP}, can be calculated as follows:[286, 287]

$$\Delta T_{\mathrm{NP}} = \frac{\sigma_{\mathrm{abs}} I}{4\pi R \kappa_{\mathrm{air}}} \tag{5.1}$$

where σ_{abs} is the absorption cross section that can be calculated using the general Mie theory,[288], I is the irradiance of the incident light, R is the nanoparticle radius, and κ_{air} is the thermal conductivity of the surrounding medium. In our system, this calculation yields a negligible temperature increase, leaving the hot carriers responsible for the catalytic enhancement. Since LSPR only occurs in the systems with a nanoparticle phase, the reaction on such systems is more affected by light compared with the systems with lower levels of Co content (**Figure 5.1**).

5.4 The Complete Picture: The Mechanism of CO_2 Reduction on Co-Doped HAP

5.4.1 Adsorption of Reactants on the Co-Doped HAP Surface

After elucidating the structure of the photocatalyst, I proceeded to study the reaction mechanism. To do this, I first modeled the adsorption of the species involved (reactants and products). The Gibbs energies for this process are given in **Table 5.1**, for the most favorable systems. It was found that while H_2, CO, and H_2O bind to metallic sites, CO_2 preferentially adsorbs on the oxygen atom of the HAP surface to form carbonate, as illustrated in **Figure 5.6**. It was also shown that the presence of vacancies in Co-HAP allows CO_2 to adsorb on the Co atom via oxygen,[289] but the ΔG of $+0.43$ eV makes this less favorable than the described adsorption on oxygen via C ($\Delta G = -0.16$ eV). The band corresponding to the O-bound CO_2 was observed in the Raman spectra at 1834 cm^{-1}, corresponding to the DFT-obtained vibrational frequency of 1855 cm^{-1} for this system. For CO_2 to be considered adsorbed, I required it to be in its activated state, i.e., the otherwise linear molecule is bent. However, such a structure could not be obtained during geometry optimization for all systems (namely Co-HAP and HAP without adsorbed water) in which CO_2 desorbs from the surface. In these cases, I would model adsorbed COOH instead of CO_2, giving the bent O–C–O geometry. I would then remove the hydrogen and re-optimize the structure with the C atom frozen during optimization. In this way, the bond between the C atom and the O atom on the HAP surface could not dissociate because the HAP surface would deform significantly, so instead CO_2 remains adsorbed in the bent geometry.

Another thing to note is that CO_2 adsorbs ~ 1 eV more easily on HAP if there is H_2O adsorbed on the nearby metal (the adsorbed water can be seen in the corresponding structures in **Figure 5.6**). Furthermore, CO_2 tends to adsorb far away from the Co doping sites, as shown by the adsorption energies on HAP and Co-HAP. Both effects are due to the local electronic structure change upon H_2O adsorption or Co doping, since CO_2 does not interact directly with either the adsorbed water molecules or the nearby metal atom. The preference of CO_2 to adsorb on the pristine HAP and away from the Co-doping site results in the adsorbed CO_2 not being affected by irradiation. This is manifested in the reaction orders of the CO production rates relative to the CO_2 pressure, which do not change significantly upon irradiation on either Co$_5$HAP (the system with only the Co-HAP phase, **Figure 5.7a**) or Co$_{15}$HAP (the system with both the Co-HAP and nanoparticle phases, **Figure 5.7c**).
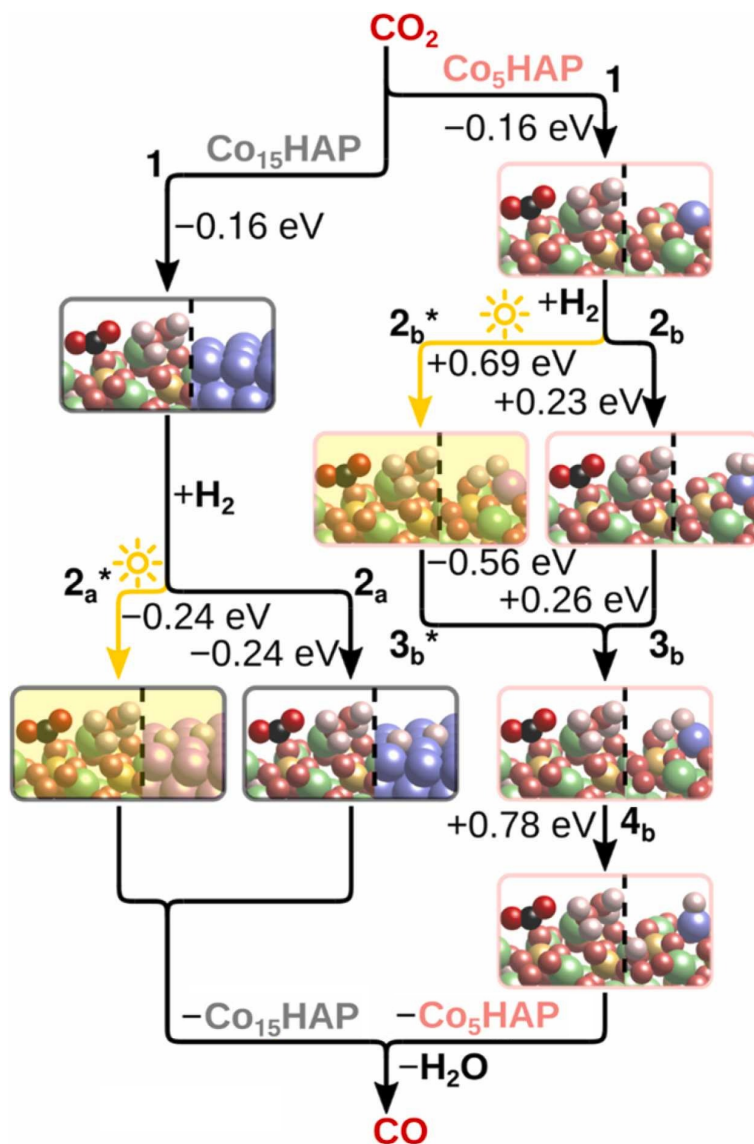
Figure 5.6: CO_2 and H_2 adsorption and the subsequent dissociation of H_2 in light and dark on $Co_{15}HAP$ and Co_5HAP. The ΔG's are shown for selected steps. Color code—Co (ground state): Blue, Co (excited state): Pink, other atoms: As above.

The adsorption of H_2 was considered in both molecular and dissociative modes. While the dissociative adsorption was more favorable on the metallic Co surface, the molecular adsorption was preferred on the other systems. Since H_2 adsorbs on the nanoparticle phase (or on the Co atom of

Table 5.1: The ΔG (eV) for the adsorption of reactants and products on different phases of Co-doped HAP at 250 °C. In the system where CO_2 was adsorbed on HAP and Co-HAP, two water molecules were present on the surface metal atom.

adsorbed species	HAP (0001)	Co-HAP (0001)	metallic Co (0001)
CO_2	-0.16	$+0.54$	$+1.15$
H_2	$+0.54$	$+0.23$	-0.24
CO	$+0.37$	-0.51	-0.90
H_2O	-0.23	-0.26	$+0.48$
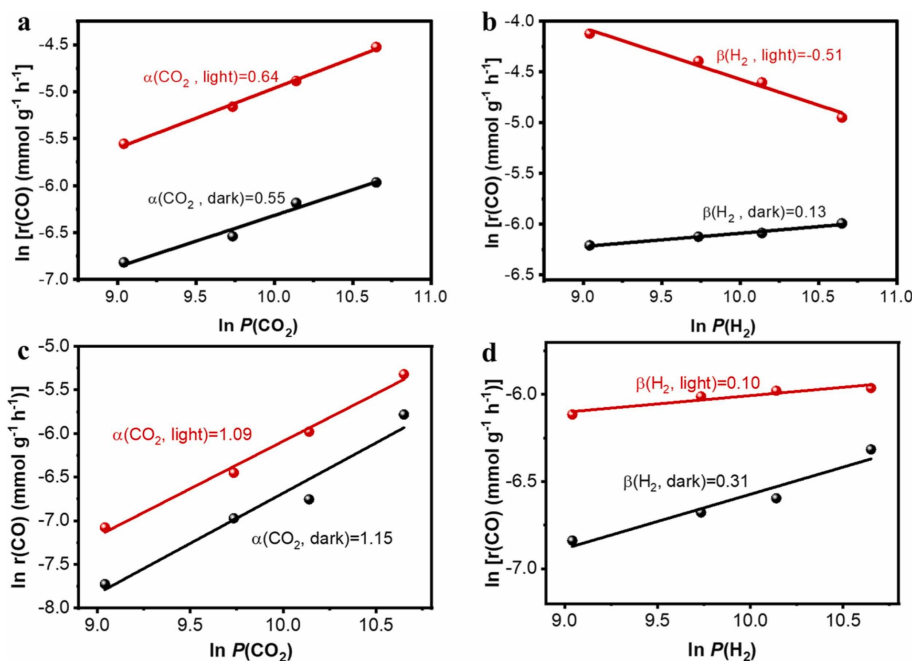
Figure 5.7: Experimentally obtained reaction orders at 250 °C in $Co_{15}HAP$ (a and b) and Co_5HAP (c and d) with respect to the partial pressure of CO_2 (a and c) and H_2 (b and d).

Co-HAP in the absence of the nanoparticle phase), it is affected by irradiation, as seen in the CO production rate relative to the H_2 pressure in light and dark (**Figure 5.7b** and **d**). To obtain the energies of H_2 adsorption on the Co-HAP phase in the presence of light, the catalyst with and without adsorbate was also modeled in the excited state by fixing the magnetization of the system to 1 μ_B (the ground state for these systems has a magnetization of 3 μ_B). The excited state energies were obtained by assuming that the electronic structure in the excited state corresponds to a unique electron

density functional. Since this approximation does not necessarily hold in the excited state (see Chapter 2), the results obtained by this approach should be confirmed by a method such as time-dependent DFT rather than taken at face value. Nevertheless, the point of this approach is to illustrate the photocatalytic potential of Co-HAP, for which the energies obtained by DFT are sufficient. The electronic energies of adsorption (**Figure 5.8**) show that in the excited state H_2 adsorbs in a partially dissociated mode (the H atoms are 1.6 Å apart) rather than molecularly as in the ground state (compare the steps $\mathbf{2}_b^*$ and $\mathbf{2}_b$ in **Figure 5.6**), illustrating the enhancement of the necessary dissociation of H_2 by irradiation. After the adsorption of H_2, the system relaxes to the ground state (step $\mathbf{3}_b$) and further (complete) dissociation proceeds (step $\mathbf{4}_b$). The ΔG of +0.78 eV for complete dissociation indicates a rather high barrier. However, this value neglects the configurational entropy of the dissociated macrostate, where the variety of surface oxygens available for proton binding introduces numerous microstates. A thorough understanding of the process would require consideration of the potential barriers associated with each binding site and the overall change in configurational entropy of the system. Nevertheless, given the temperatures at which the reaction occurs, it is likely that these entropic factors increase the viability of the dissociation process.

molecular	partially dissociated	completely dissociated
−0.40 eV	−0.15 eV	+0.17 eV
−0.09 eV*	−0.20 eV*	+0.32 eV*
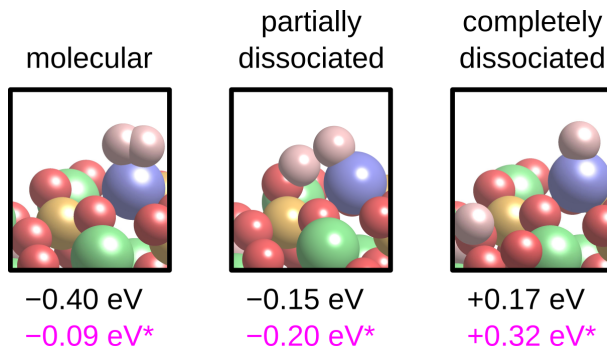
Figure 5.8: The different modes of H_2 adsorption on Co-HAP with the corresponding ΔE. The adsorption values marked with an asterisk represent the adsorption in the excited state. The figure was prepared for this thesis (not published elswhere).

In addition to the reactants, the Gibbs energies of adsorption of the products were also modeled. As shown in **Table 5.1**, H_2O preferentially adsorbs on the pristine HAP and the adsorption is favorable even at the working temperature where entropy significantly inhibits the adsorption of molecules. The presence of water on the surface metal atoms allows CO_2 adsorption as discussed above. On the other hand, CO preferentially adsorbs

on Co atoms, ideally on the fcc sites of the nanoparticle phase. The vibration of CO adsorption on the nanoparticle phase was observed in the Raman spectrum at 1698 cm^{-1}, corresponding to the value of 1735 cm^{-1} obtained by DFT. This is attributed to the CO bound by the nanoparticle Co atoms after evolving from the Co-HAP phase upon hydrogenation of CO_2.

5.4.2 Hydrogen Transfer and CO_2 Hydrogenation

After adsorption of the reactants onto the catalyst surface and dissociation of H_2 (**Figure 5.6**), the reaction proceeds as in **Figure 5.9**. The single protons coming from the H_2 dissociation hop over the HAP surface oxygen atoms to reach the adsorbed CO_2. In the case of $Co_{15}HAP$, the electrons remaining on the nanoparticle phase also need to reach CO_2 for its reduction to occur. The poor electron transfer through HAP can be somewhat improved with cobalt doping by introducing intragap states and facilitating vacancy formation.[188, 289] However, electron transport may still be difficult in Co-HAP, and the catalytic activity in the dark is similar in $Co_{15}HAP$ as in Co_5HAP (**Figure 5.1**), suggesting that the main mechanism in the former system is the same as in the latter, despite the presence of the nanoparticle phase. In light, LSPR enables the hot electron transfer from the metal nanoparticle to the semiconductor support,[41] changing the mechanism and significantly enhancing the activity in $Co_{15}HAP$.
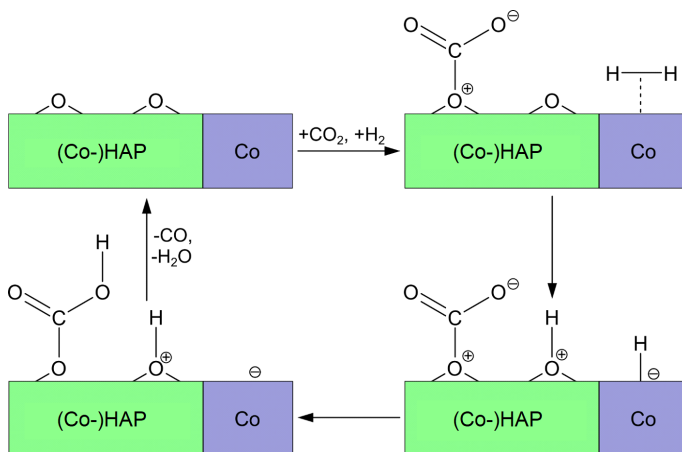
Figure 5.9: General mechanism of CO_2 hydrogenation on Co-doped HAP.

I also investigated the possibility of vacancy-driven CO_2 reduction. In this process, H_2 reduces the HAP surface, forming oxygen vacancies that subsequently reduce the CO_2 adsorbed on the nearby Co doping sites (adsorption on Co is enabled by the presence of vacancies, as described above).

For this to happen, the vacancy would have to form ($+1.1$ eV); CO_2 would have to adsorb on the Co atom ($+0.43$ eV) instead of O (-0.16 eV); and finally, an oxygen from the CO_2 would have to fill the vacancy ($+1.5$ eV barrier obtained by NEB). These unfavorable energetics rule out the possibility of a vacancy-driven reduction as described.

5.5   Conclusions

In this chapter, I have rationalized the experimental results obtained for the photothermal production of CO by hydrogenation of CO_2 on the Co-doped hydroxyapatite catalyst with a complex structure. The main model of the catalyst was the (0001) surface slab of Co-HAP, where Co replaces Ca in the HAP unit cell, preferably near the surface. I demonstrated that this model well describes the Co-doped HAP at lower Co loadings (5% initial molar ratio of Co with respect to the total metal content) by comparing the simulation results to the results of characterization techniques. When modeling higher Co loadings (15%), the (0001) surface slab of metallic Co was used to represent the experimentally observed nanoparticles. Vacancy formation in Co-HAP was shown to be facilitated by the presence of cobalt, but still thermodynamically inefficient at the working temperatures.

Light absorption in Co-HAP has been rationalized by the presence of several intragap states that are absent in pristine HAP. In the Co_5HAP system, where only the Co-HAP phase is present, light absorption can enhance catalytic activity by facilitating the dissociation of H_2. When the Co nanoparticle phase is present, absorption also occurs via LSPR. It was shown that LSPR does not significantly increase the local temperature in the modeled system, leaving the hot electrons as the main contributor to the photocatalytic enhancement in the system with two separate phases ($Co_{15}HAP$).

By studying the nature of the reactant absorption on the Co-doped HAP, I have shown that different reaction mechanisms occur at different Co loadings. In the presence of the Co nanoparticle phase, H_2 preferentially adsorbs on the nanoparticle phase where it dissociates and the hydrogen atoms are transferred to the Co-HAP phase. H_2 dissociation and transfer to CO_2 is enhanced by light, especially at the nanoparticle phase where LSPR allows hot electron transfer to the Co-HAP phase. On the other hand, at the Co-HAP phase, light is mainly responsible for the enhancement of H_2 dissociation. The difference in mechanisms has also been observed experimentally by measuring the reaction orders for CO production.

These results illustrate the value of computational chemistry in complementing experimental data and enabling the elucidation of processes oc-

curring in complex photocatalytic systems. We should keep in mind the assumptions made in this research, such as the use of idealized catalyst models and the separate study of different phases. The excited state simulations were based on the approximation that the electronic structure in the excited state corresponds to a unique electron density functional, and the corresponding predictions should ideally be confirmed with more accurate methods such as time-dependent DFT. Nevertheless, this research is a stepping stone that can guide future investigations to further improve the design of efficient photocatalytic systems.

5.6   Specific Computational Details

The kinetic energy cutoff for the plane-wave basis set was set to 450 eV. Dipole corrections were applied in the direction perpendicular to the surface slab. The GW approximation was used as implemented in VASP,[290, 291] with a low-scaling algorithm.[292, 293] The calculations were performed only for the first iteration of Hedin's equations (G_0W_0), since it was seen in the prior convergence tests that the eigenvalue-self-consistent calculation of G does not significantly affect the obtained quasiparticle energies. These calculations used a Γ-centered **k**-point, a kinetic energy cutoff of 500 eV, and 1152 quasiparticle orbitals.

The simulations on the CoO model used Dudarev's approach to Hubbard's DFT+U correction.[294] For the Co $3d$ electrons, the U parameter was set to 4.32 eV while J was set to 1.00 eV. These simulations (as well as those with the Co nanoparticle model) were repeated until all the systems studied were in the lowest energy state (I made sure that the magnetization of the systems was equal. In the CoO systems, the optimal magnetizations were between 92 and 96 μ_B. In the Co systems, the optimal magnetization was $\sim$ 59 μ_B).

Chapter 6

Conclusions

In this thesis, I covered three of my publications in which I used computational chemistry methods in a systematic way to construct models consistent with experimental data and to uncover the mechanisms between three different catalytic processes. These processes reveal different strategies and complexities that arise in the atomistic modeling of photocatalysis:

- In **Chapter 3**, I study the influence of surface oxygen vacancies and exposed surface facets on water oxidation on $BiVO_4$. Using DFT with the PBEsol functional, I show that the V–O–V bridge-forming (split) oxygen vacancies are ~ 0.6 eV more stable than their conventional (localized) counterparts on the (011) surface facet of $BiVO_4$. The models of (001) and (011) $BiVO_4$ surface facets with and without vacancies were used to study the water oxidation mechanism. It was shown that the surfaces with vacancies are selective for OER, while the pristine surfaces are selective for HPER. In particular, the (001) facet with the oxygen vacancy is the most favorable system for water oxidation, forming O_2 starting from the applied potential of 1.6 V vs. RHE. The second most favorable reaction is HPER on the (011) pristine surface, forming H_2O_2 starting from 2.1 V vs. RHE. The results were confirmed with the PBE0 functional as well as GC-DFT. A new type of $BiVO_4$ oxygen vacancy (hydrated vacancy) has also been described, where the vacancy is filled by a solvent H_2O molecule. This vacancy hydration process is thermodynamically allowed, and the resulting system is readily oxidized to the pristine surface, potentially changing the amount of oxygen vacancies on the catalyst surface during the reaction. The work demonstrates how atomistic mechanistic studies can reveal the key catalytic parameters: Activity, selectivity, and stability.

- In **Chapter 4**, I study the mechanism of photocatalytic oxazolidinone

oxidation to oxazolidinedione on mesoporous PCN. After constructing an appropriate model of the catalyst (g-CN) that fits the experimental data, I use DFT with the HSE06 functional to show that the VBM potential of g-CN is too low for the photogenerated hole to oxidize oxazolidinone, leaving PCET as the likely first step. I then propose a mechanism involving an endergonic PCET transfer from oxazolidinone to the catalyst ($\Delta G = +1.5$ eV) and use DFT with the PBE functional to model the reaction intermediates. The relatively low PCET energy is rationalized by electron delocalization in g-CN. All subsequent steps are shown to be exothermic, and the energy required for the first step is well compensated by the absorbed light and the g-CN electronic band gap of 2.6 eV. The work highlights how the atomistic study of electronic structure can be crucial to elucidate a photocatalytic mechanism.

- In **Chapter 5**, I study the mechanism of photothermal CO_2 hydrogenation to CO on Co-doped HAP. To model the system with low doping levels (Co_5HAP), the structure used was the (0001) surface slab of Co-HAP (one Ca atom substituted by Co). For higher doping levels ($Co_{15}HAP$), the (0001) surface slab of Co (representing the metallic nanoparticle phase) was also included. Having shown that the model fits the experimental data well, I demonstrated that both models allow for light absorption: Co_5HAP by intragap states in Co-HAP revealed by GW and $Co_{15}HAP$ by LSPR on the Co nanoparticles. I then used DFT with the PBE functional to model the adsorption energies for the reactants and products of the reaction and showed that while CO_2 always adsorbs on HAP (preferably far from the Co atom), H_2 adsorbs on the nanoparticle phase when it is present. Furthermore, the ability of H_2 to dissociate and transfer from the H_2 adsorption site to the CO_2 adsorption site via proton hopping across the HAP surface was demonstrated. On Co_5HAP, light absorption enhances H_2 dissociation, while on $Co_{15}HAP$, LSPR enables hot electron transfer to the HAP phase, allowing CO_2 reduction. The work emphasizes the complementarity of experimental data and theoretical simulations and the necessity of different experimental measurements to construct a suitable computational model.

This thesis has demonstrated the power of atomistic modeling in elucidating the mechanisms of various photocatalytic processes. Through the study of three different systems, I have shown how a combination of different computational chemistry methods can provide insights into the role of catalyst structure, the nature of light absorption, and the reaction mechanism in photocatalysis. Each system studied illustrates a unique approach to modeling a photocatalytic process. These approaches are not only system-specific,

but also highly dependent on the available experimental data, emphasizing their importance. The results have implications for the design of more efficient photocatalysts and contribute to the broader goal of developing sustainable energy solutions. However, while this thesis has made significant strides in understanding photocatalytic processes, there is still much work to be done. Future research could focus on refining the computational models used in this thesis to improve their predictive power. In addition, the methods developed in this thesis could be coupled with macroscale simulations or applied to the study of other photocatalytic systems, thereby broadening our understanding of photocatalysis. Finally, there is a need for further experimental work to validate and build upon the results presented in this thesis. Through continued collaboration between experimental and theoretical researchers, we can continue to advance the field of photocatalysis and move closer to a sustainable energy future.

Bibliography

[1] Marcelo S. Sthel, José G. R. Tostes, and Juliana R. Tavares. "Current Energy Crisis and Its Economic and Environmental Consequences: Intense Human Cooperation". In: *Nat. Sci.* 5 (2013), pp. 244–252.

[2] Karl Marx. *Capital: A Critique of Political Economy, Volume 1 (edited and translated by Ernest Mandel and Ben Fowkes)*. Penguin Classics, 1992.

[3] Muhammad Shahbaz, Muhammad Nasir, Erik Hille, and Mantu Kumar Mahalik. "Uk's Net-Zero Carbon Emissions Target: Investigating the Potential Role of Economic Growth, Financial Development, and RD Expenditures Based on Historical Data (1870—2017)". In: *Technol. Forecast. Soc. Change* 161 (2020), p. 120255. DOI: `https://doi.org/10.1016/j.techfore.2020.120255`. URL: `https://pure.hud.ac.uk/ws/files/21715707/UK_Paper_20200809.pdf`.

[4] Donald J. Wuebbles, David W. Fahey, Kathy A. Hibbard, David J. Dokken, Brooke C. Stewart, and Thomas K. Maycock, eds. *Climate Science Special Report: Fourth National Climate Assessment, Volume I*. Washington, DC, USA: U.S. Global Change Research Program, 2017, p. 470.

[5] Intergovernmental Panel on Climate Change (IPCC). "Summary for Policymakers". In: *The Ocean and Cryosphere in a Changing Climate: Special Report of the Intergovernmental Panel on Climate Change*. Cambridge University Press, 2022, pp. 3–36.

[6] Karn Vohra, Alina Vodonos, Joel Schwartz, Eloise A. Marais, Melissa P. Sulprizio, and Loretta J. Mickley. "Global Mortality from Outdoor Fine Particle Pollution Generated by Fossil Fuel Combustion: Results from GEOS-Chem". In: *Environ. Res.* 195 (2021), p. 110754.

[7] Eugene Coyle and Richard L. Simmons. *Understanding the Global Energy Crisis*. Purdue University Press, 2014.

[8] Stelvia Matos, Eric Viardot, Benjamin K. Sovacool, Frank W. Geels, and Yu Xiong. "Innovation and Climate Change: A Review and Introduction to the Special Issue". In: *Technovation* 117 (2022), p. 102612.

[9] Júlia T. M. Machado, Brendan Flynn, and Ian Williamson. "The National Shaping of Europe's Emerging Hydrogen Strategies: Cooperative or Competitive Hydrogen Politics?" In: *Competition and Regulation in Network Industries* 23.1 (2022), pp. 77–96.

[10] Reuters. *Oil and Gas Industry Earned \$4 Trillion Last Year, Says IEA Chief.* `https://www.reuters.com/business/energy/oil-gas-industry-earned-4-trillion-last-year-says-iea-chief-2023-02-14/`. Online; accessed 31 May 2023. 2023.

[11] Gail Tverberg. *World Energy Consumption Since 1820 in Charts.* `https://www.investing.com/analysis/world-energy-consumption-since-1820-in-charts-116764`. Online; accessed 30 May 2023. 2012.

[12] National Aeronautics and Space Administration (NASA). *World of Change: Global Temperatures.* `https://earthobservatory.nasa.gov/world-of-change/global-temperatures`. Online; accessed 30 May 2023. 2023.

[13] Oliver Morton. "A New Day Dawning?: Silicon Valley Sunrise". In: *Nature* 443.7107 (2006), pp. 19–22.

[14] Ken Butti and John Perlin. *Golden Thread: 2500 Years of Solar Architecture and Technology.* Cheshire Books, 1980.

[15] Daniel Yergin. *The Prize: The Epic Quest for Oil, Money, and Power.* Touchstone book. Simon & Schuster, 1991. ISBN: 9780671502485.

[16] Alex Omo Ibhadon and Paul Fitzpatrick. "Heterogeneous Photocatalysis: Recent Advances and Applications". In: *Catalysts* 3.1 (2013), pp. 189–218.

[17] Juan M. Coronado, Fernando Fresno, María D. Hernández-Alonso, and Raquel Portela. *Design of Advanced Photocatalytic Materials for Energy and Environmental Applications.* Springer, 2013.

[18] Akira Fujishima and Kenichi Honda. "Electrochemical Photolysis of Water at a Semiconductor Electrode". In: *Nature* 238.5358 (1972), pp. 37–38.

[19] "Chapter 6 - Photocatalysis". In: *Advanced Oxidation Processes for Waste Water Treatment.* Ed. by Suresh C. Ameta and Rakshit Ameta. Academic Press, 2018, pp. 135–175.

[20] Paweł Cieśla, Przemysław Kocot, Piotr Mytych, and Zofia Stasicka. "Homogeneous Photocatalysis by Transition Metal Complexes in the Environment". In: *J. Mol. Catal. A Chem.* 224.1 (2004), pp. 17–33.

[21] Peter Atkins, Julio De Paula, and James Keeler. *Atkins' Physical Chemistry (12th edition)*. Oxford University Press, 2022.

[22] Haowei Huang, Bapi Pradhan, Johan Hofkens, Maarten B. J. Roeffaers, and Julian A. Steele. "Solar-Driven Metal Halide Perovskite Photocatalysis: Design, Stability, and Performance". In: *ACS Energy Lett.* 5.4 (2020), pp. 1107–1123.

[23] Peng Sun, Zipeng Xing, Zhenzi Li, and Wei Zhou. "Recent Advances in Quantum Dots Photocatalysts". In: *Chem. Eng. J.* 458 (2023), p. 141399.

[24] Adriana Zaleska-Medynska. *Metal Oxide-Based Photocatalysis: Fundamentals and Prospects for Application*. Elsevier, 2018.

[25] Qingxin Jia, Katsuya Iwashina, and Akihiko Kudo. "Thin Film Electrode for Water Splitting Under Visible Light Irradiation". In: *Proc. Natl. Acad. Sci. USA* 109 (2012), pp. 11564–11569.

[26] Arumugam Malathi, Jagannathan Madhavan, Muthupandian Ashokkumar, and Prabhakarn Arunachalam. "A Review on $BiVO_4$ Photocatalyst: Activity Enhancement Methods for Solar Photocatalytic Applications". In: *Appl. Catal. A* 555 (2018), pp. 47–74.

[27] Chongfei Yu, Shuying Dong, Jin Zhao, Xiao Han, Jingzhen Wang, and Jianhui Sun. "Preparation and Characterization of Sphere-Shaped $BiVO_4$/Reduced Graphene Oxide Photocatalyst for an Augmented Natural Sunlight Photocatalytic Activity". In: *J. Alloys Compd.* 677 (2016), pp. 219–227.

[28] Man Ou, Qin Zhong, Yanxiao Zhao, Yuxiang Xue, and Fujiao Song. "Graphene-decorated 3D $BiVO_4$ Photocatalysts with Controlled Size and Shape for Efficient Visible-Light-Induced Photocatalytic Performance". In: *Mater. Lett.* 184 (2016), pp. 227–231.

[29] Yukun Li, Shuying Dong, Yifei Wang, Jingyu Sun, Yifan Li, Yunqing Pi, Limin Hu, and Jianhui Sun. "Reduced Graphene Oxide on a Dumbbell-Shaped $BiVO_4$ Photocatalyst for an Augmented Natural Sunlight Photocatalytic Activity". In: *J. Mol. Catal. A Chem.* 387 (2014), pp. 138–146.

[30]   Shuying Dong, Yanrui Cui, Yifei Wang, Yukun Li, Limin Hu, Jingyu Sun, and Jianhui Sun. "Designing Three-Dimensional Acicular Sheaf Shaped BiVO$_4$/Reduced Graphene Oxide Composites for Efficient Sunlight-Driven Photocatalytic Degradation of Dye Wastewater". In: *Chem. Eng. J.* 249 (2014), pp. 102–110.

[31]   Yan Yan, Shaofang Sun, Yang Song, Xu Yan, Weisheng Guan, Xinlin Liu, and Weidong Shi. "Microwave-Assisted In Situ Synthesis of Reduced Graphene Oxide-BiVO$_4$ Composite Photocatalysts and Their Enhanced Photocatalytic Performance for the Degradation of Ciprofloxacin". In: *J. Hazard. Mater.* 250–251 (2013), pp. 106–114.

[32]   Minna Guo, Yang Wang, Qianglong He, Wenjie Wang, Weimin Wang, Zhengyi Fu, and Hao Wang. "Enhanced Photocatalytic Activity of S-Doped BiVO$_4$ Photocatalysts". In: *RSC Adv.* 5.72 (2015), pp. 58633–58639.

[33]   Min Wang, Haoyan Zheng, Qiong Liu, Chao Niu, Yinsheng Che, and Mingyan Dang. "High Performance B Doped BiVO$_4$ Photocatalyst with Visible Light Response by Citric Acid Complex Method". In: *Spectrochim. Acta A Mol. Biomol. Spectrosc.* 114 (2013), pp. 74–79.

[34]   Jun-Qi Li, Zhan-Yun Guo, Hui Liu, Juan Du, and Zhen-Feng Zhu. "Two-Step Hydrothermal Process for Synthesis of F-Doped BiVO$_4$ Spheres with Enhanced Photocatalytic Activity". In: *J. Alloys Compd.* 581 (2013), pp. 40–45.

[35]   Lili Zhang, Guoqiang Tan, Shasha Wei, Huijun Ren, Ao Xia, and Yangyang Luo. "Microwave Hydrothermal Synthesis and Photocatalytic Properties of TiO$_2$/BiVO$_4$ Composite Photocatalysts". In: *Ceram. Int.* 39.8 (2013), pp. 8597–8604.

[36]   Wenzhong Wang, Xiangwei Huang, Shuang Wu, Yixi Zhou, Lijuan Wang, Honglong Shi, Yujie Liang, and Bin Zou. "Preparation of p–n Junction Cu$_2$O/BiVO$_4$ Heterogeneous Nanostructures with Enhanced Visible-Light Photocatalytic Activity". In: *Appl. Catal. B* 134–135 (2013), pp. 293–301.

[37]   Yanlong Tian, Binbin Chang, Zhichong Yang, Baocheng Zhou, Fengna Xi, and Xiaoping Dong. "Graphitic Carbon Nitride–BiVO$_4$ Heterojunctions: Simple Hydrothermal Synthesis and High Photocatalytic Performances". In: *RSC Adv.* 4.8 (2014), pp. 4187–4193.

[38] Long Chen, Dawei Meng, Xiuling Wu, Anqi Wang, Junxia Wang, Meihua Yu, and Yujun Liang. "Enhanced Visible Light Photocatalytic Performances of Self-assembled Hierarchically Structured $BiVO_4/Bi_2WO_6$ Heterojunction Composites with Different Morphologies". In: *RSC Adv.* 6.57 (2016), pp. 52300–52309.

[39] Lingjun Song, Youyong Pang, Yanjun Zheng, Changfeng Chen, and Lei Ge. "Design, Preparation and Enhanced Photocatalytic Activity of Porous $BiOCl/BiVO_4$ Microspheres via a Coprecipitation-Hydrothermal Method". In: *J. Alloys Compd.* 710 (2017), pp. 375–382.

[40] Mireille Ghoussoub, Meikun Xia, Paul N. Duchesne, Dvira Segal, and Geoffrey Ozin. "Principles of Photothermal Gas-Phase Heterogeneous CO_2 Catalysis". In: *Energy Environ. Sci.* 12.4 (2019), pp. 1122–1142.

[41] Akihiro Furube and Shuichi Hashimoto. "Insight into Plasmonic Hot-Electron Transfer and Plasmon Molecular Drive: New Dimensions in Energy Conversion and Nanofabrication". In: *NPG Asia Mater.* 9.12 (2017), e454.

[42] Yong Peng, Horațiu Szalad, Pavle Nikačević, Giulio Gorni, Sara Goberna, Laura Simonelli, Josep Albero, Núria López, and Hermenegildo García. "Co-Doped Hydroxyapatite as Photothermal Catalyst for Selective CO_2 Hydrogenation". In: *Appl. Catal. B* 333 (2023), p. 122790.

[43] Vijay S. Vyas, Vincent Wing-hei Lau, and Bettina V. Lotsch. "Soft Photocatalysis: Organic Polymers for Solar Fuel Production". In: *Chem. Mater.* 28.15 (2016), pp. 5191–5204.

[44] Yiou Wang, Anastasia Vogel, Michael Sachs, Reiner Sebastian Sprick, Liam Wilbraham, Savio J. A. Moniz, Robert Godin, Martijn A. Zwijnenburg, James R. Durrant, Andrew I. Cooper, and Junwang Tang. "Current Understanding and Challenges of Solar-Driven Hydrogen Generation using Polymeric Photocatalysts". In: *Nat. Energy* 4.9 (2019), pp. 746–760.

[45] Tanmay Banerjee, Filip Podjaski, Julia Kröger, Bishnu P. Biswal, and Bettina V. Lotsch. "Polymer Photocatalysts for Solar-to-Chemical Energy Conversion". In: *Nat. Rev. Mater.* 6.2 (2021), pp. 168–190.

[46] Robert Godin, Yiou Wang, Martijn A. Zwijnenburg, Junwang Tang, and James R. Durrant. "Time-Resolved Spectroscopic Investigation of Charge Trapping in Carbon Nitrides Photocatalysts for Hydrogen Generation". In: *J. Am. Chem. Soc.* 139.14 (2017), pp. 5216–5224.

[47] Kenley M. Pelzer and Seth B. Darling. "Charge Generation in Organic Photovoltaics: a Review of Theory and Computation". In: *Mol. Syst. Des. Eng.* 1.1 (2016), pp. 10–24.

[48] Fabian K. Kessler, Yun Zheng, Dana Schwarz, Christoph Merschjann, Wolfgang Schnick, Xinchen Wang, and Michael J. Bojdys. "Functional Carbon Nitride Materials—Design Strategies for Electrochemical Devices". In: *Nat. Rev. Mater.* 2.6 (2017), pp. 1–17.

[49] Wee-Jun Ong, Lling-Lling Tan, Yun Hau Ng, Siek-Ting Yong, and Siang-Piao Chai. "Graphitic Carbon Nitride (g-C$_3$N$_4$)-Based Photocatalysts for Artificial Photosynthesis and Environmental Remediation: Are We a Step Closer To Achieving Sustainability?" In: *Chem. Rev.* 116.12 (2016), pp. 7159–7329.

[50] Changbin Im, Björn Kirchhoff, Igor Krivtsov, Dariusz Mitoraj, Radim Beranek, and Timo Jacob. "Structure and Optical Properties of Polymeric Carbon Nitrides from Atomistic Simulations". In: *Chem. Mater.* 35.4 (2023), pp. 1547–1559.

[51] Shubin Yang, Yongji Gong, Jinshui Zhang, Liang Zhan, Lulu Ma, Zheyu Fang, Robert Vajtai, Xinchen Wang, and Pulickel M. Ajayan. "Exfoliated Graphitic Carbon Nitride Nanosheets as Efficient Catalysts for Hydrogen Evolution Under Visible Light". In: *Adv. Mater.* 25.17 (2013), pp. 2452–2456.

[52] Jing Xu, Liwu Zhang, Rui Shi, and Yongfa Zhu. "Chemical Exfoliation of Graphitic Carbon Nitride for Efficient Heterogeneous Photocatalysis". In: *J. Mater. Chem. A* 1.46 (2013), pp. 14766–14772.

[53] Jinshui Zhang, Mingwen Zhang, Can Yang, and Xinchen Wang. "Nanospherical Carbon Nitride Frameworks With Sharp Edges Accelerating Charge Collection and Separation at a Soft Photocatalytic Interface". In: *Adv. Mater.* 26.24 (2014), pp. 4121–4126.

[54] Zhao Yang, Yuanjian Zhang, and Zoe Schnepp. "Soft and Hard Templating of Graphitic Carbon Nitride". In: *J. Mater. Chem. A* 3.27 (2015), pp. 14081–14092.

[55] Md. A. Wahab, Jickson Joseph, Luqman Atanda, Ummul K. Sultana, Jorge N. Beltramini, Kostya Ostrikov, Geoffrey Will, Anthony P. O'Mullane, and Ahmed Abdala. "Nanoconfined Synthesis of Nitrogen-Rich Metal-Free Mesoporous Carbon Nitride Electrocatalyst for the Oxygen Evolution Reaction". In: *ACS Appl. Energy Mater.* 3.2 (2020), pp. 1439–1447.

[56] Yuyang Kang, Yongqiang Yang, Li-Chang Yin, Xiangdong Kang, Lianzhou Wang, Gang Liu, and Hui-Ming Cheng. "Selective Breaking of Hydrogen Bonds of Layered Carbon Nitride for Visible Light Photocatalysis". In: *Adv. Mater.* 28.30 (2016), pp. 6471–6477.

[57] Vincent Wing-hei Lau, Maria B. Mesch, Viola Duppel, Volker Blum, Jürgen Senker, and Bettina V. Lotsch. "Low-Molecular-Weight Carbon Nitrides for Solar Hydrogen Evolution". In: *J. Am. Chem. Soc.* 137.3 (2015), pp. 1064–1072.

[58] Ping Niu, Gang Liu, and Hui-Ming Cheng. "Nitrogen Vacancy-Promoted Photocatalytic Activity of Graphitic Carbon Nitride". In: *J. Phys. Chem. C* 116.20 (2012), pp. 11013–11018.

[59] Ping Niu, Li-Chang Yin, Yong-Qiang Yang, Gang Liu, and Hui-Ming Cheng. "Increasing the Visible Light Absorption of Graphitic Carbon Nitride (Melon) Photocatalysts by Homogeneous Self-modification with Nitrogen Vacancies". In: *Adv. Mater.* 26.47 (2014), pp. 8046–8052.

[60] Longbo Jiang, Xingzhong Yuan, Yang Pan, Jie Liang, Guangming Zeng, Zhibin Wu, and Hou Wang. "Doping of Graphitic Carbon Nitride for Photocatalysis: A Review". In: *Appl. Catal. B: Environ.* 217 (2017), pp. 388–406.

[61] Sherif A. Younis, Eilhann E. Kwon, Muhammad Qasim, Ki-Hyun Kim, Taejin Kim, Deepak Kukkar, Xiaomin Dou, and Imran Ali. "Metal-Organic Framework as a Photocatalyst: Progress in Modulation Strategies and Environmental/Energy Applications". In: *Prog. Energy Combust. Sci.* 81 (2020), p. 100870.

[62] Lijuan Shen, Ruowen Liang, and Ling Wu. "Strategies for Engineering Metal-Organic Frameworks as Efficient Photocatalysts". In: *Chin. J. Catal.* 36.12 (2015), pp. 2071–2088.

[63] Pawan Kumar, Ki Hyun Kim, Yong Hyun Kim, Jan E. Szulejko, and Richard J. C. Brown. "A Review of Metal Organic Resins for Environmental Applications". In: *J. Hazard. Mater.* 320 (2016), pp. 234–240.

[64] Naixu Li, Xinchi Liu, Jiancheng Zhou, Wenshuai Chen, and Maochang Liu. "Encapsulating CuO Quantum Dots in MIL-125(Ti) Coupled with g-C_3N_4 for Efficient Photocatalytic CO_2 Reduction". In: *Chem. Eng. J.* 399 (2020), p. 125782.

[65] Shanshan Chen, Tsuyoshi Takata, and Kazunari Domen. "Particulate Photocatalysts for Overall Water Splitting". In: *Nat. Rev. Mater.* 2.10 (2017), p. 17050.

[66] Kazuhiko Maeda and Kazunari Domen. "New Non-Oxide Photocatalysts Designed for Overall Water Splitting under Visible Light". In: *J. Phys. Chem. C* 111.22 (2007), pp. 7851–7861.

[67] Qian Wang, Takashi Hisatomi, Qingxin Jia, Hiromasa Tokudome, Miao Zhong, Chizhong Wang, Zhenhua Pan, Tsuyoshi Takata, Mamiko Nakabayashi, Naoya Shibata, Yanbo Li, Ian D. Sharp, Akihiko Kudo, Taro Yamada, and Kazunari Domen. "Scalable Water Splitting on Particulate Photocatalyst Sheets with a Solar-to-Hydrogen Energy Conversion Efficiency Exceeding 1%". In: *Nat. Mater.* 15.6 (2016), pp. 611–615.

[68] Hui Liu, Jian Yuan, Wenfeng Shangguan, and Yasutake Teraoka. "Visible-Light-Responding $BiYWO_6$ Solid Solution for Stoichiometric Photocatalytic Water Splitting". In: *J. Phys. Chem. C* 112.23 (2008), pp. 8521–8523.

[69] Won Jun Jo, Hyun Joon Kang, Ki-Jeong Kong, Yun Seog Lee, Hunmin Park, Younghye Lee, Tonio Buonassisi, Karen K Gleason, and Jae Sung Lee. "Phase Transition-Induced Band Edge Engineering of $BiVO_4$ to Split Pure Water under Visible Light". In: *Proc. Natl. Acad. Sci.* 112.45 (2015), pp. 13774–13778.

[70] Long Liao, Qiuhui Zhang, Zhihua Su, Zhongzheng Zhao, Yanan Wang, Yang Li, Xiaoxiang Lu, Dongguang Wei, Guoying Feng, Qingkai Yu, Xiaojun Cai, Jimin Zhao, Zhifeng Ren, Hui Fang, Francisco Robles-Hernandez, Steven Baldelli, and Jiming Bao. "Efficient Solar Water-Splitting Using a Nanocrystalline CoO Photocatalyst". In: *Nat. Nanotechnol.* 9.1 (2014), pp. 69–73.

[71] Lihua Lin, Takashi Hisatomi, Shanshan Chen, Tsuyoshi Takata, and Kazunari Domen. "Visible-Light-Driven Photocatalytic Water Splitting: Recent Progress and Challenges". In: *Trends Chem.* 2.9 (2020), pp. 813–824.

[72] Jing Chen, Reza Abazari, Kayode Adesina Adegoke, Nobanathi Wendy Maxakato, Olugbenga Solomon Bello, Muhammad Tahir, Sehar Tasleem, Soheila Sanati, Alexander M. Kirillov, and Yingtang Zhou. "Metal-Organic Frameworks and Derived Materials as Photocatalysts for Water Splitting and Carbon Dioxide Reduction". In: *Coord. Chem. Rev.* 469 (2022), p. 214664.

[73] Jinhui Yang, Donge Wang, Hongxian Han, and Can Li. "Roles of Cocatalysts in Photocatalysis and Photoelectrocatalysis". In: *Acc. Chem. Res.* 46.8 (2013), pp. 1900–1909.

[74] Kazuhiko Maeda, Kentaro Teramura, Daling Lu, Nobuo Saito, Yasunobu Inoue, and Kazunari Domen. "Roles of Rh/Cr_2O_3 (Core/Shell) Nanoparticles Photodeposited on Visible-Light-Responsive $(Ga_{1-x}Zn_x)(N_{1-x}O_x)$ Solid Solutions in Photocatalytic Overall Water Splitting". In: *J. Phys. Chem. C* 111.20 (2007), pp. 7554–7560.

[75] Jum Suk Jang, Hyun Gyu Kim, and Jae Sung Lee. "Heterojunction Semiconductors: A Strategy to Develop Efficient Photocatalytic Materials for Visible Light Water Splitting". In: *Catal. Today* 185.1 (2012), pp. 270–277.

[76] Sebastian Gisbertz and Bartholomäus Pieber. "Heterogeneous Photocatalysis in Organic Synthesis". In: *ChemPhotoChem* 4.7 (2020), pp. 456–475.

[77] Paola Riente and Timothy Noël. "Application of Metal Oxide Semiconductors in Light-Driven Organic Transformations". In: *Catal. Sci. Technol.* 9.19 (2019), pp. 5186–5232.

[78] Paola Riente, Alba Matas Adams, Josep Albero, Emilio Palomares, and Miquel A. Pericàs. "Light-Driven Organocatalysis using Inexpensive, Nontoxic Bi_2O_3 as the Photocatalyst". In: *Angew. Chem. Int. Ed.* 53.36 (2014), pp. 9613–9616.

[79] Vineet Jeena and Ross S. Robinson. "Convenient Photooxidation of Alcohols using Dye Sensitised Zinc Oxide in Combination with Silver Nitrate and TEMPO". In: *Chem. Commun.* 48.2 (2012), pp. 299–301.

[80] Tetsuya Shishido, Toshiaki Miyatake, Kentaro Teramura, Yutaka Hitomi, Hiromi Yamashita, and Tsunehiro Tanaka. "Mechanism of Photooxidation of Alcohol over Nb_2O_5". In: *J. Phys. Chem. C* 113.43 (2009), pp. 18713–18718.

[81] Osamu Tomita, Ryu Abe, and Bunsho Ohtani. "Direct Synthesis of Phenol from Benzene over Platinum-Loaded Tungsten(VI) Oxide Photocatalysts with Water and Molecular Oxygen". In: *Chem. Lett.* 40.12 (2011), pp. 1405–1407.

[82] Cuibo Liu, Zhongxin Chen, Chenliang Su, Xiaoxu Zhao, Qiang Gao, Guo-Hong Ning, Hai Zhu, Wei Tang, Kai Leng, Wei Fu, Bingbing Tian, Xinwen Peng, Jing Li, Qing-Hua Xu, Wu Zhou, and Kian Ping Loh. "Controllable Deuteration of Halogenated Compounds by Photocatalytic D_2O Splitting". In: *Nat. Commun.* 9.1 (2018), p. 80.

[83] Anuushka Pal, Indrajit Ghosh, Sameer Sapra, and Burkhard König. "Quantum Dots in Visible-Light Photoredox Catalysis: Reductive Dehalogenations and C–H Arylation Reactions Using Aryl Bromides". In: *Chem. Mater.* 29.12 (2017), pp. 5225–5231.

[84] Abraham D. Yoffe. "Semiconductor Quantum Dots and Related Systems: Electronic, Optical, Luminescence and Related Properties of Low Dimensional Systems". In: *Adv. Phys.* 50.1 (2001), pp. 1–208.

[85] Wen-Bin Wu, Ying-Chieh Wong, Zhi-Kuang Tan, and Jie Wu. "Photo-Induced Thiol Coupling and C–H Activation using Nanocrystalline Lead-Halide Perovskite Catalysts". In: *Catal. Sci. Technol.* 8.16 (2018), pp. 4257–4263.

[86] Aleksandr Savateev and Markus Antonietti. "Heterogeneous Organocatalysis for Photoredox Chemistry". In: *ACS Catal.* 8.10 (2018), pp. 9790–9808.

[87] Xiaoqiang Dai, Yabo Zhu, Xiaoliang Xu, and Jianquan Weng. "Photocatalysis with g-C_3N_4 Applied to Organic Synthesis". In: *Chin. J. Org. Chem.* 37.3 (2017), p. 577.

[88] Fangzheng Su, Smitha C Mathew, Lennart Möhlmann, Markus Antonietti, Xinchen Wang, and Siegfried Blechert. "Aerobic Oxidative Coupling of Amines by Carbon Nitride Photocatalysis with Visible Light". In: *Angew. Chem.* 123.3 (2011), pp. 683–686.

[89] Pengfei Zhang, Yong Wang, Haoran Li, and Markus Antonietti. "Metal-Free Oxidation of Sulfides by Carbon Nitride with Visible Light Illumination at Room Temperature". In: *Green Chem.* 14.7 (2012), pp. 1904–1908.

[90] Pengfei Zhang, Yong Wang, Jia Yao, Congmin Wang, Chao Yan, Markus Antonietti, and Haoran Li. "Visible-Light-Induced Metal-Free Allylic Oxidation Utilizing a Coupled Photocatalytic System of g-C_3N_4 and N-Hydroxy Compounds". In: *Adv. Synth. Catal.* 353.9 (2011), pp. 1447–1451.

[91] Xiufang Chen, Jinshui Zhang, Xianzhi Fu, Markus Antonietti, and Xinchen Wang. "Fe-g-C_3N_4-Catalyzed Oxidation of Benzene to Phenol Using Hydrogen Peroxide and Visible Light". In: *J. Am. Chem. Soc.* 131.33 (2009), pp. 11658–11659.

[92] Lennart Moehlmann, Moritz Baar, Julian Riess, Markus Antonietti, Xinchen Wang, and Siegfried Blechert. "Carbon Nitride-Catalyzed Photoredox C–C Bond Formation with N-Aryltetrahydroisoquinolines". In: *Adv. Synth. Catal.* 354.10 (2012), pp. 1909–1913.

[93] Lennart Moehlmann and Siegfried Blechert. "Carbon Nitride-Catalyzed Photoredox Sakurai Reactions and Allylborations". In: *Adv. Synth. Catal.* 356.13 (2014), pp. 2825–2829.

[94] Yubao Zhao, Menny Shalom, and Markus Antonietti. "Visible Light-Driven Graphitic Carbon Nitride (g-C$_3$N$_4$) Photocatalyzed Ketalization Reaction in Methanol with Methylviologen as Efficient Electron Mediator". In: *Appl. Catal. B* 207 (2017), pp. 311–315.

[95] Bartholom"aus Pieber, Menny Shalom, Markus Antonietti, Peter H. Seeberger, and Kerry Gilmore. "Continuous Heterogeneous Photocatalysis in Serial Micro-Batch Reactors". In: *Angew. Chem. Int. Ed.* 57.31 (2018), pp. 9976–9979.

[96] Bogdan Kurpil, Baris Kumru, Tobias Heil, Markus Antonietti, and Aleksandr Savateev. "Carbon Nitride Creates Thioamides in High Yields by the Photocatalytic Kindler Reaction". In: *Green Chem.* 20.4 (2018), pp. 838–842.

[97] Yitao Dai, Chao Li, Yanbin Shen, Tingbin Lim, Jian Xu, Yongwang Li, Hans Niemantsverdriet, Flemming Besenbacher, Nina Lock, and Ren Su. "Light-Tuned Selective Photosynthesis of Azo- and Azoxy-Aromatics Using g-C$_3$N$_4$". In: *Nat. Commun.* 9.1 (2018), p. 60.

[98] Aleksandr Savateev, Bogdan Kurpil, Artem Mishchenko, Guigang Zhang, and Markus Antonietti. "A "Waiting" Carbon Nitride Radical Anion: A Charge Storage Material and Key Intermediate in Direct C–H Thiolation of Methylarenes Using Elemental Sulfur as the "S"-Source". In: *Chem. Sci.* 9.14 (2018), pp. 3584–3591.

[99] Moritz Baar and Siegfried Blechert. "Graphitic Carbon Nitride Polymer as a Recyclable Photoredox Catalyst for Fluoroalkylation of Arenes". In: *Chem. Eur. J.* 21.2 (2015), pp. 526–530.

[100] Andreas Uwe Meyer, Vincent Wing-hei Lau, Burkhard K"onig, and Bettina V. Lotsch. "Photocatalytic Oxidation of Sulfinates to Vinyl Sulfones with Cyanamide-Functionalised Carbon Nitride". In: *Eur. J. Org. Chem.* 2017.15 (2017), pp. 2179–2185.

[101] Bogdan Kurpil, Katharina Otte, Markus Antonietti, and Aleksandr Savateev. "Photooxidation of N-acylhydrazones to 1,3,4-Oxadiazoles Catalyzed by Heterogeneous Visible-Light-Active Carbon Nitride Semiconductor". In: *Appl. Catal. B* 228 (2018), pp. 97–102.

[102] Tao Song, Bo Zhou, Guang-Wei Peng, Qing-Bao Zhang, Li-Zhu Wu, Qiang Liu, and Yong Wang. "Aerobic Oxidative Coupling of Resveratrol and its Analogues by Visible Light Using Mesoporous Graphitic

Carbon Nitride (mpg-C_3N_4) as a Bioinspired Catalyst". In: *Chem. Eur. J.* 20.3 (2014), pp. 678–682.

[103] Magdalena Wo'znica, Nicolas Chaoui, Soraya Taabache, and Siegfried Blechert. "THF: An Efficient Electron Donor in Continuous Flow Radical Cyclization Photocatalyzed by Graphitic Carbon Nitride". In: *Chem. Eur. J.* 20.45 (2014), pp. 14624–14628.

[104] Aleksandr Savateev, Dariya Dontsova, Bogdan Kurpil, and Markus Antonietti. "Highly Crystalline Poly(heptazine imides) by Mechanochemical Synthesis for Photooxidation of Various Organic Substrates Using an Intriguing Electron Acceptor–Elemental Sulfur". In: *J. Catal.* 350 (2017), pp. 203–211.

[105] Wei Wang, Shengping Wang, Xinbin Ma, and Jinlong Gong. "Recent Advances in Catalytic Hydrogenation of Carbon Dioxide". In: *Chem. Soc. Rev.* 40.7 (2011), pp. 3703–3727.

[106] Severin N. Habisreutinger, Lukas Schmidt-Mende, and Jacek K. Stolarczyk. "Photocatalytic Reduction of CO_2 on TiO_2 and Other Semiconductors". In: *Angew. Chem. Int. Ed.* 52.29 (2013), pp. 7372–7408.

[107] Shunya Yoshino, Akihide Iwase, Yuichi Yamaguchi, Tomiko M. Suzuki, Takeshi Morikawa, and Akihiko Kudo. "Photocatalytic CO_2 Reduction Using Water as an Electron Donor under Visible Light Irradiation by Z-Scheme and Photoelectrochemical Systems over $(CuGa)_{0.5}ZnS_2$ in the Presence of Basic Additives". In: *J. Am. Chem. Soc.* 144.5 (2022), pp. 2323–2332.

[108] Hans J. Freund and Meirion W. Roberts. "Surface Chemistry of CO_2". In: *Surf. Sci. Rep.* 25.8 (1996), pp. 225–273.

[109] S. R. Lingampalli, Mohd Monis Ayyub, and C. N. R. Rao. "Recent Progress in the Photocatalytic Reduction of Carbon Dioxide". In: *ACS Omega* 2.6 (2017), pp. 2740–2748.

[110] Samsun Nahar, M. Fauzi M. Zain, Abdul Amir H. Kadhum, Hassimi A. Hasan, and Md. Riad Hasan. "Advances in Photocatalytic CO_2 Reduction with Water: A Review". In: *Materials* 10.6 (2017), p. 629.

[111] Kohsuke Mori, Hiromi Yamashita, and Masakazu Anpo. "Photocatalytic Reduction of CO_2 with H_2O on Various Titanium Oxide Photocatalysts". In: *RSC Adv.* 2.8 (2012), pp. 3165–3172.

[112] Hua Tong, Shuxin Ouyang, Yingpu Bi, Naoto Umezawa, Mitsutake Oshikiri, and Jinhua Ye. "Nano-Photocatalytic Materials: Possibilities and Challenges". In: *Adv. Mater.* 24.2 (2012), pp. 229–251.

[113] Hang-ah Park, Jung Hoon Choi, Kyung Min Choi, Dong Ki Lee, and Jeung Ku Kang. "Highly Porous Gallium Oxide with a High CO_2 Affinity for the Photocatalytic Conversion of Carbon Dioxide into Methane". In: *J. Mater. Chem.* 22.12 (2012), pp. 5304–5307.

[114] Kazuhiko Maeda. "CO_2 Reduction Using Oxynitrides and Nitrides under Visible Light". In: *Prog. Solid State Chem.* 51 (2018), pp. 52–62.

[115] Shuaiqi Gong, Mengjie Hou, Yanli Niu, Xue Teng, Xuan Liu, Mingze Xu, Chen Xu, Vonika Ka-Man Au, and Zuofeng Chen. "Molybdenum Phosphide Coupled with Highly Dispersed Nickel Confined in Porous Carbon Nanofibers for Enhanced Photocatalytic CO_2 Reduction". In: *Chem. Eng. J.* 427 (2022), p. 131717.

[116] Dandan Li, Meruyert Kassymova, Xuechao Cai, Shuang-Quan Zang, and Hai-Long Jiang. "Photocatalytic CO_2 Reduction over Metal-Organic Framework-Based Materials". In: *Coord. Chem. Rev.* 412 (2020), p. 213262.

[117] Huijie Wang, Xin Li, Xiaoxue Zhao, Chunyan Li, Xianghai Song, Peng Zhang, Pengwei Huo, and Xin Li. "A Review On Heterogeneous Photocatalysis For Environmental Remediation: From Semiconductors To Modification Strategies". In: *Chinese J. Catal.* 43.2 (2022), pp. 178–214.

[118] Swagata Banerjee, Dionysios D. Dionysiou, and Suresh C. Pillai. "Self-Cleaning Applications of TiO_2 by Photo-Induced Hydrophilicity and Photocatalysis". In: *Appl. Catal. B* 176–177 (2015), pp. 396–428.

[119] Bipasa Samanta, Ángel Morales-Garcıa, Francesc Illas, Nicolae Goga, Juan Antonio Anta, Sofia Calero, Anja Bieberle-Hütter, Florian Libisch, Ana B. Muñoz-Garcıa, Michele Pavone, and Maytal Caspary Toroker. "Challenges of Modeling Nanostructured Materials for Photocatalytic Water Splitting". In: *Chem. Soc. Rev.* 51 (2022), pp. 3794–3818.

[120] Carlo Adamo and Denis Jacquemin. "The Calculations of Excited-State Properties with Time-Dependent Density Functional Theory". In: *Chem. Soc. Rev.* 42.3 (2013), pp. 845–856.

[121] Yeonsig Nam, Linqiu Li, Jin Yong Lee, and Oleg V. Prezhdo. "Size and Shape Effects on Charge Recombination Dynamics of TiO_2 Nanoclusters". In: *J. Phys. Chem. C* 122.9 (2018), pp. 5201–5208.

[122] Ali Hussain Motagamwala and James A. Dumesic. "Microkinetic Modeling: A Tool for Rational Catalyst Design". In: *Chem. Rev.* 121.2 (2021), pp. 1049–1076.

[123] Michele Ceriotti, Cecilia Clementi, and O. Anatole von Lilienfeld. "Introduction: Machine Learning at the Atomic Scale". In: *Chem. Rev.* 121.16 (2021), pp. 9719–9721.

[124] Bing Huang and O. Anatole von Lilienfeld. "Ab Initio Machine Learning in Chemical Compound Space". In: *Chem. Rev.* 121.16 (2021), pp. 10001–10036.

[125] Felix Musil, Andrea Grisafi, Albert P. Bartók, Christoph Ortner, Gábor Csányi, and Michele Ceriotti. "Physics-Inspired Structural Representations for Molecules and Materials". In: *Chem. Rev.* 121.16 (2021), pp. 9759–9815.

[126] Jörg Behler. "Four Generations of High-Dimensional Neural Network Potentials". In: *Chem. Rev.* 121.16 (2021), pp. 10037–10072.

[127] Julia Westermayr and Philipp Marquetand. "Machine Learning for Electronically Excited States of Molecules". In: *Chem. Rev.* 121.16 (2021), pp. 9873–9926.

[128] Yogesh K. Dwivedi, Laurie Hughes, Elvira Ismagilova, Gert Aarts, Crispin Coombs, Tom Crick, Yanqing Duan, Rohita Dwivedi, John Edwards, Aled Eirug, Vassilis Galanos, P. Vigneswara Ilavarasan, Marijn Janssen, Paul Jones, Arpan Kumar Kar, Hatice Kizgin, Bianca Kronemann, Banita Lal, Biagio Lucini, Rony Medaglia, Kenneth Le Meunier-FitzHugh, Leslie Caroline Le Meunier-FitzHugh, Santosh Misra, Emmanuel Mogaji, Sujeet Kumar Sharma, Jang Bahadur Singh, Vishnupriya Raghavan, Ramakrishnan Raman, Nripendra P. Rana, Spyridon Samothrakis, Jak Spencer, Kuttimani Tamilmani, Annie Tubadji, Paul Walton, and Michael D. Williams. "Artificial Intelligence (AI): Multidisciplinary Perspectives on Emerging Challenges, Opportunities, and Agenda for Research, Practice and Policy". In: *Int. J. Inf. Manag.* 57 (2021), p. 101994.

[129] John Storrs Hall. *Beyond AI: Creating the Conscience of the Machine.* Prometheus Books, 2007.

[130] Mike Ferguson. *What is "Artificial General Intelligence"?* `https://towardsdatascience.com/what-is-artificial-general-intelligence-4b2a4ab31180`. Online; accessed 14 June 2023. 2021.

[131] Karl Marx. *Capital: A Critique of Political Economy, Volume 3 (edited and translated by Ernest Mandel and David Fernbach).* Penguin Classics, 1993.

[132] Frederik Federspiel, Ruth Mitchell, Asha Asokan, Carlos Umana, and David McCoy. "Threats by Artificial Intelligence to Human Health and Human Existence". In: *BMJ Glob. Health* 8.5 (2023), e010435.

[133]   Eliezer Yudkowsky. *The AI Alignment Problem: Why It's Hard, and Where to Start.* Symbolic Systems Distinguished Speaker series. Stanford University, 2016.

[134]   Kaj Sotala and Lukas Gloor. "Superintelligence as a Cause or Cure for Risks of Astronomical Suffering". In: *Informatica* 41.4 (2017).

[135]   Vincent C. Müller and Nick Bostrom. "Future Progress in Artificial Intelligence: A Survey of Expert Opinion". In: *Fundamental Issues of Artificial Intelligence.* Ed. by Vincent C. Müller. Cham: Springer International Publishing, 2016, pp. 555–572.

[136]   Tel Aviv University. *Chat with OpenAI CEO and and Co-founder Sam Altman, and Chief Scientist Ilya Sutskever.* `https://www.youtube.com/watch?app=desktop&t=820&v=mC-0XqTAeMQ&feature=youtu.be`. Online; accessed 14 June 2023. 2023.

[137]   Center for AI Safety. *Statement on AI Risk.* `https://www.safe.ai/statement-on-ai-risk`. Online; accessed 14 June 2023. 2023.

[138]   Moises Álvarez-Moreno, Coen de Graaf, Núria López, Feliu Maseras, Josep M. Poblet, and Carles Bo. "Managing the Computational Chemistry Big Data Problem: The ioChem-BD Platform". In: *J. Chem. Inf. Model.* 55 (2015), pp. 95–103.

[139]   Claude Cohen-Tannoudji, Bernard Diu, and Frank Laloe. *Quantum Mechanics.* John Wiley & Sons, Inc., 1977.

[140]   Lev Landau and Evgeny Lifshitz. *Quantum Mechanics: Non-Relativistic Theory.* Butterworth-Heinemann, 1981.

[141]   Albert Messiah. *Quantum Mechanics.* Dover Publications Inc., 2014.

[142]   Herbert Enderton. *Elements of Set Theory.* Academic Press, 1977.

[143]   Patrick Suppes. *Axiomatic Set Theory.* Dover Publications Inc., 1972.

[144]   Immanuel Kant. *Critique of Pure Reason (edited and translated by Paul Guyer and Allen Wood).* Cambridge University Press, 1998.

[145]   Erwin Schrödinger. "Quantisierung als Eigenwertproblem". In: *Ann. Phys.* 385 (1926), pp. 437–490.

[146]   Richard Feynman. "Space-Time Approach to Non-Relativistic Quantum Mechanics". In: *Rev. Mod. Phys.* 20 (1948), pp. 367–387.

[147]   M. Born and R. Oppenheimer. "Zur quantentheorie der molekeln". In: *Ann. d. Phys.* 20 (1927), pp. 457–484.

[148]   M. Born and V. Fock. "Beweis des Adiabatensatzes". In: *Z. Physik* 51 (1928), pp. 165–180.

[149]   P. Hohenberg and W. Kohn. "Inhomogeneous electron gas". In: *Phys. Rev.* 136 (1964), B864.

[150]   Robert Parr and Weitao Yang. *Density-Functional Theory of Atoms and Molecules*. Oxford Science Publications, 1989.

[151]   Rene Gaudoin and Kieron Burke. "Lack of Hohenberg–Kohn Theorem for Excited States". In: *Phys. Rev. Lett.* 93 (2004), p. 173001.

[152]   Mel Levy. "Universal Variational Functionals of Electron Densities, First-Order Density Matrices, and Natural Spin-Orbitals and Solution of the v-Representability Problem". In: *Proc. Natl. Acad. Sci. U.S.A.* 76 (1979), pp. 6062–6065.

[153]   Norbert Schuch and Frank Verstraete. "Computational Complexity of Interacting Electrons and Fundamental Limitations of Density Functional Theory". In: *Nat. Phys.* 5 (2009), pp. 732–735.

[154]   W. Kohn and L. J. Sham. "Self-consistent equations including exchange and correlation effects". In: *Phys. Rev.* 140 (1965), A1133.

[155]   Llewellyn Thomas. "The Calculation of Atomic Fields". In: *Math. Proc. Camb. Philos. Soc.* 23 (1927), pp. 542–548.

[156]   Enrico Fermi. "Un Metodo Statistico per la Determinazione di alcune Prioprietà dell'Atomo". In: *Rend. Accad. Naz. Lincei.* 6 (1927), pp. 602–607.

[157]   Paul Dirac. "Note on Exchange Phenomena in the Thomas Atom". In: *Math. Proc. Camb. Philos. Soc.* 26 (1930), pp. 376–385.

[158]   David M. Ceperley and Berni J. Alder. "Ground State of the Electron Gas by a Stochastic Method". In: *Phys. Rev. Lett.* 45 (1980), p. 566.

[159]   John P. Perdew, Kieron Burke, and Matthias Ernzerhof. "Generalized Gradient Approximation Made Simple". In: *Phys. Rev. Lett.* 77 (1996), pp. 3865–3868.

[160]   Douglas Hartree and William Hartree. "Self-Consistent Field, with Exchange, for Beryllium". In: *Proc. R. Soc. A* 150 (1935), pp. 9–33.

[161]   John Perdew, Kieron Burke, and Matthias Ernzerhof. "Rationale for Mixing Exact Exchange with Density Functional Approximations". In: *J. Chem. Phys.* 105 (1996), pp. 9982–9985.

[162]   Carlo Adamo and Vincenzo Barone. "Toward Reliable Density Functional Methods Without Adjustable Parameters: The PBE0 Model". In: *J. Chem. Phys.* 110 (1999), pp. 6158–6170.

[163] Jochen Heyd, Gustavo Scuseria, and Matthias Ernzerhof. "Erratum: "Hybrid functionals based on a screened Coulomb potential" [J. Chem. Phys. 118, 8207 (2003)]". In: *J. Chem. Phys.* 124 (2006), p. 219906.

[164] Diola Bagayoko. "Understanding Density Functional Theory (DFT) and Completing It in Practice". In: *AIP Adv.* 4 (2014), p. 127104.

[165] Richard P. Feynman. "Forces in Molecules". In: *Phys. Rev.* 56 (1939), pp. 340–343.

[166] Péter Pulay. "Convergence Acceleration of Iterative Sequences: The Case of SCF Iteration". In: *Chem. Phys. Lett.* 73.2 (1980), pp. 393–398.

[167] William H. Press. *Numerical Recipes: The Art of Scientific Computing.* Cambridge University Press, 1986.

[168] Vienna Ab Initio Simulation Package. *IBRION.* https://www.vasp.at/wiki/index.php/IBRION. Online; accessed 12 June 2023. 2022.

[169] G. Makov and M. C. Payne. "Periodic Boundary Conditions in *Ab Initio* Calculations". In: *Phys. Rev. B* 51 (1995), pp. 4014–4022.

[170] Felix Bloch. "Über die Quantenmechanik der Elektronen in Kristallgittern". In: *Z. Phys.* 52 (1929), pp. 555–600.

[171] Charles Kittel, Paul McEuen, and Paul McEuen. *Introduction to Solid State Physics.* Wiley New York, 1996.

[172] David Sholl and Janice A. Steckel. *Density Functional Theory: A Practical Introduction.* John Wiley & Sons, 2011.

[173] Hendrik J. Monkhorst and James D. Pack. "Special points for Brillouin-zone integrations". In: *Phys. Rev. B* 13 (1976), pp. 5188–5192.

[174] Peter E. Blöchl. "Projector Augmented-Wave Method". In: *Phys. Rev. B* 50 (1994), pp. 17953–17979.

[175] Lars Hedin. "New Method for Calculating the One-Particle Green's Function with Application to the Electron-Gas Problem". In: *Phys. Rev.* 139 (1965), A796.

[176] Dorothea Golze, Marc Dvorak, and Patrick Rinke. "The GW Compendium: A Practical Guide to Theoretical Photoemission Spectroscopy". In: *Front. Chem.* 7 (2019), p. 377.

[177] Greg Mills and Hannes Jónsson. "Quantum and Thermal Effects in H_2 Dissociative Adsorption: Evaluation of Free Energy Barriers in Multidimensional Quantum Systems". In: *Phys. Rev. Lett.* 72 (1994), pp. 1124–1127.

[178]   Graeme Henkelman and Hannes Jónsson. "Improved Tangent Esti-
        mate in the Nudged Elastic Band Method for Finding Minimum
        Energy Paths and Saddle Points". In: *J. Chem. Phys.* 113 (2000),
        pp. 9978–9985.

[179]   Graeme Henkelman. "A Climbing Image Nudged Elastic Band
        Method for Finding Saddle Points and Minimum Energy Paths". In:
        J. Chem. Phys. 113 (2000), pp. 9901–9904.

[180]   Jan Rossmeisl, Karen Chan, Egill Skúlason, Mårten Björketun, and
        Vladimir Tripković. "On the pH Dependence of Electrochemical Pro-
        ton Transfer Barriers". In: *Catal. Today* 262 (2016), pp. 36–40.

[181]   Vienna Ab Initio Simulation Package. *Monopole Dipole and
        Quadrupole Corrections.* `https://www.vasp.at/wiki/index.php/`
        `Monopole_Dipole_and_Quadrupole_corrections`. Online; accessed
        21 March 2023. 2019.

[182]   Jens K. Nørskov, Jan Rossmeisl, Ashildur Logadottir, L. Lindqvist,
        John R. Kitchin, Thomas Bligaard, and Hannes Jónsson. "Origin of
        the Overpotential for Oxygen Reduction at a Fuel-Cell Cathode". In:
        J. Phys. Chem. B 108 (2004), pp. 17886–17892.

[183]   IUPAC. *Compendium of Chemical Terminology, 2nd ed. (the "Gold
        Book").* Compiled by A. D. McNaught and A. Wilkinson. Blackwell
        Scientific Publications, 1997.

[184]   Christophe Bureau and Gérard Lécayon. "On a Modeling of Voltage-
        Application to Metallic Electrodes Using Density Functional Theory".
        In: *J. Chem. Phys.* 106 (1997), p. 8821.

[185]   Nawras Abidi, Kang Lim, Zhi Seh, and Stephan Steinmann. "Atom-
        istic Modeling of Electrocatalysis: Are We There Yet". In: *WIREs
        Comput. Mol. Sci.* 11 (2021), p. 1499.

[186]   Georg Kresse and Jürgen Furthmüller. "Efficient iterative schemes for
        ab initio total-energy calculations using a plane-wave basis set". In:
        Phys. Rev. B 54 (1996), pp. 11169–11186.

[187]   Georg Kresse and Jürgen Furthmüller. "Efficiency of ab-initio total
        energy calculations for metals and semiconductors using a plane-wave
        basis set". In: *Computat. Mater. Sci.* 6 (1996), pp. 15–50.

[188]   Pavle Nikačević, Franziska Hegner, José Ramón Galán-Mascarós, and
        Núria López. "Influence of Oxygen Vacancies and Surface Facets on
        Water Oxidation Selectivity toward Oxygen or Hydrogen Peroxide
        with $BiVO_4$". In: *ACS Catal.* 11 (2021), pp. 13416–13422.

[189] Meysam Tayebi and Byeong-Kyu Lee. "Recent Advances in $BiVO_4$ Semiconductor Materials for Hydrogen Production using Photoelectrochemical Water Splitting". In: *Renew. Sust. Energ. Rev.* 111 (2019), pp. 332–343.

[190] Akihiko Kudo, Kazuhiro Ueda, Hideki Kato, and Ikko Mikami. "Photocatalytic O_2 Evolution Under Visible Light Irradiation on $BiVO_4$ in Aqueous $AgNO_3$ Solution". In: *Appl. Catal. A* 53 (1998), pp. 229–230.

[191] Yuriy Pihosh, Ivan Turkevych, Kazuma Mawatari, Jin Uemura, Yutaka Kazoe, Sonya Kosar, Kikuo Makita, Takeyoshi Sugaya, Takuya Matsui, Daisuke Fujita, Masahiro Tosa, Michio Kondo, and Takehiko Kitamori. "Photocatalytic Generation of Hydrogen by Core-Shell $WO_3/BiVO_4$ Nanorods with Ultimate Water Splitting Efficiency". In: *Sci. Rep.* 5 (2015), p. 11141.

[192] Jin Hyun Kim and Jae Sung Lee. "Elaborately Modified $BiVO_4$ Photoanodes for Solar Water Splitting". In: *Adv. Mater.* 31.20 (2019), p. 1806938.

[193] Le Chen, Esther Alarcón-Lladó, Mark Hettick, Ian D. Sharp, Yongjing Lin, Ali Javey, and Joel W. Ager. "Reactive Sputtering of Bismuth Vanadate Photoanodes for Solar Water Splitting". In: *J. Phys. Chem. C* 117.42 (2013), pp. 21635–21642. DOI: 10.1021/jp406019r.

[194] Meysam Tayebi, Ahmad Tayyebi, and Byeong-Kyu Lee. "Improved Photoelectrochemical Performance of Molybdenum (Mo)-Doped Monoclinic Bismuth Vanadate with Increasing Donor Concentration". In: *Catal. Today* 328 (2019), pp. 35–42.

[195] Kojiro Fuku and Kazuhiro Sayama. "Efficient Oxidative Hydrogen Peroxide Production and Accumulation in Photoelectrochemical Water Splitting Using a Tungsten Trioxide/Bismuth Vanadate Photoanode". In: *Chem. Comm.* 52.31 (2016), pp. 5406–5409.

[196] Xinjian Shi, Samira Siahrostami, Guo-Ling Li, Yirui Zhang, Pongkarn Chakthranont, Felix Studt, Thomas F. Jaramillo, Xiaolin Zheng, and Jens K. Nørskov. "Understanding Activity Trends in Electrochemical Water Oxidation to Form Hydrogen Peroxide". In: *Nat. Commun.* 8.1 (2017), p. 701.

[197] Xinjian Shi, Yirui Zhang, Samira Siahrostami, and Xiaolin Zheng. "Light-Driven $BiVO_4$ Fuel Cell With Simultaneous Production of H_2O_2". In: *Adv. Energy Mater.* 8.23 (2018), p. 1801158.

[198] Kojiro Fuku, Yuta Miyase, Yugo Miseki, Takahiro Gunji, and Kazuhiro Sayama. "Enhanced Oxidative Hydrogen Peroxide Production on Conducting Glass Anodes Modified With Metal Oxides". In: *ChemistrySelect* 1.18 (2016), pp. 5721–5726.

[199] Yuta Miyase, Soichi Takasugi, Shoji Iguchi, Yugo Miseki, Takahiro Gunji, Kotaro Sasaki, Etsuko Fujita, and Kazuhiro Sayama. "Modification of $BiVO_4$/WO_3 Composite Photoelectrodes with Al_2O_3 via Chemical Vapor Deposition for Highly Efficient Oxidative H_2O_2 Production From H_2O". In: *Sustain. Energy Fuels* 2.7 (2018), pp. 1621–1629.

[200] USP Technologies. `https://www.h2o2.com/technical-library/physical-chemical-properties/thermodynamic-properties/default.aspx?pid=50&name=Standard-Electrode-Potentials`. Online; accessed 5 April 2023.

[201] J. L. Fierro, Jose M. Campos-Martin, and Gema Blanco-Brieva. "Hydrogen Peroxide Synthesis: an Outlook Beyond the Anthraquinone Process". In: *Angew. Chem. Int. Ed.* 45 (2006), pp. 6962–6984.

[202] Samira Siahrostami, Arnau Verdaguer-Casadevall, Mohammadreza Karamad, Davide Deiana, Paolo Malacrida, Björn Wickman, Marıa Escudero-Escribano, Elisa A. Paoli, Rasmus Frydendal, Thomas W. Hansen, Ib Chorkendorff, Ifan Stephens, and Jan Rossmeisl. "Enabling Direct H_2O_2 Production Through Rational Electrocatalyst Design". In: *Nat. Mater.* 12 (2013), pp. 1137–1143.

[203] Ronald Hage and Achim Lienke. "Applications of Transition-Metal Catalysts to Textile and Wood-Pulp Bleaching". In: *Angew. Chem. Int. Ed.* 45.2 (2006), pp. 206–222.

[204] Guo-Ling Li. "First-Principles Investigation of the Surface Properties of Fergusonite-Type Monoclinic $BiVO_4$ Photocatalyst". In: *RSC Adv.* 7 (2017), pp. 9130–9140.

[205] Arthur W. Sleight, Horng Yih Chen, August Ferretti, and David E. Cox. "Crystal Growth and Structure of $BiVO_4$". In: *Mater. Res. Bull.* 14.12 (1979), pp. 1571–1581.

[206] Rengui Li, Fuxiang Zhang, Donge Wang, Jingxiu Yang, Mingrun Li, Jian Zhu, Xin Zhou, Hongxian Han, and Can Li. "Spatial Separation of Photogenerated Electrons and Holes among {010} and {110} Crystal Facets of $BiVO_4$". In: *Nat. Commun.* 4.1 (2013), p. 1432.

[207] Taifeng Liu, Xin Zhou, Michel Dupuis, and Can Li. "The Nature of Photogenerated Charge Separation Among Different Crystal Facets of BiVO$_4$ Studied by Density Functional Theory". In: *Physical Chemistry Chemical Physics* 17.36 (2015), pp. 23503–23510.

[208] Jun Hu, Wei Chen, Xin Zhao, Haibin Su, and Zhong Chen. "Anisotropic Electronic Characteristics, Adsorption, and Stability of Low-Index BiVO$_4$ Surfaces for Photoelectrochemical Applications". In: *ACS Appl. Mater. Interfaces* 10.6 (2018), pp. 5475–5484.

[209] Dongho Lee, Wennie Wang, Chenyu Zhou, Xiao Tong, Mingzhao Liu, Giulia Galli, and Kyoung-Shin Choi. "The Impact of Surface Composition on the Interfacial Energetics and Photoelectrochemical Properties of BiVO$_4$". In: *Nat. Energy* 6.3 (2021), pp. 287–294.

[210] Nathan Daelman, Franziska Simone Hegner, Marcos Rellán-Piñeiro, Marçal Capdevila-Cortada, Rodrigo Garcıa-Muelas, and Núria López. "Quasi-Degenerate States and Their Dynamics in Oxygen Deficient Reducible Metal Oxides". In: *J. Chem. Phys.* 152 (2020), p. 050901.

[211] Songcan Wang, Peng Chen, Yang Bai, Jung-Ho Yun, Gang Liu, and Lianzhou Wang. "New BiVO$_4$ Dual Photoanodes With Enriched Oxygen Vacancies for Efficient Solar-driven Water Splitting". In: *Adv. Mater.* 30.20 (2018), p. 1800486.

[212] Wenrui Zhang, Liang Song, Jiajie Cen, and Mingzhao Liu. "Mechanistic Insights Into Defect-assisted Carrier Transport in Bismuth Vanadate Photoanodes". In: *J. Phys. Chem. C* 123.34 (2019), pp. 20730–20736.

[213] Jun Hu, Xin Zhao, Wei Chen, Haibin Su, and Zhong Chen. "Theoretical Insight into the Mechanism of Photoelectrochemical Oxygen Evolution Reaction on BiVO$_4$ Anode With Oxygen Vacancy". In: *J. of Phys. Chem. C* 121.34 (2017), pp. 18702–18709.

[214] Christoph Freysoldt, Blazej Grabowski, Tilmann Hickel, Jörg Neugebauer, Georg Kresse, Anderson Janotti, and Chris G. Van de Walle. "First-Principles Calculations for Point Defects in Solids". In: *Rev. Mod. Phys.* 86.1 (2014), pp. 253–305.

[215] Cheng Cheng, Qiu Fang, Sebastián Fernandez-Alberti, and Run Long. "Controlling Charge Carrier Trapping and Recombination in BiVO$_4$ With the Oxygen Vacancy Oxidation State". In: *J. Phys. Chem. Lett* 12.14 (2021), pp. 3514–3521.

[216] Shababa Selim, Ernest Pastor, Miguel Garcia-Tecedor, Madeleine R Morris, Laia Francas, Michael Sachs, Benjamin Moss, Sacha Corby, Camilo A. Mesa, Sixto Gimenez, Andreas Kafizas, Artem A. Bakulin, and James R. Durrant. "Impact of Oxygen Vacancy Occupancy on Charge Carrier Dynamics in BiVO$_4$ Photoanodes". In: *J. Am. Chem. Soc.* 141.47 (2019), pp. 18791–18798.

[217] Weitao Qiu, Shuang Xiao, Jingwen Ke, Zheng Wang, Songtao Tang, Kai Zhang, Wei Qian, Yongchao Huang, Duan Huang, Yexiang Tong, and Shihe Yang. "Freeing the Polarons to Facilitate Charge Transport in BiVO$_4$ from Oxygen Vacancies with an Oxidative 2D Precursor". In: *Angew. Chem. Int. Ed.* 58.52 (2019), pp. 19087–19095.

[218] Xin Zhao, Jun Hu, Xin Yao, Shi Chen, and Zhong Chen. "Clarifying the Roles of Oxygen Vacancy in W-Doped BiVO$_4$ for Solar Water Splitting". In: *ACS Appl. Energy Mater.* 1.7 (2018), pp. 3410–3419.

[219] Roser Fernández-Climent, Sixto Giménez, and Miguel García-Tecedor. "The Role of Oxygen Vacancies in Water Splitting Photoanodes". In: *Sustain. Energy Fuels* 4.12 (2020), pp. 5916–5926.

[220] Zhiliang Wang, Xin Mao, Peng Chen, Mu Xiao, Sabiha Akter Monny, Songcan Wang, Muxina Konarova, Aijun Du, and Lianzhou Wang. "Understanding the Roles of Oxygen Vacancies in Hematite-Based Photoelectrochemical Processes". In: *Angew. Chem. Int. Ed.* 58.4 (2019), pp. 1030–1034.

[221] Nicklas Österbacka and Julia Wiktor. "Influence of Oxygen Vacancies on the Structure of BiVO$_4$". In: *J. Phys. Chem. C* 125.2 (2021), pp. 1200–1207.

[222] Hosung Seo, Yuan Ping, and Giulia Galli. "Role of Point Defects in Enhancing the Conductivity of BiVO$_4$". In: *Chem. Mater.* 30.21 (2018), pp. 7793–7802.

[223] Franziska Simone Hegner, Daniel Forrer, José Ramón Galán-Mascarós, Núria López, and Annabella Selloni. "Versatile Nature of Oxygen Vacancies in Bismuth Vanadate Bulk and (001) Surface". In: *The Journal of Physical Chemistry Letters* 10.21 (2019), pp. 6672–6678.

[224] Wennie Wang, Patrick James Strohbeen, Dongho Lee, Chenyu Zhou, Jason Ken Kawasaki, Kyoung-Shin Choi, Mingzhao Liu, and Giulia Galli. "The Role of Surface Oxygen Vacancies in BiVO$_4$". In: *Chem. Mater.* 32.7 (2020), pp. 2899–2909.

[225] Jianqiang Hu, Huichao He, Xin Zhou, Zhaosheng Li, Qing Shen, Wenjun Luo, Ahmed Alsaedi, Tasawar Hayat, Yong Zhou, and Zhigang Zou. "BiVO$_4$ Tubular Structures: Oxygen Defect-Rich and Largely Exposed Reactive {010} Facets Synergistically Boost Photocatalytic Water Oxidation and the Selective N=N Coupling Reaction of 5-Amino-1 H-Tetrazole". In: *Chem. Comm.* 55.39 (2019), pp. 5635–5638.

[226] Koichi Momma and Fujio Izumi. "*VESTA*: A Three-Dimensional Visualization System for Electronic and Structural Analysis". In: *Appl. Crystallogr.* 41.3 (2008), pp. 653–658.

[227] Jingxiu Yang, Donge Wang, Xin Zhou, and Can Li. "A Theoretical Study on the Mechanism of Photocatalytic Oxygen Evolution on BiVO$_4$ in Aqueous Solution". In: *Chem.—Eur. J.* 19.4 (2013), pp. 1320–1326.

[228] Abdullah Kahraman, Mahsa Barzgar Vishlaghi, Işınsu Baylam, Hirohito Ogasawara, Alphan Sennaroğlu, and Sarp Kaya. "The Fast-Track Water Oxidation Channel on BiVO$_4$ Opened by Nitrogen Treatment". In: *J. Phys. Chem. Lett.* 11.20 (2020), pp. 8758–8764.

[229] Samira Siahrostami, Guo-Ling Li, Venkatasubramanian Viswanathan, and Jens K. Nørskov. "One- or Two-Electron Water Oxidation, Hydroxyl Radical, or H$_2$O$_2$ Evolution". In: *J. Phys. Chem. Lett.* 8.6 (2017), pp. 1157–1160.

[230] Luyang Wang, Yuan Lu, Nannan Han, Chaoran Dong, Cheng Lin, Siyu Lu, Yulin Min, and Kan Zhang. "Suppressing Water Dissociation via Control of Intrinsic Oxygen Defects for Awakening Solar H$_2$O-to-H$_2$OO$_2$ Generation". In: *Small* 17.13 (2021), p. 2100400.

[231] John Buckeridge. "Equilibrium Point Defect and Charge Carrier Concentrations in a Material Determined Through Calculation of the Self-consistent Fermi Energy". In: *Comput. Phys. Commun.* 244 (2019), pp. 329–342.

[232] Songcan Wang, Peng Chen, Jung-Ho Yun, Yuxiang Hu, and Lianzhou Wang. "An Electrochemically Treated BiVO$_4$ Photoanode for Efficient Photoelectrochemical Water Splitting". In: *Angew. Chem. Int. Ed.* 56.29 (2017), pp. 8500–8504.

[233] John P. Perdew, Adrienn Ruzsinszky, Gábor I. Csonka, Oleg A. Vydrov, Gustavo E. Scuseria, Lucian A. Constantin, Xiaolan Zhou, and Kieron Burke. "Restoring the Density-Gradient Expansion for Exchange in Solids and Surfaces". In: *Phys. Rev. Lett.* 100.13 (2008), p. 136406.

[234] Kiran Mathew, Ravishankar Sundararaman, Kendra Letchworth-Weaver, T. A. Arias, and Richard G. Hennig. "Implicit Solvation Model for Density-Functional Study of Nanocrystal Surfaces and Reaction Pathways". In: *J. Chem. Phys.* 140 (2014), p. 084106.

[235] Hennig Materials Theory Lab. *VASPsol.* `https://github.com/henniggroup/VASPsol`. Online; accessed 12 April 2023. 2020.

[236] Kiran Mathew, Chaitanya Kolluru, Srinidhi Mula, Stephan Steinmann, and Richard Henning. "Implicit Self-Consistent Electrolyte Model in Plane-Wave Density-Functional Theory". In: *J. Chem. Phys.* 151 (2019), p. 234101.

[237] Rachel Steinitz-Eliyahu, Daniel Hernangómez-Pérez, Franziska S. Hegner, Pavle Nikačević, Núria López, and Sivan Refaely-Abramson. "Mixed Excitonic Nature in Water-Oxidized $BiVO_4$ Surfaces With Defects". In: *Phys. Rev. Mater.* 6 (2022), p. 065402.

[238] Alexey Galushchinskiy, Yajun Zou, Jokotadeola Odutola, Pavle Nikačević, Jian-Wen Shi, Nikolai Tkachenko, Núria López, Pau Farràs, and Oleksandr Savateev. "Insights into the Role of Graphitic Carbon Nitride as a Photobase in Proton-Coupled Electron Transfer in (sp^3)C-H Oxygenation of Oxazolidinones". In: *Angew. Chem. Int. Ed.* 62.18 (2023), e202301815.

[239] Garima Bansal, Punniyakoti Veeraveedu Thanikachalam, Rahul K. Maurya, Pooja Chawla, and Srinivasan Ramamurthy. "An Overview on Medicinal Perspective of Thiazolidine-2,4-Dione: A Remarkable Scaffold in the Treatment of Type 2 Diabetes". In: *J. Adv. Res.* 23 (2020), pp. 163–205.

[240] Panagiotis K. Chrysanthopoulos, Prashant Mujumdar, Lucy A. Woods, Olan Dolezal, Bin Ren, Thomas S. Peat, and Sally-Ann Poulsen. "Identification of a New Zinc Binding Chemotype by Fragment Screening". In: *J. Med. Chem.* 60.17 (2017), pp. 7333–7349.

[241] Weiguo Liu, Fiona Lau, Kun Liu, Harold B. Wood, Gaochao Zhou, Yuli Chen, Ying Li, Taro E. Akiyama, Gino Castriota, Monica Einstein, Chualin Wang, Margaret E. McCann, Thomas W. Doebber, Margaret Wu, Ching H. Chang, Lesley McNamara, Brian McKeever, Ralph T. Mosley, Joel P. Berger, and Peter T. Meinke. "Benzimidazolones: A New Class of Selective Peroxisome Proliferator-Activated Receptor γ (PPARγ) Modulators". In: *J. Med. Chem.* 54.24 (2011), pp. 8541–8554.

[242] Jason M. Cox, Hong D. Chu, Christine Yang, Hong C. Shen, Zhicai Wu, Jaume Balsells, Alejandro Crespo, Patricia Brown, Beata Zamlynny, Judyann Wiltsie, Joseph Clemas, Jack Gibson, Lisa Contino, Jean Marie Lisnock, Gaochao Zhou, Margarita Garcia-Calvo, Thomas Bateman, Ling Xu, Xinchun Tong, Martin Crook, and Peter Sinclair. "Mineralocorticoid Receptor Antagonists: Identification of Heterocyclic Amide Replacements in the Oxazolidinedione Series". In: *Bioorg. Med. Chem. Lett.* 24.7 (2014), pp. 1681–1684.

[243] Simon D. Shorvon. "Drug Treatment of Epilepsy in the Century of the ILAE: the Second 50 Years, 1959–2009". In: *Epilepsia* 50 (2009), pp. 93–130.

[244] S. C. Knight, V. M. Anthony, A. M. Brady, A. J. Greenland, S. P. Heaney, D. C. Murray, K. A. Powell, M. A. Schulz, C. A. Spinks, P. A. Worthington, and D. Youle. "Rationale and Perspectives on the Development of Fungicides". In: *Annu. Rev. Phytopathol.* 35.1 (1997), pp. 349–372.

[245] Kathleen A. Lewis, John Tzilivakis, Douglas J. Warner, and Andrew Green. "An International Database for Pesticide Risk Assessments and Management". In: *Hum. Ecol. Risk Assess.* 22.4 (2016), pp. 1050–1064.

[246] Hui Zhou, Sen Mu, Bai-Hao Ren, Rui Zhang, and Xiao-Bing Lu. "Organocatalyzed Carboxylative Cyclization of Propargylic Amides With Atmospheric CO_2 towards Oxazolidine-2,4-Diones". In: *Green Chem.* 21.5 (2019), pp. 991–994.

[247] Vipin A. Nair, Suni M. Mustafa, Michael L. Mohler, James T. Dalton, and Duane D. Miller. "Synthesis of Oxazolidinedione Derived Bicalutamide Analogs". In: *Tetrahedron Lett.* 47.23 (2006), pp. 3953–3955.

[248] V. Yeh and R. Iyengar. *Comprehensive Heterocyclic Chemistry III', Vol. by AR Katritzky, CA Ramsden, E. FV Scriven, and RJK Taylor.* 2008.

[249] Yi Cao, Katsutoshi Suzuki, Toshiki Tajima, and Toshio Fuchigami. "Electrolytic Partial Fluorination of Organic Compounds. Part 78: Regioselective Anodic Fluorination of 2-Oxazolidinones". In: *Tetrahedron* 61.28 (2005), pp. 6854–6859.

[250] Jean-Claude Gramain and Roland Remuson. "Photo-Oxidation of Oxazolidones and Hydantoins in the Presence of Benzophenone". In: *J. Chem. Soc. Perkin Trans.* (1982), pp. 2341–2345.

[251] Luca Capaldo and Davide Ravelli. "Hydrogen Atom Transfer (HAT): A Versatile Strategy for Substrate Activation in Photocatalyzed Organic Synthesis". In: *Eur. J. Org. Chem.* 2017.15 (2017), pp. 2056–2071.

[252] Philip R. D. Murray, James H. Cox, Nicholas D. Chiappini, Casey B. Roos, Elizabeth A. McLoughlin, Benjamin G. Hejna, Suong T. Nguyen, Hunter H. Ripberger, Jacob M. Ganley, Elaine Tsui, Nick Y. Shin, Brian Koronkiewicz, Guanqi Qiu, and Robert R. Knowles. "Photochemical and Electrochemical Applications of Proton-Coupled Electron Transfer in Organic Synthesis". In: *Chem. Rev.* 122.2 (2021), pp. 2017–2291.

[253] Elaine Tsui, Anthony J. Metrano, Yuto Tsuchiya, and Robert R. Knowles. "Catalytic Hydroetherification of Unactivated Alkenes Enabled by Proton-Coupled Electron Transfer". In: *Angew. Chem. Int. Ed.* 59.29 (2020), pp. 11845–11849.

[254] Casey B. Roos, Joachim Demaerel, David E. Graff, and Robert R. Knowles. "Enantioselective Hydroamination of Alkenes With Sulfonamides Enabled by Proton-coupled Electron Transfer". In: *J. Am. Chem. Soc.* 142.13 (2020), pp. 5974–5979.

[255] Jeffrey J. Warren, Tristan A. Tronic, and James M. Mayer. "Thermochemistry of Proton-Coupled Electron Transfer Reagents and Its Implications". In: *Chem. Rev.* 110.12 (2010), pp. 6961–7001.

[256] Xuan-Zi Fan, Jia-Wei Rong, Hao-Lin Wu, Quan Zhou, Hong-Ping Deng, Jin Da Tan, Cheng-Wen Xue, Li-Zhu Wu, Hai-Rong Tao, and Jie Wu. "EosinY as a Direct Hydrogen-Atom Transfer Photocatalyst for the Functionalization of C-H Bonds". In: *Angew. Chem. Int. Ed.* 57.28 (2018), pp. 8514–8518.

[257] Chuncheng Chen, Tao Shi, Wei Chang, and Jincai Zhao. "Essential Roles of Proton Transfer in Photocatalytic Redox Reactions". In: *ChemCatChem* 7.5 (2015), pp. 724–731.

[258] Gabriele Laudadio, Yuchao Deng, Klaas van der Wal, Davide Ravelli, Manuel Nuño, Maurizio Fagnoni, Duncan Guthrie, Yuhan Sun, and Timothy Noël. "C(sp^3)–H Functionalizations of Light Hydrocarbons Using Decatungstate Photocatalysis in Flow". In: *Science* 369.6499 (2020), pp. 92–96.

[259] Aleksandr Savateev, Indrajit Ghosh, Burkhard König, and Markus Antonietti. "Photoredox Catalytic Organic Transformations using Heterogeneous Carbon Nitrides". In: *Angew. Chem. Int. Ed.* 57.49 (2018), pp. 15936–15947.

[260] Emily J. Rabe, Kathryn L. Corp, Xiang Huang, Johannes Ehrmaier, Ryan G. Flores, Sabrina L. Estes, Andrzej L. Sobolewski, Wolfgang Domcke, and Cody W. Schlenker. "Barrierless Heptazine-Driven Excited State Proton-Coupled Electron Transfer: Implications for Controlling Photochemistry of Carbon Nitrides and Aza-Arenes". In: *J. Phys. Chem. C.* 123.49 (2019), pp. 29580–29588.

[261] Kathryn L. Corp, Emily J. Rabe, Xiang Huang, Johannes Ehrmaier, Mitchell E. Kaiser, Andrzej L. Sobolewski, Wolfgang Domcke, and Cody W. Schlenker. "Control of Excited-State Proton-Coupled Electron Transfer by Ultrafast Pump-Push-Probe Spectroscopy in Heptazine-Phenol Complexes: Implications for Photochemical Water Oxidation". In: *J. Phys. Chem. C.* 124.17 (2020), pp. 9151–9160.

[262] Doyk Hwang and Cody W. Schlenker. "Photochemistry of Carbon Nitrides and Heptazine Derivatives". In: *Chem. Commun.* 57.74 (2021), pp. 9330–9353.

[263] Qian Yang, Guanglong Pan, Jie Wei, Wentao Wang, Yurong Tang, and Yunfei Cai. "Remarkable Activity of Potassium-Modified Carbon Nitride for Heterogeneous Photocatalytic Decarboxylative Alkyl/Acyl Radical Addition and Reductive Dimerization of *para*-Quinone Methides". In: *ACS Sustainable Chem. Eng.* 9.5 (2021), pp. 2367–2377.

[264] Arjun Vijeta and Erwin Reisner. "Carbon Nitride as a Heterogeneous Visible-Light Photocatalyst for the Minisci Reaction and Coupling to H_2 Production". In: *Chem. Commun.* 55.93 (2019), pp. 14007–14010.

[265] Adam J. Rieth, Yangzhong Qin, Benjamin C. Martindale, and Daniel G. Nocera. "Long-Lived Triplet Excited State in a Heterogeneous Modified Carbon Nitride Photocatalyst". In: *J. Am. Chem. Soc.* 143.12 (2021), pp. 4646–4652.

[266] Saikat Das, Kathiravan Murugesan, Gonzalo J Villegas Rodríguez, Jaspreet Kaur, Joshua P. Barham, Aleksandr Savateev, Markus Antonietti, and Burkhard König. "Photocatalytic (Het)arylation of C(sp3)–H Bonds with Carbon Nitride". In: *ACS Catal.* 11.3 (2021), pp. 1593–1603.

[267] Vincent Wing-hei Lau and Bettina V. Lotsch. "A Tour-Guide through Carbon Nitride-Land: Structure- and Dimensionality-Dependent Properties for Photo(Electro)Chemical Energy Conversion and Storage". In: *Adv. Energy Mater.* 12.4 (2022), p. 2101078.

[268] Aleksandr Savateev, Nadezda V. Tarakina, Volker Strauss, Tanveer Hussain, Katharina ten Brummelhuis, José Manuel Sánchez Vadillo, Yevheniia Markushyna, Stefano Mazzanti, Alexander P. Tyutyunnik, Ralf Walczak, Martin Oschatz, Dirk M. Guldi, Amir Karton, and Markus Antonietti. "Potassium Poly(Heptazine Imide): Transition Metal-Free Solid-State Triplet Sensitizer in Cascade Energy Transfer and [3+2]-cycloadditions". In: *Angew. Chem. Int. Ed.* 59.35 (2020), pp. 15061–15068.

[269] Indrajit Ghosh, Jagadish Khamrai, Aleksandr Savateev, Nikita Shlapakov, Markus Antonietti, and Burkhard König. "Organic Semiconductor Photocatalyst Can Bifunctionalize Arenes and Heteroarenes". In: *Science* 365.6451 (2019), pp. 360–366.

[270] Miquel Garcia-Ratés and Núria López. "Multigrid-Based Methodology for Implicit Solvation Models in Periodic DFT". In: *J. Chem. Theory Comput.* 12 (2016), pp. 1331–1341.

[271] Sigismund Melissen, Tangui Le Bahers, Stephan N. Steinmann, and Philippe Sautet. "Relationship between Carbon Nitride Structure and Exciton Binding Energies: A DFT Perspective". In: *J. Phys. Chem. C* 119.45 (2015), pp. 25188–25196.

[272] Stefan Grimme, Jens Antony, Stephan Ehrlich, and Helge Krieg. "A Consistent and Accurate Ab Initio Parametrization of Density Functional Dispersion Correction (DFT-D) for the 94 Elements H–Pu". In: *J. Chem. Phys.* 132 (2010), p. 154104.

[273] Tooru Inoue, Akira Fujishima, Satoshi Konishi, and Kenichi Honda. "Photoelectrocatalytic Reduction of Carbon Dioxide in Aqueous Suspensions of Semiconductor Powders". In: *Nature* 277.5698 (1979), pp. 637–638.

[274] Eunhee Gong, Shahzad Ali, Chaitanya B. Hiragond, Hong Soo Kim, Niket S. Powar, Dongyun Kim, Hwapyong Kim, and Su-Il In. "Solar Fuels: Research and Development Strategies to Accelerate Photocatalytic CO_2 Conversion into Hydrocarbon Fuels". In: *Energy Environ. Sci.* 15.3 (2022), pp. 880–937.

[275] Lan Yuan, Ming-Yu Qi, Zi-Rong Tang, and Yi-Jun Xu. "Coupling Strategy for CO_2 Valorization Integrated with Organic Synthesis by Heterogeneous Photocatalysis". In: *Angew. Chem. Int. Ed.* 60.39 (2021), pp. 21150–21172.

[276] Kang-Qiang Lu, Yue-Hua Li, Fan Zhang, Ming-Yu Qi, Xue Chen, Zi-Rong Tang, Yoichi MA Yamada, Masakazu Anpo, Marco Conte, and Yi-Jun Xu. "Rationally Designed Transition Metal Hydroxide Nanosheet Arrays on Graphene for Artificial CO_2 Reduction". In: *Nat. Commun.* 11.1 (2020), p. 5181.

[277] Fan Zhang, Yue-Hua Li, Ming-Yu Qi, Yoichi MA Yamada, Masakazu Anpo, Zi-Rong Tang, and Yi-Jun Xu. "Photothermal Catalytic CO_2 Reduction over Nanomaterials". In: *Chem. Catal.* 1.2 (2021), pp. 272–297.

[278] Yong Peng, Josep Albero, Antonio Franconetti, Patricia Concepción, and Hermenegildo Garcıa. "Visible and NIR Light Assistance of the N_2 Reduction to NH_3 Catalyzed by Cs-Promoted Ru Nanoparticles Supported on Strontium Titanate". In: *ACS Catal.* 12.9 (2022), pp. 4938–4946.

[279] Lu Wang, Mireille Ghoussoub, Hong Wang, Yue Shao, Wei Sun, Athanasios A. Tountas, Thomas E Wood, Hai Li, Joel Yi Yang Loh, Yuchan Dong, Meikun Xia, Young Li, Shenghua Wang, Jia Jia, Chenyue Qiu, Chenxi Qian, Nazir P. Kherani, Le He, Xiaohong Zhang, and Geoffrey A. Ozin. "Photocatalytic Hydrogenation of Carbon Dioxide With High Selectivity to Methanol at Atmospheric Pressure". In: *Joule* 2.7 (2018), pp. 1369–1381.

[280] Kai Feng, Shenghua Wang, Dake Zhang, Lu Wang, Yingying Yu, Kun Feng, Zhao Li, Zhijie Zhu, Chaoran Li, Mujin Cai, Zhiyi Wu, Ning Kong, Binhang Yan, Jun Zhong, Xiaohong Zhang, Geoffrey A. Ozin, and Le He. "Cobalt Plasmonic Superstructures Enable Almost 100% Broadband Photon Efficient CO_2 Photocatalysis". In: *Adv. Mater.* 32.24 (2020), p. 2000014.

[281] Jiuli Guo, Paul N. Duchesne, Lu Wang, Rui Song, Meikun Xia, Ulrich Ulmer, Wei Sun, Yuchan Dong, Joel Y. Y. Loh, Nazir P. Kherani, Jimin Du, Baolin Zhu, Weiping Huang, Shoumin Zhang, and Geoffrey A. Ozin. "High-Performance, Scalable, and Low-Cost Copper Hydroxyapatite for Photothermal CO_2 Reduction". In: *ACS Catal.* 10.22 (2020), pp. 13668–13681.

[282] Ljiljana Veselinović, Ljiljana Karanović, Zoran Stojanović, Ines Bračko, Smilja Marković, Nenad Ignjatović, and Dragan Uskoković. "Crystal Structure of Cobalt-Substituted Calcium Hydroxyapatite Nanopowders Prepared by Hydrothermal Processing". In: *J. Appl. Crystallogr.* 43.2 (2010), pp. 320–327.

[283] Henrique Brasil, Albert F. B. Bittencourt, Kathlen C. E. .S Yokoo, Paulo C. D. Mendes, Lucas G. Verga, Karla F. Andriani, Richard Landers, Juarez L. F. Da Silva, and Gustavo P. Valença. "Synthesis Modification of Hydroxyapatite Surface for Ethanol Conversion: The Role of the Acidic/Basic Sites Ratio". In: *J. Catal.* 404 (2021), pp. 802–813.

[284] Alexander Slepko and Alexander A. Demkov. "First Principles Study of Hydroxyapatite Surface". In: *J. Chem. Phys.* 139.4 (2013), p. 044714.

[285] Rachel C. Elias and Suljo Linic. "Elucidating the Roles of Local and Nonlocal Rate Enhancement Mechanisms in Plasmonic Catalysis". In: *J. Am. Chem. Soc.* 144.43 (2022), pp. 19990–19998.

[286] Guillaume Baffou, Romain Quidant, and F. Javier García de Abajo. "Nanoscale Control of Optical Heating in Complex Plasmonic Systems". In: *ACS Nano* 4.2 (2010), pp. 709–716.

[287] Guillaume Baffou and Romain Quidant. "Thermo-Plasmonics: Using Metallic Nanostructures as Nano-Sources of Heat". In: *Laser Photonics Rev.* 7.2 (2013), pp. 171–187.

[288] Hendrik Christoffel van de Hulst. *Light Scattering by Small Particles.* Courier Corporation, 1981.

[289] Byoung-Hoon Lee, Eunhee Gong, Minho Kim, Sunghak Park, Hye Rim Kim, Junho Lee, Euiyeon Jung, Chan Woo Lee, Jinsol Bok, Yoon Jung, Young Seong Kim, Kug-Seung Lee, Sung-Pyo Cho, Jin-Woo Jung, Chang-Hee Cho, Sébastien Lebègue, Ki Tae Nam, Hyungjun Kim, Su-Il In, and Taeghwans Hyeon. "Electronic Interaction Between Transition Metal Single-Atoms and Anatase TiO_2 Boosts CO_2 Photoreduction with H_2O". In: *Energy Environ. Sci.* 15.2 (2022), pp. 601–609.

[290] Maxim Shishkin and Georg Kresse. "Implementation and Performance of the Frequency-Dependent *GW* Method within the PAW Framework". In: *Phys. Rev. B* 74 (3 2006), p. 035101.

[291] Maxim Shishkin and Georg Kresse. "Self-Consistent *GW* Calculations for Semiconductors and Insulators". In: *Phys. Rev. B* 75 (23 2007), p. 235102.

[292] Peitao Liu, Merzuk Kaltak, Jiří Klimeš, and Georg Kresse. "Cubic Scaling *GW*: Towards Fast Quasiparticle Calculations". In: *Phys. Rev. B* 94 (16 2016), p. 165109.

[293] Benjamin Ramberger, Zoran Sukurma, Tobias Schäfer, and Georg Kresse. "RPA Natural Orbitals and Their Application to Post-Hartree-Fock Electronic Structure Methods". In: *J. Chem. Phys.* 151.21 (2019), p. 214106.

[294] Sergei L. Dudarev, Gianluigi A. Botton, Sergey Y. Savrasov, Colin J. Humphreys, and Adrian P. Sutton. "Electron-Energy-Loss Spectra and the Structural Stability of Nickel Oxide: An LSDA+U Study". In: *Phys. Rev. B* 57 (3 1998), pp. 1505–1509.

Publications

Letter

Influence of Oxygen Vacancies and Surface Facets on Water Oxidation Selectivity toward Oxygen or Hydrogen Peroxide with BiVO$_4$

Pavle Nikačević, Franziska S. Hegner,* José Ramón Galán-Mascarós, and Núria López*

Read Online

ACCESS | Metrics & More | Article Recommendations | Supporting Information

ABSTRACT: Bismuth vanadate (BiVO$_4$) is one of the most promising photoanode materials for water oxidation. However, the water oxidation mechanism and selectivity on the different surfaces of BiVO$_4$ are still not well understood, partly because of the structural complexity introduced by the presence of oxygen vacancies in the material. Using density functional theory, we show that the (001) surface of BiVO$_4$ with subsurface vacancies is the most suitable for the oxygen evolution reaction, whereas the pristine (011) surface favors the hydrogen peroxide evolution reaction. A mechanism by which the vacancies can be removed from the surface, thereby influencing the water oxidation selectivity, is also described. Our results thus emphasize the crucial impact of the local structure on the catalytic selectivity in ternary oxides.
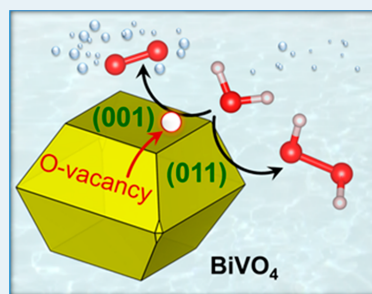
KEYWORDS: _bismuth vanadate, density functional theory, water oxidation, oxygen vacancies, selectivity, oxygen evolution reaction, hydrogen peroxide evolution_

In recent years, bismuth vanadate (BiVO$_4$) has become one of the most promising catalysts for photoelectrochemical water splitting.[1−3] It is a ternary oxide and an n-type semiconductor, which makes it suitable as a photoanode material for the oxygen evolution reaction (OER). BiVO$_4$ has a relatively low band gap of 2.4 eV and is inexpensive, nontoxic, and stable in aqueous solution.[4] In its monoclinic scheelite form, BiVO$_4$ has a remarkable half-cell solar-to-hydrogen theoretical efficiency of 8.1%.[5] However, its poor electron conductivity and slow water oxidation kinetics limit the use of nonmodified BiVO$_4$ as a practical OER catalyst.[1] In order to overcome these issues, various strategies to modify BiVO$_4$ photoanodes have been proposed.[6−8] Apart from OER, BiVO$_4$ also catalyzes the hydrogen peroxide evolution reaction (HPER)[9,10] in the presence of bicarbonate electrolyte or modified with different materials.[11−13] HPER has a standard electrode potential of 1.78 V vs standard hydrogen electrode (SHE),[14] and consumes water to produce H$_2$O$_2$. Current large-scale hydrogen peroxide production uses the anthraquinone oxidation process, which involves toxic precursors and various organic solvents.[15] An alternative means of production is highly desired,[16] as H$_2$O$_2$ has numerous applications: it is used as a bleaching agent or an oxidant and has various applications in the chemical industry, water treatment, metal processing, etc.[15,17] For photocatalytic HPER on BiVO$_4$ to be industrially viable, it needs to be better understood, particularly its selectivity with respect to the competitive OER.

One of the parameters important for the water oxidation performance on BiVO$_4$ is the exposed surface facet.[18] A nanocrystal of monoclinic scheelite BiVO$_4$ contains different surface facets, of which the (001) and (011)[19] surfaces comprise 99.3% of the nanocrystal's surface area (see Supporting Information for the detailed explanation).[20,21] These two facets were shown to lead to large anisotropies,[22−24] and their influence on the water oxidation mechanisms is considered in the present work.

On a different note, the BiVO$_4$ surfaces are not always pristine—they usually contain structural defects.[25] The most common type of defect in ternary oxide semiconductors are oxygen vacancies ($\mathcal{V}_o$).[26] Vacancies can improve a semiconductor's conductivity and charge separation efficiency by acting as shallow n-type donors.[27,28] They may also improve visible light absorption by reducing the band gap and improve the charge transfer between the material and the electrolyte (water).[29] Nonetheless, the $\mathcal{V}_o$s in semiconductors may be counterproductive for OER efficiency by acting as electron−

ACS Publications

13416
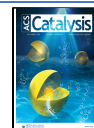
hole recombination centers[30,31] or by trapping photogenerated charge carriers or polarons and inhibiting charge transfer.[32,33] Several studies suggest that these disadvantageous effects arise from the oxygen vacancies formed in the bulk, while the advantageous effects arise from the vacancies formed on the surface of a semiconductor.[34−36] In BiVO$_4$, $\mathcal{V}_o$s significantly alter the geometric[37] and electronic[38−40] structure and thereby the water oxidation mechanism. However, their exact influence on water oxidation is not fully understood because studies are still limited and inconclusive.[40,41] Even though the vacancies may not be thermodynamically stable at the potentials necessary for water oxidation (see Supporting Information section 2.8 for analysis of the $\mathcal{V}_o$ formation energies and Pourbaix diagram), they are kinetically trapped, as experimental evidence shows,[42−44] and present in the material at high potentials. It was shown that the BiVO$_4$-based material with an exposed vacancy-rich (001) surface significantly improves photocatalytic water oxidation.[43] A theoretical study on this surface suggested that the surface oxygen vacancies increase the number of water splitting active sites and enhance hole transfer from the photoanode surface to the electrolyte.[29] In addition to that, it was shown that the vacancies lower the selectivity toward H$_2$O$_2$, therefore shifting the equilibrium toward OER.[44] The vacancies examined in these works arise when an oxygen atom from a VO$_4^{3-}$ unit is removed and the two excess electrons remain in the cavity left by that atom, with no significant changes to the local structure. In this type of defect, the vacancy is effectively localized on a single vanadium atom, which is why we label it localized vacancy ($\mathcal{V}_o^{loc}$). The two additional electrons created by removing an O atom also remain localized at the vacancy site. This doubly occupied defect state is also called F-center.[26] Recently, however, we have shown that another, distinct type of oxygen vacancy (known as split vacancy, $\mathcal{V}_o^{split}$) could exist in the bulk and on the (001) surface of BiVO$_4$,[38] which was later also found by Wang et al.[27] In this type of defect, the local structure changes after the O atom is removed—atoms move in such a way that an oxygen atom from a neighboring VO$_4^{3-}$ unit increases its coordination number by forming an oxo-bridge with the vanadium that lost an O atom. The vacancy is therefore divided (split) between two neighboring vanadium atoms, unlike $\mathcal{V}_o^{loc}$. In the bulk, the two types of vacancies have similar formation energies. However, on the (001) surface, $\mathcal{V}_o^{split}$ in the subsurface layer was found to be ~1 eV more stable than $\mathcal{V}_o^{loc}$, with a quasi-barrierless transition to $\mathcal{V}_o^{split}$ (the energy barrier being 0.1 eV or less).[38] The two vacancy types also have distinct electronic structures. $\mathcal{V}_o^{loc}$ has a single, two-electron intragap state that lies deep within the band gap. The electrons are localized between the bismuth and vanadium atoms that share the vacancy, where the missing oxygen atom would be, reducing both Bi and V. $\mathcal{V}_o^{split}$ has two single-electron intragap states, one of which is deep and localized on a vanadium atom sharing the vacancy, while the other one is shallow (close to the conduction band) and may be delocalized over different V atoms. The vanadium atoms sharing the vacancy are reduced. As the electronic structure greatly affects catalytic mechanisms and selectivity by influencing the material's conductivity and charge separation efficiency, it is important to investigate the influence of these different kinds of vacancies on the water oxidation reaction.

We first studied the oxygen vacancy formation on the (011) surface and observed that, similarly to the (001) surface, a V−O−V bridge-forming $\mathcal{V}_o^{split}$ is preferred over $\mathcal{V}_o^{loc}$. Then, we modeled the OER and HPER reactions on the (001) and the (011) surfaces with and without a $\mathcal{V}_o^{split}$ in the subsurface, where the vacancy is the most stable. With these results, we obtained a complete picture of water oxidation on BiVO$_4$, elucidating its activity and selectivity with respect to different surface facets and the presence of oxygen vacancies on these surfaces. This allows for a better understanding of the fundamental nature of the water oxidation mechanisms on BiVO$_4$, which can guide the optimization and design of more efficient and selective photoanodes.

■ COMPUTATIONAL METHODS

Density functional theory (DFT) simulations were performed using the Vienna Ab initio Simulation Package (VASP)[45,46] and the PBEsol[47] exchange-correlation functional, as described in the Supporting Information. To calculate the electronic energy as a function of applied potential on selected systems, we carried out calculations with an implicit solvent model and a modified electrochemical potential by a surface-charging method based on the linearized Poisson−Boltzmann equation, as implemented in VASPsol.[48−50] This approach is also known as grand canonical DFT (GC-DFT), due to its grand canonical description of the electrons. We also carried out calculations with the PBE0[51] functional with 10% of exact exchange as a benchmark (see Supporting Information).[38] All of the structures are uploaded to the ioChem-BD database,[52,53] where they are openly accessible. Both (001) and (011) surfaces were modeled with similar, converged layer thicknesses, as shown in Figure 1. First, we modeled different types
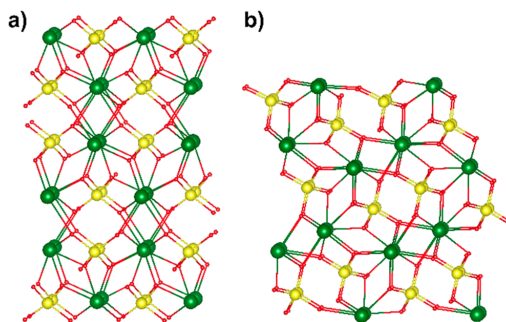
Figure 1. (a) Six-layered (001) surface slab and (b) three-layered (011) surface slab, as used in the calculations. One layer includes four BiVO$_4$ units for the (001) and eight BiVO$_4$ units for the (011) surface. Color code: Bi, V, and O are represented in green, yellow, and red, respectively (rendered with VESTA).[54]

of oxygen vacancies on the (011) surface, in order to find the most stable one. For this, we considered vacancies localized on 12 different positions in the slab, as well as two systems with a $\mathcal{V}_o^{split}$, as shown in the Supporting Information (Figure S1b).

Next, we investigated three distinct oxygen evolution reaction mechanistic pathways, as well as the pathway for H$_2$O$_2$ production, for the (001) and (011) surfaces, both pristine and with the most common vacancy type. The feasibility of the mechanisms was evaluated using the

computational hydrogen electrode (CHE) approach, at the electrolyte pH 0 and 1 bar of H_2 in the gas phase at 298 K.[55] The CHE description accuracy of the most optimal mechanisms was confirmed at the GC-DFT level. Two pathways were found in the literature[24,56] as the most likely mechanisms on the pristine (001) and (011) surfaces (Figure 2a). The first pathway (referred to as OER pathway A, shown
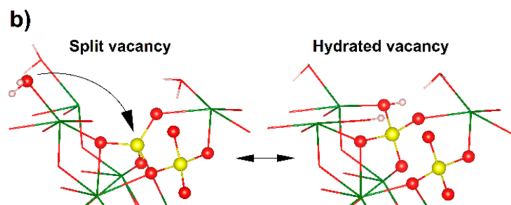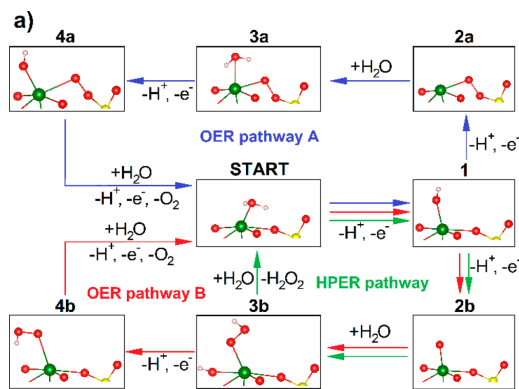

with blue arrows) was expected for the pristine (001) surface. Another mechanism (referred to as OER pathway B, shown with red arrows) was expected to happen on the pristine (011) surface. The main difference between these mechanisms is the peroxo-bridge between Bi and V atoms (intermediates **2a−4a**) that is present in pathway A, whereas pathway B includes an OOH group adsorbed to the surface (intermediates **3b** and **4b**).

With the systems containing oxygen vacancies, the vacancy creation/annihilation can be directly involved in the water oxidation mechanism.[57−59] This leads to the third OER mechanistic pathway, in which the vacancy is effectively filled by an oxygen atom coming from an adsorbed water molecule (Figure 2b). The resulting system is similar to the pristine surface, but it has two extra hydrogen atoms adsorbed, so it keeps the reduced oxidation state of the system with a vacancy; that is, it has two additional electrons. Such a system therefore contains a hydrated vacancy, which leads to a modified OER mechanism, referred to as OER pathway HV (see Supporting Information, section 2). Starting from a hydrated vacancy, the pristine surface is recovered after two hydrogen removals, and then, by evolving O_2, the vacancy is reintroduced (Figure S8).

The hydrogen peroxide evolution pathway (shown with green arrows in Figure 2a) starts in the same way as OER

pathway B. Intermediate **3b**, included in both of these mechanisms, contains an OOH group in the proximity of a hydrogen atom. Instead of oxidizing this system to form the intermediate **4b**, hydrogen peroxide can be evolved from the system. Another possible HPER mechanism includes oxidation of a different water molecule of intermediate **1** and forming another OH group instead of the oxo group as in the intermediate **2b**. Two OH groups then combine directly into hydrogen peroxide. This mechanism is not considered here, as it is less efficient than the other pathway (see Supporting Information).

■ RESULTS

Regarding vacancies on the (011) surface of $BiVO_4$, we found two stable vacancy types: a localized vacancy, $\mathcal{V}_o^{loc}$, and a split vacancy, $\mathcal{V}_o^{split}$, as on the (001) surface.[38] $\mathcal{V}_o^{split}$ was ∼0.6 eV more stable than $\mathcal{V}_o^{loc}$, and both systems have an analogous electronic structure to their (001) surface counterparts (see Supporting Information, section 2). Systems with $\mathcal{V}_o^{loc}$ have a deep intragap state with the extra electrons being paired and, therefore, no net magnetization. In the systems with $\mathcal{V}_o^{split}$, the electrons are no longer paired, and the system has a net magnetization of two.

We first analyzed the OER on the (001) surface with a $\mathcal{V}_o^{split}$ between the first two layers (Figure S1a), along with the pristine surface for comparison. The efficiency of different mechanisms can be evaluated by comparing their thermodynamic overpotentials (η_{TD}). The overpotential is calculated from the energy of the reaction step with the highest energy, namely the potential-determining step (PDS) and the equilibrium potential of the reaction. Steps that do not include transfer of charged particles are grouped together with the appropriate proton-coupled electron transfer (PCET), so that four PCET steps are obtained as in the CHE formalism.[55] The energy differences for each reaction step are presented in the Supporting Information (section 3). From these data, the reaction profiles are plotted (Figures 3 and S10). The mechanism proposed in the literature for the pristine (001) surface (OER pathway A, in blue) is significantly less efficient (η_{TD} = 1.2 V) than the mechanism happening on the (001) surface with $\mathcal{V}_o^{split}$ (following OER pathway B, in red, η_{TD} = 0.4 V). The oxygen vacancy particularly impacts the first PCET step, which is the PDS for the pristine system, lowering its energy by almost 2 eV. This step consists of a hydrogen removal, which is more efficient in all of the reaction steps happening on a surface with a vacancy (see Supporting Information, section 3). The subsurface vacancy introduces additional electrons which lie in high-energy states within the band gap and which are easily removed,[38] therefore facilitating the PCET. Hence, the subsurface split vacancies enhance OER efficiency on the (001) surface, similarly to what was found for vacancies localized in the surface layer.[29] This is also in agreement with recent experimental data, showing that vacancy-rich (001) surfaces significantly improve OER efficiency[43] and favor oxygen evolution kinetics.[60] As the adsorption of water enables vacancy hydration, a system with such a vacancy was also considered. Such a system was 0.09 eV more stable than the system with a nonhydrated, $\mathcal{V}_o^{split}$. From this energy difference, it can be calculated that 97% of the vacancies on the (001) surface are hydrated (see Supporting
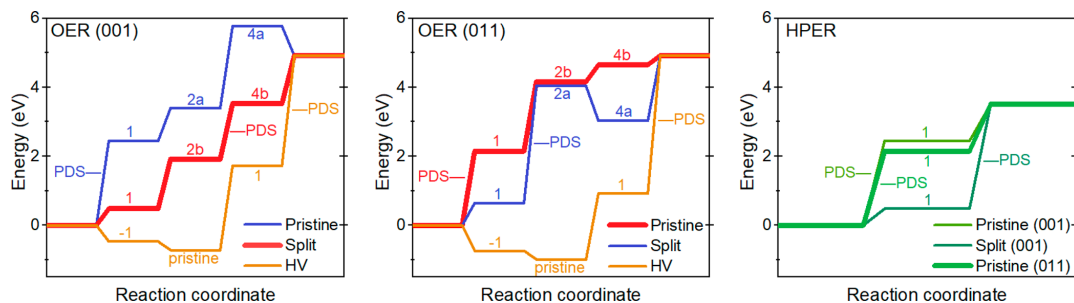
Figure 2. (a) Water oxidation mechanistic pathways on $BiVO_4$: OER pathway A, OER pathway B, and HPER pathway; (b) vacancy hydration.

Figure 3. Gibbs free energy profile of water oxidation on $BiVO_4$ (some steps are merged so that the resulting steps all include a PCET). Blue, OER pathway A; red, OER pathway B; brown, OER pathway HV; green, HPER pathway. The most optimal mechanism for each case (the lowest PDS) is represented with a thicker line.

Information). This implies that most of the subsurface vacancies tend to become hydrated when the $BiVO_4$ electrode is immersed in water. The OER mechanism with a hydrated vacancy, pathway HV (shown in brown), is not efficient on this surface because of its last two reaction steps, which correspond to a single PCET step (η_{TD} = 2.0 V). In this step, the vacancy is reintroduced into the surface, which has a high cost in energy (Figure S8). However, the first two PCET steps of these pathways (oxidation of the hydrated vacancy) are thermodynamically favorable.

For OER on the (011) surface, an analogous set of calculations was performed, and energy differences for each reaction step are presented in the Supporting Information (section 3). The corresponding reaction profiles are shown in Figures 3 and S11. The mechanism proposed in the literature for the pristine (011) surface (OER pathway B, shown in red) is the most efficient, with the second step being potential determining (η_{TD} = 0.9 V). With respect to the pristine surface, the OER efficiency is reduced when the vacancy is introduced (shown in blue, η_{TD} = 2.2 V), in contrast to what was found for the (001) surface. Again, we considered the possibility of vacancy hydration. The system containing a hydrated vacancy was 0.20 eV less stable than the system with a nonhydrated (split) vacancy. From this difference, it can be estimated that the amount of hydrated vacancies on the (011) surface is approximately 0.05%, which is negligible compared to their amount on the (001) surface (97%), where vacancy hydration was found to be thermodynamically favored. Analogously to what was found for the (001) surface, OER on the (011) surface with hydrated vacancy, pathway HV (shown in brown), is inefficient because of its last PCET step (η_{TD} = 2.8 V), while the first two steps (i.e., the oxidation of the hydrated vacancy) are thermodynamically favorable.

For the HPER, there are four systems in total to consider: the (001) and (011) surfaces, both pristine and with a $\mathcal{V}_o^{split}$ (Figures 3 and S12). For the (011) surface with a $\mathcal{V}_o^{split}$, the relevant intermediate (**2b**) could not be stabilized, and the HPER on this system is considered in the Supporting Information (section 3). Out of the remaining three systems, the preferred mechanism takes place on the pristine (011) surface, with the first step being the PDS. Its overpotential η_{TD} is equal to 0.4 V. We would like to note that Siahrostami et al. found a favorable η_{TD} of 0.2 V for HPER on the (111) surface,[61] where we would expect a higher HPER activity. However, if we consider the equilibrium nanoparticle shape

coming from the Wulff construction, the (111) surface represents a minor fraction of the total area (less than 1%, see Supporting Information, section 2.1).[21] Therefore, we kept the two most stable surfaces in our analysis.

For completeness, to confirm the accuracy of the used CHE approach and the PBEsol functional, we also performed calculations with GC-DFT at constant applied potentials and with a modified PBE0 functional with 10% exact exchange, respectively (see Supporting Information, sections 3.5 and 3.6). For the surface-charging method (GC-DFT), we took into account only the PDS of the two favored reactions (OER on the (001) surface with vacancy and HPER on the pristine (011) surface) at an applied potential of 1.6 V (vs SHE). This is the equilibrium potential of the former reaction at the CHE level. The energy of the PDS changes by less than 0.2 eV compared to the CHE approach at constant charge (Figure S16), therefore supporting the adequacy of our method. Similarly, using a hybrid functional for OER on the (001) surface with vacancy did not significantly alter the water oxidation energies (Figure S17).

So far, we have compared different mechanisms on the same surface; now, we compare the most suitable reaction mechanisms between different surfaces (Figure 4). In order
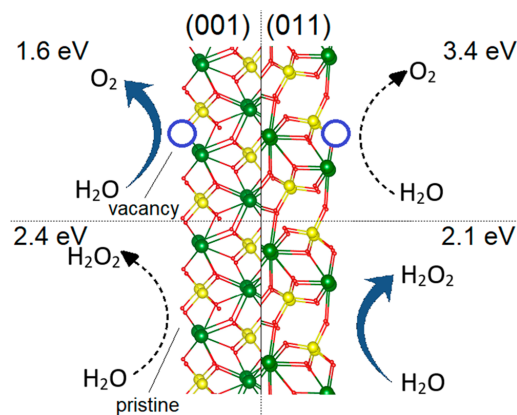

Figure 4. Most advantageous water oxidation reactions on $BiVO_4$ with the energies of their respective potential-determining steps. Two favorable processes are represented with a thicker arrow.

to elucidate the water oxidation selectivity, we compare the PDS energies directly instead of the overpotentials, as OER and HPER have different equilibrium potentials. Comparing OER on the (001) and (011) surfaces, we see that OER happens more easily on the (001) surface, as the PDS is lower in energy (1.6 eV, surface with vacancy) than on the (011) surface (2.1 eV, pristine surface). Both of these reactions follow the pathway B, so we conclude that the pathway A does not happen on BiVO$_4$ in the presence of oxygen vacancies. The OER on the (001) surface with $\mathcal{V}_o^{split}$ is also the overall most favorable water oxidation reaction on all of the systems considered, increasing by less than 0.2 eV at an applied potential of 1.6 V (Figure S16a). The second most energetically favorable reaction is HPER on the pristine (011) surface with the PDS of 2.1 eV (which decreased by only ~0.1 eV at an applied potential of 1.6 V, Figure S16b). This reaction has the equivalent PDS as the OER on the same surface. However, the second PCET step that ultimately produces hydrogen peroxide (1.4 eV) is lower in energy than the second PCET step of the OER reaction, which stops at the intermediate **2b** formation (2.0 eV). This implies that the (011) surface is more favorable for HPER than for OER. The results also suggest that oxygen vacancies in the subsurface favor oxygen evolution, whereas HPER is more favorable on the pristine material. Our theoretical prediction explains recent experiments,[44] showing that V$_2$O$_5$-treated BiVO$_4$, which has a lower amount of oxygen vacancies than the pristine material, favors HPER over OER.

It is known that bicarbonate is needed as the electrolyte for an efficient H$_2$O$_2$ evolution reaction on BiVO$_4$.[9,11,13] We propose that the bicarbonate ions may have a role in detrapping vacancies by lowering the barrier for vacancy hydration, as the oxygen vacancies are not thermodynamically stable at the potentials needed for water oxidation (they are only present because they are kinetically trapped). Consequently, removing the vacancies from the surface would shift the selectivity toward H$_2$O$_2$. However, this hypothesis would need to be tested by further calculations and experiments.

In conclusion, by modeling all of the reaction intermediates for different water oxidation mechanisms, we have shown that the most favorable electrochemical process on BiVO$_4$ is the OER on the (001) surface with a subsurface $\mathcal{V}_o^{split}$. The most energetically demanding proton-coupled electron transfer step for this reaction has an energy of 1.6 eV (η_{TD} = 0.4 V). The second most favorable process is hydrogen peroxide evolution reaction on the pristine (011) surface, with the most energetically demanding PCET step being 2.1 eV (η_{TD} = 0.4 V). Therefore, if no oxygen vacancies are present in the material, HPER on the (011) surface becomes the most favorable reaction. We have also shown that it is thermodynamically favored to fill oxygen vacancies on the (001) surface with a water molecule (vacancy hydration), which can further influence the photocatalytic activity of BiVO$_4$ by changing the number of split vacancies on its surface. Our results highlight the crucial impact of oxygen vacancies, not only on the catalytic activity but also on the water oxidation selectivity on ternary metal oxides. By controlling the exposed surface facet and the vacancy content, selectivity can be driven toward either OER or HPER, which is important for the design of novel photoelectrodes.

■ ASSOCIATED CONTENT

Ⓢ Supporting Information

The Supporting Information is available free of charge at https://pubs.acs.org/doi/10.1021/acscatal.1c03256.

Computational methods, vacancy formation energies, water oxidation intermediate energies, densities of states, GC-DFT energies, vibrational frequencies (PDF)

■ AUTHOR INFORMATION

Corresponding Authors

Franziska S. Hegner − *Institut Català d'Investigació Química (ICIQ), The Barcelona Institute of Science and Technology (BIST), 43007 Tarragona, Spain;* Present Address: Technical University of Munich (TUM), James-Franck-Straße 1, 85748 Garching, Germany; Email: fhegner@iciq.es

Núria López − *Institut Català d'Investigació Química (ICIQ), The Barcelona Institute of Science and Technology (BIST), 43007 Tarragona, Spain;* ⓞ orcid.org/0000-0001-9150-5941; Email: nlopez@iciq.es

Authors

Pavle Nikačević − *Institut Català d'Investigació Química (ICIQ), The Barcelona Institute of Science and Technology (BIST), 43007 Tarragona, Spain*

José Ramón Galán-Mascarós − *Institut Català d'Investigació Química (ICIQ), The Barcelona Institute of Science and Technology (BIST), 43007 Tarragona, Spain; Catalan Institution for Research and Advanced Studies (ICREA), 08010 Barcelona, Spain;* ⓞ orcid.org/0000-0001-7983-9762

Complete contact information is available at:
https://pubs.acs.org/10.1021/acscatal.1c03256

Author Contributions

All authors have given approval to the final version of the manuscript.

Notes

The authors declare no competing financial interest.

■ ACKNOWLEDGMENTS

■ ABBREVIATIONS

DFT, density functional theory; OER, oxygen evolution reaction; HPER, hydrogen peroxide evolution reaction; GC, Grand-Canonical; PCET, proton-coupled electron transfer; PDS, potential-determining step

■ REFERENCES

(1) Tayebi, M.; Lee, B. Recent Advances in BiVO$_4$ Semiconductor Materials for Hydrogen Production Using Photoelectrochemical Water Splitting. *Renewable Sustainable Energy Rev.* **2019**, *111*, 332−343.

(2) Malathi, A.; Madhavan, J.; Ashokkumar, M.; Arunachalam, P. A Review on BiVO$_4$ Photocatalyst: Activity Enhancement Methods for Solar Photocatalytic Applications. *Appl. Catal., A* **2018**, *555*, 47−74.

(3) Kudo, A.; Ueda, K.; Kato, H.; Mikami, I. Photocatalytic O_2 Evolution Under Visible Light Irradiation on $BiVO_4$ in Aqueous $AgNO_3$ Solution. *Catal. Lett.* **1998**, *53*, 229−230.

(4) Jia, Q.; Iwashina, K.; Kudo, A. Facile Fabrication of an Efficient $BiVO_4$ Thin Film Electrode for Water Splitting Under Visible Light Irradiation. *Proc. Natl. Acad. Sci. U. S. A.* **2012**, *109* (29), 11564−11569.

(5) Pihosh, Y.; Turkevych, I.; Mawatari, K.; Uemura, J.; Kazoe, Y.; Kosar, S.; Makita, K.; Sugaya, T.; Matsui, T.; Fujita, D.; Tosa, M.; Kondo, M.; Kitamori, T. Photocatalytic Generation of Hydrogen by Core-Shell $WO_3/BiVO_4$ Nanorods with Ultimate Water Splitting Efficiency. *Sci. Rep.* **2015**, *5*, 11141.

(6) Kim, J.; Lee, J. Elaborately Modified $BiVO_4$ Photoanodes for Solar Water Splitting. *Adv. Mater.* **2019**, *31* (20), 1806938.

(7) Chen, L.; Alarcon-Llado, E.; Hettick, M.; Sharp, I.; Lin, Y.; Javey, A.; Ager, J. Reactive Sputtering of Bismuth Vanadate Photoanodes for Solar Water Splitting. *J. Phys. Chem. C* **2013**, *117* (42), 21635−21642.

(8) Tayebi, M.; Tayyebi, A.; Lee, B. Improved Photoelectrochemical Performance of Molybdenum (Mo)-Doped Monoclinic Bismuth Vanadate with Increasing Donor Concentration. *Catal. Today* **2019**, *328*, 35−42.

(9) Fuku, K.; Sayama, K. Efficient Oxidative Hydrogen Peroxide Production and Accumulation in Photoelectrochemical Water Splitting Using a Tungsten Trioxide/Bismuth Vanadate Photoanode. *Chem. Commun.* **2016**, *52*, 5406−5409.

(10) Shi, X.; Siahrostami, S.; Li, G.; Zhang, Y.; Chakthranont, P.; Studt, F.; Jaramillo, T.; Zheng, X.; Norskov, J. Understanding Activity Trends in Electrochemical Water Oxidation to Form Hydrogen Peroxide. *Nat. Commun.* **2017**, *8*, 701.

(11) Shi, X.; Zhang, Y.; Siahrostami, S.; Zheng, X. Light-Driven $BiVO_4$ Fuel Cell with Simultaneous Production of H_2O_2. *Adv. Energy Mater.* **2018**, *8*, 1801158.

(12) Miyase, Y.; Takasugi, S.; Iguchi, S.; Miseki, Y.; Gunji, T.; Sasaki, K.; Fujita, E.; Sayama, K. Modification of $BiVO_4/WO_3$ Composite Photoelectrodes with Al_2O_3 via Chemical Vapor Deposition for Highly Efficient Oxidative H_2O_2 Production from H_2O. *Sustain. Energy Fuels* **2018**, *2*, 1621−1629.

(13) Fuku, K.; Miyase, Y.; Miseki, Y.; Gunji, T.; Sayama, K. Enhanced Oxidative Hydrogen Peroxide Production on Conducting Glass Anodes Modified with Metal Oxides. *ChemistrySelect* **2016**, *1* (18), 5721−5726.

(14) https://www.h2o2.com/technical-library/physical-chemical-properties/thermodynamic-properties/default.aspx?pid=50&name=Standard-Electrode-Potentials (accessed 2021-08-25).

(15) Campos-Martin, J. M.; Blanco-Brieva, G.; Fierro, J. L. G. Hydrogen Peroxide Synthesis: An Outlook beyond the Anthraquinone Process. *Angew. Chem., Int. Ed.* **2006**, *45* (42), 6962−6984.

(16) Siahrostami, S.; Verdaguer-Casadevall, A.; Karamad, M.; Deiana, D.; Malacrida, P.; Wickman, B.; Escudero-Escribano, M.; Paoli, E. A.; Frydendal, R.; Hansen, T. W.; Chorkendorff, I.; Stephens, I. E. L.; Rossmeisl, J. Enabling Direct H_2O_2 Production Through Rational Electrocatalyst Design. *Nat. Mater.* **2013**, *12*, 1137−1143.

(17) Hage, R.; Lienke, A. Applications of Transition-Metal Catalysts to Textile and Wood-Pulp Bleaching. *Angew. Chem., Int. Ed.* **2006**, *45* (2), 206−222.

(18) Lardhi, S.; Cavallo, L.; Harb, M. Significant Impact of Exposed Facets on the $BiVO_4$ Material Performance for Photocatalytic Water Splitting Reactions. *J. Phys. Chem. Lett.* **2020**, *11* (14), 5497−5503.

(19) In the present work, the (001), (011), (101), and (111) surfaces are labeled in the body-centered *I2/b* setting, which is convenient for computations. In the literature, they are often labeled in the conventional *C2/c* setting, as (010), ($\bar{1}$11), ($\bar{1}$10), and (011), respectively.[21]

(20) Sleight, A.; Chen, H.; Ferretti, A.; Cox, D. Crystal growth and structure of $BiVO_4$. *Mater. Res. Bull.* **1979**, *14* (12), 1571−1581.

(21) Li, G. First-Principles Investigation of the Surface Properties of Fergusonite-Type Monoclinic $BiVO_4$ Photocatalyst. *RSC Adv.* **2017**, *7* (15), 9130−9140.

(22) Li, R.; Zhang, F.; Wang, D.; Yang, J.; Li, M.; Zhu, J.; Zhou, X.; Han, H.; Li, C. Spatial Separation of Photogenerated Electrons and Holes Among {010} and {110} Crystal Facets of $BiVO_4$. *Nat. Commun.* **2013**, *4*, 1432.

(23) Liu, T.; Zhou, X.; Dupuis, M.; Li, C. The Nature of Photogenerated Charge Separation Among Different Crystal Facets of $BiVO_4$ Studied by Density Functional Theory. *Phys. Chem. Chem. Phys.* **2015**, *17* (36), 23503−23510.

(24) Hu, J.; Chen, W.; Zhao, S.; Su, H.; Chen, Z. Anisotropic Electronic Characteristics, Adsorption, and Stability of Low-Index $BiVO_4$ Surfaces for Photoelectrochemical Applications. *ACS Appl. Mater. Interfaces* **2018**, *10* (6), 5475−5484.

(25) Lee, D.; Wang, W.; Zhou, C.; Tong, X.; Liu, M.; Galli, G.; Choi, K. The Impact of Surface Composition on the Interfacial Energetics and Photoelectrochemical Properties of $BiVO_4$. *Nat. Energy* **2021**, *6*, 287−294.

(26) Daelman, N.; Hegner, F. S.; Rellan-Pineiro, M.; Capdevila-Cortada, M.; Garcia-Muelas, R.; Lopez, N. Quasi-Degenerate States and Their Dynamics in Oxygen Deficient Reducible Metal Oxides. *J. Chem. Phys.* **2020**, *152*, 050901.

(27) Wang, S.; Chen, P.; Bai, Y.; Yun, J.; Liu, G.; Wang, L. New $BiVO_4$ Dual Photoanodes with Enriched Oxygen Vacancies for Efficient Solar-Driven Water Splitting. *Adv. Mater.* **2018**, *30* (20), 1800486.

(28) Zhang, W.; Song, L.; Cen, J.; Liu, M. Mechanistic Insights into Defect-Assisted Carrier Transport in Bismuth Vanadate Photoanodes. *J. Phys. Chem. C* **2019**, *123* (34), 20730−20736.

(29) Hu, J.; Zhao, X.; Chen, W.; Su, H.; Chen, Z. Theoretical Insight into the Mechanism of Photoelectrochemical Oxygen Evolution Reaction on $BiVO_4$ Anode with Oxygen Vacancy. *J. Phys. Chem. C* **2017**, *121* (34), 18702−18709.

(30) Freysoldt, C.; Grabowski, B.; Hickel, T.; Neugebauer, J.; Kresse, G.; Janotti, A.; Van de Walle, C. First-Principles Calculations for Point Defects in Solids. *Rev. Mod. Phys.* **2014**, *86*, 253−305.

(31) Cheng, C.; Fang, Q.; Fernandez-Alberti, S.; Long, R. Controlling Charge Carrier Trapping and Recombination in $BiVO_4$ with the Oxygen Vacancy Oxidation State. *J. Phys. Chem. Lett.* **2021**, *12*, 3514−3521.

(32) Selim, S.; Pastor, E.; Garcia-Tecedor, M.; Morris, M.; Francas, L.; Sachs, M.; Moss, B.; Corby, S.; Mesa, C.; Gimenez, S.; Kafizas, A.; Bakulin, A.; Durrant, J. Impact of Oxygen Vacancy Occupancy on Charge Carrier Dynamics in $BiVO_4$ Photoanodes. *J. Am. Chem. Soc.* **2019**, *141* (47), 18791−18798.

(33) Qiu, W.; Xiao, S.; Ke, J.; Wang, Z.; Tang, S.; Zhang, K.; Qian, W.; Huang, Y.; Huang, D.; Tong, Y.; Yang, S. Freeing the Polarons to Facilitate Charge Transport in $BiVO_4$ from Oxygen Vacancies with an Oxidative 2D Precursor. *Angew. Chem., Int. Ed.* **2019**, *58* (52), 19087−19095.

(34) Zhao, X.; Hu, J.; Yao, X.; Chen, S.; Chen, Z. Clarifying the Roles of Oxygen Vacancy in W-Doped $BiVO_4$ for Solar Water Splitting. *ACS Appl. Energy Mater.* **2018**, *1*, 3410−3419.

(35) Fernandez-Climent, R.; Gimenez, S.; Garcia-Tecedor, M. The Role of Oxygen Vacancies in Water Splitting Photoanodes. *Sustain. Energy Fuels* **2020**, *4*, 5916−5926.

(36) Wang, Z.; Mao, X.; Chen, P.; Xiao, M.; Monny, S.; Wang, S.; Konarova, M.; Du, A.; Wang, L. Understanding the Roles of Oxygen Vacancies in Hematite-Based Photoelectrochemical Processes. *Angew. Chem., Int. Ed.* **2019**, *58* (4), 1030−1034.

(37) Osterbacka, N.; Wiktor, J. Influence of Oxygen Vacancies on the Structure of $BiVO_4$. *J. Phys. Chem. C* **2021**, *125*, 1200−1207.

(38) Hegner, F. S.; Forrer, D.; Galan-Mascaros, J. R.; Lopez, N.; Selloni, A. Versatile Nature of Oxygen Vacancies in Bismuth Vanadate Bulk and (001) Surface. *J. Phys. Chem. Lett.* **2019**, *10* (21), 6672−6678.

(39) Wang, W.; Strohbeen, P.; Lee, D.; Zhou, C.; Kawasaki, J.; Choi, K.; Liu, M.; Galli, G. The Role of Surface Oxygen Vacancies in $BiVO_4$. *Chem. Mater.* **2020**, *32*, 2899−2909.

(40) Seo, H.; Ping, Y.; Galli, G. Role of Point Defects in Enhancing the Conductivity of $BiVO_4$. *Chem. Mater.* **2018**, *30* (21), 7793−7802.

136

(41) Cooper, J.; Scott, S.; Ling, Y.; Yang, J.; Hao, S.; Li, Y.; Toma, F.; Stutzmann, M.; Lakshmi, K.; Sharp, I. Role of Hydrogen in Defining the n-Type Character of $BiVO_4$ Photoanodes. *Chem. Mater.* **2016**, *28* (16), 5761−5771.

(42) Wang, S.; Chen, P.; Yun, J.; Hu, Y.; Wang, L. An Electrochemically Treated $BiVO_4$ Photoanode for Efficient Photo-electrochemical Water Splitting. *Angew. Chem., Int. Ed.* **2017**, *56* (29), 8500−8504.

(43) Hu, J.; He, H.; Zhou, X.; Li, Z.; Shen, Q.; Luo, W.; Alsaedi, A.; Hayat, T.; Zhou, Y.; Zou, Z. $BiVO_4$ Tubular Structures: Oxygen Defect-Rich and Largely Exposed Reactive {010} Facets Synergistically Boost Photocatalytic Water Oxidation and Selective N≡N Coupling Reaction of 5-Amino-1H-Tetrazole. *Chem. Commun.* **2019**, *55* (39), 5635−5638.

(44) Wang, L.; Lu, Y.; Han, N.; Dong, C.; Lin, C.; Lu, S.; Min, Y.; Zhang, K. Suppressing Water Dissociation via Control of Intrinsic Oxygen Defects for Awakening Solar H_2O-to-H_2O_2 Generation. *Small* **2021**, *17*, 2100400.

(45) Kresse, G.; Furthmüller, J. Efficient Iterative Schemes for *Ab Initio* Total-Energy Calculations Using a Plane-Wave Basis Set. *Phys. Rev. B: Condens. Matter Mater. Phys.* **1996**, *54*, 11169−11186.

(46) Kresse, G.; Joubert, D. From Ultrasoft Pseudopotentials to the Projector Augmented-Wave Method. *Phys. Rev. B: Condens. Matter Mater. Phys.* **1999**, *59*, 1758−1775.

(47) (a) Perdew, J. P.; Ruzsinszky, A.; Csonka, G.; Vydrov, O.; Scuseria, G.; Constantin, L.; Zhou, X.; Burke, K. Restoring the Density-Gradient Expansion for Exchange in Solids and Surfaces. *Phys. Rev. Lett.* **2008**, *100*, 136406; Erratum. *Phys. Rev. Lett.* **2009**, *102*, 039902.

(48) Mathew, K.; Sundararaman, R.; Letchworth-Weaver, K.; Arias, T. A.; Hennig, R. G. Implicit Solvation Model for Density-Functional Study of Nanocrystal Surfaces and Reaction Pathways. *J. Chem. Phys.* **2014**, *140*, 084106.

(49) https://github.com/henniggroup/VASPsol (accessed 2021-08-25).

(50) Mathew, K.; Kolluru, V.; Mula, S.; Steinmann, S.; Hennig, R. Implicit Self-Consistent Electrolyte Model in Plane-Wave Density-Functional Theory. *J. Chem. Phys.* **2019**, *151*, 234101.

(51) Perdew, J. P.; Ernzerhof, M.; Burke, K. Rationale for Mixing Exact Exchange with Density Functional Approximations. *J. Chem. Phys.* **1996**, *105*, 9982−9985.

(52) Alvarez-Moreno, M.; de Graaf, C.; Lopez, N.; Maseras, F.; Poblet, J. M.; Bo, C. Managing the Computational Chemistry Big Data Problem: The ioChem-BD Platform. *J. Chem. Inf. Model.* **2015**, *55*, 95−103.

(53) Nikačević, P. DOI: 10.19061/iochem-bd-1-203 (accessed 2021-09-30).

(54) Momma, K.; Izumi, F. *VESTA*: A Three-Dimensional Visualization System for Electronic and Structural Analysis. *Appl. Crystallogr.* 2008, *41*, 653−658.

(55) Norskov, J.; Rossmeisl, J.; Logadottir, A.; Lindqvist, L.; Kitchin, J.; Bligaard, T.; Jonsson, H. Origin of the Overpotential for Oxygen Reduction at a Fuel-Cell Cathode. *J. Phys. Chem. B* **2004**, *108* (46), 17886−17892.

(56) Yang, J.; Wang, D.; Zhou, X.; Li, C. A Theoretical Study on the Mechanism of Photocatalytic Oxygen Evolution on $BiVO_4$ in Aqueous Solution. *Chem. - Eur. J.* **2013**, *19* (4), 1320−1326.

(57) Mefford, J.; Rong, X.; Abakumov, A.; Hardin, W.; Dai, S.; Kolpak, A.; Johnston, K.; Stevenson, K. Water Electrolysis on $La_{1−x}Sr_xCoO_{3−\delta}$ Perovskite Electrocatalysts. *Nat. Commun.* **2016**, *7*, 11053.

(58) Rong, X.; Parolin, J.; Kolpak, A. A Fundamental Relationship between Reaction Mechanism and Stability in Metal Oxide Catalysts for Oxygen Evolution. *ACS Catal.* **2016**, *6* (2), 1153−1158.

(59) Grimaud, A.; Diaz-Morales, O.; Han, B.; Hong, W.; Lee, Y.; Giordano, L.; Stoerzinger, K.; Koper, M.; Shao-Horn, Y. Activating Lattice Oxygen Redox Reactions in Metal Oxides to Catalyse Oxygen Evolution. *Nat. Chem.* **2017**, *9*, 457−465.

(60) Kahraman, A.; Vishlaghi, M.; Baylam, I.; Ogasawara, H.; Sennaroglu, A.; Kaya, S. The Fast-Track Water Oxidation Channel on $BiVO_4$ Opened by Nitrogen Treatment. *J. Phys. Chem. Lett.* **2020**, *11* (20), 8758−8764.

(61) Siahrostami, S.; Li, G.; Viswanathan, V.; Norskov, J. One- or Two-Electron Water Oxidation, Hydroxyl Radical, or H_2O_2 Evolution. *J. Phys. Chem. Lett.* **2017**, *8* (6), 1157−1160.

137

Mixed excitonic nature in water-oxidized BiVO4 surfaces with defects

Rachel Steinitz-Eliyahu [1], Daniel Hernangómez-Pérez [1], Franziska S. Hegner [2], Pavle Nikačević [2],
Núria López,[2] and Sivan Refaely-Abramson [1,*]

[1]*Department of Molecular Chemistry and Materials Science, Weizmann Institute of Science, Rehovot 7610001, Israel*
[2]*Institut Català d'Investigació Química (ICIQ), The Barcelona Institute of Science and Technology (BIST), Avenida Països Catalans, 16, 43007 Tarragona, Spain*

BiVO4 is a promising photocatalyst for efficient water oxidation, with surface reactivity determined by the structure of active catalytic sites. Surface oxidation in the presence of oxygen vacancies induces electron localization, suggesting an atomistic route to improve the charge transfer efficiency within the catalytic cycle. In this paper, we study the effect of oxygen vacancies on the electronic and optical properties at BiVO4 surfaces upon water oxidation. We use density functional theory and many-body perturbation theory to explore the change in the electronic and quasiparticle energy levels and to evaluate the electron-hole coupling as a function of the underlying structure. We show that while the presence of defects alters the atomic structure and largely modifies the wave-function nature, leading to defect-localized states at the quasiparticle gap region, the optical excitations remain largely unchanged due to the substantial hybridization of defect and nondefect electron-hole transitions. Our findings suggest that defect-induced surface oxidation supports improved electron transport, both through bound and tunable electronic states and via a mixed nature of the optical transitions, expected to reduce electron-hole defect trapping.

DOI: 10.1103/PhysRevMaterials.6.065402

I. INTRODUCTION

Metal oxide semiconductors serve as promising photoanodes for solar-driven water splitting processes [1]. Bismuth vanadate (BiVO4) is a famous example of exceeding interest, being relatively stable, nontoxic, and long lasting, with absorption well within the solar spectrum [2–10], and with suitable electronic properties for efficient oxygen evolution reaction (OER) [4,6,11,12]. Despite these appealing properties, electron conductivity and carrier transport through BiVO4 surfaces are found to be relatively low [13–15], greatly limiting its use in practical applications. This low conductance is typically attributed to fast charge recombination and polaronic interactions [16,17], strongly coupled to the surface structure [18–25] and the conditions in which it was prepared [9,19,26,27]. A broadly explored pathway to improve BiVO4 functionality is through electronic doping upon element substitution and the introduction of vacancies near the interacting BiVO4 surface [16,18,28,29]. These induce modified electronic densities and allow controllable electron mobility and electron-hole recombination rates [14,30–32].

Oxygen vacancies are abundant intrinsic defects in BiVO4 that can also be generated and controlled via external treatments, such as hydrogen annealing and nitrogen flow [16,33,34]. By acting as *n*-type donors, these defects hold the promise to significantly increase the water oxidation reaction yield [15,27,35–37]. From an electronic structure point of view, oxygen vacancies introduce localized electronic

states, allowing tunable electronic band gaps and suggesting an enhancement of the separation between photogenerated electrons and holes and an improved absorption cross section of the visible light [15,16,35,38]. On the other hand, localized defect states are considered as active electron-hole recombination centers, which can trap the photogenerated energy carriers—namely, excitons—and consequently reduce the electronic conductivity and the electron and energy transfer efficiency associated with it [27,39–42]. The role of oxygen vacancies in photogenerated carrier transport thus remains controversial, and a comprehensive understanding of the involved defect-induced phototransport mechanisms is still lacking.

Recent density functional theory (DFT) studies found that a structurally stable split oxygen vacancy, in which the vacancy is shared between two neighboring vanadium atoms in the form of a V-O-V bridge, is pivotal to the catalytic reaction that produces molecular oxygen upon water adsorption at thermodynamically stable (001) BiVO4 surfaces [25,35]. These studies showed that the change in surface structure and the underlying chemical bonding due to oxygen vacancies strongly influence the adsorbate. In particular, the main steps within the OER involve either a peroxo bridge between the Bi and V atoms at the surface, or a surface-oxo group evolving into an OOH group [25]. The electronic structure associated with the defects is thus expected to vary due to significant surface-structure modifications within the various steps in the catalytic reaction. The electronic states and the electron-hole binding associated with the vacancies within the catalytic reaction are hence nontrivial, and a predictive assessment of the electronic and excitonic
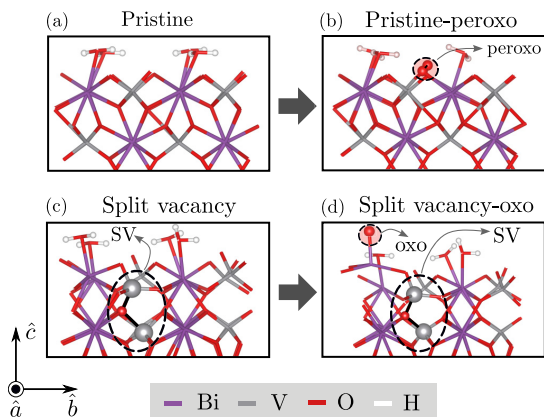

FIG. 1. Four BiVO$_4$ surface structures upon water adsorption, studied in this work: (a) a pristine surface, with full water coverage; (b) a pristine-peroxo surface, in which one water molecule per repeating cell went through oxidation; (c) a surface including a split vacancy with full water coverage; and (d) a split-vacancy-oxo surface, in which one water molecule per repeating cell went through oxidation. Oxidized water molecules are marked by red circles; black arrows represent the structural change upon oxidation. The split vacancy, appearing as a V-O-V bridge, is marked with a black dashed circle and denoted by "SV." Each structure represents the repeating unit cells in the $\hat{a}$, $\hat{b}$ direction; the $\hat{c}$ direction contains six layers as well as additional vacuum, and is shown in the SM [43] for the case of the pristine system.

fine structure as a function of these structural modifications is required.

In this work, we study the effect of oxygen vacancies on the electronic and excitonic properties in BiVO$_4$ upon surface water oxidation. We use DFT and many-body perturbation theory within the *GW* and *GW*-Bethe-Salpeter equation (*GW*-BSE) approximation to calculate the quasiparticle energies and the electron-hole coupling for representative structures found to be stable during the water oxidation stage in the catalytic cycle. We explore how the introduction of oxygen vacancies and the charge localization associated with it influence these properties. Our results show defect-localized states near the valence region, resulting from the underlying chemical bonding, with the quasiparticle band gap largely unchanged upon the inclusion of surface defects. This leads to largely mixed exciton states, hybridizing transitions between defect and nondefect bands. We find that due to this mixing, and unexpectedly, the presence of defects does not alter the exciton binding energy in the examined systems.

II. METHODOLOGY

The studied systems are shown in Fig. 1. Our focus is on the monoclinic scheelite of BiVO$_4$, considered to be the active phase at room temperature. We examine the thermodynamically most stable surface, that is the (001) facet. The calculated unit cell includes six layers, each containing four Bi and four V atoms, with a vacuum of 14 Å separating repeating cells along the $\hat{c}$ direction [see Supplemental Material (SM) [43]].

Atomic structures were relaxed using the Perdew-Burke-Ernzerhof functional revised for solids (PBEsol) following previous studies [35]. This sets a reliable DFT starting point for many-body perturbation theory. We note, however, that polaronic effects may induce additional localization and vary the electronic picture [27]. We consider four main structures occurring within two oxidation pathways, recently suggested to play a key role in the photocatalytic cycle [25]: a pristine BiVO$_4$ surface [Fig. 1(a)]; the same system after one water molecule per cell went through oxidation, resulting in a surface-peroxo group [Fig. 1(b)]; a BiVO$_4$ surface with a subsurface split vacancy (SV) [Fig. 1(c)]; and the same system after one water molecule per cell went through oxidation in the presence of a vacancy, resulting in a surface-oxo group [Fig. 1(d)].

In the following, we present the calculated quasiparticle and excitonic properties associated with these structures, and examine the electronic distribution and electron-hole coupling as a function of oxidation with and without the subsurface defects. To compute the single-particle electronic structure and the wave functions of the examined surfaces, we employ density functional theory (DFT) within the Perdew-Burke-Ernzerhof (PBE) approximation [44] for the exchange-correlation functional including spin-orbit coupling, using the QUANTUM ESPRESSO package [45]. The resulting DFT energies and wave functions are then used as a starting point for our many-body perturbation theory calculations, performed within the BERKELEY*GW* package [46]. We compute quasiparticle energy corrections applying the G_0W_0 approach within the generalized plasmon-pole model for the frequency dependence of the dielectric screening [47]. Following standard converging procedures, we consider a 30 Ry screening cutoff energy and a total of 3500 electronic bands, among them 1280 being occupied. Owing to small band dispersion (see SM) and the large size of the repeating cell, we sample the reciprocal space with a relatively coarse uniform **k**-point grid of $2 \times 2 \times 1$. To account for electron-hole coupling and excitonic properties, we employ the Bethe-Salpeter equation (BSE) formalism within the Tamm-Dancoff approximation [48], while considering 14 valence (occupied) bands and 16 conduction (empty) bands in the coupling matrices (see full computational details in the SM [43]).

III. RESULTS AND DISCUSSION

Figure 2 shows the computed DFT electronic energies and the *GW* quasiparticle energies, as well as the associated band gaps, for the pristine, pristine-peroxo, split-vacancy, and split-vacancy-oxo surface structures, respectively. Due to the relatively small band dispersion in the examined systems (see SM), we present the calculate values only at the Γ point aligned to the highest occupied state that does not have a defect character (absolute alignment between *GW* and DFT of the defect/oxo states is given in the SM [43], as well as full DFT band structures). Blue and orange colors represent the valence band maximum (VBM) and conduction band minimum (CBM), respectively. Black lines represent defect- and surface-oxidized states at the gap region. For the pristine system [Fig. 2(a)], the *GW* opens up the DFT (PBE) gap significantly (by 1.7 eV), to a value of 3.8 eV. This *GW*
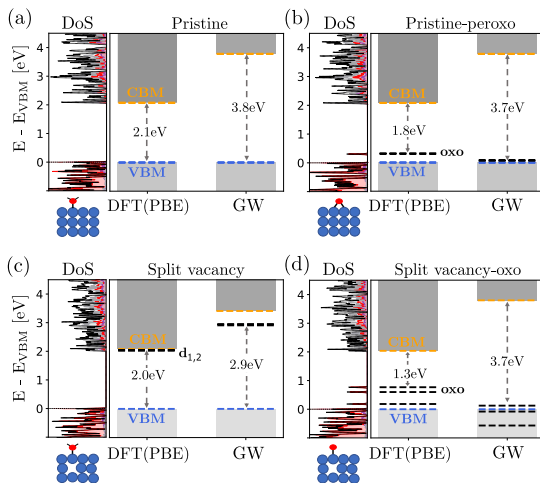
FIG. 2. Calculated DFT and *GW* electron and quasiparticle energies and band gaps, for the (a) pristine, (b) pristine-peroxo, (c) split-vacancy, and (d) split-vacancy-oxo systems at the Γ point. Pristinelike CBM and VBM states are indicated in orange and blue dashed lines, respectively, and additional oxo and defect energy levels are shown as black dashed lines. The projected density of states of each of the surface structures onto the atomic contributions is also shown (violet: Bi; gray: V; red: O; white: H), with the dashed line corresponding to the total density of states.

FIG. 3. (a) Calculated coupling matrix elements $S_{AB} = |\langle\phi_A|\phi_B\rangle|^2$ between DFT electronic states of the pristine and pristine-peroxo systems, where 0 denotes no overlap and 1 denotes complete overlap. (b) Same as in (a) for the comparison between split-vacancy and split-vacancy-oxo systems.

gap is slightly larger than the ones reported before for the bulk system, of 3.4–3.6 eV [8]. The gap increase is expected due to the reduced dielectric screening upon the inclusion of vacuum above the surface [49]. Upon water oxidation and the formation of a surface-peroxo group [Fig. 2(b)], the DFT results show an additional occupied in-gap state, which is shifted down to the VBM when including GW quasiparticle corrections.

In the presence of split vacancies [Fig. 2(c)], defect states marked as $d_{1,2}$ appear in the gap region. In this structure, the *GW* gap of 2.9 eV is significantly smaller than in the pristine case. We associate this gap reduction to fractional occupation at the CBM region, in particular to electrons localized at two V^{4+} sites, previously shown to be responsible for the instability of this structure [25,27,35]. Notably, upon oxidation of the defect surface [Fig. 2(d)], three occupied in-gap states, largely localized on the oxo group, appear at the valence edge region. The quasiparticle *GW* gap obtained is similar to the pristine and pristine-peroxo cases. These results suggest that the presence of oxygen vacancies induces localized states in addition to the pristinelike ones, in agreement with previous findings [15,27,50,51], which change their nature upon surface water oxidation. As we show in the following, these changes in the quasiparticle spectra result from the involved modifications in the chemical bonding around the missing atoms.

To further quantify the defect- and oxidation-induced change in the electronic structure, we examine the wave-function coupling before and after water oxidation, for the two pristine and the two split-vacancy structures. For this, we evaluate the coupling matrix elements between the computed
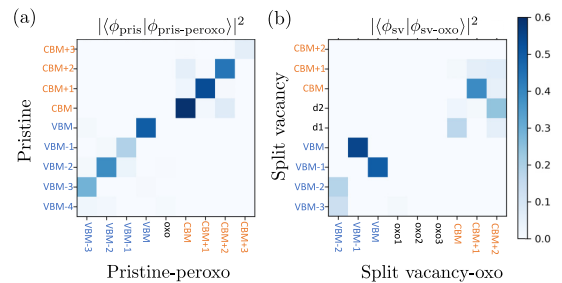
DFT wave functions of each two structures. We define the overlap matrix $S_{AB} = |\langle\phi_A|\phi_B\rangle|^2$, where A and B are different systems, and ϕ is an electronic Kohn-Sham state in a plane-wave basis set. As anticipated above, it is enough to only discuss the S matrix at the Γ point, as the other k points show a similar behavior due to the small band dispersion in the Brillouin zone (see SM [43]). Figure 3(a) shows the computed overlap between the pristine and pristine-peroxo structures, $S = |\langle\phi_{\text{pris}}|\phi_{\text{pris-peroxo}}\rangle|^2$. For this case, we find substantial coupling between the two systems—before and after surface oxidation—at the valence and conduction areas. As expected, the additional peroxo-localized in-gap states have negligible overlap with any of the pristine bands, suggesting that the local modification due to the surface oxidation and the peroxo formation is small.

In contrast, in the presence of subsurface split-vacancy defects, this picture becomes more complicated. The computed overlap between the split-vacancy and split-vacancy-oxo structures, $S = |\langle\phi_{\text{sv}}|\phi_{\text{sv-oxo}}\rangle|^2$ [Fig. 3(b)] shows that while few bands around the valence and conduction area remain of a similar nature, the defect states largely change their nature after surface oxidation. As a result, we find negligible overlap between defect states with water surface adsorbates [Fig. 2(c)] and defect states with oxidized adsorbates [Fig. 2(d)]. In other words, there are significant changes in the wave-function nature due to the surface-oxo bonding and the structural changes associated with it. We further note that the overlap matrix elements vanish almost completely when comparing between the pristine and the split-vacancy structures, and between the pristine-peroxo and the split-vacancy-oxo structures (see SM [43]). This suggests that the presence of oxygen vacancies leads to changes in the underlying bonding, which completely modifies the electronic wave functions. In addition, surface oxidation changes the surface bonding in the presence of defects, leading to the observed modifications in the electronic and quasiparticle spectra.

Having identified the change in electronic states and quasiparticle energy levels upon surface water oxidation and in the presence of defects, we now turn to compute the electron-hole coupling and the associated optical and excitonic properties. Figure 4 shows the calculated *GW*-BSE absorption spectra
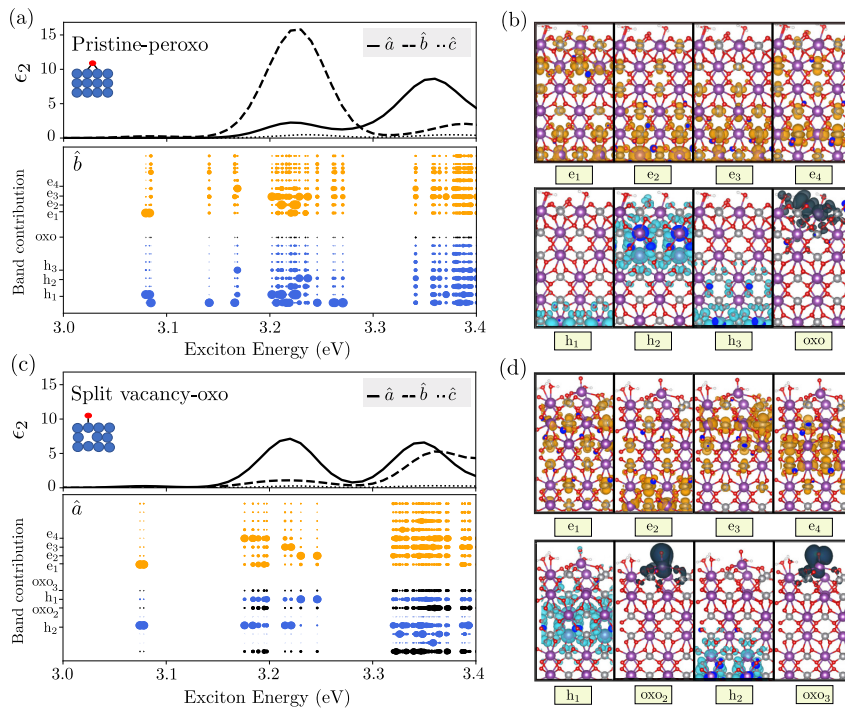
FIG. 4. (a) Calculated *GW*-BSE absorption spectra for the three main polarization directions, as well as electron-hole transitions contributing to the absorption peaks, for the pristine-peroxo system. Contributions from occupied (hole) bands are shown in blue, from unoccupied (electron) bands in orange, and from localized peroxo and oxo bands in black. Each dot in the lower panel represents the band contribution to the exciton as a function of the excitation energy, weighted by the oscillator strength at the dominating polarization direction ($\hat{b}$). (b) Representative wave-function distributions corresponding to the electron and hole Kohn-Sham states with the largest contribution to the low-energy absorption peaks. (c), (d) Same as in (a), (b) for the split-vacancy-oxo system. The exciton contributions are weighted with oscillator strength at the $\hat{a}$ polarization direction, which is the dominating one in this structure.

of the two oxidized surfaces with and without subsurface defects, pristine-peroxo and split-vacancy-oxo, upon optical excitation with light polarized at the three main crystal directions. The absorption peaks are further analyzed through the electron-hole transitions composing them. We first note that in both structures, the absorption oscillator strengths at the $\hat{a}$ and $\hat{b}$ polarization directions are much larger than at the $\hat{c}$ direction, suggesting that in-plane excitations dominate the spectra. However, while the lowest excitation peak in the pristine-peroxo case is at the $\hat{b}$ polarization direction, in the split-vacancy-oxo case it is at the $\hat{a}$ direction, serving as another signature of the significant underlying structural changes involved upon the presence of defects.

For the pristine-peroxo structure [Fig. 4(a)], the lowest bright excitation is at 3.08 eV, and the low-energy absorption peak is at 3.23 eV. These excitation energies are in good agreement with experimental findings, where the optical gap is found at ~3 eV [22,52–54]. The differences between the computed quasiparticle and optical gaps point to a relatively large exciton binding energy, on the order of 0.6 eV, suggesting strong electron-hole coupling. We note that this energy difference does not include lattice relaxation processes, which can largely reduce the band gap in these materials [11,52,53,55].

The computed excitation energies for the nonoxidized pristine case are very similar (see the computed absorption in the SM [43]), and are in good agreement with previous calculations for the bulk pristine system [8]. Such an agreement between surface and bulk structures can be explained by the local nature of the electron-hole interactions, leading to small long-range surface effects on the computed excitation energies. This points to larger exciton binding energies at the surface compared to the bulk, as expected, due to an increase in the quasiparticle gap while the optical gap remains similar.

The exciton coefficients for each excitonic state S, $A_{vc\mathbf{k}}^{S}$, quantify the coupling between an electron at band c and a hole at band v, at the k point $\mathbf{k}$. Electron-hole transitions composing the absorption spectra of the pristine-peroxo system are shown below the corresponding absorption energies in Fig. 4(a). The dot size represents the relative magnitude of the normalized exciton contribution, $\sum_{v\mathbf{k}} |A_{vc\mathbf{k}}^{S}|^2$ for unoccupied (c) bands and $\sum_{c\mathbf{k}} |A_{vc\mathbf{k}}^{S}|^2$ for occupied (v) bands, summed over all k points and scaled with the oscillator strength at the dominating polarization direction, so that only bright peaks are shown (contributions weighted by the other polarization directions are shown in the SM [43]). This analysis allows us to quantify the contribution from each electron/hole state

(orange/blue dots, respectively) to each one of the computed excitons. Black dots represent localized and occupied surface oxidation states, associated with the dashed black energy levels in Fig. 2(b). The electron/hole wave functions with the most significant contributions to low-lying excitons are shown in Fig. 4(b). Notably, the lowest bright exciton around 3.1 eV is primarily composed of transitions between the conduction electron band e_1 and a hole band below the valence region h_1. We note that this hole state is mainly localized at the bottom layer and thus may have increased delocalization when more layers are included, bringing it closer to the higher-energy hole states at the valence region. The peak around 3.2 eV already includes multiple electron-hole transitions, with additional contributions from occupied states localized at the oxidized surface-peroxo group, as well as other hole and electron states which are not associated with the surface-peroxo group.

This hybridized excitation nature is also present upon the inclusion of subsurface defects in the oxidized structure [Figs. 4(c) and 4(d)]. The lowest bright excitation is at 3.08 eV, and the low-energy absorption peak is at 3.22 eV, similarly to the pristine case. In contrast to the nondefective structure, in this case, defect-localized oxo states play a significant role in the excitation. The electron-hole contributions from defect-induced oxo states are shown as black dots in Fig. 4(c) and the associated wave functions are presented in Fig. 4(d). Notably, our *GW*-BSE results suggest that the associated excitons strongly mix defect and nondefect transitions. As a result, the overall peak position does not change compared to the nondefect case. Since the quasiparticle gap is also similar in both systems, the exciton binding energy associated with the low-energy excitation peak remains unchanged upon defect formation. However, the absorption contribution at the various polarization directions changes due to the modification in the underlying structure, reflecting a change in the directionality of the wave-function components, as discussed above.

Our results show that the low-energy exciton peaks, dominating the photoexcitation, are of a highly hybridized nature, which eventually leads to comparable excitation energies between the nondefect and the defect oxidized surface structures. This is a direct outcome of the localized nature of both nondefect and defect states in this system, as is also evident by the large quasiparticle gap and the electron-hole binding energies found with and without defects. This suggests that the role of oxygen vacancies in the associated catalytic cy-

cle mainly comes to play in the structural modification and stabilization upon water oxidation. Such a modification leads to near-gap surface states which can support the improved charge transfer, in particular upon defect charging expected to occur through electronic transport and pushing those bands deeper into the gap [15]. However, our computations show that the electron-hole transitions composing the excitons are hybridized and include both pristine and defect states, suggesting that defects cannot be trivially treated as charge traps. This implies that the many-body excitonic picture associated with photogeneration processes on $BiVO_4$ surfaces in the presence of defects can support improved carrier transport.

IV. CONCLUSION

To conclude, in this work we explored how subsurface defects alter the electronic and excitonic properties in $BiVO_4$ upon surface water oxidation. We find that the state localization due to structural modifications strongly influences the quasiparticle charge distributions and energy levels. However, oxygen vacancies only slightly change the exciton states, due to hybridized electron-hole transitions which mix defect and pristine states at similar energy regions. Our study presents a connection between the change in chemical bonding due to the presence of defects and the subsequent variations in the electronic band structure, wave functions, and optical excitations, demonstrating the nontrivial effect of defects on the mechanisms in which light is stored and energy is transferred in $BiVO_4$.

[1] C. Jiang, S. J. Moniz, A. Wang, T. Zhang, and J. Tang, Chem. Soc. Rev. **46**, 4645 (2017).

[2] Q. Jia, K. Iwashina, and A. Kudo, Proc. Natl. Acad. Sci. USA **109**, 11564 (2012).

[3] A. Kudo, K. Ueda, H. Kato, and I. Mikami, Catal. Lett. **53**, 229 (1998).

[4] I. D. Sharp, J. K. Cooper, F. M. Toma, and R. Buonsanti, ACS Energy Lett. **2**, 139 (2017).

[5] H. L. Tan, R. Amal, and Y. H. Ng, J. Mater. Chem. A **5**, 16498 (2017).

[6] K. R. Tolod, S. Hernández, and N. Russo, Catalysts **7**, 13 (2017).

[7] Z. Zhao, Z. Li, and Z. Zou, Phys. Chem. Chem. Phys. **13**, 4746 (2011).

[8] J. Wiktor, I. Reshetnyak, F. Ambrosio, and A. Pasquarello, Phys. Rev. Materials **1**, 022401(R) (2017).

[9] T. Das, X. Rocquefelte, R. Laskowski, L. Lajaunie, S. Jobic, P. Blaha, and K. Schwarz, Chem. Mater. **29**, 3380 (2017).

[10] Y. Wang, H. Shi, S. Ge, L. Zhang, X. Wang, and J. Yu, Sens. Actuators, B **336**, 129746 (2021).

[11] J. K. Cooper, S. Gul, F. M. Toma, L. Chen, P.-A. Glans, J. Guo, J. W. Ager, J. Yano, and I. D. Sharp, Chem. Mater. **26**, 5365 (2014).

[12] Y. Park, K. J. McDonald, and K.-S. Choi, Chem. Soc. Rev. **42**, 2321 (2013).

[13] F. F. Abdi, T. J. Savenije, M. M. May, B. Dam, and R. van de Krol, J. Phys. Chem. Lett. **4**, 2752 (2013).

[14] A. J. Rettie, H. C. Lee, L. G. Marshall, J.-F. Lin, C. Capan, J. Lindemuth, J. S. McCloy, J. Zhou, A. J. Bard, and C. B. Mullins, J. Am. Chem. Soc. **135**, 11389 (2013).

[15] H. Seo, Y. Ping, and G. Galli, Chem. Mater. **30**, 7793 (2018).

[16] T. W. Kim, Y. Ping, G. A. Galli, and K.-S. Choi, Nat. Commun. **6**, 8769 (2015).

[17] H. S. Park, K. E. Kweon, H. Ye, E. Paek, G. S. Hwang, and A. J. Bard, J. Phys. Chem. C **115**, 17870 (2011).

[18] S. Wang, P. Chen, Y. Bai, J.-H. Yun, G. Liu, and L. Wang, Adv. Mater. **30**, 1800486 (2018).

[19] S. Hammes-Schiffer and G. Galli, Nat. Energy **6**, 700 (2021).

[20] J. Hu, W. Chen, X. Zhao, H. Su, and Z. Chen, ACS Appl. Mater. Interfaces **10**, 5475 (2018).

[21] D. Li, Y. Liu, W. Shi, C. Shao, S. Wang, C. Ding, T. Liu, F. Fan, J. Shi, and C. Li, ACS Energy Lett. **4**, 825 (2019).

[22] H. Wu, R. Irani, K. Zhang, L. Jing, H. Dai, H. Y. Chung, F. F. Abdi, and Y. H. Ng, ACS Energy Lett. **6**, 3400 (2021).

[23] S. Lardhi, L. Cavallo, and M. Harb, J. Phys. Chem. Lett. **11**, 5497 (2020).

[24] A. Kahraman, M. B. Vishlaghi, I. Baylam, H. Ogasawara, A. Sennaroglu, and S. Kaya, J. Phys. Chem. Lett. **11**, 8758 (2020).

[25] P. Nikačević, F. S. Hegner, J. R. Galán-Mascarós, and N. López, ACS Catal. **11**, 13416 (2021).

[26] G.-L. Li, RSC Adv. **7**, 9130 (2017).

[27] W. Wang, P. J. Strohbeen, D. Lee, C. Zhou, J. K. Kawasaki, K.-S. Choi, M. Liu, and G. Galli, Chem. Mater. **32**, 2899 (2020).

[28] D. Li, W. Wang, D. Jiang, Y. Zheng, and X. Li, RSC Adv. **5**, 14374 (2015).

[29] R. Fernández-Climent, S. Giménez, and M. García-Tecedor, Sustainable Energy Fuels **4**, 5916 (2020).

[30] W. Luo, Z. Yang, Z. Li, J. Zhang, J. Liu, Z. Zhao, Z. Wang, S. Yan, T. Yu, and Z. Zou, Energy Environ. Sci. **4**, 4046 (2011).

[31] F. F. Abdi, L. Han, A. H. Smets, M. Zeman, B. Dam, and R. Van De Krol, Nat. Commun. **4**, 2195 (2013).

[32] Y. Liang, T. Tsubota, L. P. Mooij, and R. van de Krol, J. Phys. Chem. C **115**, 17594 (2011).

[33] J. K. Cooper, S. B. Scott, Y. Ling, J. Yang, S. Hao, Y. Li, F. M. Toma, M. Stutzmann, K. Lakshmi, and I. D. Sharp, Chem. Mater. **28**, 5761 (2016).

[34] N. Daelman, F. S. Hegner, M. Rellán-Piñeiro, M. Capdevila-Cortada, R. García-Muelas, and N. López, J. Chem. Phys. **152**, 050901 (2020).

[35] F. S. Hegner, D. Forrer, J. R. Galan-Mascaros, N. López, and A. Selloni, J. Phys. Chem. Lett. **10**, 6672 (2019).

[36] A. C. Ulpe, B. Anke, S. Berendts, M. Lerch, and T. Bredow, Solid State Sci. **75**, 39 (2018).

[37] J. Hu, H. He, X. Zhou, Z. Li, Q. Shen, W. Luo, A. Alsaedi, T. Hayat, Y. Zhou, and Z. Zou, Chem. Commun. **55**, 5635 (2019).

[38] W.-J. Yin, S.-H. Wei, M. M. Al-Jassim, J. Turner, and Y. Yan, Phys. Rev. B **83**, 155102 (2011).

[39] X. Zhao, J. Hu, X. Yao, S. Chen, and Z. Chen, ACS Appl. Energy Mater. **1**, 3410 (2018).

[40] T.-Y. Yang, H.-Y. Kang, U. Sim, Y.-J. Lee, J.-H. Lee, B. Koo, K. T. Nam, and Y.-C. Joo, Phys. Chem. Chem. Phys. **15**, 2117 (2013).

[41] T. Liu, M. Cui, and M. Dupuis, J. Phys. Chem. C **124**, 23038 (2020).

[42] S. Selim, E. Pastor, M. García-Tecedor, M. R. Morris, L. Francàs, M. Sachs, B. Moss, S. Corby, C. A. Mesa, S. Gimenez, A. Kafizas, A. A. Bakulin, and J. R. Durrant, J. Am. Chem. Soc. **141**, 18791 (2019).

[43] See Supplemental Material at http://link.aps.org/supplemental/10.1103/PhysRevMaterials.6.065402 for computational details (section I), band structures of the examined systems (section II), absolute defect state alignment analysis (section III), additional details of the computed overlap matrix (section IV), theoretical basis for the band contributions to the excitonic peaks (section V) and additional absorption data (section VI).

[44] J. P. Perdew, K. Burke, and M. Ernzerhof, Phys. Rev. Lett. **77**, 3865 (1996).

[45] P. Giannozzi, S. Baroni, N. Bonini, M. Calandra, R. Car, C. Cavazzoni, D. Ceresoli, G. L. Chiarotti, M. Cococcioni, I. Dabo *et al.*, J. Phys.: Condens. Matter **21**, 395502 (2009).

[46] J. Deslippe, G. Samsonidze, D. A. Strubbe, M. Jain, M. L. Cohen, and S. G. Louie, Comput. Phys. Commun. **183**, 1269 (2012).

[47] M. S. Hybertsen and S. G. Louie, Phys. Rev. B **34**, 5390 (1986).

[48] M. Rohlfing and S. G. Louie, Phys. Rev. Lett. **81**, 2312 (1998). Phys. Rev. B. **62**, 4927 (2000).

[49] D. Y. Qiu, F. H. da Jornada, and S. G. Louie, Phys. Rev. B **93**, 235435 (2016).

[50] N. Österbacka and J. Wiktor, J. Phys. Chem. C **125**, 1200 (2021).

[51] N. Österbacka, F. Ambrosio, and J. Wiktor, J. Phys. Chem. C **126**, 2960 (2022).

[52] S. Stoughton, M. Showak, Q. Mao, P. Koirala, D. A. Hillsberry, S. Sallis, L. F. Kourkoutis, K. Nguyen, L. F. J. Piper, D. A. Tenne, N. J. Podraza, D. A. Muller, C. Adamo, and D. G. Schlom, APL Mater. **1**, 042112 (2013).

[53] J. K. Cooper, S. Gul, F. M. Toma, L. Chen, Y.-S. Liu, J. Guo, J. W. Ager, J. Yano, and I. D. Sharp, J. Phys. Chem. C **119**, 2969 (2015).

[54] V. F. Kunzelmann, C.-M. Jiang, I. Ihrke, E. Sirotti, T. Rieth, A. Henning, J. Eichhorn, and I. D. Sharp, J. Mater. Chem. A (2022), doi:10.1039/d1ta10732a.

[55] D. Payne, M. Robinson, R. Egdell, A. Walsh, J. McNulty, K. Smith, and L. Piper, Appl. Phys. Lett. **98**, 212110 (2011).

Photocatalysis **Hot Paper**

Insights into the Role of Graphitic Carbon Nitride as a Photobase in Proton-Coupled Electron Transfer in (sp³)C–H Oxygenation of Oxazolidinones

Alexey Galushchinskiy⁺, Yajun Zou⁺, Jokotadeola Odutola, Pavle Nikačević, Jian-Wen Shi, Nikolai Tkachenko, Núria López, Pau Farràs, and Oleksandr Savateev*

Abstract: Graphitic carbon nitride (g-CN) is a transition metal free semiconductor that mediates a variety of photocatalytic reactions. Although photoinduced electron transfer is often postulated in the mechanism, proton-coupled electron transfer (PCET) is a more favorable pathway for substrates possessing X–H bonds. Upon excitation of an (sp²)N-rich structure of g-CN with visible light, it behaves as a photobase—it undergoes reductive quenching accompanied by abstraction of a proton from a substrate. The results of modeling allowed us to identify active sites for PCET—the 'triangular pockets' on the edge facets of g-CN. We employ excited state PCET from the substrate to g-CN to selectively cleavethe *endo*-(sp³)C–H bond in oxazolidine-2-ones followed by trapping the radical with O_2. This reaction affords 1,3-oxazolidine-2,4-diones. Measurement of the apparent pK_a value and modeling suggest that g-CN excited state can cleave X–H bonds that are characterized by bond dissociation free energy (BDFE) $\approx 100\ kcal\,mol^{-1}$.

Introduction

Oxidation and reduction of organic molecules based on single electron transfer (SET) can be designed by employing excited states of organic molecules,[1] transition metal complexes[2] and semiconductors,[3] which are collectively called 'photocatalysts'. SET reactions are energy demanding because they produce charged radical intermediates–cations and anions,[1] and require the excited state of the photocatalyst to be sufficiently oxidative and/or reductive. Redox reactions become facile when coupled with transfer of a proton—proton-coupled electron transfer (PCET, Figure 1a).[4] Unlike radical ions formed by SET, the products of PCET are electrically neutral radicals. The nature of PCET process makes the process more dependent on thermodynamic factors and kinetic behavior of a proton, including acid-base interaction between the substrate and

the catalyst and tunneling effects, rather than on pure electrochemistry to lower the energy barriers for transition states.[5,6] In fact, the activation energy is sufficiently low to drive efficient enzyme-catalyzed biochemical redox processes at low temperature.[7,8]

In the last decade, effortless and selective modification of X–H sites in organic molecules by means of PCET driven by photoredox catalysis has attracted close attention.[9–11] By combining a sufficiently oxidative excited state of a molecular sensitizer, such as an Ir-polypyridine complex, with a Brønsted base, it is possible to cleave relatively strong N–H and O–H bonds in amides and phenols to generate alkoxy and amidyl radicals respectively via *oxidative* multisite PCET.[12,13] In water, a base/oxidant couple delivers the required amount of energy to be used for homolytic X–H bond cleavage in a substrate, formal bond dissociation free energy (FBDFE, $kcal\,mol^{-1}$), which is defined by the pK_a of

[*] A. Galushchinskiy,⁺ Dr. Y. Zou,⁺ Dr. O. Savateev
Department of Colloid Chemistry, Max Planck Institute of Colloids and Interfaces
Am Mühlenberg 1, 14476 Potsdam (Germany)
E-mail: oleksandr.savatieiev@mpikg.mpg.de

Dr. Y. Zou,⁺ Dr. J.-W. Shi
State Key Laboratory of Electrical Insulation and Power Equipment, Center of Nanomaterials for Renewable Energy, School of Electrical Engineering, Xi'an Jiaotong University
Xi'an, 710049 (China)

J. Odutola, Prof. N. Tkachenko
Photonic compounds and Nanomaterials, Chemistry and Advanced material group, Tampere University (Finland)

P. Nikačević, Prof. N. López
Institut Català d'Investigació Química (ICIQ-CERCA), The Barcelona Institute of Science and Technology (BIST)
Avda. Països Catalans, 16, 43007 Tarragona (Spain)

P. Nikačević
Universitat Rovila i Virgili (URV)
Carrer de l'Escorxador, s/n, 43003 Tarragona (Spain)

Dr. P. Farràs
School of Biological and Chemical Sciences, Ryan Institute, University of Galway
Galway H91 CF50 (Ireland)

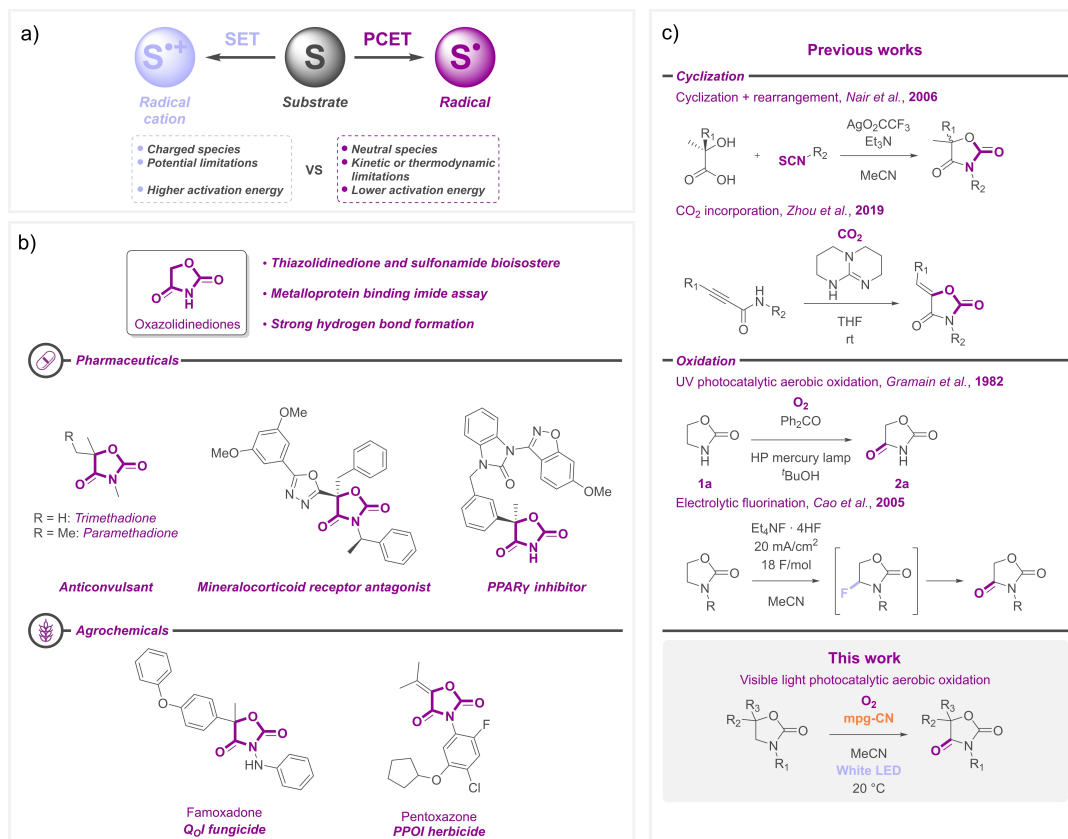[⁺] These authors contributed equally to this work.

Figure 1. Concept of this article. a) Intermediates and features of oxidative SET and PCET catalytic pathways. b) Examples of biological activity of oxazolidinedione-containing molecules. c) Formation of 1,3-oxazolidine-2,4-diones reported in literature and in this work.

the acid conjugated to the Brønsted base and reduction potential of the sensitizer excited state (E^*_{red}, V vs. NHE):[4]

$$FBDFE = 1.37pKa + 23.06E^*_{red} + 57.6 \qquad (1)$$

On the other hand, due to the presence of functional groups capable of acid-base interactions with a substrate molecule, the excited state of organic dyes, such as Eosin Y,[14] acts as hydrogen atom transfer (HAT) agent itself without adding an auxiliary base. Furthermore, inorganic semiconductors and oxoclusters are capable of engaging in PCET upon excitation with light.[15,16] The structure of heptazine-based graphitic carbon nitride (g-CN) is rich in pyridinic-like nitrogen centers.[17] Therefore, its excited state enables PCET from proton donors.[18–20] g-CN materials were postulated to mediate a number of reactions via PCET either explicitly or implicitly,[21,22] also in combination with organic bases. Related to conversion of organic molecules, cyanamide-modified carbon nitride with tributylmethylammonium dibutylphosphate as a base generates *N*-centered radical from carbamate, which undergoes intra-

molecular Giese addition to an allylic moiety.[23] Mesoporous g-CN (mpg-CN hereafter) in combination with Br• produces an alkyl radical from *N,N*-dialkylformamide and enables the subsequent C–C cross coupling with arylhalides.[24] In combination with *N*-hydroxyphthalimide (NHPI), g-CN is used for oxygenation of allylic C–H bonds.[25] Our own results strongly suggest that ionic carbon nitride, potassium poly(heptazine imide) (K-PHI), is capable of abstracting electrons and protons from amines and store them as separated charges within the material.[26,27] The photo-charged K-PHI is then used in *reductive* PCET to overcome high stability of otherwise non-reducible aryl halides and produce parent Ar–H compounds.[27]

Although the pK_a of protonated mpg-CN has not been reported, considering its nitrogen-rich structure, the valence band potential (E_{VB}) of +1.45 V vs. NHE and equation (1), we expect its excited state to be able to cleave C–H bonds, even those with moderate and relatively high BDFE. In particular, mpg-CN can oxidize *N*-alkyl amides, in which C–H BDFE is ≈89–94 kcal mol^{-1},[24] to their corresponding imides. An example of such a valuable imide moiety is 1,3-

Research Articles

oxazolidine-2,4-diones (Figure 1b, see discussion in the Supporting Information). Despite their high demand, the synthesis of 1,3-oxazolidine-2,4-diones remains challenging and inconvenient (Figure 1c). While the formation of 5-ylidene-substituted derivatives is achieved by base-catalyzed ring formation of propargylic amides with carbon dioxide,[28] regular oxazolidinediones usually require cyclization of a carbonate synthon, such as iso(thio)cyanates and α-hydroxycarboxylates,[29] which are not as readily available. An easier approach would be the oxidation of 1,3-oxazolidine-2-ones, which are either commercially available or conveniently prepared from the corresponding vicinal aminoalcohols, or by the reaction between oxiranes and isocyanates.[30] However, this pathway is not as easily achievable since oxazolidinones are quite stable against oxidation. A peak potential $E_p > 1.67–2.72$ V vs. SCE was reported,[31] requiring strong oxidizers. Indeed, there are only two publications on successful oxidation of oxazolidinones at the 4th position of the ring. In 1982, Gramain et al. reported the photocatalytic reaction of oxazolidin-2-one **1a** with oxygen under irradiation with a high pressure mercury lamp using benzophenone as a catalyst over the course of 68 hours at room temperature.[32] In 2005, Gao et al. achieved electrolytic partial fluorination of *N*-substituted oxazolidinones, where non-acyl substituents yielded unstable 4-fluoro derivatives, which were then hydrolyzed and oxidized further to diones.[31] These methods involve rather harsh conditions, such as strong UV irradiation or corrosive acidic fluoride solutions.

Herein, we choose the synthesis of 1,3-oxazolidine-2,4-diones from the corresponding oxazolidinones to study PCET with mpg-CN upon band gap excitation. Due to dual function, organobase and a sensitizer, mpg-CN excited state cleaves selectively an endocyclic C–H bond in a β-position to the amide nitrogen followed by trapping of the intermediary C-centered radical with O₂. Experimental data as well as DFT simulations indicate that combination of mpg-CN surface basic character and the potential of the valence band allows to cleave X–H bonds with ≈100 kcal mol⁻¹.
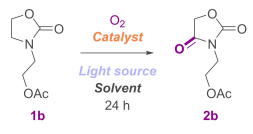
Results and Discussion

Compound **1b** possesses *endo*- and *exo*-CH₂-groups. Therefore, it is a convenient platform to investigate selectivity of oxygenation. Secondary amides are usually oxidized more easily compared to tertiary amides due to the possibility of proton abstraction or its migration to oxygen.[33] In fact, some synthetic procedures rely mechanistically on the pathway of *N*-acylimine formation during oxidation.[34] Therefore, on the one hand, oxygenation of tertiary amides represents a synthetic challenge; on the other hand, the goal of the research is to establish a synthetic procedure suitable both for *N*-substituted and unsubstituted substrates.

The first round of screening involved testing of a series of heterogeneous carbon nitride photocatalysts prepared in our lab: mpg-CN,[35] potassium poly(heptazine imide) (K-PHI)[36] and sodium poly(heptazine imide) (Na-PHI).[37] The reaction was carried out under an oxygen atmosphere in

acetonitrile under blue light irradiation (465 ± 10 nm). The highest yield of oxazolidinedione **2b** (25.5 % by qNMR with incomplete conversion of **1b**) was obtained with the mpg-CN photocatalyst (Table 1). mpg-CN also produces **2b** after three rounds of reuse (see Supporting Information for details).

K-PHI and Na-PHI gave **2b** with lower yields likely due to moderate surface area of a few tens of m² g⁻¹.[37,38] Molecular sensitizers, such as Riboflavin tetraacetate, Rhodamine B and Eosin Y gave **2b**, but with much lower yields, which nevertheless could be explained by the presence of carbonyl and/or carboxyl functionalities in their structure, which could enable PCET from **1b** in the absence of the external base. Indeed, the excited state of Eosin Y was identified as a direct HAT agent.[14] Although benzophenone was reported earlier to oxidize **1a**, likely due to interaction of amide NH with the photocatalyst C=O group, it failed to convert **1b**.[32] The excited states of Ir- and Ru-complexes are powerful SET agents, but in the absence of exogeneous base capable of engaging in multisite PCET they also failed to produce **2b**.[5] CdS and WO₃ did not give **2b** in significant quantity likely due to a lack of sufficient number of basic

Table 1: Screening for the optimal reaction conditions of oxazolidinone oxidation.[a]

Catalyst[b]		Light source[c]		Solvent[d]	
mpg-CN	25.5	UV LED (365 nm)	70.0	CH₃CN	55.5
K-PHI	21.0	Purple LED (410 nm)	14.5	MeOH	2.0
Na-PHI	7.5	Blue LED (465 nm)	25.5	EtOH	1.5
RFTA	1.0	Green LED (535 nm)	5.0	ⁿBuOH	5.0
Ir(ppy)₃	0.2	Red LED (625 nm)	0.5	ᵗBuOH	37.5
Ru(bpy)₃Cl₂ · 6H₂O	0.4	White LED	55.5	1,4-dioxane	1.5
Benzophenone	0.2	*No light*	0	Hexane	5.5
Methylene blue	0.2			Toluene	26.5
Rhodamine B	2.4			CHCl₃	13.5
Eosin Y	2.2			CH₂Cl₂	37.0
CdS	0.4			H₂O	22.5
WO₃	0.1			MeNO₂	45.0
mpg-CN (Ar, control)	2.8			DMSO	0
No catalyst	0[e]			DMF	0
No catalyst	10[f]				

[a] Reaction conditions: 0.05 mmol of **1b**, O₂ (1 bar), 2 mL of solvent (0.025 M), LED irradiation, catalyst: 5 mg (for heterogeneous, 100 g mol⁻¹), 5 mol.% (for homogeneous); yield values were obtained by quantitative ¹H NMR using 1,3,5-trimethoxybenzene as an internal standard. [b] the catalysts were screened using an optimal light source with respect to their absorption maxima, see Supporting Information for details; acetonitrile was used as a solvent. RFTA—riboflavin tetraacetate. [c] mpg-CN was used as a catalyst with acetonitrile as a solvent. [d] mpg-CN was used as a catalyst under white LED irradiation. [e] blue LED (465 nm). [f] UV LED (365 nm). Photon fluxes of LED sources: UV LED (365 nm) 0.2 µmol cm⁻² s⁻¹; purple LED (410 nm) 0.4 µmol cm⁻² s⁻¹; blue LED (465 nm) 0.8 µmol cm⁻² s⁻¹; green LED (535 nm) 0.4 µmol cm⁻² s⁻¹; red LED (625 nm) 1.6 µmol cm⁻² s⁻¹.

Research Articles

sites on the surface that are capable to participate in the PCET. In Table 1, where the yield of **2b** is low, conversion of **1b** is also close to zero. Control experiment performed under Ar confirmed that oxygen is primarily transferred from air. The reaction did not proceed in the absence of mpg-CN and irradiation at 465 nm. However, irradiation at 365 nm in the absence of mpg-CN gave **2b** with 10 % yield (photochemical process). Illumination with white LED increased the yield of **2b** to 55.5 % after 24 h irradiation time, which is due to a substantial contribution of 450 nm photons in the LED emission spectrum (Figure S28). mpg-CN produced **2b** with the yield 70 % when excited at 365 nm. Assuming that 10 % of the yield is due to photochemical conversion of **1b** (without mpg-CN), the remaining 60 % constitutes the photocatalytic part of the yield, which is close to 56 % obtained upon mpg-CN excitation with white LED. Compared to other solvents (see Supporting Information), due to polarity, chemical stability and lack of reactive C–H bonds, acetonitrile is the most suitable solvent to perform oxygenation of oxazolidinone **1b** under white LED illumination.

With the established reaction conditions using mpg-CN as the catalyst and acetonitrile as solvent, the batch experiment was scaled up to 1.25 mmol of substrate, and the reaction was performed with a series of oxazolidinones **1a–o** (Figure 2). Due to low cost of UV photons, oxygenation of *N*-aryl substituted oxazolidinones, such as **1e,f**, may in principle be conducted without mpg-CN.[39] However, our goal was to *i*) establish a general protocol applicable for a large scope of substrates, i.e., those with aromatic groups as chromophores and without chromophores, and *ii*) investigate the role of mpg-CN as the photobase. Therefore, we opted for white LED without contribution of UV photons to avoid direct excitation of the substrates. The scope demonstrated almost quantitative yield for unsubstituted oxazolidinone **1a** and moderate to good yields for *N*-substituted derivatives **1b–k** with few exceptions. Electron rich groups, such as the 4-methoxyphenyl fragment in **1h** showed typical behavior of 4-methoxyphenyl (PMP) protecting group when attached to amine or amide functionality[40]—it is readily cleaved under the photocatalytic conditions. The product of **1h** oxygenation is a parent oxazolidinedione **2a**, while only a small amount of the target product **2h** was observed. In turn, substrates **1i** and **1j** bearing *O*- and *N*-benzyl fragments gave the corresponding benzoyl-substituted oxazolidinediones (**2ia** and **2ja**, respectively) as major products with minimal to no yield of the target product of ring oxygenation only, such as **2ic**. Additionally, a product of further oxidation **2jc** was observed, and benzoic acid, the product of benzoyl cleavage, was isolated. In case of 5,5-dimethylated substrates **1l–n**, the yields decreased significantly compared to the derivatives free of the substituent in the 5th position. The selectivity of the process is also lower due to competitive oxygenation of *endo*- and *exo*-CH$_2$-groups in **1m**. Earlier, it was reported that Br• radical abstracts hydrogen in cyclic amides both from *endo*- and *exo*-CH$_2$-group with a higher preference for the former.[24] In our work, mpg-CN selectively abstracts the hydrogen atom from the *exo*-CH$_2$-group in all cases except for **1m**. However, when the

substrate contains benzylic CH$_2$, the PCET at this site becomes facile, as illustrated by oxygenation of **1i** and **1j**. Introduction of a bulky and electron donating phenyl substituent into the 5th position, compound **1o**, reduced selectivity by promoting ring decomposition side reactions. Benzoic acid was obtained as the main product in this case.

Among non-photocatalytic oxidation procedures (Figure 3, see Supporting Information for procedures and references), only catalytic RuO$_4$/NaIO$_4$ process gave reasonable quantity of **2k** on comparable scale while still being inferior to our photocatalytic approach in terms of both yield and synthetic simplicity—ruthenium tetroxide is known to be a severely toxic reagent incompatible with a number of functional groups.[41]

The information provided by conditions screening and scope studies' results gave us initial hints on the exact reaction mechanism. There are three possible pathways (Figure 4): 1) reaction of a substrate with singlet oxygen, 2) direct oxidation of a substrate via photoinduced electron transfer (PET), and 3) generation of C-centered radical via PCET. In our case, the catalytic system does not include a sacrificial electron donor which could quench the photogenerated hole and therefore promote oxygen reduction to superoxide radical. Therefore, the only possibility for oxygen activation is formation of singlet oxygen by the energy transfer (EnT) pathway from the catalyst. Indeed, sensitization of $^1O_2$ by K-PHI and mpg-CN was reported.[42]

However, screening of other well-known efficient singlet oxygen generating catalysts, such as methylene blue, Eosin Y and Rhodamine B,[43] gave minimal amounts of the target oxazolidinedione, which serves as an evidence for exclusion of this pathway from further investigation. Additionally, the reaction was carried under an oxygen pressure ranging from 1 to 4 bars (Figure 5a). We observed negligible influence of oxygen concentration on the product yield, which further disproves the involvement of active oxygen species in the reaction mechanism. Nonetheless, $^1O_2$ may still be responsible for side reactions occurring in the system, since the conversion increases at a higher oxygen pressure (Figure 5a). Another hint for direct interaction between the substrate and the catalyst is the behavior of 5-substituted oxazolidinones, such as **1l–m**, in the reaction. The distribution and yield of products, especially clearly seen for **1m**, implies the existence of a certain steric hindrance factor, which decreases reaction efficiency. This factor should be negligible if a small molecule, $^1O_2$, were to attack the substrate. To prove or disprove the involvement of PET, cyclic voltammetry experiments were performed for substrates **1b**, **1d**, **1e** and **1h** to evaluate their oxidation potentials (Figure 5b, S5). An excellent agreement between the oxidation potential of **1d**, +1.58 V vs. SCE (at half peak), and that reported earlier, +1.67 V vs. SCE (peak),[31] was found. Overall, the four compounds demonstrate higher oxidation potentials ($\geq +1.26$ V vs. SCE) than the potential of the photogenerated hole in mpg-CN (+1.20 V vs. SCE),[35] which unambiguously indicates that PET from oxazolidinones to mpg-CN is thermodynamically challenging. This fact excludes the second pathway and makes PCET the most likely mechanism of the reaction. Likewise, the
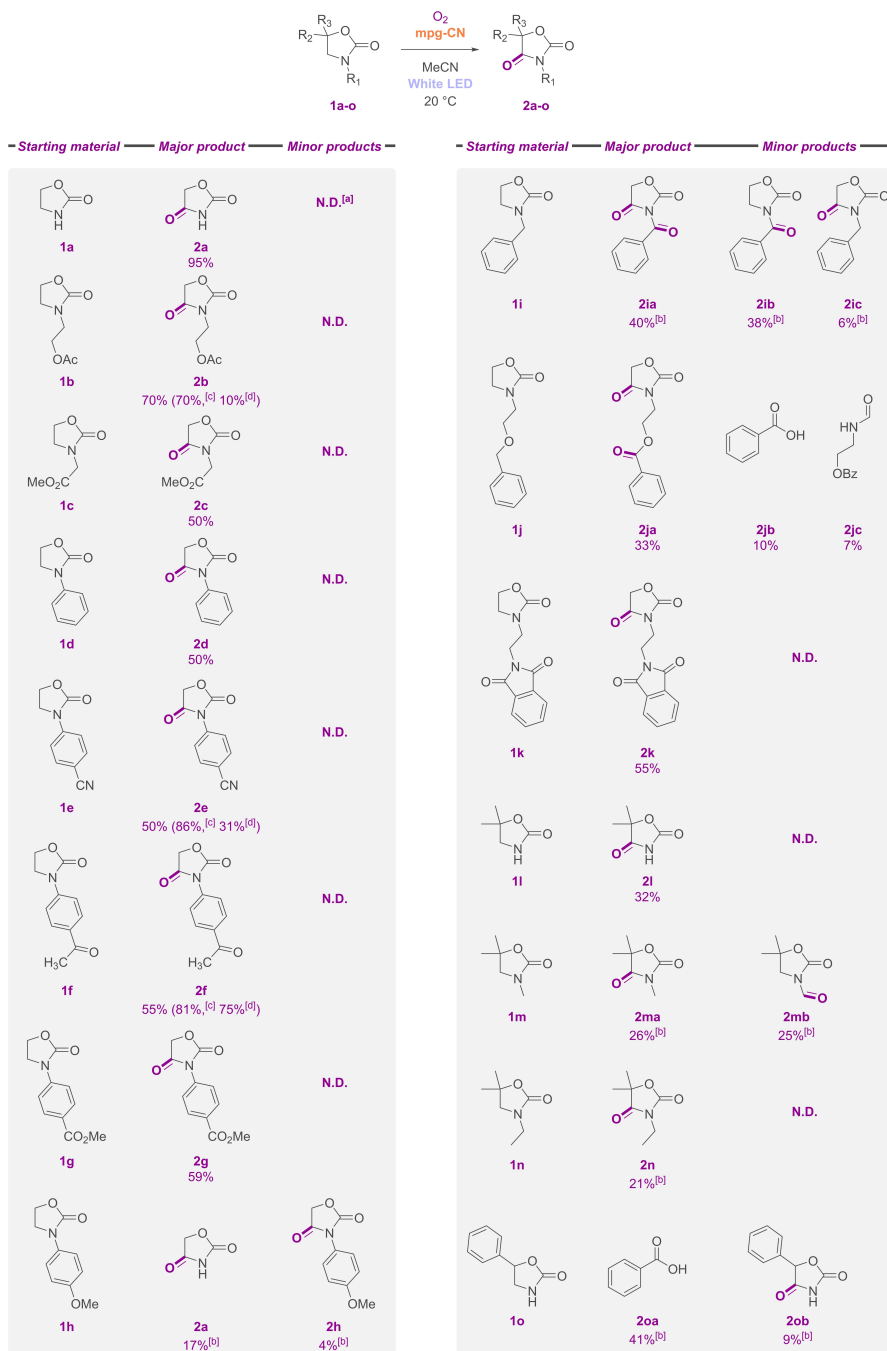
Figure 2. Scope of oxazolidinones **1a–o** used for scaled-up oxidation. Reaction conditions: **1** (1.25 mmol), O$_2$ (1 bar), acetonitrile (50 mL), mpg-CN (125 mg), white LED (4×50 W modules), 20 C. The reaction was carried out until complete consumption of a starting material is achieved (24–72 h, monitored by ^{1}H NMR). Percent values indicate isolated yields unless stated otherwise. [a] "N.D." indicates absence of data for side products (either their formation was not observed by ^{1}H NMR or reaction mixture was too complex to distinguish minor components). [b] quantitative ^{1}H NMR yields using 1,3,5-trimethoxybenzene as an internal standard. [c] **1** (0.05 mmol), UV LED (365 nm). [d] **1** (0.05 mmol), UV LED (365 nm) without mpg-CN.

Research Articles

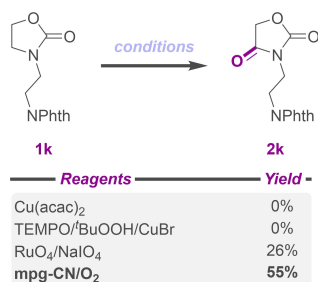*Angewandte Chemie International Edition*

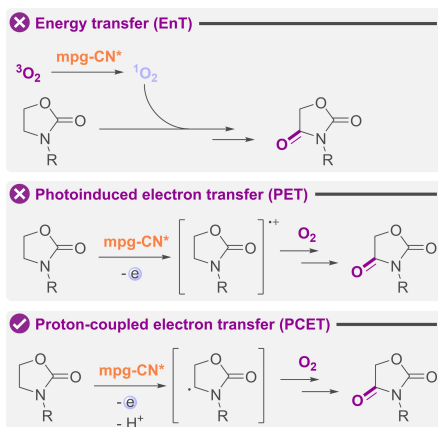**Figure 3.** Comparison of the isolated yield of **2k** using different oxidation procedures.

Figure 4. Simplified pathways of possible oxazolidinone oxidation mechanisms. Further steps regarding interaction with oxygen are omitted for clarity.

photocatalytic oxidation of oxazolidinone **1a** along with some lactams and hydantoins using benzophenone under UV is claimed to proceed via transfer of both proton and electron (Figure 1c).[32,44] We determined the apparent quantum yield (AQY) for oxidation of **1b** to be 0.026% at 465 nm and 0.065% at 365 nm excluding free-radical chain mechanism. Higher AQY obtained upon reaction mixture irradiation with UV light is explained by a higher extinction coefficient of mpg-CN.

From time resolved photoluminescence (tr-PL) spectroscopic measurements we conclude that while most of mpg-CN excited states decay rapidly, a small fraction survives for more than 400 μs after excitation (Figure 5c). In tr-PL spectra, fluorescence peak is observed at ≈472 nm (Figure 5d). The phosphorescence peak of lower intensity at ≈540 nm was measured by gating the emission from 40–100 μs with the pulsed xenon lamp. Singlet–triplet energy gap (ΔE_{ST}), determined as a difference between steady-state fluorescence and tr-PL maxima in Figure 5d, is 0.33 eV, which is consistent with the one reported earlier for K-PHI.[42,45] A relatively low ΔE_{ST} indicates that the triplet

excited state has an energy comparable to the singlet and, in combination with the lifetime exceeding the μs range, we conclude that it is beneficial for the cleavage of C–H bond in oxazolidinones. The presence of the substrate **1b** and/or O_2 does not quench neither the singlet nor the triplet excited state of mpg-CN (Supporting Information Discussion 1). Transient absorption spectra of mpg-CN in MeCN recorded under anaerobic conditions are shown in Figure 5e. A few picoseconds after excitation, there was a strong negative signal between 500–750 nm which can be attributed to the ground state bleaching, and a positive signal between 850–1280 nm which can be attributed to the photogenerated excited state of mpg-CN. The crossing point was ≈800 nm. At a delay longer than 2 ns, the intensity of the positive signal reduced at a faster rate than the negative signal and the crossing point is redshifted to ≈1200 nm. On the nanosecond time scale, the behavior of mpg-CN excited state is similar to that of K-PHI[42] as indicated by the traces at 605, 960 and 1170 nm (Figure 5f). Similar to tr-PL study, TAS did not reveal differences in mpg-CN excited states' electronic signatures and dynamics, both singlet and triplet, on presence or absence of O_2 and **1b** (Supporting Information Discussion 1). We explain these observations by the low, 0.065%, AQY of the studied reaction and the sensitivity of the instruments not high enough to detect this small quenching of mpg-CN excited states.

The reaction profile of **1b** oxidation by mpg-CN was rationalized by Density Functional Theory (DFT), as implemented in the Vienna Ab initio Simulation Package (VASP).[46] The carbon nitride was modeled as a six-heptazine-layer wide 2D surface with NH, NH_2, and OH groups at the termination sites,[24] and the reaction energy profile was obtained at the PBE level (Figure 6).[47]

All modeled structures were uploaded to the ioChem-BD database.[48] As mpg-CN is excited by light, the electrons from the valence band cross the band gap and enter the conduction band. Taking into account results of electron paramagnetic resonance spectroscopy study, hole and electron are separated by four heptazine units.[49] The calculated gap value of 2.6 eV (obtained with HSE06 a hybrid functional)[50] matches the experimental one, 2.7 eV, and explains the fact that among quasi-monochromatic light sources the reaction proceeds the most efficiently under the UV and blue LEDs (Table 1). Density of states (DOS) plot also confirms our CV results and demonstrates that highest occupied molecular orbital (HOMO) of oxazolidinone **1b** is significantly lower than the valence band of mpg-CN, indicating the impossibility of PET when it is not coupled with a proton transfer. As the oxazolidinone **1b** is oxidized, an electron and a proton are transferred from to the carbon nitride scaffold (PCET). This results in the formation of the oxazolidinone **1b** radical, **Int1**, as well as the hydrogenated carbon nitride radical [mpg-CN+H]•. Whether the [mpg-CN+H]• radical is formed in the excited state or directly in the ground state has little effect on the reaction energetics, as its Fermi level is close to the conduction band due to the extra electron present in the system (Figure S11). To assess the position of the additional H atom in the [mpg-CN+H]• system, an extensive search for the different positions was
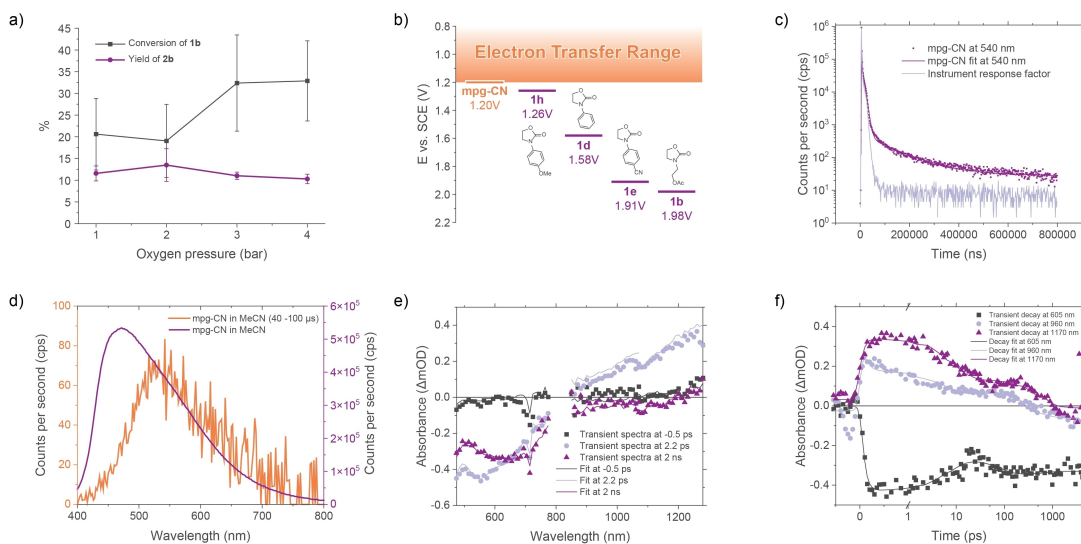
Research Articles

Angewandte Chemie International Edition

Figure 5. Investigation of oxazolidinone photocatalytic oxidation mechanism. a) Yield of **2b** and conversion of **1b** in the photocatalytic reaction performed under different oxygen pressures. Error bars represent average ± std (*n* = 3). b) mpg-CN valence band potential and half-peak oxidation potentials of **1b**, **1d**, **1e** and **1h** with respect to SCE. Orange gradient band indicates the upper limit of potential range, where SET from a substrate to mpg-CN excited state is thermodynamically feasible. c) Tr-PL decay of mpg-CN and the IRF. d) Steady-state fluorescence (magenta) and tr-PL (orange) spectra of mpg-CN, the latter was measured by gating the emission from 40–100 μs with the pulsed xenon lamp. e) Transient absorption spectra of mpg-CN in MeCN under N₂. The spectra are cut off around 800 nm due to fundamental of the laser. f) Transient decay of mpg-CN in MeCN under N₂. The first picosecond is in linear scale while the rest has a logarithmic scale.

performed. We found that depending on the location of the hydrogen atom, the relative energy of the system spans over 3 eV (Figure S7). The lowest energy position of **Int1** (ΔE = +1.4 eV) corresponds to the structure in which hydrogen atom is located inside the 'triangular pocket' and attached to the nitrogen atom of the heptazine unit. In the following step, the radical **Int1** traps oxygen molecule with the formation of a peroxo radical **Int2** (ΔE = −1.3 eV). An alternative mechanistic pathway, according to which O₂ molecule captures the hydrogen atom from [mpg-CN+H]• instead and forms the HO₂• is by +0.4 eV uphill with the respect to **Int1** (Figure S9). Therefore, it is thermodynamically less favourable and can be discarded. The peroxo radical **Int2** recovers H-atom from [mpg-CN+H]• and creates a hydroperoxide intermediate **Int3** (ΔE = −1.1 eV), from which a water molecule is eliminated, and **2b** is produced (ΔE = −3.0 eV).

In the absence of photoexcitation, the H-atom transfer from **1b** to carbon nitride would be the only non-spontaneous step. To make sure that the energy of this step is computed accurately, we also simulated the H-atom transfer to another proposed model of polymeric carbon nitride—melon-CN.[51] The melon model gave energies for the transfer within 0.3 eV of our mpg-CN model (Table S3), justifying the use of the mpg-CN model. We then proceeded to compute a more accurate electronic energy change for the H-atom transfer to mpg-CN using the HSE06 hybrid functional. After including the vibrational frequencies of adsorbates and gas-phase entropies, we determined the Gibbs

free energy change of +1.5 eV for this step. This value is significantly smaller compared to *endo*-C–H BDFE in β-position to amide nitrogen in **1b** of 4.03 eV or 92.9 kcal mol⁻¹ in vacuum. In other words, the intrinsically highly exergonic homolytic C–H bond cleavage becomes more facile when H-atom is transferred to mpg-CN.

In order to assess the range of X–H bonds that mpg-CN excited state may cleave homolytically, we measured the pK_a value of protonated mpg-CN in water, which is 6.60 ± 0.3. The heterogeneous material contains myriads of protonation sites that are different in their basicity. The obtained value should be considered as 'apparent' or 'average' pK_a value. Due to mutual electron-withdrawing effect of (sp²)N atoms, the pK_a of bare heptazinium cation must be close to zero or even negative. However, the measured pK_a describes protonated mpg-CN as a weak acid. Such a discrepancy might be explained by the mutual effect of adjacent heptazine units that form a 'triangular pocket' and thus stabilize a proton similarly to a proton sponge. Using the obtained pK_a value and E_{VB} of +1.45 V vs. NHE,[35] according to the equation (1) we determine FBDFE to be 100 ± 0.4 kcal mol⁻¹ or 4.32 ± 0.02 eV. In other words, upon mpg-CN band gap excitation, it is able to cleave X–H bonds with BDFE < 100 kcal mol⁻¹ (Supporting Information Discussion 4).

Upon band gap excitation, carbon nitrides with even more positive potential of the valence band, such as that in K-PHI (+2.2 V vs. NHE),[52] and higher surface basicity (pK_a of the conjugated acid > 6.6), can cleave even stronger
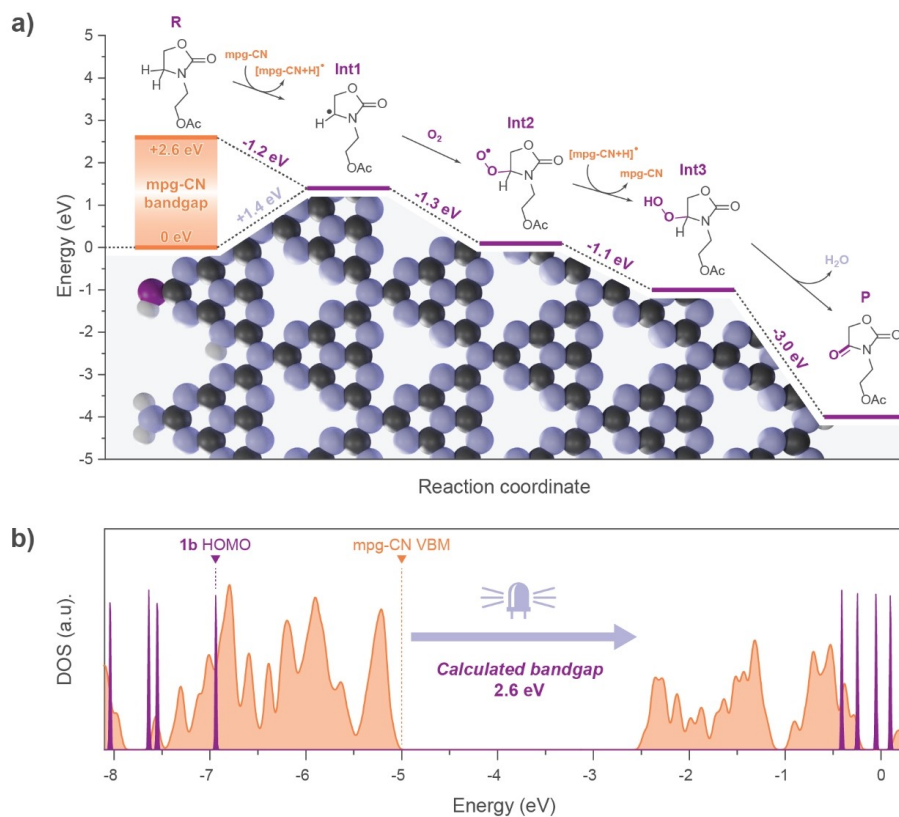
Figure 6. DFT results. a) Proposed mechanism for oxazolidinone **1b** oxidation at mpg-CN with potential energy differences of the respective intermediates. The mpg-CN + H model used in DFT calculations is shown in the lower part of the figure. The model contains NH, NH$_2$, and OH groups at the surface terminations, which is consistent with the experimental data.[24] b) DOS for mpg-CN (orange) and oxazolidinone **1b** (purple). The DFT energy scale corresponds to the energies obtained directly from the VASP output files. The correspondence between the two systems was confirmed by aligning the energies of oxygen 2 s electrons between these systems (not shown in the figure).

polar X–H bonds. By substituting pK_a and E_{VB} with these values in equation (1), we deduce that FBDFE >117.4 kcal mol^{-1}, which is close to O–H BDFE in water, 123 kcal mol^{-1}.[4] Indeed, K-PHI liberates O$_2$ from water upon illumination, when sacrificial electron acceptor effectively removes the photogenerated electrons from the conduction band.[38] In this work, K-PHI also demonstrates comparable and high activity in oxidation of **1b** (Table 1).

There are already many examples of photocatalytic reactions enabled by g-CNs that proceed via cleavage of C–H, O–H and N–H bonds with BDFE 80–123 kcal mol^{-1} (Table S4).[22,23,38,52–54] A basic environment is often required to facilitate cleavage of strong X–H bonds.[21,23] However, even without adding a base, mpg-CN, K-PHI and Na-PHI photocatalyze to some extent cleavage of O–H and N–H bonds in carboxylic acids and carbamates. A combination of the more basic character of the photocatalyst surface due to the presence of deprotonated imide moieties and the 0.7 V more positive potential of the valence band in ionic g-CNs compared to covalent g-CN is responsible for higher yields

in oxidation of toluene to dibenzyldisulfide[52] and Minisci coupling.[22] Overall, the results summarized in Table S4 support our conclusions that g-CN materials serve as photobases to mediate an oxidative ES-PCET. Nevertheless, exogenous base is beneficial to suppress the transfer of a proton back to the intermediary radical and thus achieve higher yields in a chosen reaction.

As inferred from equation (1), high FBDFE required for the cleavage of strong X–H bonds may in principle be achieved by combining in one pot a superbase (large pK_a) and a strong oxidant (highly positive E_{red}). In practice, FBDFE values for base/oxidant couples are limited to 71–98 kcal mol^{-1}, as the superbases are electron rich and would simply react with strong oxidants.[55] Except for the pendant NH- and NH$_2$-groups, carbon nitrides are free of X–H bonds, which explains the high chemical stability of this class of photocatalysts. Overall, increasing the surface basicity, e.g., by deprotonated cyanamide moieties[56,57] and shifting E_{VB} to more positive values by incorporating electron-accepting moieties, are two strategies that may be employed

Research Articles

to design and synthesize semiconductor materials to perform X–H functionalization of organic compounds via excited state PCET.

Conclusion

We established an optimal photocatalytic method to convert oxazolidinones to their respective 2,4-diones using an inexpensive heterogeneous mpg-CN photocatalyst and oxygen gas as an oxidant on a mmol batch scale. The heterogeneous organophotocatalytic approach is superior compared to homogeneous photoredox catalysis and non-photocatalytic systems, such as $RuO_4/NaIO_4$, in terms of yield and convenience of handling the reagents. A number of evidences, including insensitivity of the product yield to O_2 pressure, high oxidation potential of oxazolidinones, $+1.26...1.98$ V vs. SCE and time-resolved spectroscopic data, unambiguously exclude SET and EnT pathways. DFT simulations suggest that the initial step, (sp^3)C–H bond cleavage in oxazolidinone via PCET, is uphill. mpg-CN as the organophotocatalyst makes it possible to overcome the energy barrier by converting the energy of the electromagnetic radiation into the driving force for PCET.

Conflict of Interest

A patent WO/2019/081036 has been filed by Max Planck Gesellschaft zur Förderung der Wissenschaften E.V. in which O.S. is listed as a co-author.

Data Availability Statement

The data that support the findings of this study are available from the corresponding author upon reasonable request. The computed structures can be retrieved in the ioChem-BD database [48].

[1] N. A. Romero, D. A. Nicewicz, *Chem. Rev.* **2016**, *116*, 10075–10166.

[2] C. K. Prier, D. A. Rankic, D. W. C. MacMillan, *Chem. Rev.* **2013**, *113*, 5322–5363.

[3] H. Kisch, *Angew. Chem. Int. Ed.* **2013**, *52*, 812–847; *Angew. Chem.* **2013**, *125*, 842–879.

[4] J. J. Warren, T. A. Tronic, J. M. Mayer, *Chem. Rev.* **2010**, *110*, 6961–7001.

[5] E. C. Gentry, R. R. Knowles, *Acc. Chem. Res.* **2016**, *49*, 1546–1556.

[6] C. Costentin, M. Robert, J.-M. Savéant, *Acc. Chem. Res.* **2010**, *43*, 1019–1029.

[7] R. Tyburski, T. Liu, S. D. Glover, L. Hammarstrom, *J. Am. Chem. Soc.* **2021**, *143*, 560–576.

[8] J. Bonin, M. Robert, *Photochem. Photobiol.* **2011**, *87*, 1190–1203.

[9] L. Capaldo, D. Ravelli, *Eur. J. Org. Chem.* **2017**, 2056–2071.

[10] L. Capaldo, D. Ravelli, M. Fagnoni, *Chem. Rev.* **2022**, *122*, 1875–1924.

[11] P. R. D. Murray, J. H. Cox, N. D. Chiappini, C. B. Roos, E. A. McLoughlin, B. G. Hejna, S. T. Nguyen, H. H. Ripberger, J. M. Ganley, E. Tsui, N. Y. Shin, B. Koronkiewicz, G. Qiu, R. R. Knowles, *Chem. Rev.* **2022**, *122*, 2017–2291.

[12] E. Tsui, A. J. Metrano, Y. Tsuchiya, R. R. Knowles, *Angew. Chem. Int. Ed.* **2020**, *59*, 11845–11849; *Angew. Chem.* **2020**, *132*, 11943–11947.

[13] C. B. Roos, J. Demaerel, D. E. Graff, R. R. Knowles, *J. Am. Chem. Soc.* **2020**, *142*, 5974–5979.

[14] X.-Z. Fan, J.-W. Rong, H.-L. Wu, Q. Zhou, H.-P. Deng, J. D. Tan, C.-W. Xue, L.-Z. Wu, H.-R. Tao, J. Wu, *Angew. Chem. Int. Ed.* **2018**, *57*, 8514–8518; *Angew. Chem.* **2018**, *130*, 8650–8654.

[15] C. Chen, T. Shi, W. Chang, J. Zhao, *ChemCatChem* **2015**, *7*, 724–731.

[16] G. Laudadio, Y. Deng, K. v. d. Wal, D. Ravelli, M. Nuño, M. Fagnoni, D. Guthrie, Y. Sun, T. Noël, *Science* **2020**, *369*, 92–96.

[17] A. Savateev, I. Ghosh, B. König, M. Antonietti, *Angew. Chem. Int. Ed.* **2018**, *57*, 15936–15947; *Angew. Chem.* **2018**, *130*, 16164–16176.

[18] E. J. Rabe, K. L. Corp, X. Huang, J. Ehrmaier, R. G. Flores, S. L. Estes, A. L. Sobolewski, W. Domcke, C. W. Schlenker, *J. Phys. Chem. C* **2019**, *123*, 29580–29588.

[19] K. L. Corp, E. J. Rabe, X. Huang, J. Ehrmaier, M. E. Kaiser, A. L. Sobolewski, W. Domcke, C. W. Schlenker, *J. Phys. Chem. C* **2020**, *124*, 9151–9160.

[20] D. Hwang, C. W. Schlenker, *Chem. Commun.* **2021**, *57*, 9330–9353.

[21] Q. Yang, G. Pan, J. Wei, W. Wang, Y. Tang, Y. Cai, *ACS Sustainable Chem. Eng.* **2021**, *9*, 2367–2377.

[22] A. Vijeta, E. Reisner, *Chem. Commun.* **2019**, *55*, 14007–14010.

[23] A. J. Rieth, Y. Qin, B. C. M. Martindale, D. G. Nocera, *J. Am. Chem. Soc.* **2021**, *143*, 4646–4652.

[24] S. Das, K. Murugesan, G. J. Villegas Rodríguez, J. Kaur, J. P. Barham, A. Savateev, M. Antonietti, B. König, *ACS Catal.* **2021**, *11*, 1593–1603.

[25] P. Zhang, Y. Wang, J. Yao, C. Wang, C. Yan, M. Antonietti, H. Li, *Adv. Synth. Catal.* **2011**, *353*, 1447–1451.

[26] Y. Markushyna, P. Lamagni, C. Teutloff, J. Catalano, N. Lock, G. Zhang, M. Antonietti, A. Savateev, *J. Mater. Chem. A* **2019**, *7*, 24771–24775.

[27] S. Mazzanti, C. Schritt, K. Brummelhuis, M. Antonietti, A. Savateev, *Exploration* **2021**, *1*, 20210063.

Research Articles

Angewandte
International Edition **Chemie**

[28] H. Zhou, S. Mu, B.-H. Ren, R. Zhang, X.-B. Lu, *Green Chem.* **2019**, *21*, 991–994.

[29] a) V. A. Nair, S. M. Mustafa, M. L. Mohler, J. T. Dalton, D. D. Miller, *Tetrahedron Lett.* **2006**, *47*, 3953–3955; b) J. M. Cox, H. D. Chu, C. Yang, H. C. Shen, Z. Wu, J. Balsells, A. Crespo, P. Brown, B. Zamlynny, J. Wiltsie, J. Clemas, J. Gibson, L. Contino, J. Lisnock, G. Zhou, M. Garcia-Calvo, T. Bateman, L. Xu, X. Tong, M. Crook, P. Sinclair, *Bioorg. Med. Chem. Lett.* **2014**, *24*, 1681–1684.

[30] V. Yeh, R. Iyengar, *Comprehensive Heterocyclic Chemistry III*, Elsevier, Amsterdam, **2008**, pp. 487–543.

[31] Y. Cao, K. Suzuki, T. Tajima, T. Fuchigami, *Tetrahedron* **2005**, *61*, 6854–6859.

[32] J.-C. Gramain, R. Remuson, *J. Chem. Soc. Perkin Trans. 1* **1982**, 2341–2345.

[33] a) W. Huang, M. Wang, H. Yue, *Synthesis* **2008**, 1342–1344; b) S. Biswas, H. S. Khanna, Q. A. Nizami, D. R. Caldwell, K. T. Cavanaugh, A. R. Howell, S. Raman, S. L. Suib, P. Nandi, *Sci. Rep.* **2018**, *8*, 13649; c) J. Sperry, *Synthesis* **2011**, 3569–3580.

[34] a) K. C. Nicolaou, C. J. Mathison, *Angew. Chem. Int. Ed.* **2005**, *44*, 5992–5997; *Angew. Chem.* **2005**, *117*, 6146–6151; b) W. Lu, C. Mei, Y. Hu, *Synthesis* **2018**, *50*, 2999–3005.

[35] I. Ghosh, J. Khamrai, A. Savateev, N. Shlapakov, M. Antonietti, B. Konig, *Science* **2019**, *365*, 360–366.

[36] A. Savateev, D. Dontsova, B. Kurpil, M. Antonietti, *J. Catal.* **2017**, *350*, 203–211.

[37] Z. Chen, A. Savateev, S. Pronkin, V. Papaefthimiou, C. Wolff, M. G. Willinger, E. Willinger, D. Neher, M. Antonietti, D. Dontsova, *Adv. Mater.* **2017**, *29*, 1700555.

[38] A. Savateev, S. Pronkin, J. D. Epping, M. G. Willinger, C. Wolff, D. Neher, M. Antonietti, D. Dontsova, *ChemCatChem* **2017**, *9*, 167–174.

[39] M. Sender, D. Ziegenbalg, *Chem. Ing. Tech.* **2017**, *89*, 1159–1173.

[40] P. G. M. Wuts, *Greene's Protective Groups in Organic Synthesis*, 5th ed., Wiley, Hoboken, **2014**.

[41] V. S. Martín, J. M. Palazón, C. M. Rodríguez, C. R. Nevill, D. K. Hutchinson, *Encyclopedia of Reagents for Organic Synthesis*, Wiley, Hoboken, **2013**.

[42] A. Savateev, N. V. Tarakina, V. Strauss, T. Hussain, K. ten Brummelhuis, J. M. Sánchez Vadillo, Y. Markushyna, S. Mazzanti, A. P. Tyutyunnik, R. Walczak, M. Oschatz, D. M. Guldi, A. Karton, M. Antonietti, *Angew. Chem. Int. Ed.* **2020**, *59*, 15061–15068; *Angew. Chem.* **2020**, *132*, 15172–15180.

[43] a) Y. Zhang, C. Ye, S. Li, A. Ding, G. Gu, H. Guo, *RSC Adv.* **2017**, *7*, 13240–13243; b) F. Stracke, M. Heupel, E. Thiel, *J. Photochem. Photobiol. A* **1999**, *126*, 51–58.

[44] a) J.-C. Gramain, R. Remuson, Y. Troin, *J. Chem. Soc. Chem. Commun.* **1976**, 194–195; b) J.-C. Gramain, R. Remuson, Y. Troin, *Tetrahedron* **1979**, *35*, 759–765.

[45] A. Galushchinskiy, K. ten Brummelhuis, M. Antonietti, A. Savateev, *ChemPhotoChem* **2021**, *5*, 1020–1025.

[46] a) G. Kresse, J. Furthmuller, *Phys. Rev. B* **1996**, *54*, 11169–11186; b) G. Kresse, D. Joubert, *Phys. Rev. B* **1999**, *59*, 1758–1775.

[47] J. P. Perdew, K. Burke, M. Ernzerhof, *Phys. Rev. Lett.* **1996**, *77*, 3865–3868.

[48] P. Nikačević, **2023**, DOI: 10.19061/iochem-bd-1-249.

[49] A. Actis, M. Melchionna, G. Filippini, P. Fornasiero, M. Prato, E. Salvadori, M. Chiesa, *Angew. Chem. Int. Ed.* **2022**, *61*, e202210640; *Angew. Chem.* **2022**, *134*, e202210640.

[50] a) J. Heyd, G. E. Scuseria, M. Ernzerhof, *J. Chem. Phys.* **2003**, *118*, 8207–8215; b) J. Heyd, G. E. Scuseria, M. Ernzerhof, *J. Chem. Phys.* **2006**, *124*, 219906.

[51] V. W. Lau, B. V. Lotsch, *Adv. Energy Mater.* **2022**, *12*, 2101078.

[52] A. Savateev, B. Kurpil, A. Mishchenko, G. Zhang, M. Antonietti, *Chem. Sci.* **2018**, *9*, 3584–3591.

[53] T. Song, B. Zhou, G.-W. Peng, Q.-B. Zhang, L.-Z. Wu, Q. Liu, Y. Wang, *Chem. Eur. J.* **2014**, *20*, 678–682.

[54] Y. Cai, Y. Tang, L. Fan, Q. Lefebvre, H. Hou, M. Rueping, *ACS Catal.* **2018**, *8*, 9471–9476.

[55] C. R. Waidmann, A. J. M. Miller, C.-W. A. Ng, M. L. Scheuermann, T. R. Porter, T. A. Tronic, J. M. Mayer, *Energy Environ. Sci.* **2012**, *5*, 7771–7780.

[56] J. Kröger, F. Podjaski, G. Savasci, I. Moudrakovski, A. Jiménez-Solano, M. W. Terban, S. Bette, V. Duppel, M. Joos, A. Senocrate, R. Dinnebier, C. Ochsenfeld, B. V. Lotsch, *Adv. Mater.* **2022**, *34*, 2107061.

[57] I. F. Teixeira, N. V. Tarakina, I. F. Silva, N. López-Salas, A. Savateev, M. Antonietti, *Adv. Sustainable Syst.* **2022**, *6*, 2100429.

154

Contents lists available at ScienceDirect

Applied Catalysis B: Environmental

Co-doped hydroxyapatite as photothermal catalyst for selective CO_2 hydrogenation

Yong Peng [a], Horatiu Szalad [a], Pavle Nikacevic [b, c], Giulio Gorni [d], Sara Goberna [a], Laura Simonelli [d], Josep Albero [a], Núria López [b], Hermenegildo García [a]

[a] Instituto Universitario de Tecnología Química (CSIC-UPV), Universitat Politècnica de València, Avda. De los Naranjos s/n, Valencia 46022, Spain
[b] Institut Català d´Investigació Química (ICIQ), The Barcelona Institute of Science and Technology (BIST), Avda. Països Catalans 16, Tarragona 43007, Spain
[c] Universitat Rovira i Virgili (URV), Carrer de l´Escorxador s/n, Tarragona 43003, Spain
[d] ALBA Synchrotron Light Facility, Carrer de la Llum 2-26, Cerdanyola del Vallès 08290, Spain

ARTICLE INFO

ABSTRACT

The rational design and in deep understanding of efficient, affordable and stable materials to promote the light-assisted production of fuels and commodity chemicals is very appealing for energy crisis and climate change amelioration. Herein, we have prepared a series of Co-doped hydroxyapatite (HAP) catalysts with different Co content. The materials structure has been widely investigated by XRD, FT-IR, HRTEM, XPS, XAS, as well as computational simulations based on Density Functional Theory (DFT) with PBE functional. At low Co loading, there is a partial substitution of Ca cations in the HAP structure, while higher loadings promote the precipitation of small (~ 2 nm) Co nanoparticles on the HAP surface. For the optimal Co content, a constant CO rate of 62 mmol·g^{-1}·h^{-1} at 1 sun illumination and 400 °C, with the material being stable for 90 h. Visible and NIR photons have been determined responsible of the light-assisted activity enhanced. Mechanistic studies based on both experimental and DFT simulations show that H_2 preferentially adsorbs to metallic Co, while CO_2 adsorbs to the HAP surface oxygen. Moreover, both direct photo- and plasmon-driven contributions have been separated in order to study their mechanisms independently.

1. Introduction

Photocatalytic reduction of abundant resources, such as H_2O, N_2 or CO_2 has been proposed as an attractive approach for the environmentally friendly and sustainable production of high added-value fuels and chemicals.[1–5] Unlike other chemical processes, photocatalysis can directly utilize natural sunlight as a driving force to perform the chemical transformations without the need for prior light-to-electricity conversion by means of photovoltaic devices or wind turbines [6–8].

Photochemical solar fuel production is currently limited by the low light-to-chemical efficiency and the fact that in semiconductor-based photocatalysts[9] light harvesting is usually limited to UV and visible blue light.[1] In the semiconducting photocatalyst, photons with energy equal to or greater than the semiconductor band gap are converted into electron/hole pairs, the bottlenecks being to increase the efficiency of charge separation and to slow down the recombination kinetics to give change for electron transfer with substrates adsorbed on the particle surface.

As an alternative mechanism to the classical photoinduced charge separation in semiconductors,[10,11] photons from the visible and near infrared (NIR) region can interact with metal nanoparticles supported on thermally insulating materials[12] by the localized metal surface plasmon resonance (LSPR). In this pathway, photon absorption increases the catalytic conversion rates at the metal nanoparticle by the localized heating due to thermalization of the photon energy and generation of "hot carriers" that influence the electronic structure of the species involved in the reaction.[13–15] For example, Feng et al. reported a plasmonic structure of porous silica needles containing Co nanoparticles.[16] This photocatalyst absorbs light over the entire solar spectrum and promotes efficient photothermal of CO_2 to CO and CH_4 with a conversion rate of 0.61 mol·g^{-1}·h^{-1} without external heating under 20 Suns of illumination. Alternatively, Guo et al. developed a Cu-substituted hydroxyapatite (HAP) catalyst that exhibited very high activity in the reverse water gas shift (RWGS) reaction,[17] with a CO production rate of 0.9 mmol·g^{-1}·h^{-1} under 40 suns light irradiation and without external heating.

In fact, HAP $(Ca_{10}(PO_4)_6(OH)_2)$ is a well-known structure that can be found in nature as minerals or in bones and animal teeth. These materials can be easily prepared in large-scale from abundant raw materials,[16] allowing a large number of partial cation substitutions due to their high stability and structural flexibility.[18] Thus, Ca ions can be partially replaced by various divalent cations, such as Sr^{2+}, Ba^{2+}, Zn^{2+}, Cu^{2+}, or Co^{2+}. Moreover, they are thermally isolating materials, which make HAP very promising candidates as photothermal catalysts.

Herein, we have prepared a series of Co-doped HAP photocatalysts with increasing Co content for the selective gas-phase continuous flow CO_2 hydrogenation. CoHAP is a highly active and CO-selective photothermal CO_2 hydrogenation catalyst when exposed to 1 sun and controlled external heating. Mechanistically, we have isolated both direct photo- and plasmon-driven mechanisms in order to study them separately. Moreover, it has been revealed that the mechanisms occur depending on the Co doping level, reaching a maximum CO rate of 62 mmol·g^{-1}·h^{-1} at 1 sun illumination and 400 °C, with the material being stable for 90 h operation under continuous flow. These results pave the way for the design of efficient, affordable and stable materials to promote the light-assisted production of fuels and commodity chemicals.

2. Experimental section

2.1. Materials preparation

The synthesis of Co$_x$HAP catalysts followed a coprecipitation route as previously reported.[17] In a general procedure, the $Ca(NO_3)_2$ and $Co(NO_3)_2$ salts, with a Co to Ca atomic ratio equal to x% were solubilized in 100 mL of Milli-Q water. The pH of this solution was then adjusted to 10–11 by dropwise addition of an ammonium hydroxide solution. Then, 100 mL of a previously prepared phosphate solution (0.4 wt%) containing a stoichiometric amount of phosphate with respect to the total cations was added dropwise with vigorous stirring. The resulting suspension was then heated to 90 °C and stirred continuously for another 2 h, after which both heating and stirring were stopped. The solid was aged overnight, filtered, and dried in an electric oven at 100 °C. The prepared solid was then ground to a fine powder and calcined at 500 °C for 5 h at a heating rate of 2 °C/min, unless otherwise specified.

2.2. Characterization

Powder X-ray diffraction (PXRD) patterns were recorded on a Shimadzu XRD-7000 diffractometer by using Cu κ_α radiation ($\lambda = 1.5418$ Å), operating at 40 kV and 40 mA at a scan rate of 10° per min in the 2–90° 2θ range. Transmission electron microscopy (TEM) images were obtained using a Philips CM300 FEG microscope operating at 200 kV, coupled with an X-Max 80 energy dispersive X-ray (EDX) detector (Oxford instruments). The microscope is equipped with the STEM unit, the dark-field and high-angle field (HAADF) image detectors. The SEM images were collected with a JEOL JSM 6300 instrument equipped with an Oxford Instruments X-MAX detector. Co and Ca contents were determined by inductively coupled plasma-optical emission spectrophotometry (ICP-OES, Varian 715-ES, CA, USA). Diffuse reflectance UV/Vis spectra (DRS) in the 200–2000 nm range were collected in a Varian Cary 5000 spectrophotometer. X-ray photoelectron spectra (XPS) were measured on a SPECS spectrometer equipped with a Phoibos 150 MCD-9 detector using a nonmonochromatic X-ray source (Al) operating at 200 W. Samples for XPS were activated *in-situ* at 400 °C for 2 h in a pre-chamber under at 1×10^{-9} mbar prior to measurement. Fitting of the experimental data to individual components was calculated from the area of the corresponding peaks after nonlinear background subtraction of the Shirley type. Atomic ratios of the different elements were determined from the areas of the corresponding XPS

peaks, corrected by the response factor of the spectrometer. The *in-situ* FTIR spectra were collected with a Bruker "Vertex 70″ and a Thermo Nicolet 8700 spectrophotometer equipped with a DTGS detector (4 cm^{-1} resolution, 32 scans). An IR cell allowing *in situ* treatments under controlled atmosphere and temperature from 25 to 500 ºC was connected to a vacuum system with gas dosing device. Self-supporting pellets (approximately 10 mg cm^{-2}) were prepared from the sample powders by compaction and treated in a hydrogen stream (30 mL min^{-1}) at 400 ºC for 2 h before testing. *In-situ* Raman spectra were obtained using a Renishaw "*in Via*" spectrophotometer equipped with an Olympus optical microscope. Samples were pretreated with H_2 at 400 °C for *in-situ* activation prior to spectrum collection. The H_2 desorption was monitored with a thermal conductivity detector (TCD) and a mass spectrometer following the characteristic mass of H_2 at 15 a.m.u. The CO_2 adsorption isotherms in the low-pressure range were measured in a Micromeritics ASAP 2010 instrument using ~200 mg of catalyst placed on a sample holder, which was then immersed in a liquid circulation thermostatic bath for precise temperature control. Prior to each measurement, the sample was treated overnight at 350 °C under vacuum and then measured at 0 °C.

The Co and Ca K-edge absorption spectra were collected at room temperature at the CLAESS beamline of the ALBA synchrotron.[19] The beam was monochromatized by means of a Si(111) double crystal monochromator, while the higher harmonics were rejected by choosing the correct angle and coating of the collimating and focusing mirrors. Data analysis was performed according to standard procedure using the Demeter XAS package[20]. The Fourier Transforms (FTs) of the Co and Ca K-edge EXAFS oscillations were extracted in the k-range of $2.43 − 9$ Å^{-1} and the R-range between 1.3 and 23 Å with a Hanning window function. The available k ranges do not allow for modeling due to the correlations existing between the parameters. While quantification is not available, the data allow for a qualitative comparison as commented below.

2.3. Photo-assisted CO_2 hydrogenation

The photo-assisted CO_2 hydrogenation reactions were carried out in a customized glass flow reactor, as previously reported by our group. [21] Specifically, the reactor is wrapped with a heating ribbon and the temperature is controlled by a K-type thermocouple measuring the temperature of the catalyst surface. The catalyst surface is irradiated by a light beam introduced through a quartz optical fiber. In a typical test, 100 mg of catalyst was loaded onto the porous frit bed of the flow reactor and activated *in-situ* at 400 °C for 2 h. The feeding gas of CO_2 and H_2 was then introduced from the bottom of the reactor and flowed through the illuminated photocatalyst bed. The products were analyzed online using Varian gas chromatography (TCD detector and Carboxen®−1010 PLOT Capillary GC Column, L × I.D. 30 m × 0.53 mm, average thickness 30 μm).

3. Results and discussion

3.1. Materials preparation and characterization

Co-doped HAP (Co$_x$HAP) samples with different Co/Ca ratios (5, 10, 15 and 20 mol%) were prepared according to the synthetic procedure described in detail in the Experimental Section and illustrated in Scheme 1. For comparison purposes, HAP without Co was also prepared using an identical procedure. The final Co content in the Co$_x$HAP samples was determined by ICP-OES, resulting in a Co loading in Co$_x$HAP (x $\in$ {5, 10, 15, 20}) of 3.46, 5.88, 8.75 and 11.38 wt%, respectively.

XRD patterns confirmed the successful formation of HAP with hexagonal structure (JCPDS No. 09–0432, Fig. S1 in Supporting Information). The experimental as well as the simulated (Fig. S2) XRD of Co$_5$HAP and Co$_{10}$HAP show very similar patterns to HAP, although
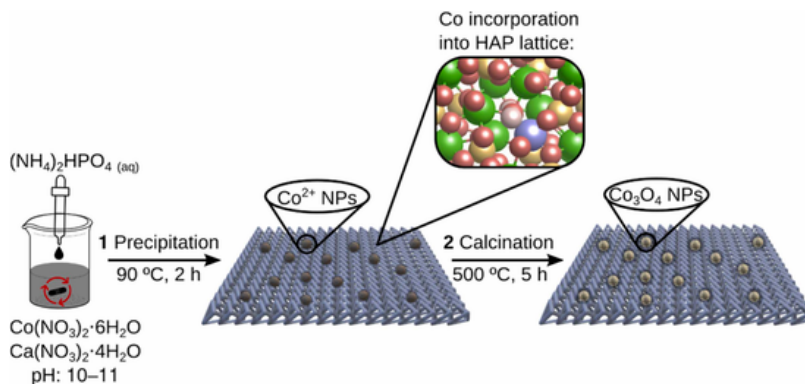
Scheme 1. Co_xHAP preparation procedure including precursor precipitation (**1**) and subsequent calcination (**2**). Color code O: red, Co: purple, Ca: green, P: orange and H: white.

the diffraction peaks become broader, indicating lower crystallinity. Higher Co loadings, as in $Co_{15}HAP$ and $Co_{20}HAP$ samples, resulted in the disappearance of the HAP diffraction peaks (Fig. S1). These XRD data suggest that at low Co/Ca ratios, Co can be incorporated into the HAP structure with some distortion of the crystal lattice as a consequence of the ionic radius difference between Ca^{2+} and Co^{2+},[18] while further Co addition promotes phase segregation with a lack of crystallinity.

Despite the significant structural changes upon Co loading, the BET surface area and the average pore size of the Co_xHAP samples, determined by isothermal N_2 adsorption-desorption measurements, remain very similar (see Fig. S3 and Table S1). The large surface area values of these Co_xHAP samples are due to the reticular structure, as confirmed by HR-FESEM (Fig. S4). Furthermore, elemental mapping from a selected HR-FESEM image shows that Co is homogeneously distributed throughout the whole particle (Fig. S5).

Besides XRD, the changes in the HAP structure upon Co^{2+} loading can also be observed by Fourier-transformed infrared spectroscopy (FT–IR) (Fig. S6). The FT–IR spectrum of HAP shows the typical asymmetric stretching and bending modes of PO_4^{3-} groups in the range of 951–1124 cm^{-1} and 529–611 cm^{-1}, respectively,[22] and the characteristic ·OH vibrational bands at ~3563 (ν_{OH}) and 630 cm^{-1} (δ_{OH}).[23] Upon Co^{+2} loading, the bands of both vibrational and bending modes of PO_4^{3-} gradually become broader, reflecting the distortion of the PO_4^{3-} configuration, probably due to the replacement of Ca^{2+} by Co^{2+} ions. In addition, the loss of the -OH signal and the appearance of an HPO_4^{2-} band at ~2924 cm^{-1} suggest a cationic deficiency in the structure.

The catalyst structure was further investigated using computational simulations based on Density Functional Theory (DFT) with PBE functional.[24] Co-doped HAP was modeled as (0001) surface slab of HAP, [25,26] with one calcium atom substituted by cobalt (Fig. S7a). The doping site was determined to segregate toward the surface by comparing the relative energies of substitution of calcium ions by cobalt at different positions (Fig. S8). Metallic cobalt, as in the nanoparticles (*vide infra*) was modeled as the lowest-energy (0001) facet of hcp–Co (Fig. S7b). Optimized structures were in good agreement with the experimental measurements and were subsequently used to elucidate the reaction mechanism.

In order to further investigate the bulk structural characteristics in Co_xHAP samples, X-ray absorption spectroscopy (XAS) measurements were performed for CaHAP, Co_5HAP and $Co_{15}HAP$ (Fig. 1). The XANES Co K-edge spectra of Co_xHAP samples and Co^{2+} references (CoO, $Co(OH)_2$, Co_3O_4) and their corresponding first derivatives are shown in Fig. 1a. The common rising edge at around 7716 eV indicates a Co oxidation state close to 2 + , which is consistent with the most stable DFT-

obtained magnetic moments for the Co atoms of 3 μ_B (high-spin d^7) and 1 μ_B (low-spin d^7).[16] However, some differences in the rising edges can be observed at higher energies due to the different Co local environment. The rising edge of $Co_{15}HAP$ samples is shifted to lower energy with respect to $Co(OH)_2$ and Co_3O_4 references, which is consistent with a lower oxidation state of Co or an elongated Co–O local bond. In addition, Co_5HAP shows a shift in spectral weight from lower (7716 eV) to higher (7721 eV) energies, indicating structural changes with increasing Co incorporation. The global Co K-edge XANES shape is compatible with the Co per Ca replacement due to its similarity to the Ca K-edge XANES shown in Fig. 1c. The slight increase in spectral weight around 7727 eV for the highest Co content could be compatible with the presence of Co_2O_3 impurities.

It is also worth noticing that the Co k-edge pre-peak intensity slightly decreases for the Co5HAP sample (see Fig. S9 **a**), in agreement with the expansion of the first shell (Fig. S9 **c**), which corresponds to a reduced hybridization between the Co 3d and the ligand p states. The filling of the gap between the Co K-edge pre-peak and the rising edge (around 7711 eV) after the reaction (green curve) could correspond to intra-site excitation, as reported earlier.[27] The Co k-edge pre-peak shifts toward higher energy in the Co5HAP is compatible with a different 3d levels configurations, which could depend from a change in the oxidation state, local magnetic moment, or local geometry. The shift of the rising edge inflection points toward higher energies (Fig. S9 **b**) could support a slight global increase in the cobalt oxidation state for the Co5HAP once compared with the Co15HAP sample.

The Fourier Transforms of the measured (Fig. 1**b**) and simulated (Fig. S10) EXAFS Co-K edge show a broad first shell peak (Co–O ~ 1.5 Å) and a strong damping of the more distant contributions. $Co_{15}HAP$ samples appear to have a contracted first shell (smaller Co–O distance). It is known from the literature that the replacement of Ca by ions with smaller ionic radius provokes a decrease in cell volume due to the smaller ionic radius and the more electronegative character of Co^{2+} compared to Ca^{2+},[18,28–30] while the incorporation of 3d-metal ions into the hexagonal channel of the apatite structure causes instead the expansion of the unit cell.[31,32] Therefore, the contraction of the Co–O first shell at low cobalt content in the structure suggests that when the content is low Co ions are incorporated into the hexagonal channel of the structure replacing some Ca positions, resulting in a unit cell contraction. The unit cell contraction of 1% (along the *b* direction) was also predicted by the DFT simulations (Table S2).

On the other hand, the FT signal corresponding to the second shell (Co–P ~ 2.3 Å) decreases in intensity with increasing the Co content in the calcined samples (from Co_5HAP to $Co_{15}HAP$), indicating a less ordered structure. This disorder increase correlates well with the ob-

3

Fig. 1. XANES Co K-edge spectra (a) and their first derivatives (inset) as well as the corresponding Fourier transforms (b) of the different Co$_x$HAP samples studied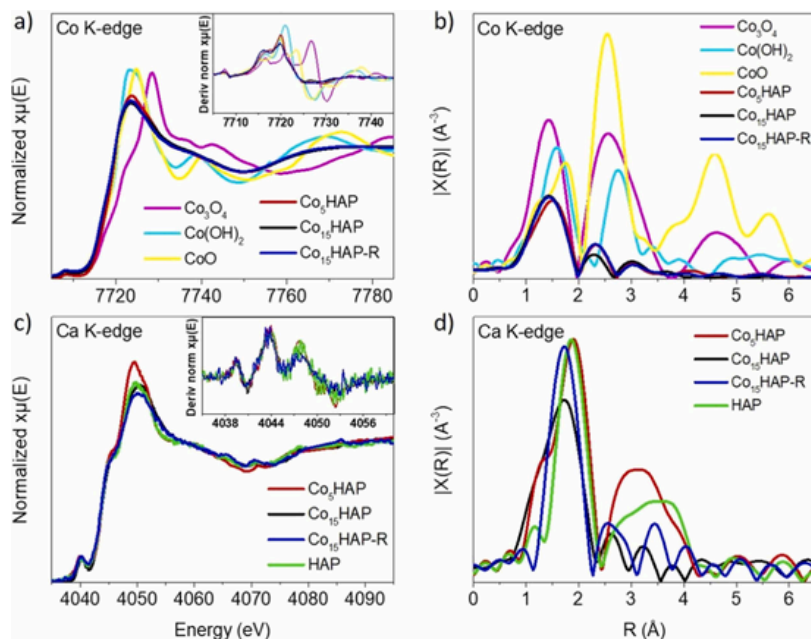. XANES Ca K-edge spectra (c) and their first derivatives (inset) as well as the corresponding Fourier transforms (d) of the different Co$_x$HAP samples studied.

served broadening of the XRD peaks, indicating a decrease in crystallinity with increasing Co incorporation. The Co$_{15}$HAP sample shows increased intensity on the FT second shell (Co-P ~ 2.3 Å) feature after the H$_2$ reduction, while the first shell signal remains unchanged. This suggests some sort of activation process that induces local ordering on the Co–P network.

The XANES Ca K-edge spectra of Co$_x$HAP samples (Fig. 1c) are similar to those of HAP, except that the energy position of the white line (at ~4050 eV) of samples with higher Co content (Co$_{15}$HAP) that shifts to higher energies with respect to the other samples, which may be indicative of local contraction. The pre-edge region at 4039.5 eV due to the 1 s → 3d electron transition, which is sensitive to the local distortion around calcium sites, is nearly identical regardless of Co content, suggesting that the local environment of Ca atoms is approximately the same in all Co$_x$HAP samples.

The Fourier Transforms of the measured and simulated EXAFS Ca-K edge spectra are shown in Fig. 1d and Fig. S9, respectively. For Co$_5$HAP, the first Ca–O shell (~ 1.8 Å) appears to be nearly coincident to that of HAP. However, the Co$_{15}$HAP sample shows a contracted first shell (smaller R distance). It is clear that the first shells around both Ca and Co contract by increasing the amount of Co incorporated into the HAP lattice, probably due to a contraction of the lattice parameters as a consequence of a high degree of Ca^{2+}-by-Co^{2+} substitution. It is noteworthy that the intensity of the FT signals is significantly lower in the case of Co$_{15}$HAP. The decrease in intensity could reflect a loss of order around calcium due to structural distortions of the HAP lattice caused by the increasing Co incorporation. This effect agrees well with the XRD data, showing a loss of crystallinity at high Co content. Interestingly, for the Co$_{15}$HAP system, the FT signal of the first shell increases significantly after reduction (Co$_{15}$HAP-R) indicating an increase in local structural order, consistent with increase in the structural order in the Co–P network detected at the Co K-edge (Fig. 1b).

The particle morphology of the Co$_x$HAP samples was studied in detail by HR-TEM (Fig. 2). The HR-TEM images show lattice fringes of 0.250 and 0.291 nm, corresponding to the interplanar spacing of the

(301) and (211) facets of HAP. Interestingly, HR-TEM images of Co$_x$HAP samples revealed the presence of small and homogeneously distributed nanoparticles in the case of Co$_{10}$HAP, Co$_{15}$HAP and Co$_{20}$HAP samples. The concentration and size of these nanoparticles increased with the Co content, resulting in values of 1.0 ± 0.3, 1.3 ± 0.3 and 1.8 ± 0.5 nm for Co$_{10}$HAP, Co$_{15}$HAP and Co$_{20}$HAP, respectively, after measurement of a statistically relevant number of these nanoparticles. According to previous XAS characterization these nanoparticles correspond to Co oxides formed by the excess of Co that does not become incorporated into the HAP lattice.

However, we were not able to identify the surface Co based NPs by EDX mapping that shows a homogenous distribution of all the elements (Fig. 2 **n-r**). This EDX information is compatible with the main proportion of Co element being incorporated in the HPA lattice together with Ca, and thus results in an overall homogenous distribution of Co and Ca elements. Changes in the crystallinity upon Co loading increase reported by XRD can also be observed in electron microscopy. Specifically, CaHAP shows very high crystallinity with a few grain boundaries, but the crystalline degree decreases with the Co content. Especially, amorphous phase appears in the case of Co$_5$HAP (red arrow mark in Fig. 2d), and a more obvious mixture of crystalline and amorphous areas can be observed in Fig. 2f (Co$_{10}$HAP), which is consistent with the decrease in peak intensity and broadening of peak width in XRD. This increase in the amorphous phase domains as the Co loading increases is reflected in the case of Co$_{15}$HAP and Co$_{20}$HAP. Therefore, the lack of long-range crystallinity can be the explanation for the amorphous character of Co$_{15}$HAP and Co$_{20}$HAP samples.

The diffuse reflectance UV–vis–NIR absorption spectra of the Co$_x$HAP samples were recorded. They are shown in Fig. S11. As can be seen there, pristine HAP shows negligible absorption in the visible and NIR regions, which is consistent with its large band gap as also estimated by *GW* approximation-based simulations (band gap of 6 eV for the (0001) surface slab of HAP; Fig. S12a). In comparison, the simulations indicate that Co$_x$HAP should exhibit several additional states within the band gap (Fig. S12b),[33] allowing for specific electronic
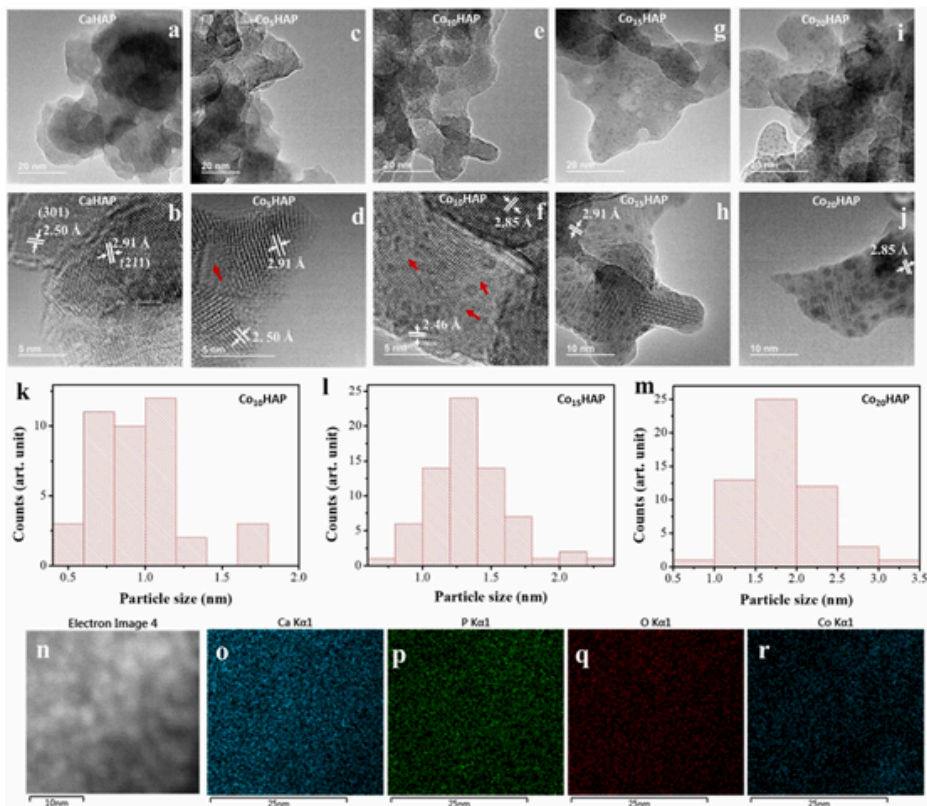
Fig. 2. HRTEM images of CaHAP (a and b), Co$_5$HAP (c and d), Co$_{10}$HAP (e and f), Co$_{15}$HAP (g and h) and Co$_{20}$HAP (i and j). (Red arrows points to the amorphous area). The histograms of nanoparticle size distribution in Co$_{10}$HAP (k), Co$_{15}$HAP (l) and Co$_{20}$HAP (m) are also shown. Images from n to r are the EDX mapping of Co$_{15}$HAP sample.

transitions. There are five new states (both occupied and empty) localized within 2 eV from the valence band maximum. In fact, Co$_5$HAP shows a continuous absorption decreasing in intensity from the UV towards the NIR zone, and a broad and low intensity band in the region from 1000 to 1800 nm with relative maxima at 1330 and 1500 nm. Interestingly, further increase in Co^{2+} content promotes a drastic change in the diffuse reflectance absorption spectra. A strong band in the visible region with three maxima at 518, 581 and 624 nm, together with two shoulders at about 412 and 748 nm were recorded in the absorption spectra of Co$_{10}$HAP, Co$_{15}$HAP and Co$_{20}$HAP. In addition, the intensity of the visible and NIR bands increased with Co^{2+} content. The shoulders observed at 412 and 748 nm were attributed to surface-anchored band gap energy transitions in Co$_3$O$_4$, as reported previously, [34] while the main absorption feature in the visible region, centered at 581 nm, could be due to new transitions in HAP upon Co^{2+} substitution. It is worth noting that this absorption band, which lacks noticeable shoulders, can also be observed in Co$_x$HAP samples before calcination (Fig. S11b), suggesting that this absorption band originates from Co^{2+} ions in HAP structure, while calcination could promote the formation of Co$_3$O$_4$ nanoparticles from the Co^{2+} excess and migration from the HAP lattice in the sample surface.

Further confirmation of Co$_3$O$_4$ nanoparticle formation in the Co$_x$HAP surface can be provided by XPS. The high-resolution XPS Co 2p spectrum of Co$_{15}$HAP and the best fit to individual components is shown in Fig. S13a. As can be seen there, the XPS Co 2p spectrum shows two major components at 782.2 eV and 798.0 eV, together with their

corresponding satellite peaks at 785.8 and 803.3 eV assigned to Co^{2+}, and two minor components at 780.9 eV and 796.7 eV assigned to Co^{3+} species.[35–37] These data confirm the presence of Co$_3$O$_4$ in the Co$_x$HAP surface, in good agreement with the diffuse reflectance UV-Vis-NIR absorption and Raman spectroscopy experiments (*vide infra*).

Overall, the characterization data support the complete incorporation of Co^{2+} into the HAP lattice in Co$_5$HAP and the coexistence of Co^{2+} in the HAP and Co oxide nanoparticles, the latter increasing in density as the Co loading in the material increases. Sample activation causes a partial migration of Co^{2+} from the HAP structure to extra-framework positions.

3.2. Photo-assisted CO$_2$ hydrogenation

Photo-assisted CO$_2$ hydrogenation reactions were carried out in continuous flow using a customized glass reactor with a thin circular (2.5 cm diameter) photocatalyst bed deposited on a porous quartz frit through which the gas flows from the bottom. The photocatalyst is illuminated from above by a quartz optical fiber inserted into the reactor (see Fig. S14 for details of the reaction setup and conditions). The temperature of the photocatalyst bed was measured under illumination and equilibrated to the desired value prior to photocatalytic hydrogenation. Irradiation was performed using the collimated output beam of a 150 W Xe lamp at 1080 W·m^{-2}, which resulted in a steady temperature of 156 °C without any external heating. Higher temperatures were

achieved using an electric heater controlled by a thermocouple placed on the photocatalyst bed.

Prior to starting the photocatalytic reactions, the Co_xHAP samples were activated *in situ* in the reactor at 400 °C for 2 h in H_2 flow. This temperature was chosen based on the thermo-programmed reduction (TPR) data shown in Fig. S15. In these TPR measurements, Co_xHAP samples exhibit weak reduction peaks at temperatures below 400 °C, while more pronounced reduction peaks appear at temperatures between 600 and 700 °C. Since the maximum reaction temperature in this study is 400 °C, no significant structural changes in the samples are expected under reaction conditions after their prior activation.

To investigate the structural changes that occur during the activation step in $Co_{15}HAP$, *quasi-in situ* XPS studies were performed to determine the changes in the XPS Co spectra. The high-resolution XPS Co 2p spectrum of activated $Co_{15}HAP$ shows no components attributable to Co^{3+}, while typical components of Co^{2+} and Co^0 were recorded at 782.2 eV and 778.0 eV, respectively (Fig. S12a). These data would indicate a reduction of Co_3O_4 nanoparticles to Co^{2+} and metallic Co^0. Our DFT simulations for CoO show that its hydrogenation to metallic Co is extremely favorable with $\Delta G = -3.21$ eV, suggesting that the hydrogenation of Co_3O_4 should also be favorable. However, it is worth noting that the Co^{2+}/Co ratio at the $Co_{15}HAP$ surface is still as high as 3.4, indicating that the Co^{2+} species in the HAP lattice remain unchanged during the treatment. These results are in good agreement with the TPR data (Fig. S15), where the reduction peaks in $Co_{15}HAP$ below 400 °C (attributed to Co_3O_4 reduction) are much smaller than those at about 650 °C, which are attributed to the massive Co^{2+} reduction to metallic Co. The high-resolution O 1 s spectra of activated and non-activated $Co_{15}HAP$ do provide a complementary information. They are shown in Fig. S13b. As can be observed there, the high-resolution XPS O 1 s spectrum of $Co_{15}HAP$ shows three main components centered at 528.8, 531.5 and 533.5 eV due to Co oxides (Co_3O_4), phosphate oxygen or hy-

droxide, and adsorbed water, respectively.[38,39] However, only one component at 531.3 eV can be observed upon activation, confirming the partial reduction of Co species. No changes in the XPS Ca 2p and P 2p spectra (Fig. S13c and **d**) indicate that the Co_xHAP structure was preserved upon activation. On the other hand, according to the diffuse reflectance UV–vis–NIR spectra, the visible absorption band derived from Co^{2+}-doping of HAP was preserved upon activation, while the features assigned to Co_3O_4 have disappeared after the activation process, in good agreement with the XPS results (Fig. S16).

Further evidence for the reduction of Co_3O_4 nanoparticles upon activation is provided by *in-situ* Raman experiments. Fig. S17 shows several Raman spectra of $Co_{15}HAP$ under H_2 flow at different temperatures. At room temperature, five Raman modes at 688, 617, 522, 479 and 192 cm^{-1} are observed, all of which are attributed to Co_3O_4, along with a weak peak at 955 cm^{-1} attributed to phosphate.[40,41] The vibrational peaks attributed to Co_3O_4 gradually disappear when the temperature reaches 300 °C, indicating Co_3O_4 reduction. On the contrary, the phosphate peak at 955 cm^{-1} remained unchanged during the *in-situ* H_2 treatment, demonstrating that the $Co_{15}HAP$ structure is preserved after activation.

The photocatalytic activity of Co_xHAP samples was first evaluated at 250 °C, either in the dark or under 1080 W/m^2 light irradiation. The results are summarized in Fig. 3a. As shown in Fig. 3a, the CO_2 conversion at 250 °C in the dark and after 1 sun irradiation using Co_5HAP was of 0.40% and 0.75%, respectively, with full (100%) selectivity toward CO. The small activity increase in light for the Co_5HAP system can be attributed to a photocatalytic enhancement of H_2 dissociation on Co-doped HAP *(vide infra)*. The CO_2 conversion increases with the Co loading up to a maximum conversion of 4.73% under 1 sun illumination, with CO selectivity above 99%, for $Co_{15}HAP$. However, only 1.1% conversion and 93% CO selectivity were achieved under dark conditions for this sample. HAP was also tested under dark and light conditions for
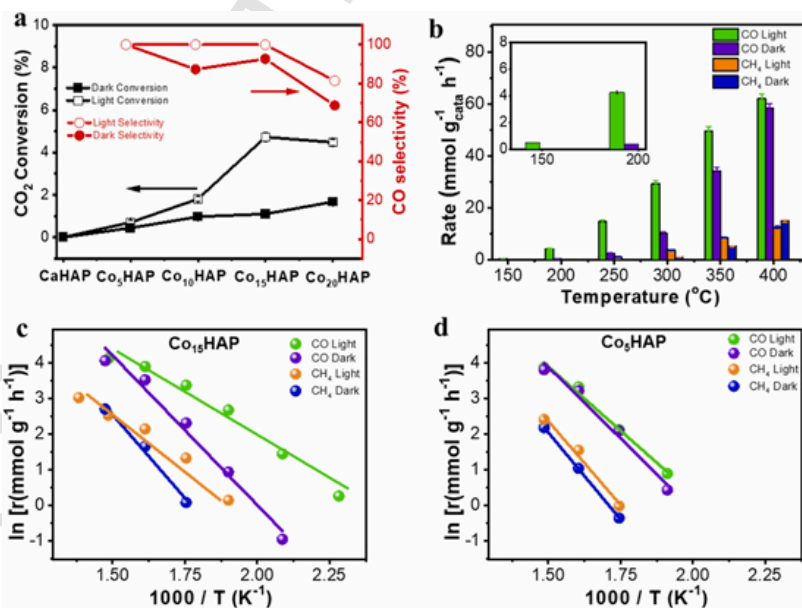

Fig. 3. (a) CO_2 conversion (black squares) and CO selectivity (red circles) of the samples studied at 250 °C under light illumination (empty circles and squares) and dark (filled circles and squares). (b) CO (green and purple columns) and CH_4 (orange and blue columns) production rates under light irradiation (green and orange) and dark (purple and blue) conditions, respectively, using $Co_{15}HAP$ at different temperatures. The inset shows magnification of the production rates at 156, 165 and 200 °C. Arrhenius plots of CO formation under light (green) and dark (purple) and CH_4 formation under light (orange) and dark (blue), respectively, obtained from the CO and CH_4 production rates at different temperatures using $Co_{15}HAP$ (c) and Co_5HAP (d). Reaction conditions: CO_2 13 mL/min + H_2 13 mL/min; 100 mg catalysts, 1080 W/m^2 light intensity.

6

CO_2 hydrogenation, but negligible amounts of CO or CH_4 were detected. Therefore, the Co species present in Co_xHAP appear to be responsible for the photocatalytic activity.

$Co_{15}HAP$ was then tested at different reaction temperatures, both under dark and one sun irradiation. As shown in Fig. 3**b**, CO evolution starts at 1080 W·m^{-2} light irradiation without external heating (T = 156 °C) and reaches 0.5 mmol·g^{-1}·h^{-1} (0.14% CO_2 conversion). In the dark at 156 °C, CO levels were below the detectable limit, and even at 200 °C under dark conditions, the CO production rate obtained (0.1 mmol·g^{-1}·h^{-1}) was still lower than that under irradiation without external heating, indicating that light effectively assists the reaction. The CO production rate increased exponentially with temperature, reaching 62 mmol of CO·g^{-1}·h^{-1} and 12.6 mmol of CH_4·g^{-1}·h^{-1} at 400 °C under one sun irradiation, corresponding to 17.8% CO_2 conversion. This CO_2 conversion is among the highest conversions in continuous flow operation at atmospheric pressure and light intensity of 1 sun using earth-abundant transition metal-based catalysts (see Table S3 for a comparison of the photocatalytic activity of $Co_{15}HAP$ with current state-of-the-art photocatalysts). It is worth noting that light irradiation resulted in an 11-fold increase in CO production under irradiation at 200 °C, while this factor decreases with temperature to ~1.2 at 400 °C. This trend can be rationalized by considering the operation of two different mechanisms. While the photocatalytic CO_2-based mechanism should predominate at low temperatures (< 250 °C) due to the negligible production rates of the purely thermo-catalytic mechanism at low temperatures, the thermo-catalytic CO production should dominate at higher temperatures, according to the Arrhenius theory. Additional experiments using isotopically labelled $^{13}CO_2$ were performed in order to rule out any carbon contamination as a source of the carbon products. The results are shown in Fig. S18. As can be seen there, only ^{13}CO was detected, confirming $^{13}CO_2$ as the main reagent and the presence of $^{13}CH_4$ was also confirmed.

Regarding the product distribution, it appears that small Co loadings favor CO selectivity, but an increase in Co content results in lower CO selectivity (up to ~70%), obtaining CH_4 as a co-product. The occurrence of an optimal Co loading could be justified by the occurrence of two opposing factors: (1) the increase in Co loading should lead to an increase in the number of active sites, resulting in higher activity, but (2) high Co loadings should also lead to larger average nanoparticle size and wider size distribution, as observed in Fig. 2, resulting in a decrease in photocatalytic activity.

The influence of temperature under light and dark conditions was further investigated. Arrhenius plots of CO and CH_4, under one sun and dark conditions, in $Co_{15}HAP$ and Co_5HAP are shown in Fig. 3**c** and **d**, respectively. The activation energies ($E_{a, app}$) for CO and CH_4 production under dark and light irradiation were calculated according to the Arrhenius equation and are summarized in Table S4. In all cases, the $E_{a, app}$ for CO formation is lower than that of CH_4, both under illuminated and dark conditions, in good agreement with the obtained production rates (Fig. 3b). On the other hand, the obtained $E_{a, app}$ for CO and CH_4 formation is higher for Co_5HAP than for $Co_{15}HAP$ under 1080 W·m^{-2} illumination, while $E_{a, app}$ values remain almost coincident in the dark. Furthermore, small differences in $E_{a, app}$ can be found for Co_5HAP under illuminated and dark conditions, while in the $Co_{15}HAP$ sample the $E_{a, app}$ under illumination is approximately half of the $E_{a, app}$ in the dark for both CO and CH_4. These results indicate a greater influence of light irradiation in $Co_{15}HAP$ than in Co_5HAP. The significant activity enhancement of light in the $Co_{15}HAP$ system can be attributed to the metallic Co nanoparticles absorbing light through the localized surface plasmon resonance (LSPR). This happens *via* two mechanisms: (1) hot carrier generation by intra/interband excitation and (2) local temperature increase.[42] The temperature increase was calculated according to ref. [43,44] and was found to be less than 1 μK. This leaves the plasmon-induced hot electron activation as the main contribution to the increased activity under illumination.

We were also interested in investigating which frequencies of the electromagnetic spectrum contribute to the photo-assisted CO_2 hydrogenation. To obtain this information, the CO production rate with $Co_{15}HAP$ and Co_5HAP was measured either with filtered light irradiation using different cut-off filters or in the dark, keeping constant the temperature at the catalyst bed at 250 °C. The results are shown in Fig. S19 **a** and **b**. As can be seen, both Co_xHAP samples behave similarly. UV light (λ < 380 nm) does not contribute significantly to the light-enhanced CO production, and the CO production rate is similar to that under dark conditions. Similarly, NIR light (λ > 830 nm) does not promote significant CO production enhancement upon irradiation. Therefore, the main contributor to the light-enhanced CO production rate appears to be the visible region. In fact, wavelengths below 455 nm only contribute a 8.9% of the total enhancement, while the remaining 90% of the light enhancement comes from the range of wavelengths between 455 and 750 nm. We have measured the UV–vis–NIR diffuse reflectance spectrum of activated $Co_{15}HAP$ ($Co_{15}HAP$-R) and compared it with the spectrum of the sample before activation (Fig. S16). As can be observed, the activated sample shows a narrower spectrum with a prominent band centered at 581 nm, but lacking the shoulders and the NIR band present in the $Co_{15}HAP$ sample before activation. These spectral changes may reflect the disappearance of the Co oxides detected in the sample prior to activation. Nevertheless, the absorption band between 450 and 750 nm in the visible region of the $Co_{15}HAP$-R spectrum is in perfect agreement with the photocatalytic activity as determined with filtered light illumination, indicating that this band in the visible region is uniquely responsible for the Co_xHAP photo-response.

3.3. Reaction mechanism

To gain additional insight into the reaction mechanism, *operando* Raman measurements were performed under reaction conditions. Fig. S20 shows the Raman spectra collected from the *in situ* activated $Co_{15}HAP$ sample under the reactant gas mixture (CO_2 at 10 mL·min^{-1} + H_2 at 10 mL·min^{-1}) at 250 °C under light irradiation and dark conditions. It can be observed that several vibrational bands are present only under light irradiation. The peaks centered at 1581 and 1414 cm^{-1} can be assigned to polydentate/bidentate carbonate species,[45] while the bands at 1698 and 1834 cm^{-1} can be assigned to CO adsorbed on metallic Co (1735 cm^{-1} by DFT) and CO_2 adsorbed on HAP at a surface oxygen site (1855 cm^{-1} by DFT), respectively. The detected species suggest that the CO_2 is bound to the catalyst surface *via* *O, forming carbonate species, which are later probably reduced by hydrogen spillover from the Co nanoparticles, forming formate species, which finally decompose to CO (Fig. S21).[46] This is in agreement with the adsorption energies obtained by DFT simulations, which show that H_2 preferentially adsorbs to metallic Co, while CO_2 adsorbs to the HAP surface oxygen (Fig. 4). Additional bands at 680 and 610 cm^{-1} were assigned to Co_3O_4, indicating partial reoxidation of the metallic Co nanoparticles under the reaction conditions, which could be attributed to oxidation by CO_2 or the evolved H_2O product.

As noted above, the $E_{a, app}$ for $Co_{15}HAP$, obtained from the Arrhenius plot (Fig. 3c), show different values under illuminated and dark conditions, *i.e.*, they are lower under light illumination. These differences in $E_{a, app}$ indicate differences in the rate-determining step for this reaction under light irradiation and dark conditions. $E_{a, app}$ was derived from temperature measurements at the catalysts bed surface. Although it has been reported that the local temperature at the nanoscale on the active sites could be higher,[47] no direct evidences has been provided. Moreover, our theoretical simulations indicate a negligible change in the local temperature, and therefore it may be reasonable to draw conclusions based on these E_a values only.

Therefore, the partial reaction orders of H_2 and CO_2 under dark and light illumination were estimated for $Co_{15}HAP$ and Co_5HAP, since this parameter is measured at a constant temperature, and is generally inde-
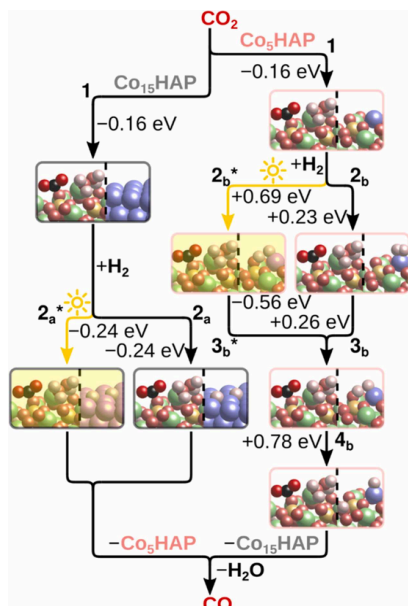
7

Fig. 4. CO_2 hydrogenation reaction pathway on $Co_{15}HAP$ (left) and Co_5HAP (right), with and without light, along with Gibbs free energy changes for selected processes. Visualized with VESTA.[48] Color code: Ca green; Co (ground state) blue; Co (excited state) pink; P yellow; O red; H white.

pendent of the reaction temperature. As shown in Fig. 5, the CO_2 reaction orders in $Co_{15}HAP$ under dark and light conditions were 0.55 and 0.64, respectively. These values are similar, indicating no significant effect of light on CO_2 activation. Similarly, Co_5HAP presents CO_2 reaction order values under dark and light conditions of 1.15 and 1.09, respec-

tively. The DFT simulations show that CO_2 binds to HAP ($\Delta G = -0.16$ eV; step **1** in Fig. 4) rather than to Co nanoparticles ($\Delta G = +1.15$ eV; Table S5), and preferentially to the pristine material than to the Co-doped material ($\Delta G = +0.54$ eV for the Co-doped HAP; Table S5). This implies that in the real system, CO_2 tends to adsorb on the HAP surface oxygen atoms far from the Co site, so that the adsorbed CO_2 and the reaction intermediates derived from it are not directly affected by the photoexcitation. On the contrary, the H_2 reaction order in $Co_{15}HAP$ changes from 0.13 to -0.51 with illumination, while the values obtained for Co_5HAP do not change much (0.31 and 0.10 in dark and light, respectively). This is consistent with the fact that H_2 preferentially adsorbs on metallic Co ($\Delta G = -0.24$ eV; step 2_a) rather than on Co-doped HAP ($\Delta G = +0.23$ eV; step 2_b) and is thus affected by the LSPR induced by light on metallic Co in the $Co_{15}HAP$ system. The more exergonic and dissociative adsorption of H_2 on metallic Co also rationalizes the higher CO_2 hydrogenation activity on $Co_{15}HAP$ compared to Co_5HAP. The negative reaction order measured for $Co_{15}HAP$ can be understood as dissociative H_2 adsorption competing with CO_2 adsorption and decreasing the reaction rate.

In addition, an estimate of the CO_2 and H_2 reaction orders of the Co nanoparticles can be obtained by subtracting the values obtained from $Co_{15}HAP$ from those the ones obtained from Co_5HAP. As can be seen in Fig. S22, the CO_2 reaction order remained very similar in light and dark conditions with values close to 1, while the H_2 reaction order was negative in both dark and light conditions. This indicates that the H_2 dissociatively adsorbed on the Co nanoparticles spills over to all the sites and competes with CO_2 adsorption and activation.

The tendency of CO_2 and H_2 to adsorb to different sites in both Co_5HAP and $Co_{15}HAP$ keeps the adsorbed reactants spatially separated, but for the reaction to occur, they must clearly come close together. This can occur if the H_2 molecule dissociates and the individual proton atoms migrate to the CO_2 adsorption sites by hopping over oxygen atoms across the HAP surface. To investigate the feasibility of this process, the dissociation of H_2 on Co-doped HAP was modeled so that a single H atom leaves the Co site and adsorbs on a distant oxygen. In the dark, H_2 was first molecularly adsorbed ($+0.23$ eV; step 2_b) and then partially dissociated ($+0.26$ eV; step 3_b) by an H atom moving to one of
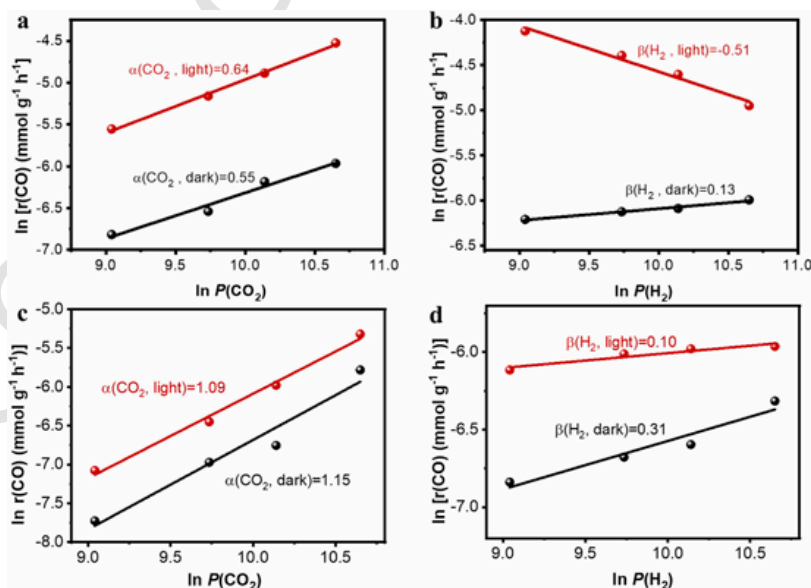

Fig. 5. Dependence of the CO production rate at 250 °C with the CO_2 partial pressure in dark (black) and light irradiation (red) (a and c) and H_2 partial pressure in dark (black) and light irradiation (red) (b and d) in $Co_{15}HAP$ (a and b) and Co_5HAP (c and d).

the three nearby oxygen atoms in the form of a hydroxyl group. With light, H_2 is directly adsorbed in the partially dissociated state (step 2_b*) because it is more stable than the molecularly adsorbed state (Table S6), indicating that irradiation facilitates H_2 dissociation. This result illustrates the photocatalytic potential of Co-doped HAP.

After the formation of the partially dissociated state, ΔG for further (complete) dissociation was found to be + 0.78 eV (step 4_b), which is a rather high barrier. However, this barrier does not take into account the configurational entropy of the dissociated state which consists of many possible microstates, since there are many surface oxygens to which the hydrogen can jump. The high dissociation entropy would make the process feasible at the temperatures at which the reaction is performed. It is important to note that while the entropic effects promote H_2 dissociation, they also tend to make H_2 and CO_2 adsorption less favorable.

Having justified the transfer of protons between different sites, the transfer of electrons between the sites still remains to be explained. The intragap states introduced by the Co doping of HAP (Fig. S11) allow an enhanced electron transfer, especially during photoexcitation. In the case of $Co_{15}HAP$, photoexcitation allows for improved hot-electron transfer from the Co nanoparticle to the HAP phase by LSPR.[49] Another way to improve light absorption and charge transfer in a semiconductor is through oxygen vacancy formation,[50] which can be facilitated by doping with transition metals.[51] Our simulations show that the Gibbs energy required to form the oxygen vacancy by the oxidation of H_2 to H_2O in Co-doped HAP is 1.1 eV, compared to 2.1 eV for the pristine HAP.

Another point to note is that the calculated energies of CO_2 adsorption on HAP refer to the systems where H_2O is adsorbed on the surface metal atom (left undercoordinated by the surface cleavage), as seen in Fig. 4. In the absence of water molecules, the adsorption is ~1 eV less favorable (in both pristine and Co-doped HAP), even though the adsorbed CO_2 does not directly interact with H_2O or the metal on which H_2O is adsorbed. This is feasible in the real system, since water adsorption is favorable for HAP even at working temperatures (ΔG = −0.23 eV; Table S5). On the other hand, H_2 does not adsorb on Co of Co-doped HAP when water already adsorbed. However, since the Gibbs free energy change of water adsorption on Co-doped HAP is not too low (ΔG = −0.26 eV), a significant number of Co sites should be left uncoordinated by water, allowing H_2 adsorption. All the computed structures can be obtained in ref. [52].

3.4. Stability

The stability of $Co_{15}HAP$ as a selective photocatalyst for CO_2 hydrogenation was evaluated by performing the CO_2 hydrogenation reaction continuously for 90 h at the highest temperature (400 °C) under light irradiation. As shown in Fig. S23, $Co_{15}HAP$ exhibited high stability under these conditions, with only a 5% activity decrease in the CO formation rate after 90 h of reaction (from 73 mmol·g^{-1}·h^{-1} to 69.3 mmol·g^{-1}·h^{-1}). The XRD pattern of $Co_{15}HAP$ after continuous reaction for 90 h at 400 °C shows the same amorphous structure, with no evidence of agglomerated Co species (Fig. S24). The high dispersity and size of Co nanoparticles in $Co_{15}HAP$ after 90 h reaction was also confirmed by HR-TEM images (Fig. S25). The high stability of the supported nanoparticles could be attributed to a strong interaction with the support as a consequence of their growth from metal excess from the lattice upon thermal treatment, as reported previously.[53] Moreover, the porous structure, morphology and surface composition of $Co_{15}HAP$ remained unchanged as evidenced by HR-FESEM images (Fig. S26) and XPS measurements (Fig. S27).

These results are particularly interesting for potential industrial applications. The characterization after 90 h of reaction at the highest temperature does not suggest any structural or morphological changes,

and therefore, it can assumed that this material could work continuously for even longer period, especially using lower temperatures.

4. Conclusion

It has been shown that the combination of framework and non-framework Co atoms in the hydroxyapatite structure renders a photocatalyst efficient to promote the light-assisted reverse water gas shift with a very high CO selectivity, which depends on the Co loading of the photocatalyst and the operating conditions. Sample characterization after the reductive H_2 activation pretreatment shows that the fine cobalt oxide nanoparticles present in Co_xHAP samples at Co loading > 5% are converted to metallic cobalt, while a significant percentage of Co^{+2} remains in the hydroxyapatite framework positions. The most active sample, $Co_{15}HAP$, is able to achieve 21.4% conversion under continuous flow and one sun illumination at 400 °C, which compares favorably with previously reported photocatalysts. At 300 °C and ambient pressure, CO formation rates up to 30 mmol$_{CO}$ g$_{catalyst}^{-1}$h^{-1} are achieved under one sun illumination, which is more than a 3-fold increase compared to the same process in the dark. The photocatalytic activity results from light absorption in the visible region and has been correlated with the presence of Co in the samples. The $Co_{15}HAP$ photocatalyst is remarkably stable, with only a 5% decrease in the CO formation rate after 90 h of operation and no observable changes in the physicochemical properties of the material. On the way to industrial application of photocatalytic processes, especially for solar fuels production, the present results show that it is possible to operate photocatalytic processes under continuous flow with high CO_2 conversions and remarkable photocatalytic activity at moderate temperatures.

CRediT authorship contribution statement

Yong Peng and Horatiu Szalad prepared the materials and performed the photocatalytic tests, Pavle Nikacevic and Núria López performed the theoretical calculations. Giulio Gorni, Sara Goberna and Laura Simonelli performed the XAS measurement and interpreted the results. Josep Albero and Hermenegildo García designed the research. The draft was written by Josep Albero and revised with the contribution of all authors.

Declaration of Competing Interest

The authors declare that they have no known competing financial interests or personal relationships that could have appeared to influence the work reported in this paper.

Data Availability

Data will be made available on request.

Appendix A. Supporting information

Supplementary data associated with this article can be found in the online version at doi:10.1016/j.apcatb.2023.122790.

References

[1] E. Gong, S. Ali, C.B. Hiragond, H.S. Kim, N.S. Powar, D. Kim, H. Kim, S.-I. In, Solar fuels: research and development strategies to accelerate photocatalytic CO$_2$ conversion into hydrocarbon fuels, Energy Environ. Sci. 15 (2022) 880–937.

[2] J. Yu, T. Zhang, N. Wu, Solar photocatalysis, Sol. RRL 5 (2021) 2100037.

[3] A. Galushchinskiy, R. González-Gómez, K. McCarthy, P. Farràs, A. Savateev, Progress in development of photocatalytic processes for synthesis of fuels and organic compounds under outdoor solar light, Energy Fuels 36 (2022) 4625–4639.

[4] Y.-H. Chen, M.-Y. Qi, Y.-H. Li, Z.-R. Tang, T. Wang, J. Gong, Y.-J. Xu, Activating two-dimensional Ti3C2Tx-MXene with single-atom cobalt for efficient CO$_2$ photoreduction, Cell Rep. 2 (2021) 100371.

[5] S.-H. Li, M.-Y. Qi, Y.-Y. Fan, Y. Yang, M. Anpo, Y.M.A. Yamada, Z.-R. Tang, Y.-J. Xu, Modulating photon harvesting through dynamic non-covalent interactions for enhanced photochemical CO$_2$ reduction, Appl. Catal. 292 (2021) 120157.

[6] N.S. Lewis, Research opportunities to advance solar energy utilization, Science 351 (2016) 1920.

[7] F. Zhang, Y.-H. Li, M.-Y. Qi, Z.-R. Tang, Y.-J. Xu, Boosting the activity and stability of Ag-Cu$_2$O/ZnO nanorods for photocatalytic CO$_2$ reduction, Appl. Catal. 268 (2020) 118380.

[8] H.-K. Wu, Y.-H. Li, M.-Y. Qi, Q. Lin, Y.-J. Xu, Enhanced photocatalytic CO$_2$ reduction with suppressing H$_2$ evolution via Pt cocatalyst and surface SiO$_2$ coating, Appl. Catal. 278 (2020) 119267.

[9] T. Inoue, A. Fujishima, S. Konishi, K. Honda, Photoelectrocatalytic reduction of carbon dioxide in aqueous suspensions of semiconductor powders, Nature 277 (1979) 637–638.

[10] L. Yuan, M.-Y. Qi, Z.-R. Tang, Y.-J. Xu, Coupling strategy for CO$_2$ valorization integrated with organic synthesis by heterogeneous photocatalysis, Angew. Chem. Int. Ed. 60 (2021) 21150–21172.

[11] K.-Q. Lu, Y.-H. Li, F. Zhang, M.-Y. Qi, X. Chen, Z.-R. Tang, Y.M.A. Yamada, M. Anpo, M. Conte, Y.-J. Xu, Rationally designed transition metal hydroxide nanosheet arrays on graphene for artificial CO$_2$ reduction, Nat. Commun. 11 (2020) 5181.

[12] M. Ghoussoub, M. Xia, P.N. Duchesne, D. Segal, G. Ozin, Principles of photothermal gas-phase heterogeneous CO$_2$ catalysis, Energy Environ. Sci. 12 (2019) 1122–1142.

[13] F. Zhang, Y.-H. Li, M.-Y. Qi, Y.M.A. Yamada, M. Anpo, Z.-R. Tang, Y.-J. Xu, Photothermal catalytic CO$_2$ reduction over nanomaterials, Chem. Catal. 1 (2021) 272–297.

[14] Y. Peng, J. Albero, A. Franconetti, P. Concepción, H. García, Visible and NIR light assistance of the N$_2$ reduction to NH$_3$ catalyzed by Cs-promoted Ru nanoparticles supported on strontium titanate, ACS Catal. 12 (2022) 4938–4946.

[15] L. Wang, M. Ghoussoub, H. Wang, Y. Shao, W. Sun, A.A. Tountas, T.E. Wood, H. Li, J.Y.Y. Loh, Y. Dong, M. Xia, Y. Li, S. Wang, J. Jia, C. Qiu, C. Qian, N.P. Kherani, L. He, X. Zhang, G.A. Ozin, Photocatalytic hydrogenation of carbon dioxide with high selectivity to methanol at atmospheric pressure, Joule 2 (2018) 1369–1381.

[16] K. Feng, S. Wang, D. Zhang, L. Wang, Y. Yu, K. Feng, Z. Li, Z. Zhu, C. Li, M. Cai, Z. Wu, N. Kong, B. Yan, J. Zhong, X. Zhang, G.A. Ozin, L. He, Cobalt plasmonic superstructures enable almost 100% broadband photon efficient CO$_2$ photocatalysis, Adv. Mater. 32 (2020) 2000014.

[17] J. Guo, P.N. Duchesne, L. Wang, R. Song, M. Xia, U. Ulmer, W. Sun, Y. Dong, J.Y.Y. Loh, N.P. Kherani, J. Du, B. Zhu, W. Huang, S. Zhang, G.A. Ozin, High-performance, scalable, and low-cost copper hydroxyapatite for photothermal CO$_2$ reduction, ACS Catal. 10 (2020) 13668–13681.

[18] L. Veselinovic, L. Karanovic, Z. Stojanovic, I. Bracko, S. Markovic, N. Ignjatovic, D. Uskokovic, Crystal structure of cobalt-substituted calcium hydroxyapatite nanopowders prepared by hydrothermal processing, J. Appl. Crystallogr. 43 (2010) 320–327.

[19] L. Simonelli, C. Marini, W. Olszewski, M. Ávila Pérez, N. Ramanan, G. Guilera, V. Cuartero, K. Klementiev, CLÆSS: The hard X-ray absorption beamline of the ALBA CELLS synchrotron, Cogent Phys. 3 (2016) 1231987.

[20] B. Ravel, M. Newville, ATHENA, ARTEMIS, HEPHAESTUS: data analysis for X-ray absorption spectroscopy using IFEFFIT, J. Synchrotron Radiat. 12 (2005) 537–541.

[21] D. Mateo, J. Albero, H. García, Titanium-perovskite-supported RuO$_2$ nanoparticles for photocatalytic CO$_2$ methanation, Joule 3 (2019) 1949–1962.

[22] J. Gómez-Morales, C. Verdugo-Escamilla, R. Fernández-Penas, C.M. Parra-Milla, C. Drouet, F. Maube-Bosc, F. Oltolina, M. Prat, J.F. Fernández-Sánchez, Luminescent biomimetic citrate-coated europium-doped carbonated apatite nanoparticles for use in bioimaging: physico-chemistry and cytocompatibility, RSC Adv. 8 (2018) 2385–2397.

[23] K. Lin, Y. Zhou, Y. Zhou, H. Qu, F. Chen, Y. Zhu, J. Chang, Biomimetic hydroxyapatite porous microspheres with co-substituted essential trace elements: Surfactant-free hydrothermal synthesis, enhanced degradation and drug release, J. Mater. 21 (2011) 16558–16565.

[24] J.P. Perdew, K. Burke, M. Ernzerhof, Generalized gradient approximation made simple, Phys. Rev. Lett. 77 (1996) 3865–3868.

[25] H. Brasil, A.F.B. Bittencourt, K.E.S. Yokoo, P.C.D. Mendes, L.G. Verga, K.F. Andriani, R. Landers, J.L.F. Da Silva, G.P. Valença, Synthesis modification of hydroxyapatite surface for ethanol conversion: The role of the acidic/basic sites ratio, J. Catal. 404 (2021) 802–813.

[26] A. Slepko, A.A. Demkov, First principles study of hydroxyapatite surface, J. Chem. Phys. 139 (2013) 044714.

[27] L. Simonelli, E. Paris, C. Iwai, K. Miyoshi, J. Takeuchi, T. Mizokawa, N.L. Saini, High resolution x-ray absorption and emission spectroscopy of LixCoO$_2$ single crystals as a function delithiation, J. Phys.: Condens. Matter 29 (2017) 105702.

[28] H.R. Low, N. Phonthammachai, A. Maignan, G.A. Stewart, T.J. Bastow, L.L. Ma, T.J. White, The crystal chemistry of ferric oxyhydroxyapatite, Inorg 47 (2008) 11774–11782.

[29] T.J. White, D. ZhiLi, Structural derivation and crystal chemistry of apatites, Acta Cryst. B 59 (2003) 1–16.

[30] K. Zhu, K. Yanagisawa, R. Shimanouchi, A. Onda, K. Kajiyoshi, Preferential occupancy of metal ions in the hydroxyapatite solid solutions synthesized by hydrothermal method, J. Eur. Ceram. 26 (2006) 509–513.

[31] P.E. Kazin, O.R. Gazizova, A.S. Karpov, M. Jansen, Y.D. Tretyakov, Incorporation of 3d-metal ions in the hexagonal channels of the Sr$_5$(PO$_4$)$_3$OH apatite, Solid State Sci. 9 (2007) 82–87.

[32] T. Baikie, S.S. Pramana, C. Ferraris, Y. Huang, E. Kendrick, K.S. Knight, Z. Ahmad, T.J. White, Polysomatic apatites, Acta Cryst. B 66 (2010) 1–16.

[33] L. Hedin, New method for calculating the one-particle green's function with application to the electron-gas problem, Phys. Rev. 139 (1965) A796–A823.

[34] C. Ravi Dhas, R. Venkatesh, K. Jothivenkatachalam, A. Nithya, B. Suji Benjamin, A. Moses Ezhil Raj, K. Jeyadheepan, C. Sanjeeviraja, Visible light driven photocatalytic degradation of Rhodamine B and Direct Red using cobalt oxide nanoparticles, Ceram. Int. 41 (2015) 9301–9313.

[35] T.J. Chuang, C.R. Brundle, D.W. Rice, Interpretation of the x-ray photoemission spectra of cobalt oxides and cobalt oxide surfaces, Surf. Sci. 59 (1976) 413–429.

[36] Y. Bi, Z. Cai, D. Zhou, Y. Tian, Q. Zhang, Q. Zhang, Y. Kuang, Y. Li, X. Sun, X. Duan, Understanding the incorporating effect of Co^{2+}/Co^{3+} in NiFe-layered double hydroxide for electrocatalytic oxygen evolution reaction, J. Catal. 358 (2018) 100–107.

[37] H. Liu, S. Cao, J. Zhang, S. Liu, C. Chen, Y. Zhang, S. Wei, Z. Wang, X. Lu, Facile control of surface reconstruction with Co^{2+} or Co^{3+}-rich (oxy)hydroxide surface on ZnCo phosphate for large-current-density hydrogen evolution in alkali, Mater 20 (2021) 100448.

[38] D. Ressnig, M. Shalom, J. Patscheider, R. Moré, F. Evangelisti, M. Antonietti, G.R. Patzke, Photochemical and electrocatalytic water oxidation activity of cobalt carbodiimide, J. Mater. Chem. A 3 (2015) 5072–5082.

[39] R. Gresch, W. Müller-Warmuth, H. Dutz, X-ray photoelectron spectroscopy of sodium phosphate glasses, J. Non-Cryst. 34 (1979) 127–136.

[40] Y. Wang, X. Wei, X. Hu, W. Zhou, Y. Zhao, Effect of formic acid treatment on the structure and catalytic activity of Co$_3$O$_4$ for N$_2$O decomposition, Catal 149 (2019) 1026–1036.

[41] U. Anjaneyulu, D.K. Pattanayak, U. Vijayalakshmi, Snail shell derived natural hydroxyapatite: effects on NIH-3T3 cells for orthopedic applications, Mater. Manuf. Process. 31 (2016) 206–216.

[42] R.C. Elias, S. Linic, Elucidating the roles of local and nonlocal rate enhancement mechanisms in plasmonic catalysis, J. Am. Chem. Soc. 144 (2022) 19990–19998.

[43] G. Baffou, R. Quidant, F.J. García de Abajo, Nanoscale control of optical heating in complex plasmonic systems, ACS Nano 4 (2010) 709–716.

[44] G. Baffou, R. Quidant, Thermo-plasmonics: using metallic nanostructures as nano-sources of heat, Laser Photonics Rev. 7 (2013) 171–187.

[45] A. Efremova, T. Rajkumar, Á. Szamosvölgyi, A. Sápi, K. Baán, I. Szenti, J. Gómez-Pérez, G. Varga, J. Kiss, G. Halasi, Á. Kukovecz, Z. Kónya, Complexity of a Co$_3$O$_4$ system under ambient-pressure CO$_2$ methanation: influence of bulk and surface properties on the catalytic performance, J. Phys. Chem. C. 125 (2021) 7130–7141.

[46] L. Liu, A.V. Puga, J. Cored, P. Concepción, V. Pérez-Dieste, H. García, A. Corma, Sunlight-assisted hydrogenation of CO$_2$ into ethanol and C2+ hydrocarbons by sodium-promoted Co@C nanocomposites, Appl. Catal. 235 (2018) 186–196.

[47] R. Verma, R. Belgamwar, V. Polshettiwar, Plasmonic photocatalysis for CO$_2$ conversion to chemicals and fuels, ACS Mater. 3 (2021) 574–598.

[48] K. Momma, F. Izumi, VESTA: a three-dimensional visualization system for electronic and structural analysis, J. Appl. Crystallogr. 41 (2008) 653–658.

[49] A. Furube, S. Hashimoto, Insight into plasmonic hot-electron transfer and plasmon molecular drive: new dimensions in energy conversion and nanofabrication, NPG Asia Mater. 9 (2017) e454-e454.

[50] P. Nikačević, F.S. Hegner, J.R. Galán-Mascarós, N. López, Influence of oxygen vacancies and surface facets on water oxidation selectivity toward oxygen or hydrogen peroxide with BiVO$_4$, ACS Catal. 11 (2021) 13416–13422.

[51] B.-H. Lee, E. Gong, M. Kim, S. Park, H.R. Kim, J. Lee, E. Jung, C.W. Lee, J. Bok, Y. Jung, Y.S. Kim, K.-S. Lee, S.-P. Cho, J.-W. Jung, C.-H. Cho, S. Lebègue, K.T. Nam, H. Kim, S.-I. In, T. Hyeon, Electronic interaction between transition metal single-atoms and anatase TiO$_2$ boosts CO$_2$ photoreduction with H$_2$O, Energy Environ. Sci. 15 (2022) 601–609.

[52] https://iochem-bd.iciq.es/browse/review-collection/100/53695/51454418e7670d87acc8905d.

[53] M. Kothari, Y. Jeon, D.N. Miller, A.E. Pascui, J. Kilmartin, D. Wails, S. Ramos, A. Chadwick, J.T.S. Irvine, Platinum incorporation into titanate perovskites to deliver emergent active and stable platinum nanoparticles, Nat. Chem. 13 (2021) 677–682.

UNIVERSITAT ROVIRA I VIRGILI
ATOMISTIC INSIGHTS INTO PHOTOCATALYTIC MECHANISMS: MODELING SELECTED PROCESSES WITH DENSITY
FUNCTIONAL THEORY
Pavle Nikačević

UNIVERSITAT
ROVIRA i VIRGILI